Anionic Synthesis of Branched Polymer Architectures and their Mechanical and Rheological Properties

Zur Erlangung des akademischen Grades eines

DOKTORS DER NATURWISSENSCHAFTEN
(Dr. rer. nat.)

von der KIT-Fakultät für Chemie und Biowissenschaften
des Karlsruher Instituts für Technologie (KIT)

genehmigte

Dissertation

von

M.Sc. Max Gerrit Schußmann
aus Weinstadt

Erster Gutachter: Prof. Dr. Manfred Wilhelm
Zweiter Gutachter: Prof. Dr. Valerian Hirschberg
Tag der mündlichen Prüfung: 05.05.2025

Die vorliegende Arbeit wurde von Februar 2022 bis März 2025 unter der Betreuung von Herrn Prof. Dr. Manfred Wilhelm am Institut für Technische Chemie und Polymerchemie (ITCP) des Karlsruher Institut für Technologie (KIT) - Universitätsbereich angefertigt.

Ich versichere hiermit wahrheitsgemäß, die Arbeit selbstständig verfasst, alle benutzten Hilfsmittel vollständig und genau angegeben, und alles kenntlich gemacht zu haben, was aus Arbeiten anderer unverändert oder mit Abänderungen entnommen wurde, sowie die Satzung des KIT zur Sicherung guter wissenschaftlicher Praxis in der jeweils gültigen Fassung beachtet zu haben.

_____

Max Gerrit Schußmann

Karlsruhe, den 13.03.2025

If I have seen further than others, it is by standing upon the shoulders of giants.

Abstract

The relationship between the molecular structure of polymers and the resulting macroscopic properties is a longstanding challenge to chemists, polymer physicists and engineers. The molecular structure like the topology or block copolymer composition determines the processing and the resulting product properties significantly. To relate the topology of a polymer chain to their properties, well-defined model systems are needed. In this present work, a new fast and scalable synthesis route is developed to access well-defined pom-pom shaped polymers with systematically varied molecular parameters for the first time. Pom-poms consist of a linear backbone with multiple arms attached at each end. The developed synthesis route utilizes a poly(2-vinylpyridine-*b*-styrene-*b*-2-vinylpyridine) triblock copolymer (P2VP-*b*-PS-*b*-P2VP) as the backbone of the pom-poms. The multi-armed stars at each end are formed by grafting living PS anions onto the short P2VP outer blocks. Because the synthesis route consists of only two reaction steps, more than 300 g of well-defined pom-poms with precisely controllable molecular weights could be synthesized in one batch.

To characterize the melt rheological behavior, the synthesized pom-poms with varying arm and backbone molecular weight, as well as different arm numbers are investigated in small amplitude oscillatory shear (SAOS), startup shear and uniaxial extension experiments. In SAOS, the relaxation behavior of the arms and the backbone was probed, confirming the predicted dynamic dilution of the backbone in the arms, and revealing differences of pom-poms to linear chains and combs. In startup shear, the dependency of the stress overshoot strain only on the arm molecular weight suggests that the orientation of the backbone chain into the flow direction is dominated by the stars at the end of the backbones and not the backbone entanglements. Additionally, a double stress overshoot was found for one sample and for pom-poms for the first time. In literature, a double stress overshoot can be found for one comb and one bidisperse linear sample. This suggests that the double stress overshoot is a universal feature for polymer samples with two sufficiently separated relaxation times. Additionally, the Cox-Merz rule, relating the absolute magnitude of the complex viscosity to the steady state shear viscosity, was found to hold true for pom-poms with an effective backbone entanglement of $Z_{b,eff} > 3$. For $Z_{b,eff} < 3$, the steady state shear viscosity is higher than the absolute magnitude of the complex viscosity. In uniaxial extension, a rise of the extensional viscosity η_E above the linear viscoelastic envelope η_{LVE}^+ (LVE) is known as strain hardening. Experimentally, it was demonstrated that the strong strain hardening shown by the pom-poms can be correctly predicted by the Considère factor $f_c = [q^2/\ln(\sqrt{3}q)]$ using the relation $\eta_E = f_c \cdot \eta_{LVE}^+$. This relation enables the prediction of the extensional viscosity over the whole relaxation range of a pom-pom using only the arm number q and the LVE obtained from small amplitude oscillatory shear. The Considère factor is also found to be equal to the maximum strain hardening factor $SHF_{max} = f_c$, which is widely used in industry to quantify strain hardening as a result of long chain branching e.g. in low density polyethylene and compare between samples.

To investigate the influence of branched topologies on block copolymers, poly(isoprene-*b*-styrene) block copolymers were synthesized with varying number of stars threaded along a backbone and varying molecular parameters. Tensile testing at room temperature revealed a strong influence of the molecular parameters on the ultimate tensile stress and strain at break. While an increase of both could be detected up to eight arm stars, no further increase was measured for fifteen arms. The ultimate tensile stress was found to increase with increasing arm molecular weight. The number of threaded stars along the backbone showed no influence on the ultimate tensile stress.

Overall, this work shows the significance of branched molecular architectures on the material properties in the melt and solid state. A new synthesis route has been developed to easily access large amounts of homo- and block copolymers with a well-defined branched topology enabling the systematic characterization. Pom-poms with systematically varying molecular parameters, narrow dispersity and topological purity were synthesized for the first time. Significant progress in the understanding of the structure-property relationship between molecular topology and melt flow behavior of branched systems has been made. This advanced fundamental understanding of polymer physics can for example in the future be used to design high-performance materials.

Kurzfassung

Die Beziehung zwischen der molekularen Struktur von Polymeren und den daraus resultierenden makroskopischen Eigenschaften ist seit der Entdeckung der Polymere eine große Herausforderung für Chemiker, Polymerphysiker und Ingenieure. Die molekulare Struktur wie zum Beispiel die Topologie oder die Zusammensetzung von Blockcopolymeren beeinflusst die Verarbeitungs- und Produkteigenschaften maßgeblich. Um die Topologie einer Polymerkette mit ihren Eigenschaften in Beziehung zu setzen, werden definierte Modellsysteme benötigt. In dieser Arbeit wurde ein neuer, schneller und skalierbarer Syntheseweg entwickelt, um gut definierte pom-pom-förmige Polymere zu erhalten. Pom-poms bestehen aus einem linearen Rückgrat an dessen Enden jeweils mehrere Verzweigungen angebracht sind. Bei der neuentwickelten Syntheseroute wird ein Poly(2-vinylpyridin-*b*-styrol-*b*-2-vinylpyridin) Triblockcopolymer (P2VP-*b*-PS-*b*-P2VP) als Rückgrat der Pom-Poms verwendet. Die Verzweigungen werden durch Aufpfropfen von lebenden Polystyrolanionen auf die kurzen, äußeren P2VP-Blöcke mit dem Rückgrat verknüpft. Aufgrund der Einfachheit der Syntheseroute und der zwei Reaktionsschritte konnten über 300 g Pom-poms in einer Charge innerhalb von wenigen Tagen hergestellt werden.

Das Fließverhalten der synthetisierten Pom-poms mit systematisch variierendem Arm- und Rückgratmolekulargewicht und Armanzahl wurde unter oszillatorischer Scherung mit kleiner Amplitude (SAOS), kontinuierlicher Scherung und uniaxialer Dehnung untersucht. Unter SAOS wurde das Relaxationsverhalten der Arme und des Rückgrats untersucht. Theoretisch vorhergesagte dynamische Verdünnung des Rückgrats in den Armen konnte bestätigt werden und Unterschiede von Pom-poms zu linearen Ketten und Kämmen aufzeigt. Unter kontinuierlicher Scherung konnte die Abhängigkeit der Dehnung am Stressmaximum nur vom Armmolekulargewicht festgestellt werden. Dies deutet darauf hin, dass die Orientierung des Rückgrats in Strömungsrichtung von den Sternen an dessen Enden dominiert wird und nicht von den Verschlaufungen des Rückgrats abhängt. Für Pom-Poms wurde zum ersten Mal ein doppeltes Stressmaximum für eine Probe gefunden. Der Vergleich mit Literaturdaten zu einer kammförmigen und einer bidispersen linearen Probe mit doppeltem Stressmaximum weist darauf hin, dass ein doppeltes Stressmaximum ein universelles Merkmal für Proben mit zwei definierten Relaxationszeiten ist, sofern die Relaxationszeiten sich ausreichend unterscheiden. Die Cox-Merz-Regel sagt aus, dass der Betrag der komplexen Viskosität und die Scherviskosität im stationären Zustand gleich ist. Für Pom-Poms mit effektiven Rückgratverschlaufungen $Z_{b,eff} > 3$ konnte festgestellt werden, dass die Cox-Merz-Regel zutrifft. Für $Z_{b,eff} < 3$ wurde festgestellt, dass die Scherviskosität höher ist als der Betrag der komplexen Viskosität. In uniaxialer Dehnung wird ein Anstieg der Dehnungsviskosität η_E über die lineare viskoelastische Einhüllende η_{LVE}^+ (LVE) als Dehnverfestigung bezeichnet. Experimentell konnte festgestellt werden, dass die Dehnverfestigung durch den Considère-Faktor $f_c = [q^2/\ln(\sqrt{3}q)]$ über die Beziehung $\eta_E = f_c \cdot \eta_{LVE}^+$ korrekt vorhergesagt werden kann. Diese gefundene Beziehung ermöglicht die Vorhersage der Dehnungsviskosität über den gesamten Relaxationsbereich eines Pom-poms, wobei nur die Armzahl q und die aus der

oszillierenden Scherung mit kleiner Amplitude gewonnene LVE verwendet werden. Zusätzlich konnte ermittelt werden, dass der Considère-Faktor gleich dem maximalen Dehnverfestigungsfaktor $SHF_{max} = f_c$ ist, welcher in der Industrie häufig zur Quantifizierung der Dehnverfestigung als Resultat von Langkettenverzweigungen wie zum Beispiel in niederdichtem Polyethylen und zum Vergleich zwischen mehreren Proben verwendet wird.

Um den Einfluss verzweigte Topologien auch in Blockcopolymeren zu untersuchen, wurde Poly(isopren-b-styrol) Blockcopolymere mit unterschiedlichen Topologien und molekularen Parametern mittels der neu entwickelten P2VP-Route und der Epoxidroute synthetisiert. Im Zugversuch zeigte sich ein starker Einfluss der molekularen Parameter auf die Bruchspannung und die Bruchdehnung. Während für Sterne mit bis zu acht Armen ein Anstieg beider Größen festgestellt werden konnte, wurde bei fünfzehn Armen kein weiterer Anstieg mehr gemessen. Die Bruchspannung nimmt mit zunehmendem Molekulargewicht der Arme zu. Die Anzahl der Sterne, die auf ein Rückgrat aufgefädelt sind, haben kein Einfluss auf die Bruchspannung.

Insgesamt konnte in dieser Arbeit die Bedeutung der verzweigten Molekülarchitektur für die Materialeigenschaften in der Schmelze und im Festkörper gezeigt werden. Es wurde eine neue Syntheseroute entwickelt, die einen einfachen Zugang zu großen Mengen gut definierter verzweigter Topologien für Homo- und Blockcopolymere ermöglicht und die systematische Charakterisierung der Pom-pom-Topologie erlaubt. Zum ersten Mal konnten monodisperse Pom-poms mit systematisch variierenden molekularen Parametern mithilfe einer neuentwickelten Syntheseroute synthetisiert werden. Bedeutende Fortschritte im Verständnis der Struktur-Eigenschafts-Beziehung zwischen molekularer Topologie und Schmelzflussverhalten verzweigter Systeme konnten erzielt werden. Dieses grundlegende Verständnis der Polymerphysik kann in Zukunft zum Beispiel für das Design von Hochleistungsmaterialien genutzt werden.

Contents

1 Introduction

Polymers have been used by mankind for centuries due to their uniquely useful combination of properties like mechanical strength and lightweight. Evidence of the use and modification of polymers goes back to the year 1000 BC. in central america.[1] Natural rubber found in the rubber tree sap was modified using carbon black and other suspended particles, and used as a ball in an ancient ball game. Only at the end of the 19th century, the scientific community started more fundamental investigations into the nature of polymeric materials. The scientific discourse culminated in an extensive debate about the potential existence of large molecules and their bonding in the 1910s. At the end of the debate, the idea of Herman Staudinger´s idea of long molecules made of small repeating units covalently linked together prevailed. Hermann Staudinger was professor for organic chemistry in Karlsruhe between 1907 and 1912.[2–4] The commercialization of the first synthetic polymers started with phenolic resins (Bakelite) at the same time. In the 1930s, many thermoplastics we still use today were commercialized such as polyvinylchloride, polyethylene, polystyrene, and polyamides.[5] The plastic materials made from these polymers are extremely versatile due to their modification possibilities on a monomer level by monomer alterations, on the molecular level by e.g. architecture or block copolymers, and on a macroscopic level through additives such as filler, softening agents, and their processing.[6]

The molecular structure of polymers can vary largely from linear polymers to star and comb shaped architectures. More complex architectures like dendrimers are also possible as well as undefined structures with randomly distributed branches as well as many more unique architectures.[7] One of the most investigated materials in polymer melt rheology is low density polyethylene (LDPE) due to its unique properties. LDPE is the second most produce plastic worldwide with 58 Mt per year in 2024.[8] LDPE is synthesized at high pressure through a free radical polymerization mechanism. Characteristic for the molecular architecture of LDPE are branches of different lengths and positions as well as branches on branches, due to termination and other side reactions like backbiting.[9] This results in a complex molecular structure of LDPE and therefore a complex melt flow behavior. In the late 1990s, research in polymer physics focused on the fundamental understanding of the influence of branches onto the flow characteristics. The goal was the prediction of the flow behavior based solely on the molecular structure. Their work started with the pom-pom topology, which consist of a linear backbone chain with multiple branches of the same length at each end as shown in Figure 1 a). The complex structure of LDPE can be reduced to an ensemble of pom-pom subunits as schematically shown in Figure 1b). The reduction to the pom-pom topology enabled the development of constitutive equations known as the pom-pom model by McLeish and Larson.[10,11] In their model, the stress response of a pom-pom to an applied deformation can be calculated with a single constitutive differential equation (see chapter 4, page 22).
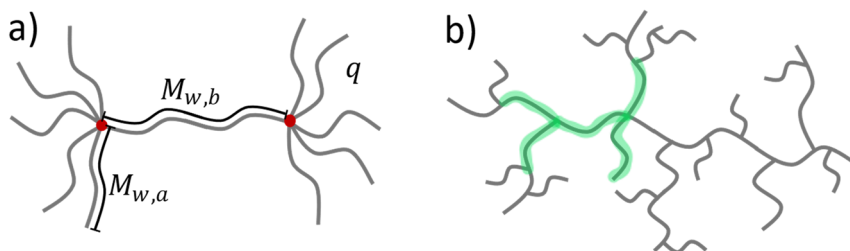
Figure 1: a) Schematic illustration of the pom-pom topology with five arms at each end of the backbone. The molecular parameters backbone molecular weight $M_{w,b}$, arm molecular weight $M_{w,a}$ and arm number q are indicated. b) Molecular structure of LDPE with a highlighted pom-pom subunit.

Only a handful pom-pom shaped polymers were be synthesized in the years following the development of the pom-pom model.[12,13] Sufficiently precise synthesis is only possible through anionic polymerization but is considered a difficult polymerization technique due to high purity requirements. Therefore, the crucial rheological experimental data on pom-pom systems required for comparison to the theoretical model is extremely limited. Comparison data is crucial to validate the assumptions in the model and the underlying polymer physics. Experimental data on homopolymer pom-poms is only available in two previous works as discussed in detail in chapter 5, page 30. The understanding of the dynamics of branched polymers can also be utilized to developed new high-performance materials. Long chain branches lead to desirable melt properties like high strain hardening and low viscosity. Based on this knowledge gap in the understanding of branched chain dynamics due to the lack of sufficient material and experimental data, this thesis focusses on the synthesis and rheological characterization of highly defined, branched polymers, particularly the pom-pom topology. A new synthesis route for branched polymers is developed to access the pom-pom topology easily and with the required purity. The new synthetic route enables a fast synthesis and systematic variation of the molecular parameters for the first time. The rheological experiments are conducted in shear and uniaxial extension on a large pom-pom data set for the first time. The data is analyzed systematically, and the findings are compared to the predictions of the existing models.

In chapter 2, polymer synthesis is introduced in general and with particular attention to branched polymers synthesized by anionic polymerization. Rheology in general and focused on polymer melts is discussed in chapter 3. Current models to describe chain dynamics in polymer melts are summarized in chapter 4. In chapter 5, the literature on branched model systems is reviewed with a focus on the used branching chemistry, chromatographical analysis, and conducted rheological experiments. In chapter 6, pom-poms are synthesized using a new, simplified and scalable route for well-defined pom-poms and other branched systems and characterized. The following chapter 7 concentrates on the rheological characterization in oscillatory shear, simple shear, and uniaxial extension and comparison of the experimental data to the pom-pom model. In chapter 8, the synthesis of branched block copolymers with varying topology is presented and their mechanical properties are investigated using tensile testing. In chapter 9, the insights of the experimental work are summarized, and the thesis is concluded by an outlook to future projects.

2 Polymer Synthesis

2.1 General Aspects of Polymer Synthesis

A polymer is a substance or material with a high relative molar mass that consists of very large macromolecules that are constituted by many covalently bound, repeating subunits, as described by the International Union of Pure and Applied Chemistry.[14] Hermann Staudinger was awarded the Nobel prize in 1953 for his works on the field of macromolecular chemistry. In his Nobel lecture, he defined macromolecules as "substances with a molecular weight greater than ten thousand [g mol^{-1}]".[4] Since the beginning of polymer science in the early 20th century by the demonstration of the existence of macromolecules by Hermann Staudinger and coworkers,[3,15] many polymerization techniques have been developed and can be classified into step growth and chain growth polymerization. Most chain growth polymerization reactions are driven by the enthalpic gain of the newly formed bonds typically by converting C=C double bonds into C-C single bonds or by releasing ring tension. Chain growth polymerization techniques can be divided into three main categories by their reaction mechanism as shown in Figure 2.[6]
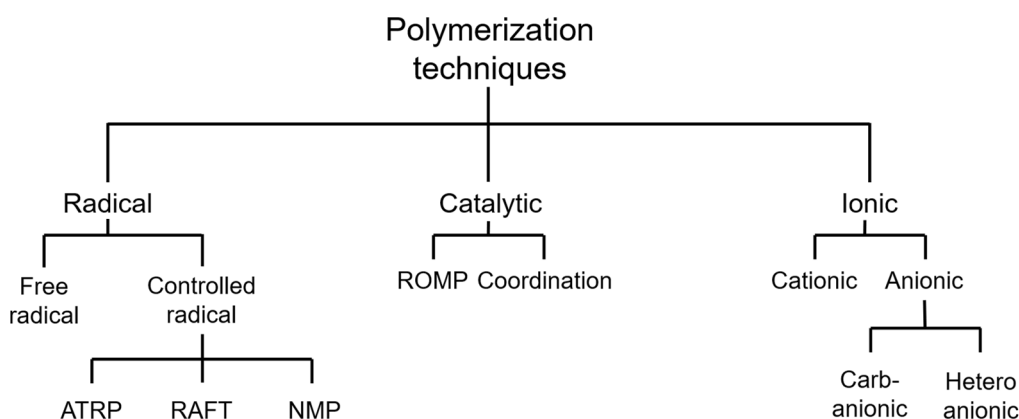

Figure 2: Overview of the developed polymerization techniques chain growth polymerizations sorted by nature of their propagating species during the polymerization. Controlled radical polymerization techniques are atom transfer radical polymerization (ATRP), reversible addition-fragmentation chain-transfer polymerization (RAFT) and nitroxide-mediated radical polymerization (NMP). Catalytic polymerization technique is either ring opening metathesis polymerization (ROMP) or coordination polymerization.

2.2 Carbanionic Polymerization

Living carbanionic polymerization was first reported by Michael Szwarc in 1956. For the first reported anionic chain-growth polymerization, sodium naphthalene was used to initiate the

polymerization of styrene through an electron transfer from the naphthalene anion onto the styrene.[16] Termination reactions, that typically occur for other non-living polymerization reactions, are prevented by the repulsive Coulomb forces of the negatively charges of the reactive species. Due to absence of termination reactions and backbiting, a low dispersity of typically $Đ = 1.01 - 1.1$ is obtained for the resulting polymers. Additionally, due to the living character of the anion complex architectures such as block copolymers and branched topologies can be easily synthesized.[7] Despite its synthetic advantage, the use of anionic synthesis in research and industry is limited with about 3 million tons annually.[17] Due to the high required purity of the reagents, anionic polymerization is intensive in time and cost. Therefore, it is only used for applications where precise chain lengths, terminal functionality, or block copolymers are needed. Industrial examples include the synthesis of block copolymers for thermoplastic elastomers, poly(ethylene oxide), and its copolymers with propylene oxide.[8,18]

Monomers and solvents used in anionic polymerization are limited by the required inertness towards the propagating anionic species. Aprotic solvents with low electrophilicity are necessary to prevent termination reactions. Frequently used monomers are vinyl monomers with electron withdrawing groups to activate the carbon-carbon double bond for nucleophilic attack of the initiator. Nucleophiles with varying strength are used as initiators. Monomers and initiators can be categorized into four different classes depending on their reactivity and are shown in Figure 3.[7]
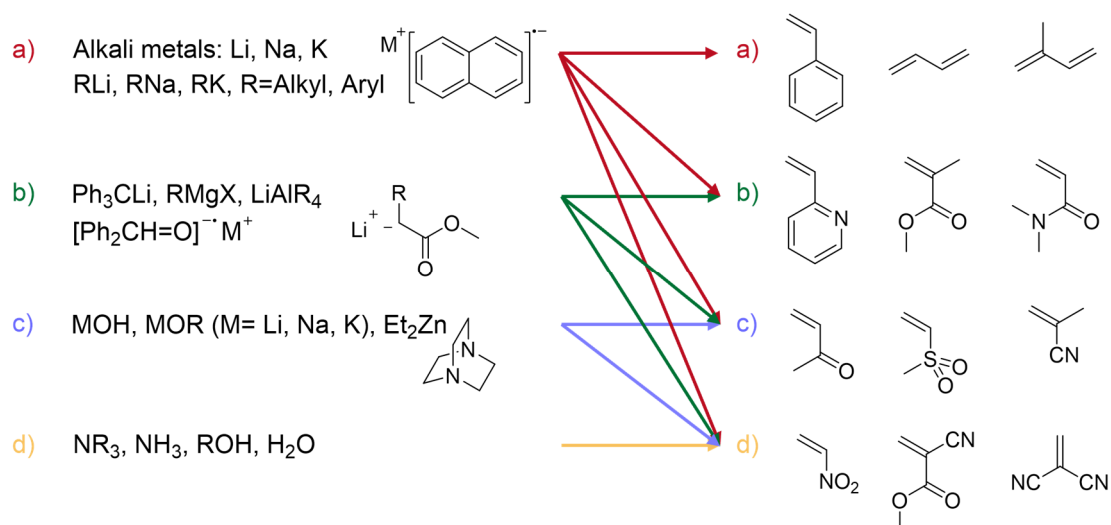

Figure 3: Left side: Initiators used for anionic polymerization. Right side: Examples of monomers typically used in anionic polymerization.

The monomer reactivity against a nucleophilic attack is directly related to the strength of the electron withdrawing group and possible mesomeric stabilization of the resulting anion. The reactivity of several monomers is given in Figure 4.
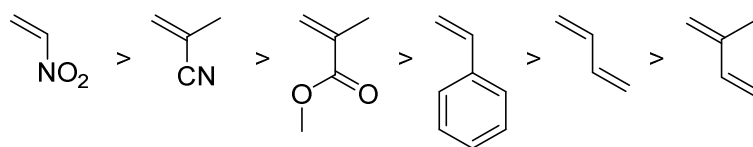
Figure 4: Effect of the electron withdrawing group onto the reactivity of vinyl monomers towards nucleophilic attack sorted from highest to lowest reactivity.

Next to vinyl monomers, monomers containing heterocycles can also undergo anionic ring-opening polymerizations, e.g. epoxides or lactones as shown in Figure 5.
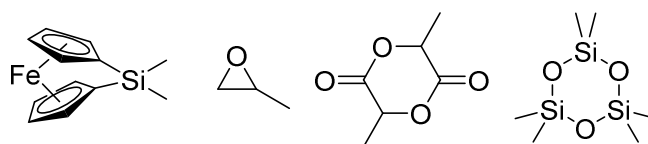

Figure 5: Examples of monomers that can undergo anionic ring-opening polymerization, left to right: (1,1'-ferrocenediyl)dimethylsilane, propylene oxid, lactide, and hexamethylcyclotrisiloxan.

For the initiation reaction of vinyl monomers, two initiator types are commonly used. Sodium naphthalene can be used in a one electron transfer onto the monomer. After formation of the negatively charged styrenyl radical, dimerization leads to formation of the bianion as shown in Figure 6. An α,ω-functional dicarbanion is obtained, which can be beneficial for some synthesis paths, e.g. symmetric block copolymers.[19] Chain growth occurs on two sites at the same time.
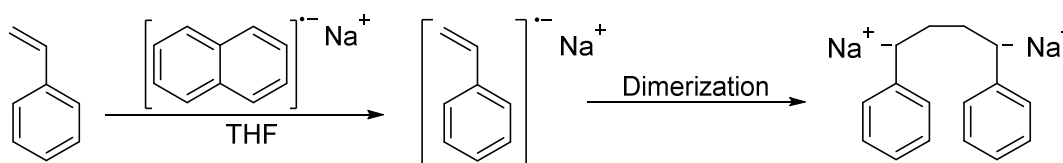
Figure 6: Initiation of styrene with sodium naphthalene. One electron transfer and subsequent dimerization leads to the formation of the dianion.

The sodium naphthalene (NaNp) is formed by electron transfer from metallic sodium onto the naphthalene. The additional electron is delocalized across the aromatic system. Resonance structures are shown in Figure 7. The NaNp is typically used with polar solvents such as THF as NaNp is insoluble in polar solvents.[9]

Figure 7: Resonance structures of sodium naphthalene. The additional electron is delocalized across the aromatic system.

Alternatively, the polymerization reaction can be initiated by alkali-metal organyls. The nucleophilic addition of the initiator onto the β-carbon of the double bond is shown exemplary for the initiation of styrene by *sec*-Butyllithium (*s*-BuLi) in Figure 8.
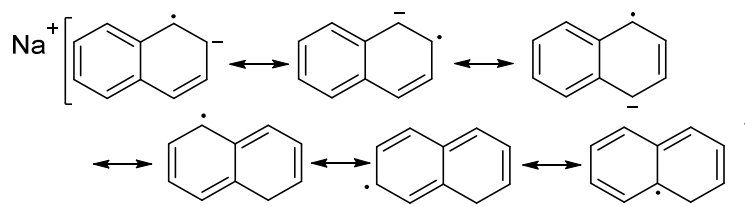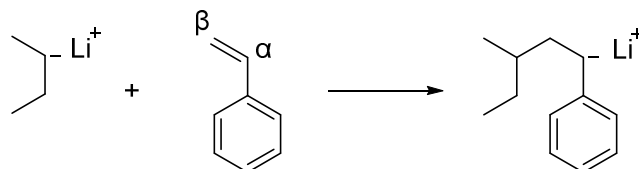

Figure 8: Initiation of styrene with sec-butyllithium (s-BuLi). The resulting anion is stabilized by the aromatic ring, favouring an attack of the nucleophile at the β position of styrene.

Organolithium initiators can form aggregates in solution. Depending on the polarity of the solvent, aggregates between monomers up to hexamers can be found. Tetramer and hexamers are typically found for *s*-BuLi in hydrocarbon solvents. In polar solvents, the aggregates of *s*-BuLi are broken down towards monomers and dimers.[20,21]

The solvent used during the polymerization heavily influences the reaction kinetics and the microstructure of the final polymer. Polar solvents solvate ions better than non-polar solvents. Therefore, an ionic bond is favored for the propagating styrenyl lithium species as shown in Figure 9. In a polar solvent, the nucleophilicity of the carbon is higher due to ionic character of the lithium carbon bond. As a result, also the polymerization rate is higher than in nonpolar solvents. In nonpolar solvents, the covalent bond between carbon and lithium is favored due to an increased solubility in the nonpolar solvents. Herein, the nucleophilicity and therefore the polymerization rate is reduced.[9,19]

polar solvent   non-polar solvent
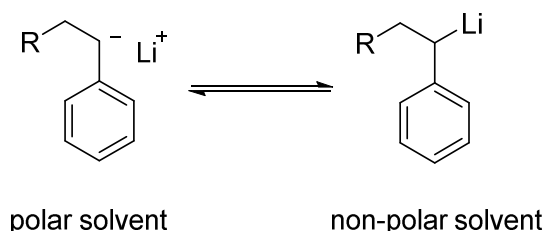
Figure 9: Solvent influence on the bond between the carbon and lithium in the propagating styrenyl lithium species.

In the case of dienes, the solvent influences the microstructure of the resulting polydiene. For polar solvents, an addition through one double bond is favoured resulting in a predominant 1,2 and 3,4 microstructure. A predominant 1,4 microstructure is a result of a polymerization in non-polar solvent. In Figure 10, possible microstructures of polyisoprene are shown.[7]

1,4-trans   1,4-cis   1,2   3,4
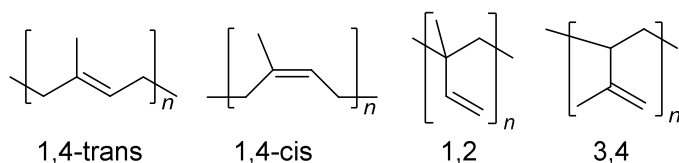
Figure 10: Polyisoprene microstructures as a result of the anionic polymerization of isoprene in polar solvent (predominant 1,2 and 3,4) and nonpolar solvent (predominant 1,4-trans and 1,4-cis).

The ideal kinetics of an anionic polymerization are based on the following assumptions:[19]

- The initiation rate is much faster than the propagation rate. Therefore, every chain starts growing at the same time.
- The chain length does not influence the propagation rate.
- The number of growing chains remains constant.
- The polymerization continues until all monomer is fully consumed or the polymerization is terminated.

With these assumptions, the probability $P(n)$ to find a polymer chain with the chain length n is given by a Poisson distribution with the number average degree of polymerization P_n by the relation

$$P(n) = \frac{(P_n-1)^{n-1}*e^{(1-P_n)}}{(n-1)!} \qquad (1)$$

As a result, the polydispersity $Đ$, defined as the ratio of weight average molecular weight to number average molecular weight, is small compared to other polymerization techniques. It is given by the ratio of weight to number average molecular weight by

$$Đ = \frac{M_w}{M_n} = 1 + \frac{P_n}{(P_n+1)^2} \cong 1 + \frac{1}{P_n} \qquad (2)$$

The polydispersity found experimentally e.g. via size exclusion chromatography are typically in the range of $Đ = 1.01 - 1.1$. Due to nonideal factors in the polymerization, e.g. a inhomogeneous solution during the monomer addition, the polydispersity is higher than predicted by the ideal kinetics.[22]

Termination of the anionic polymerization can be caused by impurities in the reagents or on purpose at the end of the polymerization as shown in Figure 11. Most common impurities in the reagents are water and oxygen. Water impurities protonate the carbanion of the propagating species, terminating the growth of this chain. Oxygen reacts with the carbanion to from a radical, which can then dimerize to form a chain with a characteristic double molecular weight. The anion of the propagating species can also be used in selective reactions to form an end group. This is exemplary on the bottom of Figure 11 where ethylene oxide is used to form a terminal alcohol group.
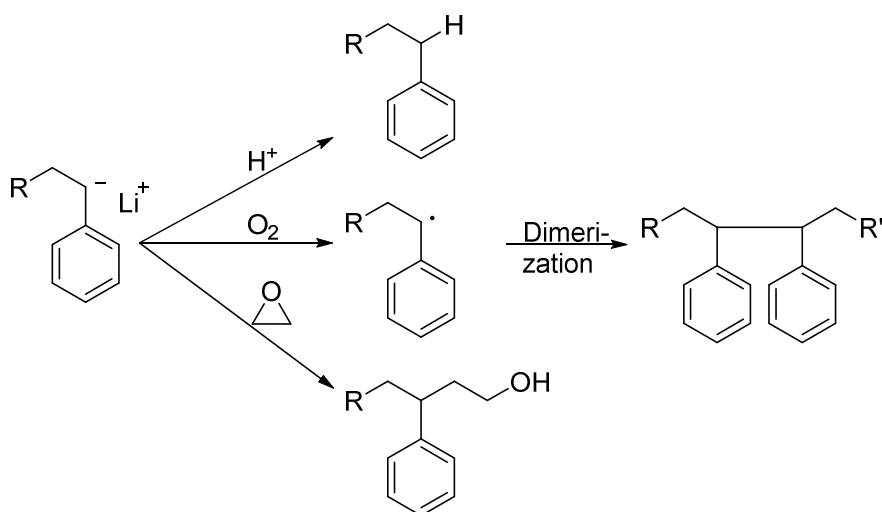
Figure 11: Termination reaction of a polystyrenyl lithium with a proton, O₂ followed by dimerization and functionalization with ethylene oxide to form a terminal alcohol group.

2.3 Branched Polymers

Multiple branched topologies can be obtained when branches are attached to linear chains in different locations.[23] An overview of defined branched architectures is found in Figure 12. If all branches are attached at one branch point, a star is obtained. For two branched points, H-shaped, super H or pom-poms are obtained depending on the number of arms. For multiple branching points, dendritic, combs other topologies can be obtained. Branches can also be attached in a random fashion like found e.g. for LDPE.[24]
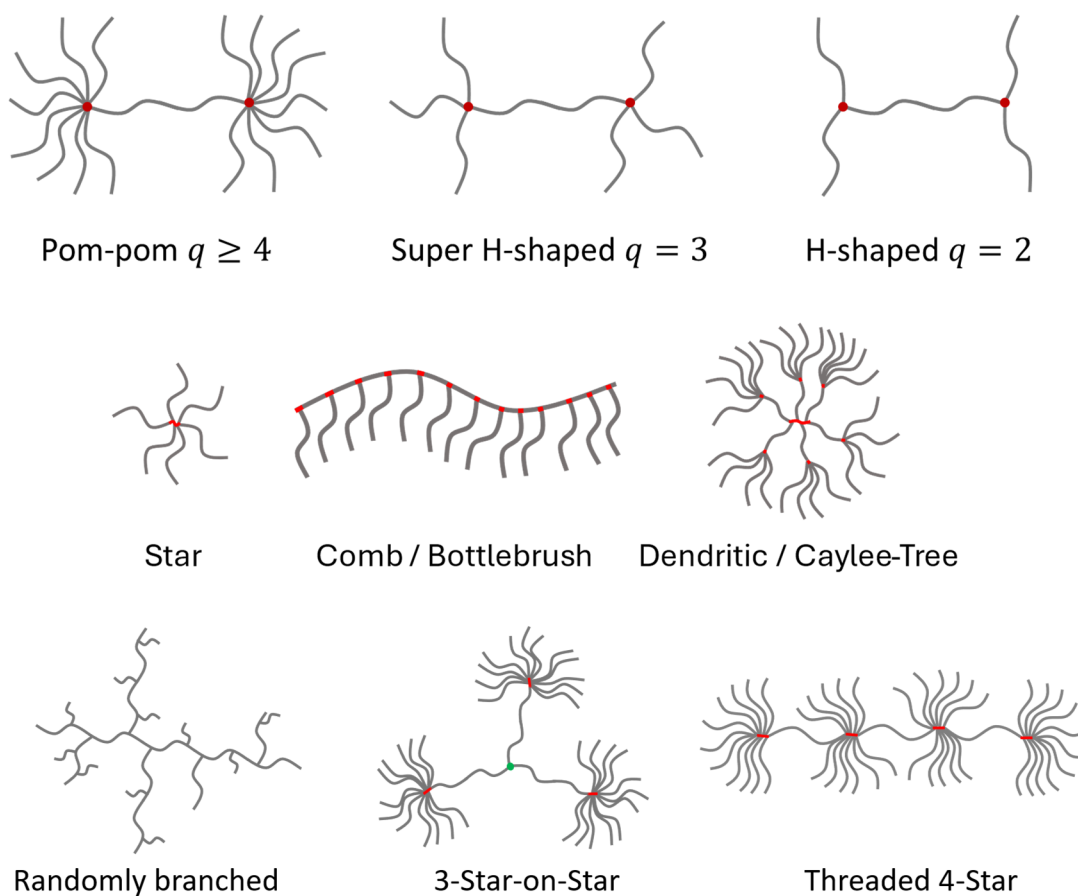
Figure 12: General overview of defined branched architectures.

To synthesize branched architectures, three grafting strategies have been developed as illustrated in Figure 13. A common approach is to use functional groups in the backbone and the terminal functional groups of the side chains to attach the side chains onto the backbone. This grafting onto approach is very common when using anionic polymerization due to the high nucleophilicity of the propagating anion (see chapter 5) but can also be used in e.g. cationic polymerization.[25] In the grafting from approach, functional sites in the backbone are converted to start the polymerization process. The side chains grow simultaneously from the backbone. This approach is for example utilized to synthesize polylactic acid side chains in a super H polymer[26] and can also be used with controlled radical polymerization with the used of multifunctional initiators.[27] The third technique is utilizing side chains with terminal vinyl monomers and copolymerization with monomer to form combs or stars. This approach is popular with free and controlled radical polymerization techniques[27,28] as well as anionic polymerizations (see chapter 5).

Grafting onto

Grafting from

1) Initiator
2) Monomer

Grafting through

Monomer + H₂C=CH

Initiator

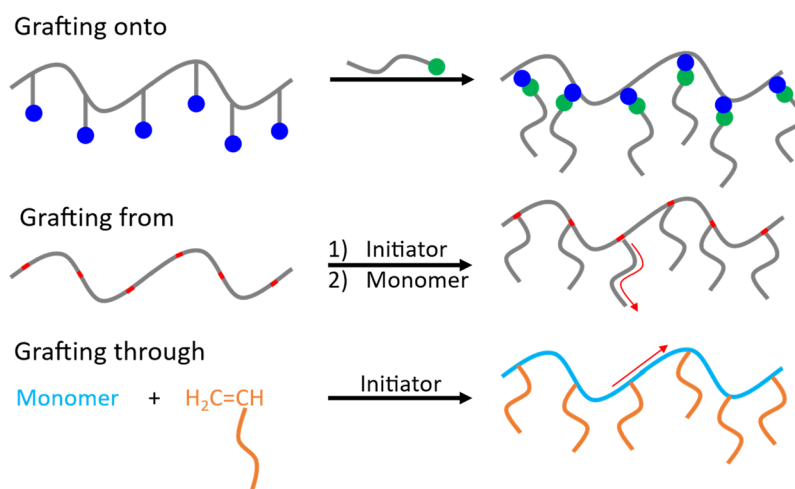Figure 13: Grafting onto techniques used for the synthesis of branched structures illustrated by combs. Top: grafting onto functional groups, middle: grafting from functional groups, bottom: grafting trough terminal functional groups.

3 Introduction to Rheology

Rheology is the science of the flow and deformation of materials.[29,30] Materials can possess a wide spectrum of characteristics ranging from fast flowing water to slow flowing honey as well as materials that stay in place if no external stress is applied but can be stirred like whipped cream. From painting, pumping oil, concrete or polymers and manufacturing plastic parts, understanding of the flow behavior of these complex materials and their description is needed in all aspects of modern life.

3.1 Basics and Phenomenological Models

The simplest rheological experiment is the shearing of a sample between two parallel plates as illustrated in Figure 14. The material (blue) is placed between two parallel plates with a distance h between the plates. The upper plate is displaced with the force F by the distance s.[31]
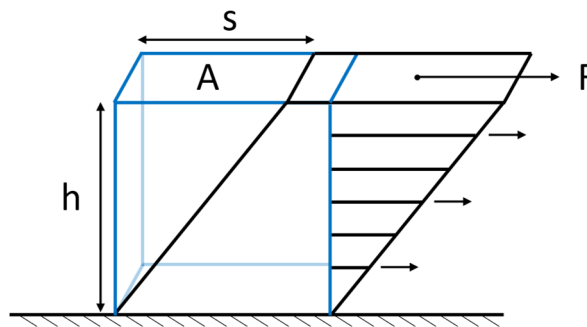
Figure 14: The shear experiment consists of two parallel plates with distance h. The upper plate with the area A is deformed using the force F resulting in a deformation s.

In the shear experiment, a force is applied to the upper plate and displaces the material. The shear stress σ is given by

$$\sigma = \frac{F}{A} \tag{3}$$

where F is the applied force and A is the area of the plate. The shear strain γ is defined as the absolute deflection normalized to the plate distance

$$\gamma = \frac{s}{h} \tag{4}$$

The shear rate $\dot{\gamma}$ therefore can be derived as

$$\dot{\gamma} = \frac{\mathrm{d}\gamma}{\mathrm{d}t} = \frac{v}{h} = \frac{1}{h}\left(\frac{\mathrm{d}s}{\mathrm{d}t}\right) \tag{5}$$

Ideal elastic materials can be modeled by the Hookean spring model as illustrated in Figure 15 a). When a force is applied, the spring is deformed immediately. Once the force is released, the system immediately returns to the equilibrium state. The stress σ is directly proportional to the deformation with the shear modulus G

$$\sigma = G\gamma \qquad (6)$$

The higher the shear modulus, the stiffer the material.[32]

a) Hookean spring model   b) Ideal elastic behavior

Figure 15: Hookean spring model: a) schematic representation of the model by a weight attached to a spring, b) oscillatory deformation and stress response of the Hookean spring model.

Ideal liquids can be described by the Newtonian dashpot as illustrated in Figure 16 a). When a force is applied, the system induces a resistance against the deformation but deforms at a rate proportional to the force. After removal of the force, the system remains at the current deformation. The stress σ is proportional to the applied shear rate $\dot{\gamma}$ by

$$\sigma = \eta\dot{\gamma} \qquad (7)$$

where η is the dynamic viscosity is the proportionality constant.

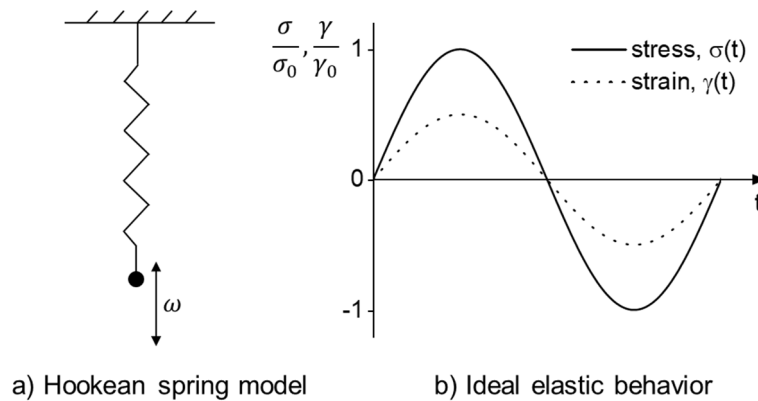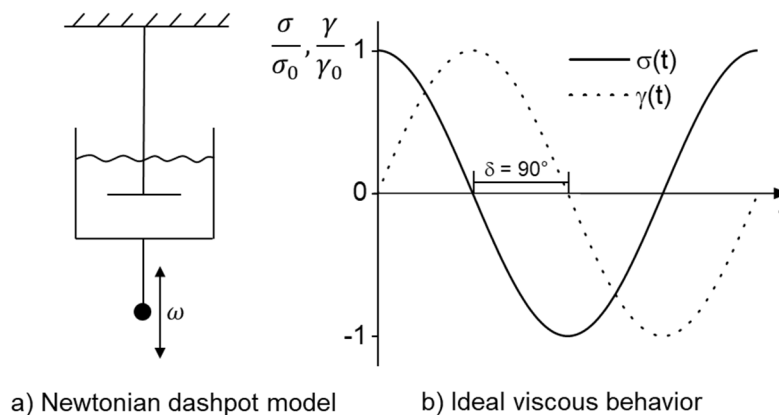a) Newtonian dashpot model   b) Ideal viscous behavior

Figure 16: Newtonian dashpot model: a) schematic representation of the model by a weight attached to a dashpot, b) oscillatory deformation and stress response of the Newtonian dashpot model.

A force can also be applied in oscillatory fashion resulting in an oscillating deformation of the material. The oscillatory deformation can be described over a time t with

$$\gamma(t) = \gamma_0 \sin(\omega_1 t) \tag{8}$$

where γ_0 is the strain amplitude and ω_1 is the excitation angular frequency. For the Newtonian dashpot, the resulting shear stress is obtained by combining equation (8) and equation (6) resulting in

$$\sigma(t) = \eta \gamma_0 \cos(\omega_1 t) \tag{9}$$

For the Hookean spring, the combination of equation (8) and equation (7) yields

$$\sigma(t) = G \gamma_0 \sin(\omega_1 t) \tag{10}$$

Figure 15 b) and Figure 16 b) graphically illustrate the oscillatory response of the two models to oscillatory deformations. Stress and strain are in phase for the Hookean spring. For the Newtonian dashpot there is a 90 ° phase shift between the excitation and the response.

Almost all real-life materials are not ideal materials. Some part of their stress response is of viscous and some of elastic nature resulting in a phase shift between stress and strain of $0° < \delta < 90°$. Therefore, the term viscoelastic material is coined, and the spring and dashpot model are combined to the describe the viscoelastic response of the material. The parallel combination of the two is referred to as Kelvin-Voigt model and the in series is called Maxwell model. Both are schematically shown in Figure 17.[30]

$$\sigma = \sigma_e + \sigma_v$$
$$\gamma = \gamma_e = \gamma_v$$

$$\sigma = \sigma_e = \sigma_v$$
$$\gamma = \gamma_e + \gamma_v$$

a) Kelvin-Voigt model: creep-recovery   b) Maxwell model: stress-relaxation
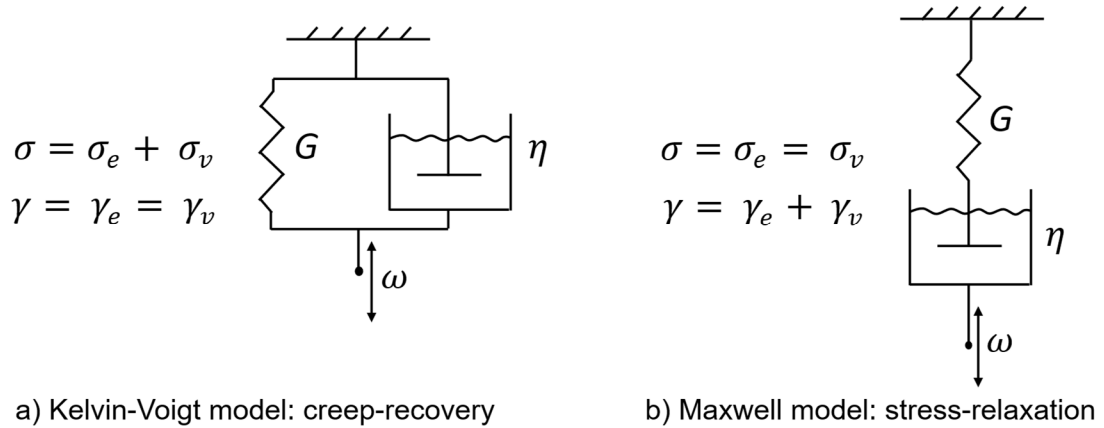
Figure 17: a) Kelvin-Voigt model: combination of spring and dashpot in series, b) Maxwell model: combination of spring and dashpot in parallel.

The Kelvin-Voigt model is used to describe the behavior of a viscoelastic solid. After a force is applied, the system is deformed over time. The system returns to its initial state after the force is removed. The total deformation is the deformation of the individual elements, while the stress is given by their sum. The elastic stress and strain are denoted with 'e' and the viscous with 'v'.

$$\sigma = \sigma_e + \sigma_v \tag{11}$$

$$\gamma = \gamma_e = \gamma_v \tag{12}$$

The Maxwell model is used to describe the behavior of a viscoelastic liquid. After a force is applied, the system deforms instantly, but the stress is relaxed over time. The system remains at its current deformation and does not return to the initial state after the force is removed. The total deformation is the sum of the deformation of the individual elements, while the stress is equal for both elements.

$$\sigma = \sigma_e = \sigma_v \tag{13}$$

$$\gamma = \gamma_e + \gamma_v \tag{14}$$

The first order differential equation for the Maxwell model is obtained from substitution of equation (14) with equation (6) and (7) resulting in

$$\dot{\gamma} = \frac{\dot{\sigma}}{G} + \frac{\sigma}{\eta} \tag{15}$$

If an oscillatory shear with $\dot{\gamma}(t) = \gamma_0 \omega_0 \cos(\omega_1 t)$ and the relaxation time

$$\tau = \frac{\eta}{G} \tag{16}$$

is applied the stress response is obtained as

$$\sigma(t) = \gamma_0 (G' \sin(\omega_1 t) + G'' \cos(\omega_1 t)) \tag{17}$$

with the storage modulus G', which characterizes the elastic contribution to the system, and the storage modulus G'', which characterizes the viscous contribution, being

$$G'(\omega) = G \frac{(\omega\tau)^2}{1 + (\omega\tau)^2} \tag{18}$$

$$G''(\omega) = G \frac{\omega t}{1 + (\omega\tau)^2} \tag{19}$$

As a result, $G' \propto \omega^2$ and $G'' \propto \omega^1$ for small frequencies and $G' = G$ and $G'' \propto \omega^{-1}$ at high frequencies as shown in Figure 18.[31]
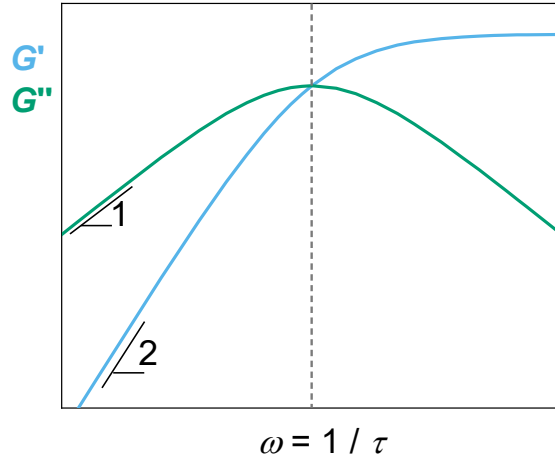
Figure 18: Storage modulus G' and loss modulus G'' shown as a function of angular frequency ω with the relaxation time τ of the system.

The phase angle, the phase shift between the stress and strain can also be obtained by

$$tan\delta = \frac{G''}{G'} \tag{20}$$

The absolute magnitude of the complex viscosity can be obtained from the relation

$$|\eta^*| = \frac{\sqrt{G'^2 + G''^2}}{\omega} \tag{21}$$

and the absolute magnitude of the complex modulus from

$$|G^*| = \sqrt{G'^2 + G''^2} \tag{22}$$

The viscoelastic response of a sample to a set deformation rate is dependent on the relation to the characteristic relaxation time. Therefore, dimensionless numbers have been introduced to relate the elastic forces to the viscous forces.[33] The Weissenberg number Wi relates the characteristic time of a fluid to the rate of deformation. In this thesis, the Wi number is used for uniaxial extensional data against the longest relaxation time τ_L of the sample obtained from the inverse crossover frequency into the terminal regime

$$Wi = \tau_L \cdot \dot{\varepsilon} \tag{23}$$

The Deborah number De is used to relate the characteristic time of a fluid to the duration of the deformation. In this thesis, the De number is used in oscillatory shear data against τ_L

$$De = \tau_L \cdot \omega \tag{24}$$

3.2 Small Amplitude Oscillatory Shear

In an oscillatory shear experiment, a sinusoidally varying shear strain or shear stress and angular frequency is applied to the sample. The oscillatory excitation allows for a characterization of the viscous and elastic contributions of the materials response. In small amplitude oscillatory shear (SAOS) experiments, small amplitudes are used during the oscillatory excitation to obtain a linear response of the material. The storage and loss modulus, G' and G'', are independent of the applied strain. The strain range of the linear response is highly dependent on the material. For most polymeric samples such as polymer melts, the SAOS regime can be found up to $\gamma_0 = 5$ % strain. For cement pastes, the critical strain can be as low as 0.01 %. SAOS is one of the most widely used characterization methods for viscoelastic properties for polymer melts and solutions.[30] For polymer melts, the investigation of the moduli as a function of frequency in SAOS is a powerful tool to obtain different relaxation times of the polymer such as the longest relaxation time or segmental relaxation time.

The time-temperature superposition principle (TTS) allows for the investigation of the viscoelastic response of a material over a large frequency range through superposition of frequency response at a fixed frequency range at varying temperatures. Typical measurements obtain frequency data for 0.01 to 100 Hz. Using TTS, the relaxation behavior of a polymer melt over up to 30 decades can be investigated.[34] Every relaxation process has a specific relaxation time at a given temperature as a result of the activation energy required for the relaxation process. Therefore, the frequency response at a frequency range set, e.g. by the rheometer, can be changed by varying the temperature. The individual frequency sweeps can be superimposed to form the mastercurve of a polymer melt using the horizontal shift factor given by the Williams-Landell-Ferry (WLF) equation

$$\log a_T = \frac{C_1(T - T_{ref})}{C_2 + (T - T_{ref})} \qquad (25)$$

where the measurement temperature is T, the reference temperature is T_{ref}. The shift factor $a_T = \omega_{ref}/\omega$ and C_1 and C_2 are empirical, polymer specific parameters. If $T_{ref} = T_g$, then universal parameters of $C_1 = -17.4$ and $C_2 = 51.6$ K can be used.[35] For polystyrene with $T_g = 105$ °C, $C_1 = 5.6$ and $C_2 = 120$ K at $T_{ref} = 443$ K are obtained.[36] The TTS principle is only valid as long as there is no phase transition or structural changes in the investigated temperature range such as crystallization or curing. Some polymer melts show thermorheological complex behavior and the TTS principle fails.[37]

The master curve of a polymeric material contains crucial information about its molecular structure like molecular weight, dispersity, molecular architecture, mixture of chains, crosslinking an many others. For linear low disperse polymers, the mastercurve can be divided into four different regimes as shown in Figure 19.[30]
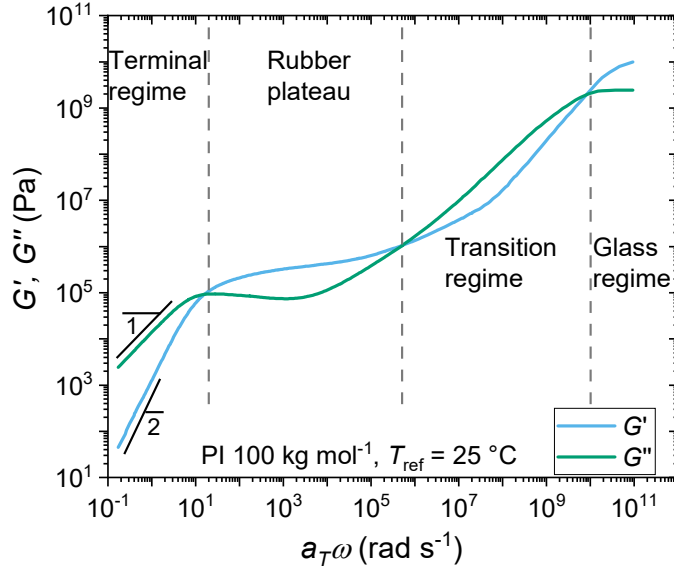
Figure 19: Mastercurve of a linear polyisoprene with M_w = 100 kg mol⁻¹ resulting in an entanglement number of Z = 15.6 at a reference temperature T_{ref} = 25 °C.[38] The four characteristic regimes are separated by crossover of the moduli.

The terminal regime is found at the lowest frequencies and is characterized by $G' \propto \omega^2$ and $G'' \propto \omega^1$ for low disperse homopolymers. Herein, the excitation frequency is slower than the longest relaxation time of the polymer, resulting in a viscous flow. At higher frequencies, the rubber regime is found. Its characteristic is the nearly constant storage modulus, also called the plateau modulus and is typically between 10^4 Pa and 10^6 Pa for most polymers. The polymer chains form a temporary network through chain entanglements and therefore show a network like response. The third regime is the transition regime where the loss modulus is increasing sharply, followed by the glassy regime at the highest frequencies. In the glassy regime, the polymer is below the glass transition temperature T_g and resembles a glass with high moduli typically between 10^8 Pa and 10^9 Pa.[30]

An alternative way to plot linear viscoelastic data is the van Gurp-Palmen plot (vGP plot).[37] This plot was proposed by van Gurp and Palmen and displays the loss angle δ on a linear scale versus the absolute magnitude of the complex modulus $|G^*|$ on a logarithmic scale to test the validity of the time temperature superposition. If frequency data obtained at multiple temperatures all fall on the same line in such a plot, the TTS principle is valid. Data plotted in the usual manner of moduli versus angular frequency, can appear to show valid TTS, while in the vGP-plot the failure of the TTS principles shows more clearly.
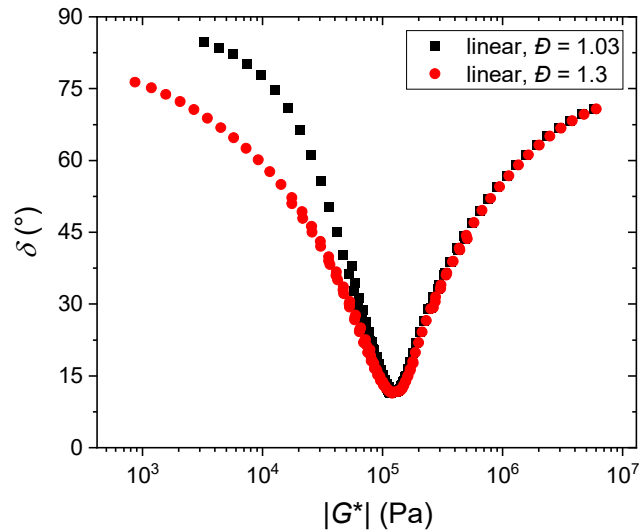
Figure 20: Van Gurp-Palmen plot of two linear polymers with the same chemistry and different polydispersity.

Later, Trinkle and Friedrich showed that the vGP-plot can be used to estimate the polydispersity of linear polymers.[39,40] They found that a lower modulus at $\delta = 60\,°$ indicates a higher polydispersity. Additionally, they suggested that it might be used to detect long chain branching in polyethylene (PE). Lohse *et al.*[41] showed this for hydrogenated polybutadienes with long chain branches. Note that although the vGP plot does indeed show branching contributions much more clearly than the G', G'' vs $a_T\omega$ display, a minimum in the vGP plot only represents a relaxation time of a polymer chain. If a vGP plot shows two minima, this only indicates two different, sufficiently separated relaxation times. The two relaxation times could be a result of a polymer chain with a long main chain and branches or a mixture of short and long chains. Size exclusion chromatography or equivalent methods are needed to differentiate between mixtures (two or more species in elugram) and branched polymers (only one species in elugram). For examples see discussion in chapter 7.4.

3.3 Startup Shear

Most industrial processes do not apply an oscillatory excitation to the viscoelastic material but rather a simple shear deformation.[30] This simple shear deformation is the predominant flow applied by the screws in the extruder which are typically used for the processing of viscoelastic materials like polymer melts, dough or yoghurt. For most simple shear experiments, the strain rate is large, so the material stress response is nonlinear. For polymer melts, shear thinning behavior is observed typically. If the applied shear rate is smaller than the characteristic longest relaxation time, no shear thinning is observed, and the steady state shear viscosity is found to be the same as the zero-shear viscosity obtained from SAOS. For polymer melts, the nonlinear response, before the steady state is reached, is called startup shear and can give information on chain dynamics, especially for branched polymers and mixtures.[42]

In startup shear at a fixed shear rate, the shear stress growth function $\sigma^+(t,\dot{\gamma})$ is given by equation (3) and gives the shear stress growth coefficient $\eta^+(t,\dot{\gamma})$ by

$$\eta^+(t,\dot{\gamma}) = \frac{\sigma^+(t,\dot{\gamma})}{\dot{\gamma}} \qquad (26)$$

The steady state shear viscosity $\eta_{Steady-State}$ is given by

$$\eta_{Steady-State}(\dot{\gamma}) = \eta^+(t,\dot{\gamma})|_{t\to\infty} \qquad (27)$$

Since the stress response is nonlinear, the stress is a function of applied strain. To apply a uniform deformation across the sample, a cone – plate geometry (CP) is used. The CP geometry is illustrated in Figure 21 a). Simple shear deformations at high shear rates are highly susceptible to shear instabilities like edge fracture or shear banding. The cone partitioned plate geometry (CPP) was developed to delay these shear instabilities and is illustrated in Figure 21 b).[43–45] The outer ring holds the sample in place to reduce the effect of instabilities onto the measurement, while the inner plate is connected to the transducer of the rheometer and measures the stress response. The CCP geometry enables factor of ~ 10 higher shear rates compared to regular CP geometry.
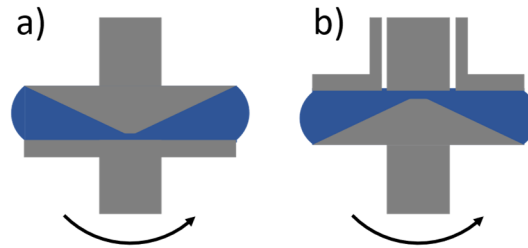

Figure 21: a) Illustration of a cone plate geometry with a loaded sample (blue). b) Cone partitioned plate geometry with a loaded sample (blue). The upper plate geometry is divided into two parts with only the inner part being connected to the transducer of the rheometer.

The steady state shear viscosity $\eta_{Steady-State}(\dot{\gamma})$ is notoriously difficult to measure especially at high shear rates due to several flow instabilities, but it is highly important to material pro-cessing. Contrary, the complex shear viscosity and its absolute magnitude $|\eta^*(\omega)|$ is easy to measure, as shear instabilities typically are rare in SAOS, but is not relevant for industrial processing as there is no material displacement after a full oscillation cycle. A connection between the two viscosities was intensively discussed and an empirical correlation was found by Cox and Merz.[46]

$$|\eta^*(\omega)| = \eta_{Steady-State}(\dot{\gamma})\big|_{\dot{\gamma}=\omega} \qquad (28)$$

Despite being derived from simple empirical observations, there a many examples where the Cox-Merz rule holds true.[47–50] Exceptions have been found as well, especially for highly branched topologies.[51] See also results in chapter 7.1.2.

3.4   Uniaxial Extension

The elongational rheology of polymer melts is crucial for industrial processing especially for film blowing. Extensional flow can cause strong orientation of the polymer chains therefore has a high influence on the properties of the final product. Extensional flow can be divided into uniaxial flow where the sample is extended in one direction and biaxial flow where the sample is extended in two directions simultaneously. Uniaxial extension of a cylindrical specimen is shown in Figure 22.[30]
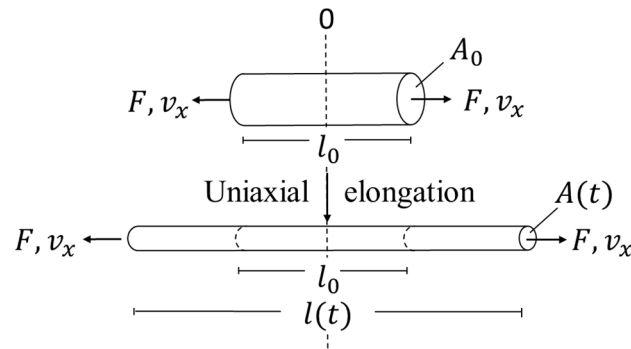

Figure 22: Schematic illustration of the deformation of a cylindrical specimen under uniaxial extension.

In uniaxial extension, the applied deformations to the specimens are typically large. Therefore, the Hencky notation of the strain is used as introduced below. The tensile stress σ applied to the specimen is given by equation (3) with the time dependent cross-section A and the force F applied to the cross-section. During extension, constant volume is assumed. With the initial cross section A_0, the length of the initial sample l_0 and time dependent sample length l is given by

$$A_0 \cdot l_0 = A \cdot l \qquad (29)$$

Contrary to the definition used for small deformations, the differential strain is defined by relating the chain in length dl to the actual length l and not to the initial length l_0

$$d\varepsilon_H = dl/l \qquad (30)$$

or

$$\varepsilon_H = \int_{l_0}^{l} d\varepsilon_H = \int_{l_0}^{l} \frac{dl}{l} = \ln\frac{l}{l_0} \qquad (31)$$

The quantity ε_H is called the Hencky strain[52] and preferably used for large deformations as in uniaxial extension. From equation (31), the Hencky strain rate follows as

$$\dot{\varepsilon} = \frac{d\varepsilon_H}{dt} = \frac{d(\ln l/l_0)}{dt} = \frac{1}{l}\frac{dl}{dt} = \frac{v}{l} \qquad (32)$$

with v being the stretching velocity. For convenience, the index "H" is omitted and $\dot{\varepsilon}$ is the Hencky strain rate. The time and Hencky strain rate dependent extensional stress is called the tensile stress growth function $\sigma_E^+(t, \dot{\varepsilon})$ as defined in equation (3). The extensional viscosity η_E results from the tensile stress growth coefficient $\eta_E^+(t, \dot{\varepsilon})$ for constant strain rates and $t \to \infty$.[30,33]

$$\eta_E = \eta_E^+(t, \dot{\varepsilon})|_{t\to\infty} = \sigma_E^+(t, \dot{\varepsilon})/\dot{\varepsilon} \qquad (33)$$

Like the shifting of frequency sweeps in SAOS to form the mastercurve, extensional data measured at different temperatures can be shifted onto the same reference temperature. Using TTS for extensional data, the extensional behavior from near the glassy region to the terminal regime can be characterized. To shift the tensile stress growth coefficient to a different temperature, the same shift factors a_T as obtained from the WLF equation for SAOS are used resulting in

$$\eta_E^+(T_{ref}) = a_T \cdot \eta_E^+ \text{ with } t_{T_{ref}} = a_T \cdot t \text{ and } \dot{\varepsilon}_{T_{ref}} = \dot{\varepsilon} / a_T \qquad (34)$$

4 Constitutive Equations for Polymer Melts

4.1 General Tube Model

The movement of polymer chains on a microscopic level can be described within the frame of the tube theory. The first idea of the movement of polymer chains within a large tube was introduced by de Gennes.[53] Doi and Edwards further developed the model to explain different molecular relaxation mechanisms.[54] Tube-based models quickly emerged as an important tool to describe the dynamics of polymer chains.[30,55–57] In the tube model, the many-body problem of a polymer melt is reduced to observation of a single chain. This probe chain is moving through a hypothetical tube made of topological constraints (entanglements) imposed by the surrounding matrix chains as illustrated in Figure 23.
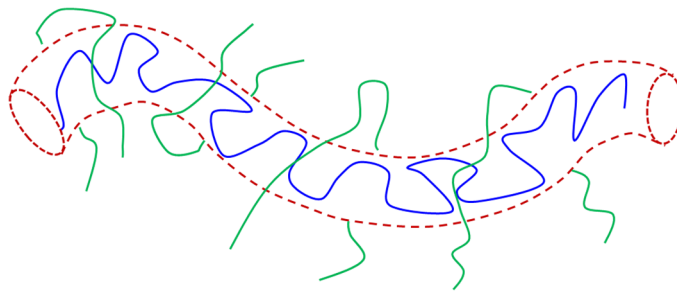
Figure 23: Schematic illustration of the hypothetical tube (dashed red) confining the test chain (solid blue) formed by the surrounding chains (solid green).

The tube restricts the probe chain to movements along the tube direction. To describe the stress relaxation of an imposed strain, multiple mechanisms have been observed and implemented into the tube model as described in the following. De Gennes, Doi and Edwards included reptation and contour length fluctuations (CLF). Reptation described the curvilinear diffusion of the probe chain along the tube and is shown schematically in Figure 24.
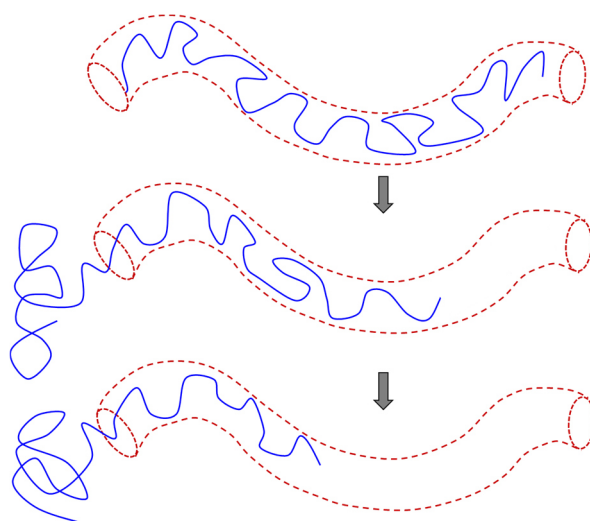
Figure 24: Illustration of the reptation process. The test chain escapes from its tube by a snake-like motion.

After movement of the chain and freeing part of its occupied volume, entanglements in this part are lost and the stress imposed by these entanglements is relaxed. The tube diameter is wider than the probe chain and therefore the chain is wrinkled on a monomer level. The ends of the chain can extend and contract. The end retraction releases stress especially for shorter chains or at branch points and is known as CLF and schematically shown in Figure 25.
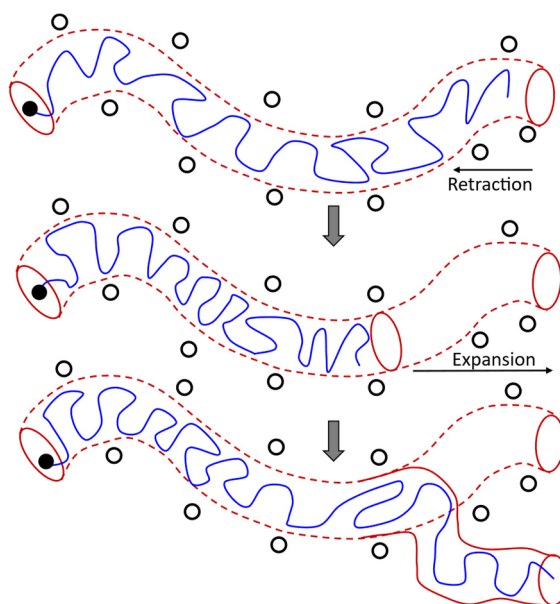
Figure 25: Illustration of the contour length fluctuation process. The probe chain retracts and expands its ends. The end of the probe chain can enter a new tube. Tube forming matrix chains indicated by black circles.

For systems with short and long chains, e.g. bidisperse blends or branched polymers, dynamic tube dilution (DTD) occurs.[58] The shorter chains relax first and then act as a solvent towards the longer chains. The relaxation of the longer chains is accelerated by the solvent. In the tube

model picture, the tube diameter increases after dilution of the long chain in the relaxed short chains. When large deformations are applied to the chain that result in a nonlinear response, additional phenomena as convective constraint release (CCR) and chain stretch can be observed.[59,60] The tube around the probe chain consists of many matrix chains. The matrix chains relax by the same mechanisms as the probe chain, therefore constraint forming the tube can be lost and the probe chain can shift vertically. Due to the implementation of these mechanisms, tube models have been improved to near quantitative agreement in SAOS with linear, comb, H-shaped and pom-poms.[61–70]

4.2 Pom-pom Model

The research on the pom-pom topology was inspired by the leading work of Thomas C. B. McLeish and coworkers on constitutive modelling of branched polymers. The aim was to use the fundamental understanding of the dynamics of branched polymers to develop a model describing their stress response upon deformation.[10,24,71,72] Especially the flow properties of the widely used commodity plastic, LDPE, were of interest due to its unique rheological behavior. The topology of LDPE consists of branches with varying length, position and priority of relaxation due to their random introduction during the free radical polymerization process. To reduce the complexity of the topology, the pom-pom topology was introduced containing exactly two branch points at each end of a backbone with branches of the same length. With this reduced topological complexity, the pom-pom constitutive equations were developed to describe the macroscopic stress response from a molecular level. The pom-pom topology is the simplest branched topology containing at least two branching points, which are needed to induce strain hardening. Strain hardening in extensional flow is the increase of the tensile stress growth coefficient above the linear viscoelastic envelope. Based on the tube model, McLeish and Larson developed constitutive equations to describe shear and extensional melt rheology of a pom-pom shaped polymer molecule.[10] Within the pom-pom model the stress is given by

$$\boldsymbol{\sigma}(t) = \frac{15}{4} G_0 \phi_b \left(\phi_b \lambda^2(t) + \frac{2q s_c(t)}{2q Z_a + Z_b} \right) \boldsymbol{S}(t) \quad \text{with} \quad \phi_b = \frac{Z_b}{2q Z_a + Z_b} \tag{35}$$

where Z_b and Z_a are the number of entanglements of the backbone and the arms respectively, q is the arm number of each star of the pom-pom, ϕ_b is the volume fraction of the backbone, $\lambda(t) = [1, q]$ is the stretch parameter, $\boldsymbol{S}(t)$ is the orientation tensor, $s_c(t)$ is the branch point withdrawal parameter, and G_0 is the plateau modulus. The pom-pom model has been successfully applied to model the extensional flow behavior of low-density polyethylene (LDPE) and other long-chain branched (LCB) systems like combs or LCB-styrene-butadiene-rubbers.[24,72–74]

The pom-pom model attributes two relaxation times to the backbone: the orientation relaxation time τ_b, describing the alignment of the backbone tube due to flow, and the stretch relaxation time τ_s, describing the stretch of the backbone chain in flow. In extension with $\dot{\varepsilon} > 1/\tau_s$, the backbone is stretched due to the friction of the branchpoints. At sufficiently high strains, the backbone reaches its maximum stretch $\lambda = q$ and thereafter the arms are retracted into the backbone tube, resulting in a steady state stress as illustrated in Figure 26. The retraction of the

arms is called branch point withdrawal and takes place at the time t_q and strain ε_q of maximum backbone stretch. Hierarchical relaxation of the arms before the relaxation of the backbone is essential in the pom-pom model. Therefore, the pom-pom model is limited to strain rates smaller than the inverse of the arm relaxation time $1/\tau_a$ since no stress contribution of the arms is implemented in equation (35).
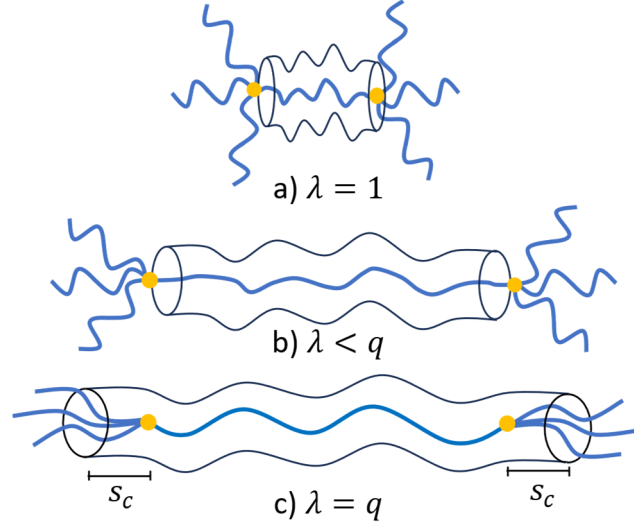

Figure 26: A pom-pom polymer shown schematically with a backbone and 2q dangling arms, q = 3, under various degrees of stretch. The backbone stretch is denoted as $\lambda(t)$ and the path length of the branch point withdrawal is denoted as $s_c(t)$. Redrawn from McLeish and Larson.[10]

The extensional viscosity η_E is defined as the steady state of the time dependent tensile stress growth coefficient $\eta_E^+(t)$ in the pom-pom model and typically found experimentally as the maximum of η_E^+ with respect to time in the experiment, can be derived as

$$\eta_E = \frac{15}{4} G_0 \phi_b^2 q^2 \dot{\varepsilon}^{-1} = \frac{15}{4} G_0 \left(\frac{Z_b}{2qZ_a + Z_b} \right)^2 q^2 \dot{\varepsilon}^{-1} \qquad (36)$$

The pom-pom model has been extended to include the second normal stress difference[75] in shear as well as stress overshoots[76] in uniaxial extension as found in LDPE[77] and recently in star polymers.[78]

The Considère criterion (named after the French engineer *Armand Gabriel Considère*) originates from solid state mechanics and states that a sample undergoes homogenous uniaxial extension until the strain of the maximum force $\delta F/\delta \varepsilon < 0$. This criterion was applied to polymeric liquids.[79–82] Beyond the maximum stress, the material is not stretched homogenously and instead undergoes dynamical failure like necking or rupture. The Considère criterion is only valid for fast $\dot{\varepsilon}$ compared to the characteristic relaxation time τ of the material $\dot{\varepsilon}\tau \gg 1$. Corrections for Hencky strain rates where time is relevant were evaluated by Fielding and coworkers.[83,84] McKinley and Hassager[85] applied the Considère criterion onto the pom-pom constitutive equations and developed a relation for the extensional viscosity of the pom-pom topology for rapid stretching. Rapid stretching is assumed for strain rates $\dot{\varepsilon} > 1/\tau_s$, where the viscous components can be neglected, and the strain energy is stored as elastic energy only.

The application of the Considère criterium onto the pom-pom constitutive equations by McKinley and Hassager is summarized in the following. The tensile stress growth coefficient η_E^+ normalized to the zero-shear viscosity η_0 can be expressed as a function of q, t_q, τ_b, the Hencky strain to sample failure ε_f, and the strain of maximum backbone stretch ε_q within the pom-pom model as

$$\log(\eta_E^+(t,\dot{\varepsilon})/\eta_0)|_{\varepsilon_f \to \varepsilon_q} = \log\left(\frac{3q^2}{\varepsilon_q}\right) + \log\left(\frac{t_q}{\tau_b}\right) \tag{37}$$

Equation (37) is valid for the limiting case of $\varepsilon_f \to \varepsilon_q$. In the limit of $\varepsilon_f = \varepsilon_q$, η_E^+ can be simplified to the steady state extensional viscosity $\eta_E^+(t,\dot{\varepsilon}) \to \eta_E$ at a constant strain rate.

$$\frac{\eta_E}{\eta_0} = \frac{3q^2}{\varepsilon_q} \cdot \frac{t_q}{\tau_b} = \frac{3q^2}{\tau_b} \cdot \frac{1}{\dot{\varepsilon}} \tag{38}$$

This result may be compared with the linear viscoelastic envelope (LVE), which is approximated in the pom-pom model by

$$\eta_{LVE}^+ = 3\eta_0 \left[1 - e^{\left(-\frac{t_q}{\tau_b}\right)}\right] \tag{39}$$

Which can be approximated with a first-order Taylor polynomial expansion for small times $\frac{t_q}{\tau_b} \ll 1$, yielding

$$\eta_{LVE}^+ \simeq 3\eta_0 \left(\frac{t_q}{\tau_b}\right) \tag{40}$$

Rearranging of equation (40) for $\left(\frac{t_q}{\tau_b}\right)$ and substituting it in equation (38) gives

$$\eta_E \simeq \eta_{LVE}^+ \cdot \frac{q^2}{\varepsilon_q} \tag{41}$$

During the extension, the strain of the sample increases until the Hencky strain to sample failure ε_f is reached. At the maximum stress, a force balance between the resistance against withdrawal of the branch point into the tube and further stretching of the backbone is reached. The maximum stress is reached at $\lambda = q$ and followed by a plateau for $\lambda > q$ for $q \geq 2$ (see Figure 27 a)). In the rapid stretching limit, the Hencky strain at failure can be derived through calculation of the force balance at maximum backbone stretch and is given by

$$e^{2\varepsilon_f} + 2e^{-\varepsilon_f} = 3q^2 \tag{42}$$

For $q \geq 2$, ε_q can be approximated using $e^{2\varepsilon_f} \gg e^{-\varepsilon_f}$ with

$$\varepsilon_q = \varepsilon_f \simeq \ln(\sqrt{3}q) \tag{43}$$

Combining equation (42) and equation (43) yields

$$\eta_E \simeq \eta_{LVE}^+ \cdot \left[\frac{q^2}{\ln(\sqrt{3}q)}\right] \tag{44}$$

predicting the increase of the extensional viscosity above the LVE by the Considère factor $f_c = [q^2/\ln(\sqrt{3}q)]$, see also Figure 27 b). The Considère factor f_c is directly related to the maximum achievable strain hardening factor SHF_{max}, see chapter 7.1.3. The strain hardening

factor is given by $SHF = \eta_E(\dot{\varepsilon})/\eta_{DE}(\dot{\varepsilon})$ with η_{DE} as the steady state viscosity of the Doi-Edwards model. The relation between the Considère factor and the arm number with exemplary $q = 11, 22, 30$ is shown in Figure 27 b). For comparison, commercial LDPE typically has moderate strain hardening with SHF_{max} around 10. A pom-pom analogue polymer chain would only need around five arms per branch point ($q = 5$), 10 in total, to reach similar SHF_{max}, underlining the immense potential of the pom-pom topology to tune strain hardening.
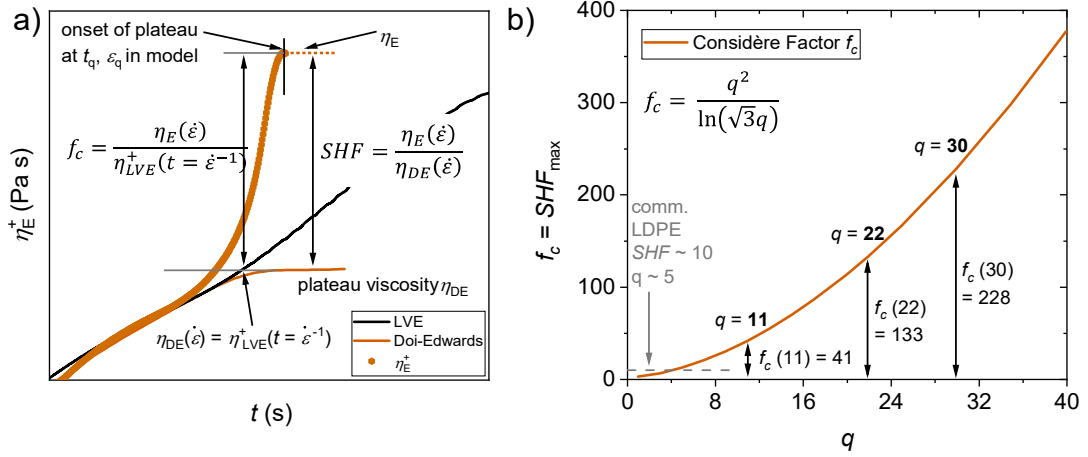

Figure 27: a) Schematic relations between η_E, η_{DE}, η_{LVE}^+, f_c and SHF. The Considère factor is equal to the maximum strain hardening factor $SHF_{max} = f_c$, see discussion. b) Relation of the Considère factor f_c and the arm number q of a pom-pom. Values for $q = 11, 22, 30$ are given as examples matching q of the synthesized samples. Adapted from Schußmann et al.[86] under the Creative Commons Attribution 4.0 International License.

The relaxation dynamics of the whole chains, in the case of pom-pom of the arms and the backbone, are accumulated in the LVE. The linear viscoelastic envelope η_{LVE}^+ (LVE) is defined by the complex viscosity, taking the Trouton ration, the Cox-Merz and Gleissle mirror rule into account.

$$\eta_{LVE}^+(t) = 3\eta(\dot{\gamma} = \frac{2\pi}{t})$$

(45)

When a sample is subjected to sufficiently high, extensional stress or strain, it will undergo failure. Depending on the conditions, multiple failure mechanisms can take place. The pom-pom model states that the mechanism to reduce stress on the backbone is branch-point withdrawal at sufficiently high strains and strain rates, resulting in a steady-state viscosity. During the branch point withdrawal, the tube of the backbone expands, and the branch point including the arms is retracted into the backbone tube.[12,87] At very higher rates, the failure mechanism for linear chains was experimentally shown to be elastic rupture through chain scission for elastomers[88] and recently for polymer melts by chemoluminescence.[89] Elastic fracture has been approached theoretically by considering the macroscopic force on a single carbon-carbon bond. A maximum fracture stress $\sigma_E^{Fracture}$ before bond dissociation could be calculated from the C-C bond energy U and the strain energy on a Kuhn segment w_c by using the relation[90]

$$w_c = 3kTf\lambda\varphi = U \tag{46}$$

with f being the molecular stress and λ being the molecular stretch. A C-C bond energy in hydrocarbons of $U = 348$ kJ mol^{-1} is used.

4.3   Molecular Stress Function Model

The molecular stress function model is based on the Doi-Edwards tube model (DE). The DE model only predicts shear and extensional thinning. Modification of the DE model was therefore necessary to account for the experimentally observed strain hardening in some polymer melts under uniaxial extension. The molecular stress function model (MSF)[91,92] and its extension the hierarchical multimode molecular stress function model (HMMSF)[93–98] assume a decreasing tube diameter during the extensional flow. The stress tensor $\boldsymbol{\sigma}(t)$ in the MSF model is given by

$$\boldsymbol{\sigma}(t) = \int_{-\infty}^{t} m(t - t')f^2(t,t')\boldsymbol{S}_{DE}^{IA}(t,t')dt' \tag{47}$$

with the orientation tensor the memory $\boldsymbol{S}_{DE}^{IA}$, the tube diameter ratio $f(t,t')$, and the memory function $m(t - t')$ defined by

$$m(t - t') = \frac{dG(t - t')}{dt'} \tag{48}$$

with the relaxation modulus $G(t)$. For long chain branched polymers, f is defined by the ratio of the initial tube diameter a_0 to the time dependent tube diameter a by

$$f(t,t') = \frac{a_0}{a(t,t')} \tag{49}$$

For the HMMSF model, the stress tensor is extended to include the hierarchical relaxation of multiple modes to

$$\boldsymbol{\sigma}(t) = \sum_i \int_{-\infty}^{+\infty} \frac{\partial G_i(t - t')}{\partial t'} f_i^2(t,t')\boldsymbol{S}_{DE}^{IA}(t,t')dt' \tag{50}$$

The stress is a sum over all stress contributions from the discrete Maxwell modes which describe the relaxation modulus $G(t)$ given by

$$G(t) = \sum_i G_i(t) = \sum_i g_i exp(t/\pi_i) \tag{51}$$

The molecular stress function $f_i = f_i(t,t')$ can be obtained by integration of the evolution equation of

$$\frac{\partial f_i}{\partial t} = f_i(\boldsymbol{K}:\boldsymbol{S}) - \frac{1}{\alpha}\left(\frac{1}{\tau_i} + \beta CR\right)\left[(f_i - 1)\left(1 - \frac{2}{3}w_i^2\right) + \frac{2}{9}f_i^2(f_i^3 - 1)w_i^2\right] \tag{52}$$

with the velocity gradient tensor $\boldsymbol{K}$ and the dilution exponent α with $\alpha = 1$ for long chain branched melts and $\alpha = 4/3$ for linear chains (compare Figure 50, page 68). CR is a dissipative constraint release term which is zero for uniaxial extensional flow and non-zero in shear. Using the dilution modulus G_D, the mass fraction w_i of the chain segments, which take the hierarchical relaxation into account, can be calculated by

$$w_i^2 = \frac{G(t=\tau_i)}{G_D} = \frac{1}{G_D}\sum_{j=1}^n g_j \exp\left(-\tau_i/\tau_j\right) \quad \text{for} \quad \tau_i > \tau_D$$

$$w_i^2 = 1 \quad \text{for } \tau_i \leq \tau_D \tag{53}$$

Dynamic dilution starts at time $t = \tau_D$ with the disentanglement time τ_D, when the relaxation modulus $G(t)$ has decreased to the dilution modulus G_D. Within the HMMSF model, the dilution modulus is the only fitting parameter. For the PS pom-poms in this thesis, the dilution modulus is equal to the plateau modulus G_N^0 determined from linear viscoelasticity.

Using the discrete linear relaxation spectrum und the only fitting parameter G_D, it was shown that the HMMSF model can predict the nonlinear response in startup shear and uniaxial extension for a variety of polymers with low dispersity e.g. linear chains, bidisperse blends, stars, combs, and bottlebrushes as well as a variety of commercial randomly branched samples such as LDPE.[87,93–95,97,99–104]

5   Previous Works on Branched Systems

This chapter summarizes previous works on the flow behavior of defined branched systems as published of January 2025. The synthesis, chromatographical analysis, and investigated deformations are summarized. Possibilities of side products beyond the target topology are discussed. The literature review focuses on combs, H-/super H- and pom-pom, and dendrimers due to their strain hardening characteristics in extensional flow and their relevance for industrial processing of branched structures like LDPE.

Adding branches to a linear chain can yield a wide variety of topologies. An overview of the possible topologies is shown in Figure 28. Adding one branch to a linear chain result in the star topology. The topologies with two branching points are called the H/super H and pom-pom topologies depending on the number of branches. H-shaped polymers have two branches on each side resembling the letter H. Super H polymers have three or four branches per side and pom-poms have five or more branches are attached at each end. When a lot of branches are attached in different places, comb, bottlebrush and dendrimers can be obtained. Tadpoles are a combination of ring and branched polymers.
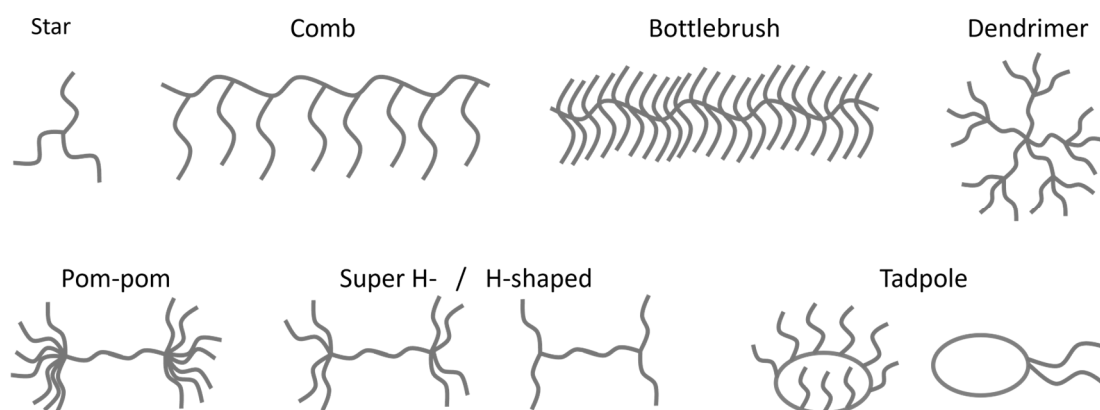

Figure 28: Overview of the branched topologies investigated by the work reviewed in this chapter.

Number of publications as a function of the publishing year of the rheological data on defined branched systems are shown in Figure 29 for the reviewed literature. The first works were published by Archer and coworkers (synthetically) and McLeish and coworkers (theoretically) in 1998 and 1999, respectively. Following these initial works, many studies were conducted in between 2006 and 2014, dropping off in the late 2010s. Recently, in 2023 and 2024, the number of publications increased significantly again. A new high was reached in 2024 with studies including refined synthesis routes, in depth characterization and rheological measurements as discussed below.
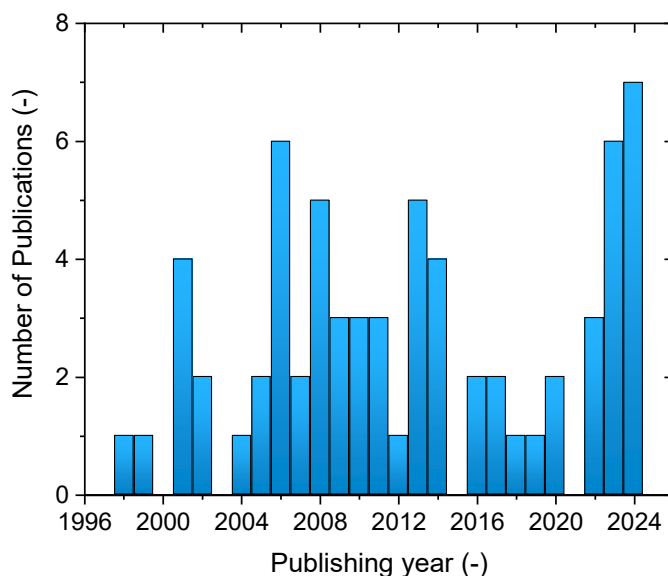
Figure 29: Number of publications on the rheology of defined branched systems between 1996 and 2024.

The branching moieties of the synthesis routes are grouped by resulting topology and shown in Figure 30, Figure 31, and Figure 32. The literature is summarized in Table 1 (starting page 39) and nomenclature is used according to this table with Y_x. The topology is indicated by Y with C for comb, PE for defined branched polyethylenes, DE for dendrimers, H for super H- and H shaped polymers, P for pom-poms, and TP for tadpoles. The works are grouped by synthesized samples and x indicates the number of the group. All polymers except C_8 and H_4 are synthesized based on living anionic polymerizations.[7] For C_8, olefin metathesis with a Grubbs catalyst is used and anionic ring opening polymerization is employed for H_4.
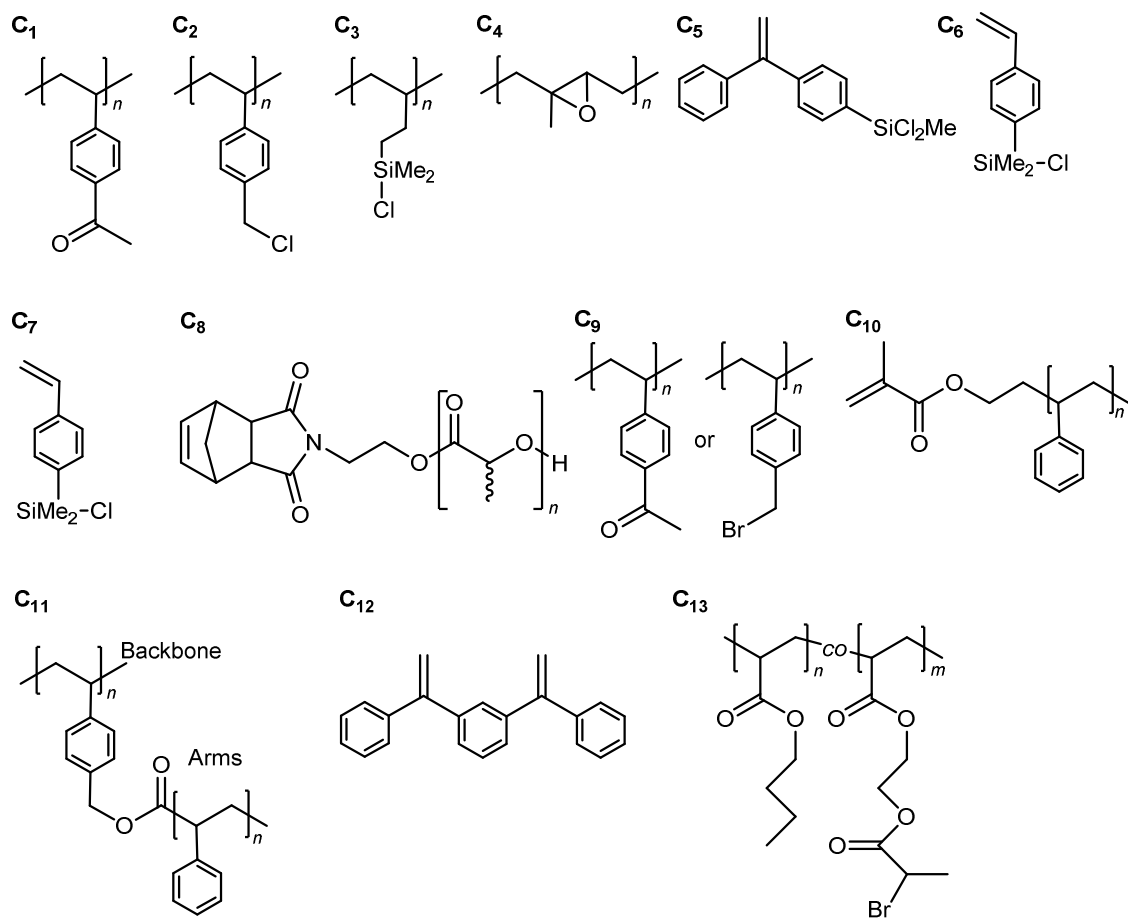
Combs

Combs are synthesized by grafting onto a functionalized backbone (C_1, C_2, C_3, C_4, C_9, C_{11}) or copolymerization of a macromonomer (C_5, C_6, C_7, C_{10}). Grafting through approaches can be used to obtain dense bottlebrushes (C_8). All branching moieties are shown in Figure 30. Thermal gradient interaction chromatography (TGIC) analysis of C_2 revealed no side products next to the target comb architecture. The average arm number across all combs is four arms per comb. TGIC shows that the sample contains combs with one to ten arms. Similarly, TGIC analysis of C_{11} also reveals no side products. This suggests that the grafting onto strategy is suitable for synthesis of combs with high architectural purity. Comb C_6, C_7, and C_{10} use the macromonomer approach. Herein, the side chains are terminated with a vinyl moiety and the macromonomers are copolymerized with monomer in a second polymerization to yield the comb topology. No advanced chromatographical analysis was conducted. It is possible, that the branches are not randomly distributed along the backbone as with the grafting onto approach due to preferred copolymerization of the monomer or the macromonomer resulting in a gradient. This is especially likely, if there are differences between the head of the macromonomer and the monomer like in C_{10} (methacrylate macromonomer and styrene as the monomer). TGIC analysis of C_5, an asymmetric exact comb, revealed many side products, consisting of low and high

molecular weight. The employed chlorosilane linking approach yields the desired product, but side products cannot be removed by simple solution fractionation due to the small molecular weight difference. For C_{12}, stars containing anions at the end of two arms are polymerized and then a condensation reaction is used to link them together. Using TGIC, unreacted stars are detected in the crude product, but they can be removed by simple solution fractionation due to a larger molecular weight difference of more than factor of three. Grafting from approaches can also be utilized to synthesize combs as shown with C_{13} but are rarely used.

The defined branched polyethylenes synthesized in PE_1 consist of a comb, a H-, super H and one pom-pom sample. For all systems, the desired topologies are synthesized through polybutadiene with high 1,4-microstructure content followed by hydrogenation to yield PE. The comb is synthesized by grafting onto the backbone after PPM similar to C_3. Super H-/H-shaped and pom-pom samples are synthesized by chlorosilane linking reactions similar to exact comb C_5. Due to the similar reaction procedure, side product in the final product might remain undetected in SEC characterization.

Combs

Polyethylenes PE₁

Super H (x = 3) and **H-shaped** (x = 2) via:

Cl$_x$Si——PB——SiCl$_x$ + LiPB
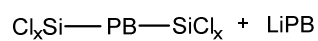
Comb via:

Star via:

Pom-Pom via Cl$_3$Si-CH$_2$CH$_2$-SiCl$_3$
(PB)$_5$SiCl+ Li-PB-Li
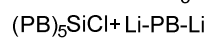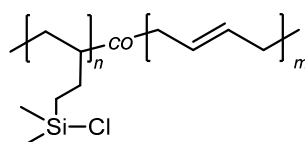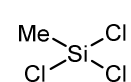
Figure 30: Branching moieties used for the synthesis of the combs C₁ - C₁₃ and the defined polyethylenes.

Dendrimers

Dendrimers are mostly synthesized through a core first approach. An initiator carrying a protected functional group is used to initiate the polymerization and the living chains are grafted onto the core to yield a star (G_1). The functional group is deprotected and the second generation of branches can be grafted onto (G_2). This approach is used for DE_1, DE_2, DE_3 up to 4th generation dendrimers.

DE_4 uses an initiator with a protected functional group to polymerize the inner branches before end capping and grafting onto. The functional group is deprotected to link the dendrons together to for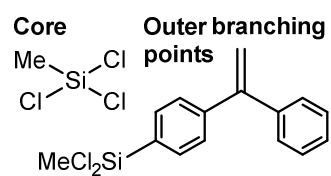m the dendrimer (G_2). TGIC reveals a high product purity of 83% of the target architecture. Some dendrimers are missing one of the outer branches because of non-quantitative grafting onto of the Cl_2Si terminated chains or insufficient functionalization. DE_5 employs a convergent approach, starting with macromonomer polymerization to form the outer branches, followed by monomer for the inner branches and chlorosilane crosslinking.

Super H-/H-shaped

H- and Super-H topologies are synthesized either through the arm-first or the backbone-first route. In the backbone-first route, a bifunctional initiator is used to polymerize the backbone followed by end capping with $MeSiCl_3$ for H and $SiCl_4$ for Super-H to obtain a α,ω-functionalized backbone. The arms are directly grafted onto the backbone (H_1, H_2, H_4). For H_1, TGIC revealed that this synthesis route yields a majority of the target topology. High and low molecular weight side products are found in the final product even after multiple fractionation steps. In the arm-first route, the arms for the H and Super-H are linked together leaving one remaining functional group. H_3 uses a $SiCl_2$-functionalized DPE to link the arms together followed by grafting from the DPE double bond and linking with Me_2SiCl_2. Depending on the sample, only 30-70 % of chains have the target architecture as shown only by TGIC. Incomplete grafting onto and initiation results in side products with missing arms or star topology. H_5 uses $MeSiCl_3$ in the branching point followed by grafting onto of the backbone polymerized by a bifunctional initiator. No side products are found in the final product by TGIC.

Dendrimers

DE₁

Core   **Outer branching points**

Me Si Cl
Cl Si Cl

MeCl₂Si

DE₂

PS

CH₂Br   CH₂Br

DE₃

PMMA

CH₂Br   CH₂Br

DE₄

HO   OH

OH

Core   **Outer branching points**

Me Si Cl
Cl Si Cl

DE₅

SiMe₂-Cl

Super H-/H-shaped

H₁

Initiator   **Branching point**

Me Si Cl
Cl Si Cl

H₂

Initiator

Branching point

Me or Cl Si Cl
Cl Si Cl

H₃

SiCl₂Me

H₄

for **H-shaped**

for **super H**

H₅

Arms   **Backbone**

PS Si
PS Si Cl

+ NaNp
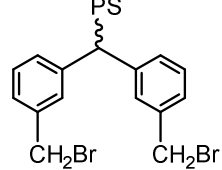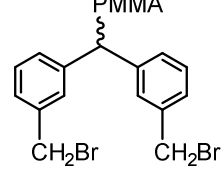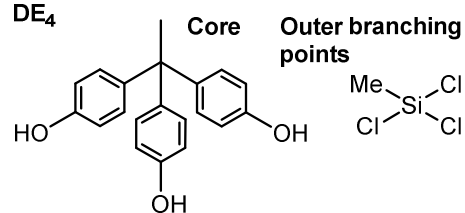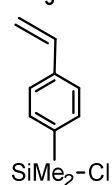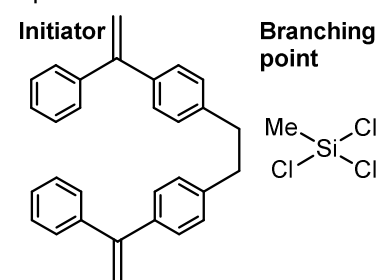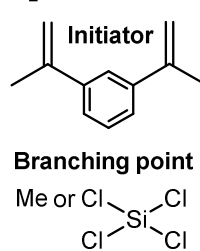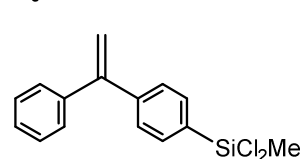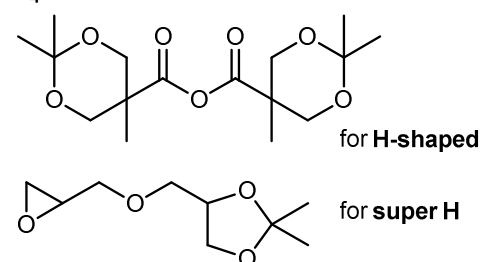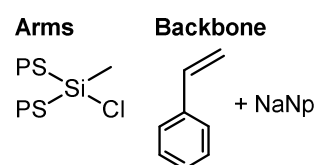
Figure 31: Branching moieties used for the synthesis of the dendrimers DE₁ – DE₅ and the Super H-/H-shaped samples H₁ – H₅.

Pom-poms

For the pom-poms, two synthesis routes are reported. For P_1 and P_2, the strategy is to use a triblock copolymer with short outer blocks and after post-polymerization reaction (PPM), grafting onto the outer blocks. Due to the short length of the outer blocks compared to the middle block, the outer blocks can be considered as branching points. P_3 utilized the same triblock backbone approach, but no PPM is necessary due to the copolymerization of P2VP. The functional groups used for grafting onto of P_1, P_2, and P_3 are shown in Figure 32. After the grafting onto, some unreacted arms remain, which can be easily separated due to the high molecular weight difference. As with C_2, a distribution of arms around the determined arm number average is likely. For P_4 and P_5, a macromonomer based route is used. The macromonomer is polymerized to form the stars at the ends of the backbone followed by monomer addition to the living stars and linking to form the backbone. No TGIC data is available for these samples. Based on test reactions for the linker in P_5, for both P_4 and P_5 contaminations with stars and asymmetric stars might be possible.

Tadpole

The tadpole topology is realized through a combination of the copolymerization of a functional monomer followed by PPM and grafting onto by the arms. The intermediate products are carefully purified through preparative HPLC fractionation. TGIC shows no side products in the final product.

Pom-poms
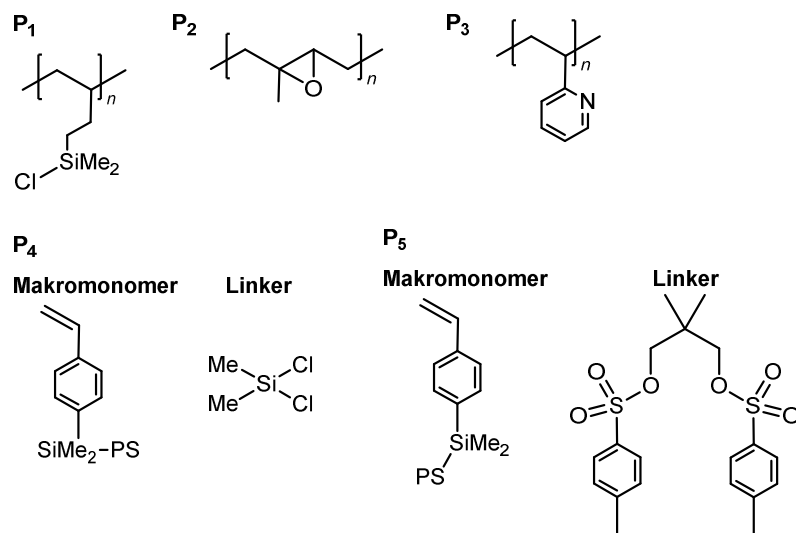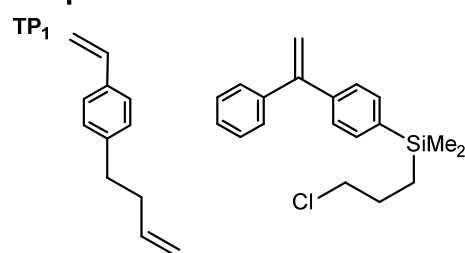
Figure 32: Branching moieties used for the synthesis of the pom-poms $P_1 – P_5$ and the Tadpoles TP_1.

In conclusion, many different synthesis routes can be used to access defined branched topologies. Chromatographical investigations using SEC equipped with a MALLS detector and especially TGIC are necessary to identify side products with similar molecular weights. Using chlorosilane compounds as linking agents has shown to yield significant side products in many cases, which cannot be identified in standard SEC. Nevertheless, the use of chlorosilane compounds as linking agents was demonstrated successfully yielding pure and well-defined products as shown with H_5 and DE_4 suggesting that details of e.g. the execution of the reaction step or the reactant purity are pivotal here. Grafting onto approaches and linking through ether or ester formation have shown to yield well-defined products.

The flow behavior of the synthesized branched architectures was mainly probed in SAOS. Uniaxial extension experiments were conducted for half of the samples, while nonlinear startup shear deformations were only investigated for ~ 42 % of samples. This might be partially due to small sample amounts (< 500 mg). Scaling of the known synthesis routes to yield higher product quantities would be beneficial as analysis of nonlinear relaxation behavior is especially important when investigating more complex topologies as the influence of these topologies might be hidden in linear regime as discussed in chapter 7.4. Furthermore, rarely any application focused testing of the synthesized materials like foaming or electrospinning is conducted. Utilization of well-defined branched polymers in such applications could pave the way for their unique properties to be used in real life applications. Upscaling of known
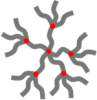
synthesis routes is also necessary for this aspect. Other powerful characterization techniques like NMR or dielectric spectroscopy to investigate the polymer dynamics are also rarely used. These techniques could give valuable insights into the chain dynamics which are not accessible via rheology.

Table 1: Overview over previous works on the synthesis of defined branched systems, their chromatographical and rheological analysis. Overview is focused on the chemistry used to introduce the branching, possible side products other than the target topology and on the investigated deformations in rheology. The number of samples is given in the column number of samples (NoS).
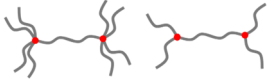
Category	Authors	Topology	Branching Moiety	NoS	Chromatography	Topological Impurities	Rheological Tests	Modelling	Other Applications	Ref.
Combs										
C_1	Abbasi, Faust, Wilhelm, and Coworkers	PS comb	Grafting onto acetylated PS after Friedel-Craft-Acetylation	15	SEC (DRI + MALLS Detectors)	Unknown	SAOS, uniaxial extension, MAOS	EHMMSF	Foaming, Electrospinning	[99,105 –110]
C_2	Read, McLeish, Chang, and Coworkers	PS comb	Grafting onto Chloromethylated PS after PPM	2	TGIC, SEC (DRI + MALLS Detectors)	none, on average 4 arms, distributed between 1 and 10	SAOS	None	None	[111]
C_3	Fernyhough, McLeish, and Coworkers	PB comb	Grafting onto Clorosilylgroup after hydrosylilation	10	SEC (DRI + MALLS Detectors)	Unknown	SAOS	Tube model for combs	None	[70,99, 100]
C_4	Gauthier and Co., Wilhelm and Co.	PI comb	Grafting onto epoxy group after epoxidation of PI	5	SEC (DRI + MALLS Detectors)	Unknown	SAOS	None	Multi-quantum NMR	[101, 102]

C_5	Hadjichristidis, Vlassopoulus, v. Ruymbeke, Chang, and Coworkers	PB exact, asymmertric comb	Endcapping with Cl_2Si-functionalized DPE, Grafting from	2	TGIC, SEC (DRI + MALLS Detectors)	Missing branches, condensation products, 19 identifiable side products	SAOS, Startup shear	Time marching algorithm, Tube model	Shear measurements with flow-birefringence apparatus	[116–118]
C_6	Hadjichristidis, Lee, van Ruymbeke, and Coworkers	PS, PI, PB comb, star-comb, comb-on-comb	Endcapping with 4-Chlormethylstyrene, copolymerisation of isoprene and macromonomer	2	SEC (DRI + MALLS Detectors)	Unknown	SAOS, step strain stress relaxation	Time marching algorithm (TMA)	None	[119–123]
C_7	Hadjichristidis, Leal, van Ruymbeke, and Coworkers	PI comb	Endcapping with 4-Chlormethylstyrene, copolymerisation of isoprene and macromonomer	4	SEC (DRI + MALLS Detectors)	Unknown	SAOS, step strain stress relaxation	TMA	None	[107, 109, 111, 112]
C_8	Hillmyer, Bates, and Coworkers	PLA star, comb, bottle-brush	Grafting through ring-opening metathesis	11	SEC (DRI + MALLS Detectors)	Unknown	SAOS, uniaxial extension	None	SAXS	[126]
C_9	Kempf, Wilhelm, and Coworkers	PS, PpMS Comb	Grafting onto acetylated PS, Grafting onto brominated PpMS	10	SEC (DRI + MALLS Detectors)	Unknown	SAOS, MAOS, uniaxial extension	Pom-pom model fitting	None	[114, 115]

C_{10}	Hepperle, Münstedt, Wagner, and Coworkers	PS comb	Endcapping with methacrylate ester, copolymerisation of styrene and macro-monomer	11	SEC (DRI + MALLS Detectors)	Unknown	SAOS, step strain stress relaxa-tion, uniaxial extension	MSF	None	[129–131]
C_{11}	Roovers, Vlassopou-lus, van Ruymbeke, Hyun, Wilhelm, Chang, and Coworkers	PS comb	Cloromethylation of backbone, endfunci-tonalization with carboxylic acid, nucleophilic attack to link arms to back-bone	18	TGIC, SEC (DRI + MALLS Detectors)	none, narrow molecular weight distri-butions in TGIC	SAOS, start-up shear, cessation of steady shear, MAOS, uniaxial extension	Tube model	None	[51,62, 73,109, 119–125]
C_{12}	Liu, Wang, Chang, and Coworkers	PS comb in tricresyl phos-phate	Endcapping and condensation using DDPE	2	TGIC, SEC (DRI + MALLS Detectors)	minor, nar-row molecu-lar weight distributions in TGIC	SAOS, start-up shear, step extension	None	None	[126, 127]
C_{13}	Ahmadi, v. Ruymbeke and Coworkers	PnBA comb	Copolymerization, grafting from	8	SEC (RI Detector)	Unknown	SAOS	None	None	[141]

Defined Polyethylenes										
PE$_1$	Hadjichris-tidis, Lohse, and Coworkers	PE comb, pom-pom, super H-, H-shaped	Comb: Grafting onto after hydrosylilation; pom-pom, super H-, H-shaped via Cl$_x$Si endcapping and grafting onto	17	SEC (DRI + MALLS Detectors)	Unknown	SAOS, uniaxial extension	None	None	[41, 129]
Dendrimers										
DE$_1$	Orfanou, Hadjichris-tidis, van Ruymbeke, Watanabe, and Coworkers	PB, PI star-dendrimer	Divergent, outer generations: end capping with Cl$_2$Si-functionalized DPE, grafting from; Inner branching point end capping with Cl$_3$SiMe	8	SEC (DRI + MALLS Detectors)	Unknown	SAOS, uniaxial extension	TMA	Dielectric spectrosco-py	[143–147]
DE$_2$	Haraguchi and Hirao	PS pom-pom-dendrimer	Divergent, grafting onto after PPM	5	SEC (DRI + UV Detec-tors)	Unknown	None	None	None	[148]
DE$_3$	Hirao, van Ruymbeke, Huang, ans Coworkers	PMMA star-dendrimer	Divergent, functional-ized initiator, grafting onto after PPM	7	SEC (DRI, viscosity, MALLS Detectors)	Unknown	SAOS, uniaxial exten-sion, flow cessation in exten-sion	TMA	None	[67, 136, 137]

DE₄	Hutchings, Read, McLeish, Chang, and Coworkers	PB, PS star-dendrimer	Functionalized initiator and endcapping, graphting onto, PPM, Linking	3	TGIC, SEC (DRI, viscosity, MALLS Detectors)	82.6 % desired product, 13.7 % is missing one arm, 3.7 % high Mw product	SAOS	BoB Model	None	[151–153]
DE₅	Knauss and Huang	PS star-dendrimer	Convergent, end capping with 4-Chlormethylstyrene, copolymerization of Styrene and macro-monomer	10	SEC (DRI + MALLS Detectors)	Unknown	None	None	None	[154]

Super H / H-shaped										
H$_1$	McLeish, Allgaier, Read, Chang, and Coworkers	PB, PI, partially deuterated H	Binfunctional initiator, endcapping with MeSiCl$_3$, grafting onto	5	TGIC, SEC (DRI, UV, MALLS)	Majority of desired product, low and high Mw side products in significant amounts	SAOS, strep strain stress relaxation, startup shear, uniaxial extension	BoB model	None	[64,71,155,156]
H$_2$	Islam, Archer, Juliani, and Coworkers	PB super H	Binfunctional initiator, endcapping with MeSiCl3 or SiCl$_4$, grafting onto	8	SEC (DRI, UV)	Unknown	SAOS, strep strain stress relaxation	Tube model based	None	[157–160]
H$_3$	Mays, Larson, Chang, and Coworkers	PB H shaped	Grafting Onto, grafting from, and linking	5	TGIC, SEC (RI, MALLS)	30 - 77 % desired product, various side products, mostly star/asymmetric star	SAOS	Tube model based	None	[161–163]

H$_4$	Frey, Hillmyer, Bates	PLA, PLA-*b*-PI H, super H	Bifunctional initiator, endcapping with multifunctional alcohol, grafting from	8	SEC (DRI, MALLS)	Unknown	SAOS, uniaxial extension	None	MALDI, DOSY, TEM, SAXS	[26,164]
H$_5$	Roovers, van Ruymbeke, Vlassopoulus, and Coworkers	PS H, H in solution, H in linear	Endcapping using SiMeCl$_3$ resulting in (PS)$_2$SiMeCl, grafting onto	6	TGIC, SEC (DRI, MALLS)	None	SAOS, startup shear	TMA, BoB model, slip-link simulations	None	[61,165–172]

Pom-poms

P$_1$	Hadjichristidis, and Coworkers	PS-*b*-PB pom-pom	Triblock copolymer (PB-*b*-PS-*b*-PB), hydrosilylation, grafting onto	4	SEC (UV, LALLS)	Unknown	SAOS	None	None	[173]
P$_2$	Hirschberg, Wilhelm, and Coworkers	PS, PS-*b*-PI pom-pom	Triblock copolymer (PI-*b*-PS-*b*-PI), epoxidation, grafting onto	24	SEC (DRI, UV, MALLS)	Unknown	SAOS, startup shear, uniaxial extension	EHMMSF	Foaming, SAXS, AFM, Tensile Testing	[86,96,100,174–181]
P$_3$	Schußmann, Hirschberg, and Coworkers	PS pom-pom, PS-*b*-PI star	Triblock copolymer (P2VP-*b*-PS-*b*-P2VP), grafting onto	3	SEC (DRI, UV, MALLS)	Unknown	SAOS, uniaxial extension	None	SAXS, Tensile testing	[182]

P$_4$	Knauss, van Ruymbeke, and Coworkers	PS pom-pom	Convergent, macro-monomer-*b*-styrene polymerization, linking	6	SEC (DRI, MALLS)	Unknown	SAOS	TMA	None	[13,36]
P$_5$	Nielsen, Hassager, Wagner, and Coworkers	PS pom-pom	Convergent, macro-monomer-*b*-styrene polymerization, linking	1	SEC (DRI, MALLS)	Unknown	SAOS, uniaxial extension	MSF, slip-link simula-tions	None	[12,87, 171]
Tadpoles										
TP$_1$	Doi, Takano, Takahashi, Matsushita, and Coworkers	PS circu-lar comb, Ring with branches	Copolymerization of styrene and 4-(3-butenyl)-styrene, endcapping, ring closing, hydrosilyla-tion and grafting onto	7	TGIC, SEC (RI, UV, MALLS)	None	SAOS	Rouse based model-ling	None	[184–186]

6   Synthesis of Pom-pom Polymers

Advantages and drawbacks of previous works are discussed in chapter 6.1 together with the synthesis route newly developed the in this thesis. In chapter 6.2, detailed synthetic procedures are given for the routes used in this thesis to access the pom-pom topology. Detailed molecular characteristics of the pom-poms (chapter 6.3) and additional characterization (chapter 6.4) is described afterwards.

Parts of this chapter have been published in preceding publications.[86,175,178,182]

6.1   Use of Functional Groups

To correlate the rheological response with the molecular properties of branched polymers, it is of utmost importance to have well-defined, low disperse chains. The synthesis route is crucial for topological purity. Most routes lack the ability to synthesize high arm numbers ($q > 5$ per side),[145,148,158,160,187,188] contain significant topological impurities,[116,155,163] or utilize time consuming reaction procedures.[173,189] An overview over established synthesis paths and the newly developed paths is illustrated in Figure 33. For a detailed overview see chapter 5.
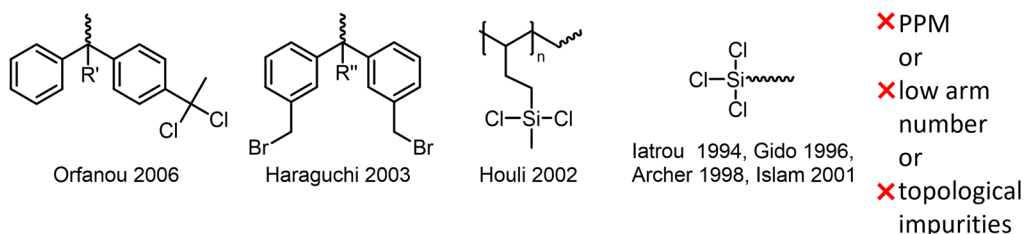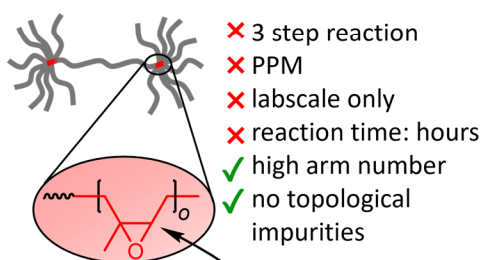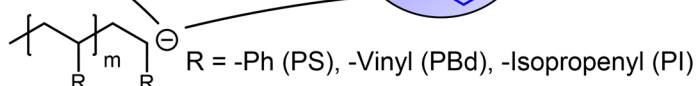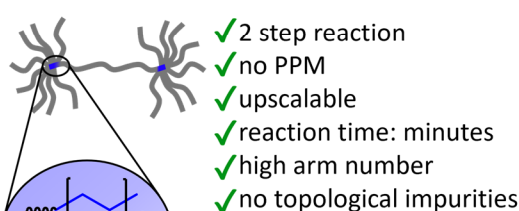
Figure 33: Functional groups used in grafting onto reactions to introduce branching in previous works and in this work. Dashed bonds represent polymer chains. References mentioned in the figure are Orfanou 2006[145], Haraguchi 2003[148], Houli 2002[173], Iatrou 1994[187], Gido 1996[188], Archer 1998[160], Islam 2001[158].

The synthesis route developed by Orfanou et al.[145] utilizes functionalized 1,1-diphenylethylene moieties (DPE). Living polybutadiene anions are grafted onto the benzylic position while avoiding attack onto the double bond by careful stoichiometric addition. Subsequent addition of s-BuLi leads to initiation of the macromonomer trough the preserved double bound and is followed by monomer addition for the backbone formation. Haraguchi et al.[148] started with a bifunctional initiator and a protected DPE moiety to endcap the backbone in α and ω position. Deprotection leads to the bromine functionality shown in Figure 33. Both synthesis routes can be used to yield the desired pom-pom product in five synthesis steps. Synthesis effort is high, especially for the preparation of the functionalized DPE moieties. Both synthesis routes are prone to lead to topological impurity in case of incomplete conversion or unintended termination.

Houli et al.[173] used a PB-b-PS-b-PB triblock with short outer blocks followed by post-polymerization modification (PPM) and grafting onto to yield PB-g-PS pom-poms. While the synthesis route of Houli et al.[173] is fairly elegant and yields product of high topological purity (same functional group as C_2, see discussion in chapter 5), good control over branching point placement and high possible arm numbers, the synthesis procedure is also challenging and lengthy. The hydrosilylation of the vinyl groups of the outer poly(1,2-butadiene) block precursor has a total reaction time of two day. The subsequent purification from unreacted Me$_2$SiClH and other silyl chlorine species requires drying under high vacuum for 5 days. Therefore, the synthesis is unsuitable for large sample libraries with varying molecular parameters. For upscaling beyond to the multiple gram scale, a quicker approach is needed.

Yuan and Gauthier[115] synthesized PI combs with high 1,4-microstructure through epoxidation of the double bound in the backbone chain and grafting onto of the arms. The concepts of utilizing triblock copolymers with short outer blocks introduced by Houli et al. was adapted by Röpert et al.[177,178] for the synthesis of PS pom-poms. As the outer blocks, PI was used instead of PB, reducing synthesis difficulty away from the cancerous gas butadiene. The PPM in the epoxy route requires a reaction time of 45 min for the epoxidation using H$_2$O$_2$/HCOOH and subsequent freeze drying of the backbone overnight. The hydrosilylation reaction of Houli et al. requires a reaction time of two days and subsequent drying for five days resulting in a total time of seven days. Therefore, the epoxy route significantly reduces the required time from seven to one day for the PPM step. This reaction is well suited for the synthesis of stars,[78] pom-poms,[177] multistar[181] and branch-on-branch[190] polymers due to a free choice of isoprene and styrene block order. The epoxy route significantly reduces the total required synthesis time, and a well-defined product is obtained. Nevertheless, a major part of the synthesis time is spent on the PPM and this reaction step is prone to introducing impurities into the backbone, which then can lead to termination of the living arms instead of the grafting onto in the third reaction step. Upscaling from multiple grams of product to multiple hundred grams is still significantly hindered by the PPM. If the monomer repeating units of the outer blocks could be grafted onto by the living arms without preceding PPM, the synthesis procedure would be significantly more suitable for upscaling. A reduction from three to two synthesis steps would reduce the total synthesis time additionally. Additionally, branched polymers of dienes like PB, PI or biobased ones like polyfarnesene or polymyrcene are not possible.

In 1994, Watanabe and coworkers[191] tried to synthesize linear PS-*b*-P2VP-*b*-PB triblock polymers via coupling of living PB anions with PS-P2VP-C1 diblock prepolymers. While attempting to link the two precursor polymers using a nucleophilic attack onto the chlorine functionality, they discovered that PB anions can attack the nucleophilic pyridine ring as well as the terminal chlorine moiety. This discovery of the grafting onto of strongly nucleophile polymers onto the pyridine ring enables the two-step pom-pom synthesis via the so called P2VP route without the need for any PPM as illustrated in illustrated in Figure 33. For a PS pom-pom, a P2VP-*b*-PS-*b*-P2VP triblock copolymer is used as the backbone and directly followed by grafting onto the pyridine ring by the arms. For stars, a short P2VP polymer can be used. The synthetic effort compared to the epoxy route is reduced by one third in respect to total time. With the P2VP route, synthesis in the 100 g to 1 kg scale was achieved as described in detail in chapter 6.2 with over 300 g in one batch. Stars and pom-poms can be easily synthesized using the P2VP route.[182] Branch-on-branch or multistars are not possible with the P2VP route as P2VP anions cannot initiate styrene and diene monomers.

During processing at industrial scales, the polymer melt is subjected to an unique combination of shear and extensional deformations. For example, high shear rates occur during coating or complex deformations during extrusion foaming, which both cannot be accounted for in experiments with standard rotational rheometers. Therefore, higher quantities (typically > 100 g) are needed, enabling measurements with capillary rheometers for high shear rates or on a small-scale extruder for foam extrusion for the direct evaluation of pom-poms and other complex branched topologies. The full potential of the defined branched materials and relevance to industry can only then be investigated properly. As a proof of concept, over 300 g of pom-pom 300k-2x24-40k was synthesized as described in detail in the following section and the foam properties were evaluated after blending with commercial PS and foam extrusion. In Figure 34, the strong effect on the cell size and morphology by adding only 15 wt% of the pom-pom is shown. The foam cells are substantially increased in size and the foam density is reduced, which is beneficial for e.g. increased heat insulation. The foaming process was conducted in the group of Prof. Ulrich Handge, Technische Universität Dortmund.
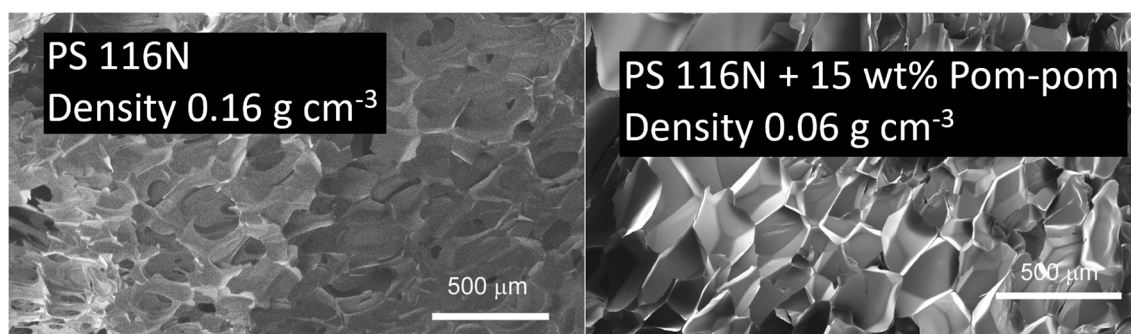
Figure 34: SEM pictures of the foamed PS 116N pure (left) and blended with 15 wt% pom-pom (300k-2x24-40k). The addition of the pom-pom reduced the foam density by a factor of 2.6.

Note that the P2VP route requires strong nucleophilicity such as alkali metal carbanions to enable the attack onto the weakly electrophile C6 carbon of the pyridine ring, as illustrated in Figure 35. The reactivity of the epoxy group is increased by the ring tension of the three membered ring and therefore weaker nucleophiles are theoretically also sufficient for the grafting

reaction. The epoxy functionality could also be useful when synthesizing branched structures with different chemistry than PS/dienes as for example polyethylene oxide, polypropylene oxide, polylactic acid, or polyesters.
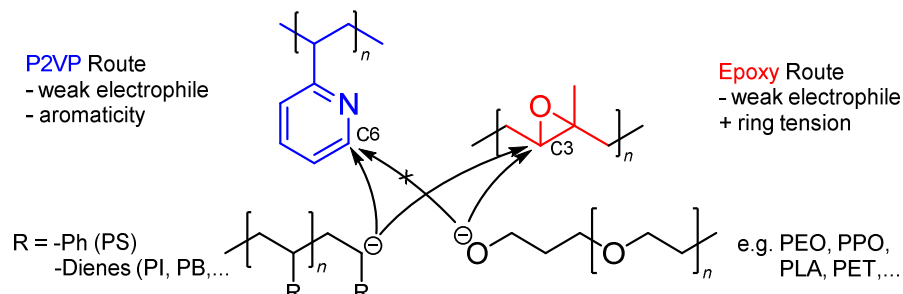
Figure 35: Illustrations of the grafting reaction onto the functional group of the epoxy and P2VP route. Characteristics of the functional groups are illustrated next to them.

6.2   Experimental Procedures

In this section, detailed experimental procedures are given for typical reactions using the epoxy and the P2VP grafting routes for the synthesis of the pom-poms within this thesis.

Epoxy route

The reaction scheme of the epoxy route is illustrated in Figure 36. In the first step, the backbone is polymerized through sequential monomer addition of isoprene, styrene and isoprene at room temperature by *s*-BuLi as an initiator in cyclohexane. After initiation of the first isoprene block, the reaction mixture is stirred for 4 h. After styrene addition, the reaction mixture is stirred for 16 h and after the second isoprene addition for another 4 h. The polymerization is terminated with degassed methanol. The triblock is obtained by precipitation from methanol and dried under reduced pressure to remove residual solvents as they interfere with the epoxidation reaction in the following step. The molecular weight of the PI block is kept at 5000 g mol^{-1} / ~ 70 monomer repeating units and the amount of styrene is adjusted according to the desired total backbone molecular weight. For the samples with a backbone of $M_{w,b}$ = 14.5 kg mol^{-1}, the PI block was reduced to 2000 g mol^{-1} / ~ 29 monomer repeating units (compare Table 2). A typical reaction is conducted using 200 mL dry cyclohexane, 9.9 mL styrene (9.0 g, 0,086 mol), 0.74 mL isoprene (1.08 g, 0,016 mol), 0.077 mL *s*-BuLi (0.1 mmol, 0.077mL).
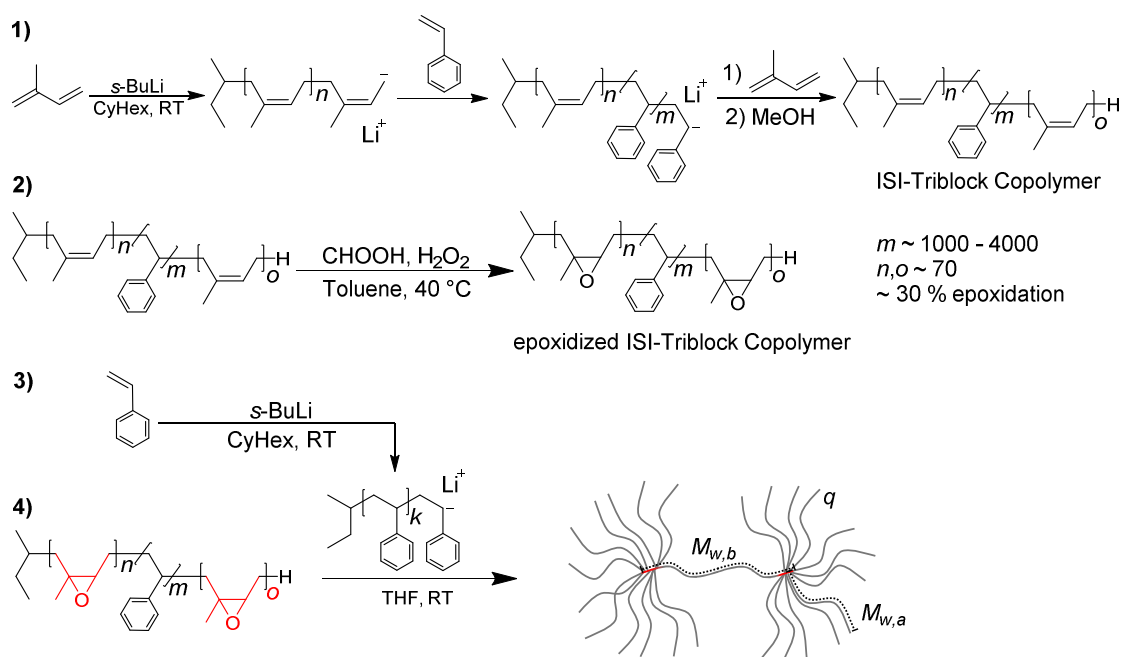
Figure 36: Reaction scheme for the synthesis of PS pom-poms using the epoxy route with the reaction steps 1) polymerization of the ISI backbone, 2) epoxidation of the backbone, 3) polymerization of the arms and 4) grafting of the living arms on the backbone. Adapted from Schußmann et al.[86] under the Creative Commons Attribution 4.0 International License.

In the second step, the PI outer blocks of the backbone are epoxidized using formic acid and aqueous H_2O_2. The reaction procedure is adapted from Yuan and Gauthier.[115] The ISI triblock (10 g, 10 wt% PI) is dissolved in 200 mL toluene and 0.75 g formic acid is added. Upon heating to 40 °C, 1.77 g H_2O_2 (30% aqueous solution) is added dropwise, and the reaction mixture is stirred for 50 min. The organic phase was washed with 50 mL saturated NaCl solution three times and precipitated in methanol. The precipitate was dissolved in purified 1,4-dioxane and freeze dried. 1,4-Dioxane was purified by distillation under reduced pressure to remove any impurities and stabilization agents, as they would remain in the epoxidized triblock after freeze drying. The impurities would then terminate the living chain ends of the arms in reaction step 4 and prevent the grafting onto reaction. Typically, 30 % of the PI repeating units are epoxidized. The isolated peak (k) at around 2.70 ppm in the ^{1}H NMR spectrum indicates the peroxide formation as shown in Figure 37.

Figure 37: ^{1}H NMR Spektrum of the epoxidized ISI triblock showing a) the full spectrum and b) a zoom from 5.5 – 2.5 ppm (solvent: CDCl$_3$, 400 MHz, 1024 Scans).

The arms are typically polymerized using 200 mL cyclohexane, 22.0 mL styrene (20.0 g, 0.192 mol) and 0.77 mL *s*-BuLi (1.00 mmol). The polymerization mixture is stirred for 16 h at room temperature. A sample of the arms is removed for characteriza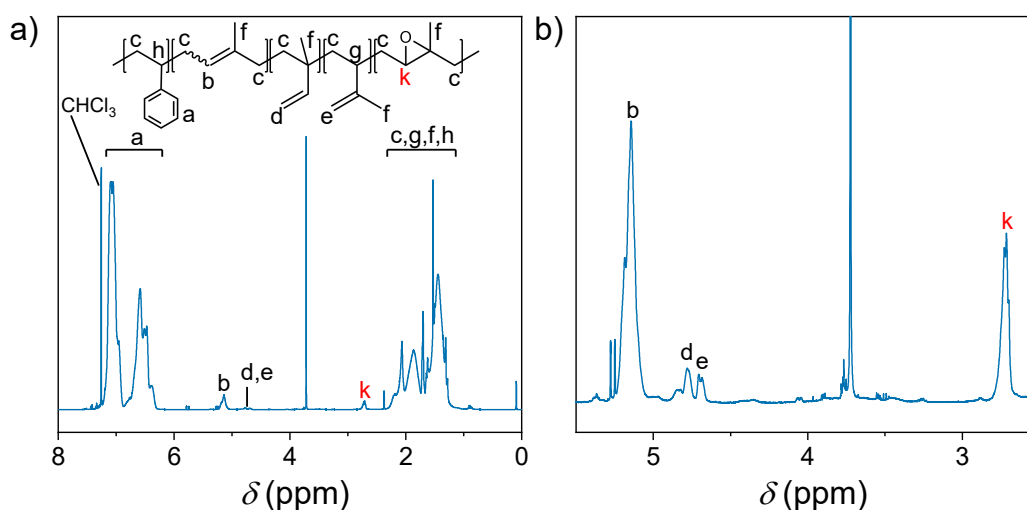tion before addition to the backbone. The reaction mixture can heat itself and lead to a thermal runaway, due to the exothermic nature of the polymerization. Therefore, as a guide for the used flasks (one neck, one Schlenk valve, round bottom, 250 mL, Schott Duran), a room temperature water bath equipped with a stir bar should be placed underneath the reaction flask, if 0.5 mL of *s*-BuLi per 100 mL of cyclohexane or more is added for the initiation of styrene. Other monomers and solvent combinations may differ. In the fourth step, the living arms are grafted onto the epoxidized ISI backbone. The backbone is dried thoroughly under high vacuum beforehand. THF (typically 200 mL) is freshly distilled onto the backbone. The living arms are added to the backbone solution at room temperature and the reaction mixture (50/50 vol% THF/Cyclohexane) is typically stirred for one day. The arms are typically added in 25% excess to compensate for partial termination due to impurities in the backbone. As an example, for a pom-pom with a targeted arm number of 2x12, a ration of backbone to arms of 1:30 is used for the reaction. For high arm or backbone molecular weights, high arm numbers or more concentrated solutions, the reaction time is increased up to 3 days. Residual living arms are terminated by degassed methanol and the reaction mixture is precipitated in methanol. Typically, 20 – 50 % arms are unreacted and not attached to the backbone. They are removed be fractionation from THF/MeOH solution. The final product together with 0.1 wt% antioxidant (2,6-di-tertbutyl-4-methylphenol, BHT) was dissolved in 1,4-dioxane and freeze dried. Typically, 10 g of fractionated, final product are obtained. The grafting reaction of the arms onto the backbone increases the overall molecular weight and therefore reduces the elution volume in SEC. The elution volume shifts from 13.7 mL for the backbone to 12.5 mL indication a successful grafting reaction as shown in Figure 38.
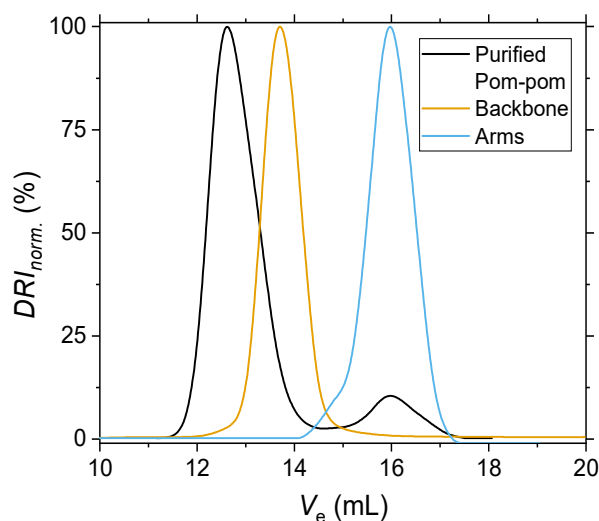
Figure 38: Elugram of the arms, the backbone and the fractionated pom-pom for the sample 100k-2x12-24k.

To calculate the arm number of the pom-pom, the elugram with the DRI signal of the arms before grafting and the crude grafting product are used. The areas under the peaks of the product and the unreacted arms, the molecular weight of the arms, and the used masses give the arm number with the following relation

$$n_{arms} = \frac{n_{arms,total} - n_{arms,residual}}{n_{backbone}} \tag{54}$$

The total molecular weight of the pom-poms was confirmed by multiangle laser light scattering (MALLS).

P2VP route

The P2VP route is shown in Figure 39. This route can be used in a larger laboratory scale (LLS) to synthesize in total 310 g of pom-pom polymer in one batch. A procedure for the LLS is given here. The P2VP route can also be used in the 10 g scale. The initiator solution is synthesized by addition of 0.63 g potassium and 0.883 g naphthalin to a 250 ml flask. 130 mL of dry THF is distilled into the flask and the solution is stirred for three days. In the first reaction step, a 2 L, two necked round bottom flask is charged with 4 mL NaNp solution (0.05 M, 0.2 mmol) in 1000 mL freshly distilled THF at −80 °C. After the addition of 58.6 mL Styrene (53.3 g, 0.512 mol), the polymerization is allowed to proceed for 20 min. After completion of the PS block, 6.9 mL 2-Vinylpyridine (6.72 g, 0.064 mol) is added and after 5 min the polymerization is terminated by 1 mL MeOH. The polymer is precipitated from MeOH. The precipitated triblock copolymer is dissolved in purified 1,4-dioxane and freeze-dried.
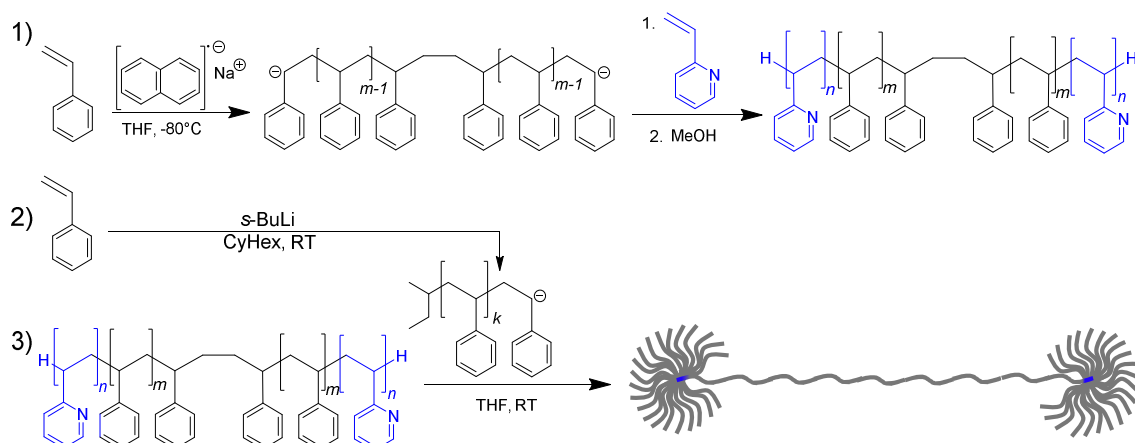
Figure 39: Reaction scheme for the synthesis of PS pom-poms using the P2VP route with the reaction steps 1) polymerization of the 2VP-S-2VP backbone, 2) polymerization of the arms and 3) grafting of the living arms on the backbone. Adapted from Schußmann et al.[182] under the Creative Commons Attribution 4.0 International License.

In the second reaction step, the arms are polymerized similar to the epoxy route in cyclohexane with *s*-BuLi as an initiator. For the LLS, 50 ml styrene is added to 2.5 L of cyclohexane and initiated by 5.1 mL *s*-BuLi solution (1.4 M, 7.34 mmol). A custom made 3 L round bottom flask with a Young valve near the bottom was used for the addition of the living arms in the third reaction step (see Figure 40 left picture). Other techniques such as cannula transfers turned out unsuitable for the amount of reaction mixture or the required purity. Styrene is added gradually over 10 h (Total styrene: 285.4 g, 2.74 mol) for the temperature of the reaction mixture to be around 30 °C. If styrene is added to quickly or all at the same time the reaction can proceed into thermal runaway.

In the third reaction step, the arms are grafted on to the P2VP-*b*-PS-*b*-P2VP backbone. The dried backbone (32.5 g) is dissolved in 300 mL THF in a 3 L, three-necked round bottom flask. The flask containing the living arms is attached through the Young valve as shown in Figure 40 right picture and the solution is added. The reaction is stirred for 16 h at room temperature. Residual arms are terminated with 1 mL degassed MeOH. The polymer is precipitated from MeOH and fractionated with MeOH/THF.
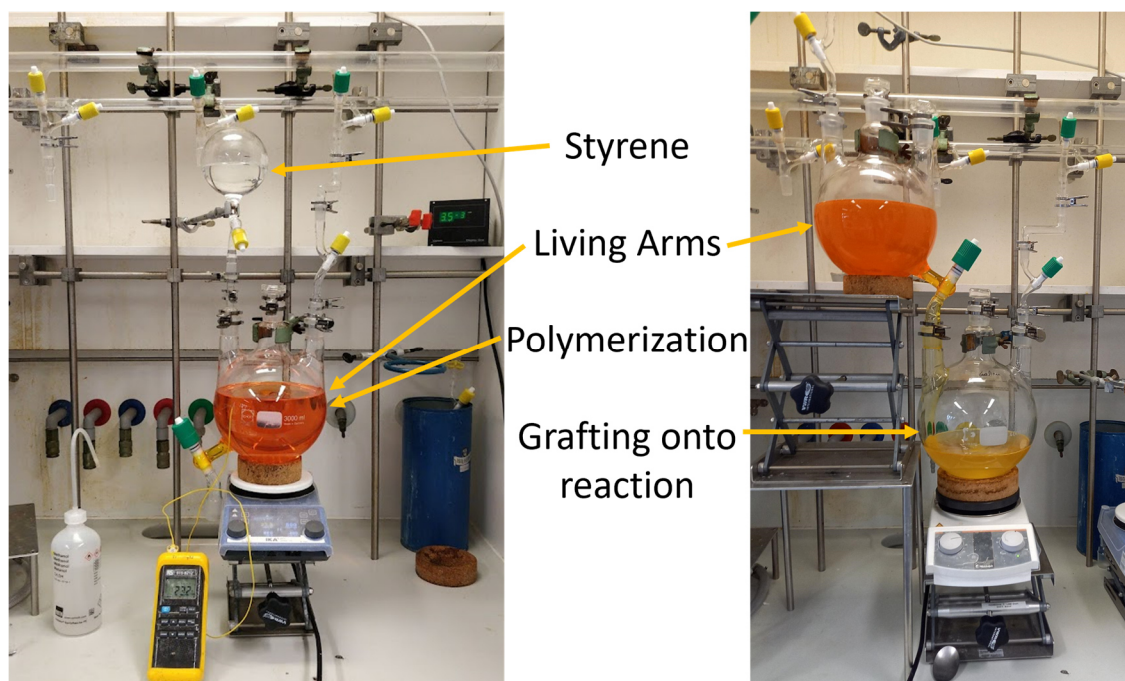
Figure 40: Left picture: Polymerization of the arms in cyclohexane. Right picture: Grafting of the arms onto the P2VP-b-PS-b-P2VP backbone. The arm solution is added through the Young valve installed near the bottom of the 3 L flask.

Similar to the epoxy route, the crude product of the P2VP route contains some unreacted arms. The elugram of the crude product of 300k-2x24-40k is shown in Figure 41 and shows roughly 20 % of unreacted arms. After one fractionation step from THF/MeOH, less than 5 % unreacted arms remain due to the big difference in molecular weight. The fractionated pom-pom and 0.1 wt% antioxidant (BHT) are dissolved in 1,4-dioxane and freeze dried. The separation of two polymers by solution precipitation is effective if the apparent molecular weight difference is above a factor of 10. Below a factor of 5, the fractionation is very inefficient and almost no separation between the two polymer species is achieved. Apparent molecular weight of the branched species corresponding to a linear polymer with the same elution volume can be used for this approximation. No difference can be observed within the uncertainty of the experiment when the multi angle laser light scattering (MALLS) and the differential refractive index (DRI) trace of the purified pom-pom are compared. As MALLS is especially sensitive to high molecular weight products, coupling reactions to form high molecular site products as observed with other synthesis routes (compare chapter 5) are not observed with the P2VP route.
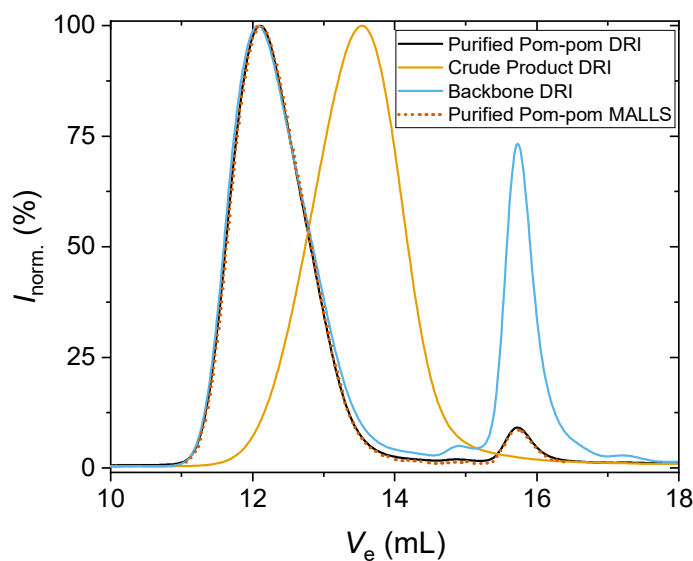
Figure 41: Elugram of the pom-pom 300k-2x24-40k showing the backbone, the crude and the purified product (MALLS and DRI trace).

The grafting reaction onto the pyridine ring can also be observed using ^{1}H NMR. As shown in Figure 42 a), the C6 carbon, on which the grafting onto takes place, has an isolated peak around $\delta = 8.2$ ppm labelled **1** (C6-H). In Figure 42 b), the peak integral of **1** is reduced due to the replacement of the hydrogen by the PS arm during the nucleophilic addition and rearomatization to the ring.[192–195] Due to the low concentration of **1** protons, the integral is partially overlapped by the neighboring peaks. To obtain the correct integral, a Gaussian function is fitted to the neighboring peak and its intensity is subtracted. The ratios determined in the NMR spectrum show a ratio of 2.84:1000 (**1**:**2**). Using the arm number estimated from the SEC traces to calculate the ratio of **1** and **2**, an integral ratio of 2.6:1000 is obtained. Both methods are therefore in good agreement with each other, confirming the molecular structure of the pom-pom with $q = 24$. The grafting density of the herein-reported grafting procedure is around one out of five P2VP monomer repeating units, similar to previously reported observations.[191]
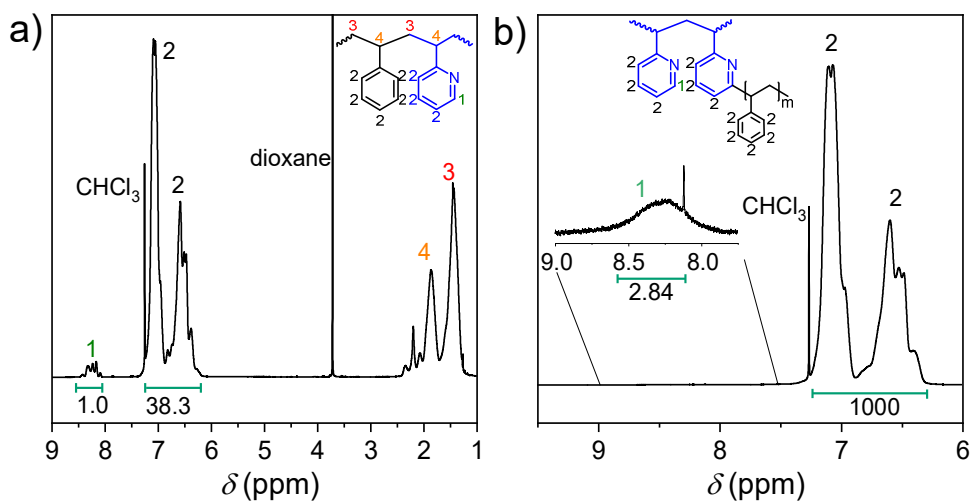
Figure 42: ^1H NMR spectrum of a) the 2VP-S-2VP backbone and b) the pom-pom 300k-2x24-40k (solvent: CDCl$_3$, 400 MHz, 1024 Scans). Numbers on the peaks refer to the corresponding protons shown in the inlet. Adapted from Schußmann et al.[182] under the Creative Commons Attribution 4.0 International-al License.

6.3 List and Classification of Synthesized Polymers

Samples with star topology are named $1xq - M_{w,a}$. Pom-poms are named after the scheme $M_{w,b} - Yxq - M_{w,a}$. Combs are named after $M_{w,b} - q - M_{w,a}$. The backbone molecular weight is $M_{w,b}$, the arm molecular weight is $M_{w,a}$, and the arm number is q. In Table 2, the molecular parameters as well as dispersities and branching chemistry of all synthesized samples is listed to give an overview of the materials investigated in this thesis. Size exclusion chromatograms can be found in Figure 43, page 59 or preceding publications.[106,178,181,196]

Table 2: Overview of molecular parameters and branching chemistry of the synthesized and investigated samples. Additional samples are provided by a) Prof. Valerian Hirschberg, b) Anika Goecke, c) Dr. Lorenz Faust, and d) Dr. Marie-Christin Röpert.

Sample	$M_{w,b}$ [kg mol^{-1}]	$Đ_b$	$M_{w,a}$ [kg mol^{-1}]	$Đ_a$	$M_{w,total}$ [kg mol^{-1}]	q	$Đ_t$	Branching moiety
Pom-pom $M_{w,b} - 2xq - M_{w,a}$								
14k-2x14-3k	14.5	1.06	2.8	1.05	93	2x14	1.06	Epoxy
14k-2x12-5k	14.5	1.06	4.8	1.04	130	2x12	1.06	Epoxy
100k-2x11-9k	100	1.05	9	1.02	298	2x11	1.13	Epoxy
100k-2x12-24k	100	1.05	24	1.05	600	2x12	1.18	Epoxy
100k-2x12-40k	100	1.05	40	1.08	1060	2x12	1.16	Epoxy
100k-2x14-50k	100	1.05	50	1.20	1500	2x14	1.27	Epoxy
100k-2x12-120k[d]	100	1.05	120	1.12	2980	2x12	1.56	Epoxy
100k-2x14-300k[d]	100	1.05	300	1.14	8220	2x14	1.27	Epoxy
100k-2x5-25k	100	1.05	25	1.05	350	2x5	1.12	Epoxy
100k-2x22-25k	100	1.05	25	1.14	1200	2x22	1.15	Epoxy
220k-2x12-25k	220	1.06	25	1.03	622	2x12	1.08	Epoxy
220k-2x10-40k	220	1.06	40	1.03	1020	2x10	1.09	Epoxy
220k-2x3-70k	220	1.06	70	1.04	640	2x3	1.11	Epoxy
300k-2x15-2.5k	300	1.40	2.5	1.06	375	2x15	1.40	P2VP
300k-2x14-4k	300	1.40	4.8	1.05	412	2x14	1.40	P2VP
300k-2x9-8k	300	1.40	7.8	1.04	440	2x9	1.40	P2VP
300k-2x24-40k	300	1.40	40	1.03	2220	2x24	1.40	P2VP
400k-2x12-23k	400	1.10	23	1.03	952	2x12	1.14	Epoxy
400k-2x13-40k	400	1.10	40	1.03	1440	2x13	1.15	Epoxy
Additional Pom-poms								
280k-2x30-7k[a]	280	1.04	7	1.03	700	2x30	1.16	Epoxy
280k-2x22-22k[a]	280	1.04	22	1.08	1248	2x22	1.15	Epoxy
Additional Star								
1x11-27k[b]			27	1.07	275	1x11	1.09	Epoxy
Additional Combs								
290k-50-6k[c]	290	1.10	6	1.04	590	50	1.09	Acetyl
290k-100-6k[c]	290	1.10	6	1.06	890	100	1.07	Acetyl
310k-100k-15k[c]	310	1.10	15	1.03	1810	103	1.33	Acetyl
290k-60-44k[c]	290	1.10	44	1.05	2930	60	1.03	Acetyl
Linear 290k[c]					290		1.10	-
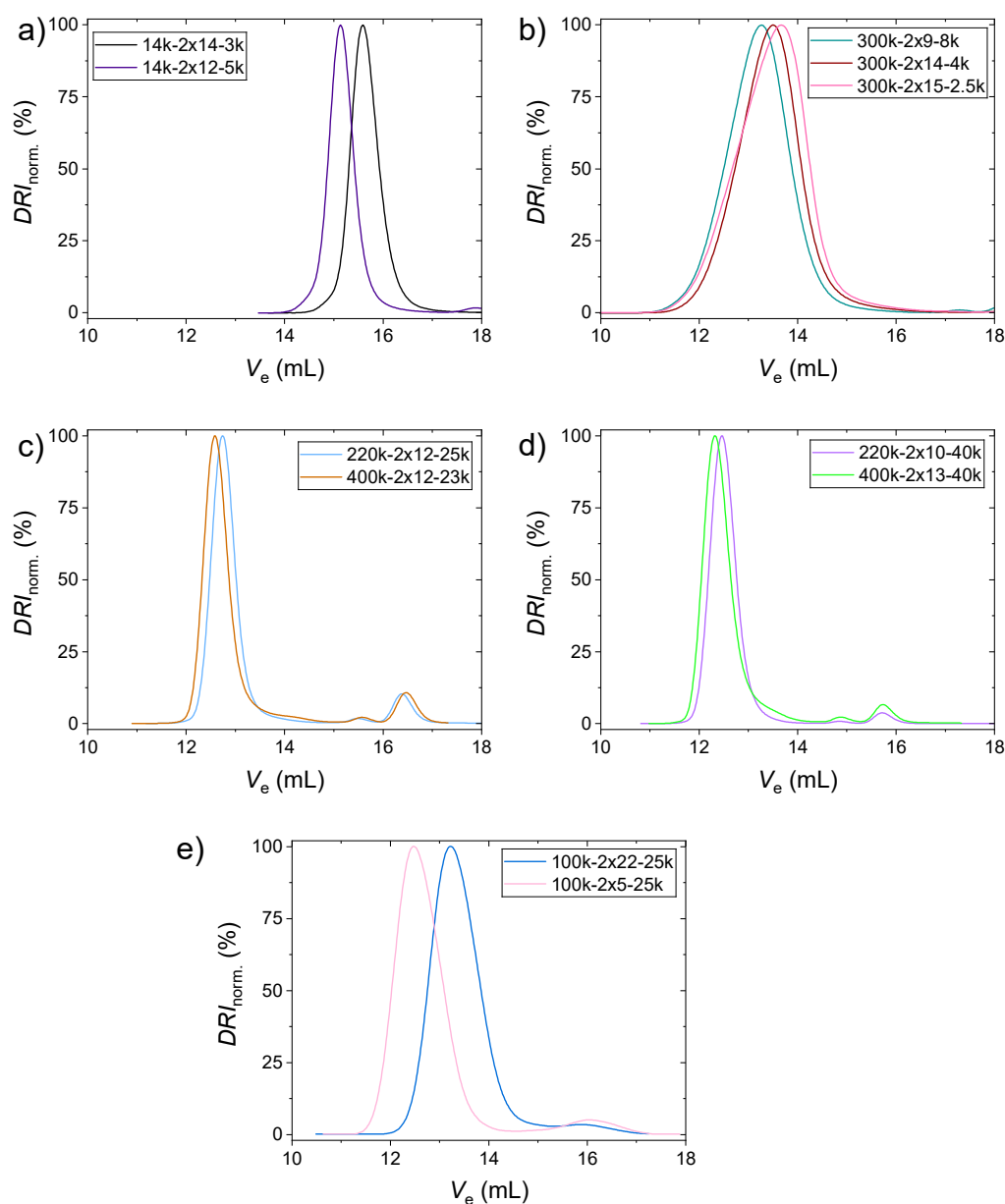
Figure 43: SEC Elugram of the various pom-poms synthesized within this thesis.

6.4 Additional Characterization

To investigate whether the arms of the pom-poms have any influence on the glass transition temperature T_g of the material, differential scanning calorimetry (DSC) was used. The glass transition temperature was obtained from the second heating run. Typically, 5 mg were sealed in an aluminum cup and heated with a heating rate of 10 K min^{-1}. Entangled pom-poms are shown in Figure 44 a) und the two fully unentangled samples are shown in Figure 44 b). For the entangled systems, no reduction of T_g is observed. For the two unentangled systems, the T_g is

slightly reduced as expected for short span molecular weight $M_{w,span} = M_{w,b} + 2\,M_{w,a}$. A similar reduction as in linear polymers with the same $M_{w,span}$ is observed, suggesting no influence of the topology on the glass transition temperature.[197]
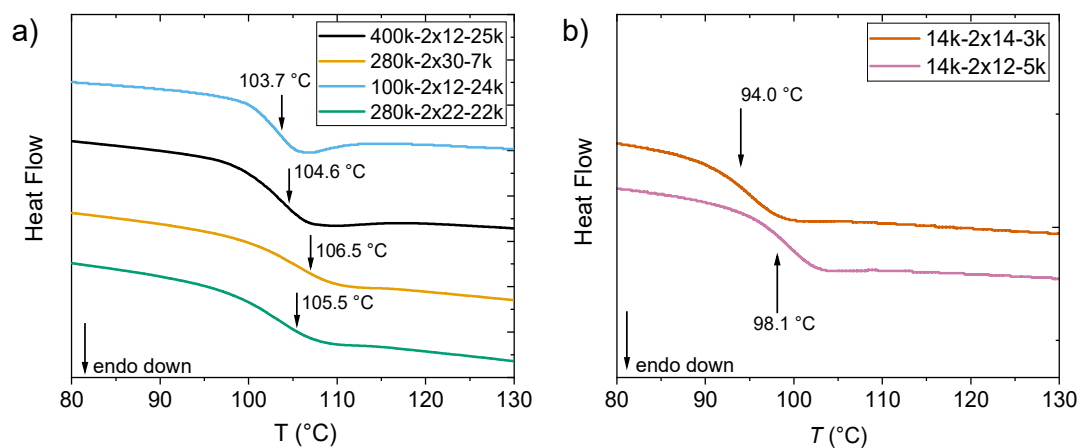
Figure 44: DSC curves of various pom-poms obtained with a heating rate of 10 K min^{-1}. The second heating run is shown.

7 Rheology on Branched Polymers

In this chapter the flow behavior of different branched architectures is investigated by small amplitude oscillatory shear (SAOS), startup shear and uniaxial extension experiments. SAOS relaxation behavior is analyzed to investigate the relaxation times of arms and backbone. Dilution effects are evaluated in the tube model picture. Insights into chain orientation and stretch are gained through startup shear experiments and uniaxial extension. Lastly, a new use case of the UXF geometry is proposed to measure the tensile stress growth function at $\varepsilon > 4$.

Findings discussed in this chapter have been partly published beforehand in manuscripts in Nature Communications[86] (chapter 7.1.1, 7.1.3, and 7.5), Physics of Fluids[175] (chapter 7.1.2 and 7.1.2), and Rheologica Acta[96] (chapter 7.5).

7.1 Pom-poms

In this section rheological data on pom-poms in SAOS, startup and extension are shown and analyzed in respect to chain relaxation times, dynamic dilution, chain orientation and stretching.

7.1.1 Small Amplitude Oscillatory Shear

In this section the oscillatory shear response of the pom-pom samples is discussed. The section is divided into pom-poms with entangled arms, pom-poms with unentangled arms and fully unentangled pom-poms.

Pom-poms with entangled arms

Polymer chains can be entangled or unentangled based on their molecular weight. The pom-pom samples consisting of the arms and a backbone can be divided into four main categories. The categories are assigned based on entangled or unentangled arms and an entangled or unentangled backbone. One example of each category is shown in Figure 45 a).

Category 1 is represented by 14k-2x12-5k (shown) and 14k-2x14-3k. As neither the backbone nor the arms are entangled, a Rouse regime and a terminal regime at low frequencies is found as typically found for unentangled polymers. Category 2 is represented by 100k-2x11-9k (shown), 300k-2x15-2.5k, 300k-2x14-4k, 300k-2x9-8k, and 280-2x30-7k with unentangled arms and a self-entangled backbone. The sample shows a small Rouse regime at high frequencies (10^2 - 10^4 rad s^{-1}) due to the unentangled arms, followed by a rubber plateau due to the self-entangled backbone ($3 - 10^2$ rad s^{-1}), and a terminal regime identified by the slopes of $G' \propto \omega^2$ and $G'' \propto \omega^1$ (< 1 rad s^{-1}). Category 3 samples have entangled arms and no self-entangled backbone and are 100k-2x5-25k, 100k-2x12-24k (shown), 100k-2x22-25k, 100k-2x12-40k, 100k-2x12-50k, and 300k-2x24-40k. They show three relaxation regimes: at low frequencies ($< 10^{-1}$ rad s^{-1}), the

terminal regime is found; at medium frequencies (0.3 – 10 rad s^{-1}), a Rouse relaxation regime can be identified where G' and G'' increase in parallel; at high frequencies (3 10^1 – 3 10^3 rad s^{-1}), a rubber plateau is found where $G' > G''$. The high frequency rubber plateau is a result of the longer arms compared to Category 2 samples. It is a result of arm and backbone entanglement effects. The Rouse relaxation behavior reveals a not self-entangled backbone caused by dynamic dilution of the backbone in the arms. The samples 220k-2x12-25k, 220k-2x10-40k (shown), 220k-2x3-70k, 280k-2x22-22k, 400k-2x12-23k and 400k-2x13-40k have self-entangled backbones and entangled arms and belong to category 4. They show two rubber plateaus (10^{-3} – 10^3 rad s^{-1}), due to their self-entangled backbone and entangled arms, as well as a terminal regime (< 10^{-3} rad s^{-1}). In Figure 45 b) the van Gurp-Palmen plot (δ vs. $|G^*|$) is shown exemplary for all four categories. The two different relaxation times of the arm and the backbone can be identified clearly for all samples. An overview over the molecular properties deciding the rheological behavior of the samples is given in Table 3. Additionally, the entanglement state and the resulting pom-pom category is shown.

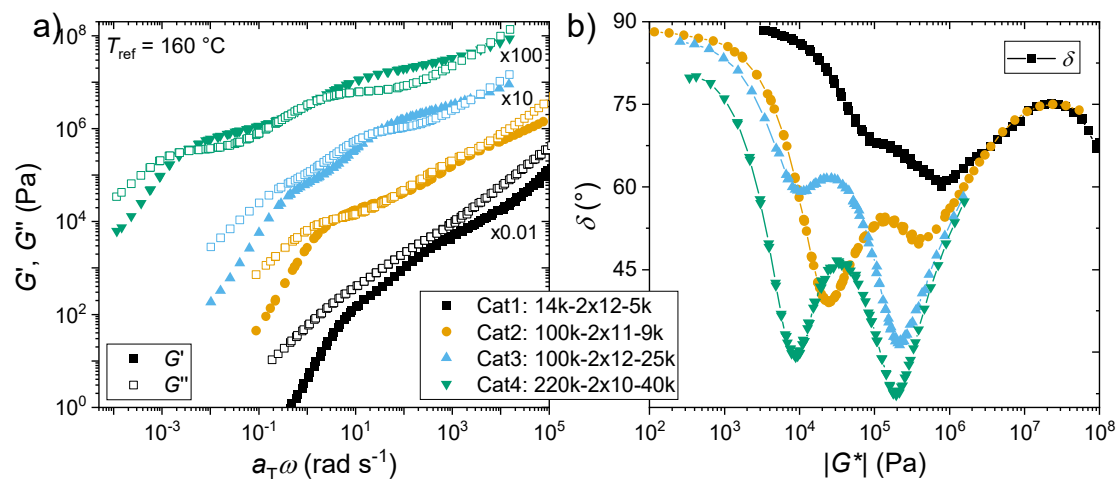*Figure 45: a) Mastercurve of exemplary pom-poms in category 1 represented by 14k-2x12-5k, category 2 represented by 100k-2x11-9k, category 3 represented by 100k-2x12-24k, and category 4 represented by 220k-2x10-40k. In b) their van Gurp-Palmen plot is displayed. It clearly shows distinct relaxation mechanism for arms and backbone. Adapted from Schußmann et al.[175] under the Creative Commons Attribution 4.0 International License.*

Table 3: Overview of arm numbers and of the entanglements of arms and backbone (δ < 45°). N = No, Y = Yes. Categories are assigned based entanglement state of the arms and the backbone determined based on SAOS. Samples are listed based on increasing backbone molecular weight.

Sample	Z_b	Z_a	q	ϕ_b	$Z_{b,eff}$	Backbone self-entangled	Arms entangled	Cate-gory
14k-2x14-3k	0.83	0.17	14	0.15	0.13	N	N	1
14k-2x12-5k	0.83	0.29	12	0.11	0.09	N	N	1
100k-2x11-9k	5.95	0.54	11	0.34	2.00	Y	N	2
100k-2x5-25k	5.95	1.49	5	0.29	1.70	N	Y	3
100k-2x12-24k	5.95	1.43	12	0.15	0.88	N	Y	3
100k-2x22-25k	5.95	1.49	22	0.08	0.50	N	Y	3
100k-2x12-40k	5.95	2.38	12	0.09	0.56	N	Y	3
100k-2x12-50k	5.95	2.98	12	0.07	0.46	N	Y	3
220k-2x12-25k	13.1	1.49	12	0.27	3.51	Y	Y	4
220k-2x10-40k	13.1	2.38	10	0.22	2.82	Y	Y	4
220k-2x3-70k	13.1	4.17	3	0.34	4.50	Y	Y	4
280k-2x22-22k	16.7	1.31	22	0.22	3.74	Y	Y	4
280k-2x30-7k	16.7	0.42	30	0.40	6.67	Y	N	2
300k-2x15-2.5k	17.9	0.15	15	0.36	6.41	Y	N	2
300k-2x14-4k	17.9	0.29	14	0.38	6.70	Y	N	2
300k-2x9-8k	17.9	0.48	9	0.48	8.62	Y	N	2
300k-2x24-40k	17.9	2.38	24	0.14	2.51	N	Y	3
400k-2x12-23k	23.8	1.37	12	0.42	10.0	Y	Y	4
400k-2x13-40k	23.8	2.38	13	0.28	6.61	Y	Y	4

The SAOS mastercurves of the 24k-series (1x11-27k, 100k-2x12-24k, 220k-2x12-25k, 400k-2x12-23k) are shown in Figure 46 a) at a reference temperature of T_{ref} = 140 °C. For the star, one rubber plateau followed by a terminal regime is found as described for star polymers.[198] For the pom-pom with $M_{w,b}$ = 100 kg mol^{-1} only one rubber plateau, corresponding to arm-arm and arm-backbone interactions, is observed. The backbone of the pom-pom with $M_{w,b}$ = 100 kg mol^{-1} is not self-entangled, meaning the backbones are not entangled with the backbones of other pom-poms at low angular frequencies, and therefore no second rubber plateau is shown. Distinct rubber plateaus for arms and backbones can be seen for the samples with $M_{w,b}$ = 220 kg mol^{-1} and $M_{w,b}$ = 400 kg mol^{-1}. Within these two later samples, the backbones are self-entangled. The rubber plateau of the backbone is shifted to lower moduli compared with linear chains due to dynamic dilution of the backbone in the arms (see discussion Figure 50, page 68). In Figure 46 b), the phase angle δ is shown as a function of the angular frequency. Similarly to the mastercurves, the two self-entangled backbones of the high $M_{w,b}$ pom-poms can be identified. In these two samples, the phase angle of the low-frequency minimum goes to $\delta_{b,min}$ < 45°, indicating the self-entangled backbones ($Z_{b,eff} \gtrsim 3$). The separa-

tion of the rubber plateaus is influenced by the difference in molecular weight and the backbone volume fraction. Higher molecular weight differences between arms and backbone and therefore higher relaxation times difference are leading to a more distinct separation between the two rubber plateaus. Volume fraction and molecular weight of the arms and the backbone will influence their respective minimum of the phase angle. Similar observations can be made for the 40k-series as shown in Supplementary Figure 1 in the appendix, page 130.
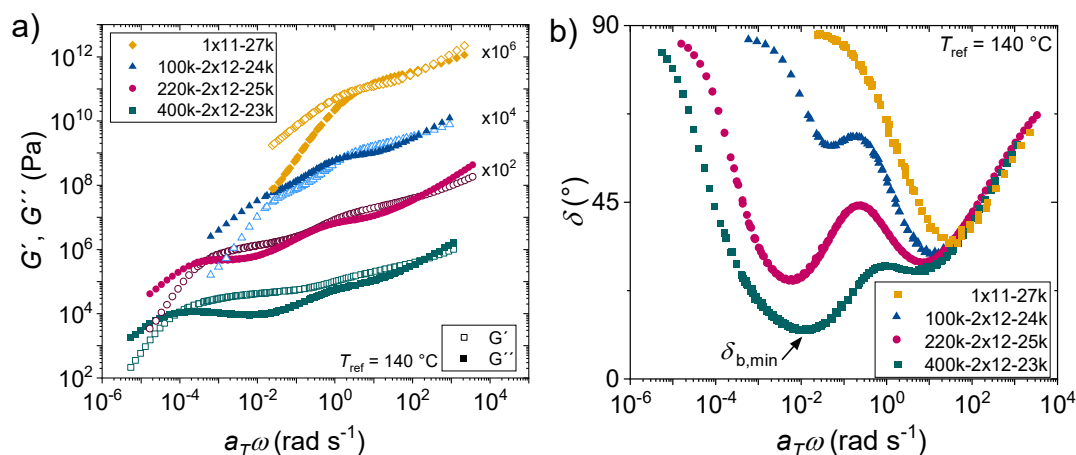

Figure 46: a) Mastercurves of the 24k-series of three pom-poms and a star. b) Phase angle δ as a function of the angular frequency $a_T\omega$. All data is shown at a reference temperature of $T_{ref} = 140\,°C$.

To analyze the relaxation behavior in more detail, G' is shown in Figure 47 as a function of $a_T\omega$. For the star polymer, the rubber plateau is found between $a_T\omega = 10^2 – 10^4$ rad s^{-1} and the storage modulus decays quickly at lower angular frequencies. In a), a second rubber plateau can be seen, increasing from a small shoulder for 100k-2x-12-24k to a full second rubber plateau for 400k-x12-23k. Around 1 rad s^{-1}, an increase of the storage modulus with increasing backbone molecular weight can be seen and this translates into an increase of the rubber plateau width. Therefore, a contribution of the backbone to the arm rubber plateau can be concluded. This contribution might be due to entanglements between the backbone and the arms resulting in an increased modulus. In Figure 41 b) around 0.1 rad s^{-1}, the dilution of the backbone in the arms is clearly visible. When the arm number is increased from $q = 5$ to $q = 22$, the storage modulus is decreasing due to the accelerated backbone relaxation.
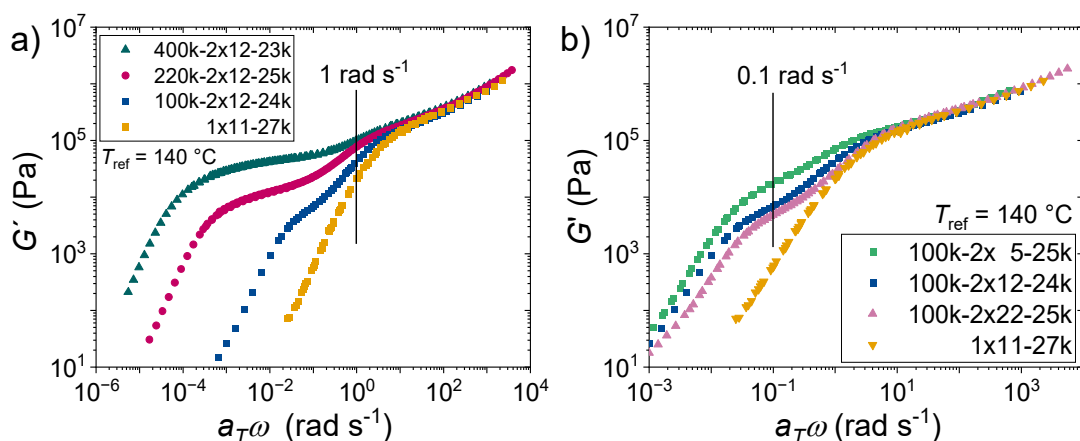
Figure 47: Storage modulus G' of three pom-poms and a star samples with $M_{w,a} \sim 25$ kg mol^{-1} and varying other molecular parameters given as a function of angular frequency $a_T\omega$ at a reference temperature of $T_{ref} = 140$ °C.

Pom-poms with unentangled arms

Long chain branches increase the relaxation time of a branched polymer compared to its linear analog due to hindrance of reptation by the branch. Short chain branches accelerate the relaxation due to their diluting effects on the main chain and do not increase resistance against reptation.[30] For LDPE, many studies investigated the influence of various branch sizes and their effects. For PE, branches below six carbons are considered short and above 50 carbons are considered long.[199] No further information about the transition between short and long chain branches and the exact length of the transition is known. To address this knowledge gap, three pom-pom samples with a long, well entangled backbone and three different arm lengths are synthesized using the P2VP route (described in detail in chapter 6, page 47ff.). A backbone molecular weight of $M_{w,b} = 300$ kg mol^{-1}, arm number $q \sim 14$, and arm molecular weights of $M_{w,a} = 2.5$, 4.8 and 7.8 kg mol^{-1} resulting in $Z_a = 0.15$, 0.29 and 0.46 were chosen (see Table 2). The mastercurves of the three pom-poms are shown in Figure 48 a). From the shape of the mastercurves, no clear effect of the branches can be seen. The overall shape is similar to that of linear polymers. In the inset of Figure 48 a), the longest relaxation time τ_L determined from the inverse crossover frequency as a function of the arm molecular weight is shown. The arm molecular weight influences τ_L. For the samples 300k-2x15-2.5k and 300k-2x14-4k, τ_L is reduced compared to the linear equivalent. For 300k-2x9-8k, τ_L is similar to the linear equivalent. This shows that similar to earlier works, very short branches dilute the main chain and therefore accelerating the relaxation. This data set suggests that the dilution of short branches is dominant for $M_{w,a} < 8$ kg mol^{-1} for PS, corresponding to $M_{w,a} \sim M_{w,e}/2$, $Z_a < 0.5$ kg mol^{-1} in general. In Figure 48 b), the van Gurp-Palmen plot, phase angle δ as a function of absolute magnitude of the complex modulus $|G^*|$, is shown. Within this plot, multiple relaxation times, e.g. from the branches and the backbone chain can be easily identified. Each minimum is a result of an individual relaxation time. For samples 300k-2x15-2.5k and 300k-2x14-4k, no second relaxation time is shown in the vGP plot. For 300k-2x9-8k, a shoulder can be identified around 4 10^5 Pa, as a result of the longer branches. If the branching number is increased even further like for the

sample 280k-2x30-7k, a distinct shoulder can be seen and for entangled arms (220k-2x12-25k) a minimum is formed. In SAOS, branches with $M_{w,a} < M_{w,e}/2$ act as short chain branches and with $M_{w,a} \geq M_{w,e}/2$ act as long chain branches. Discussion on the transition of short chain branches is continued at Figure 68, page 87 with uniaxial extensional data.
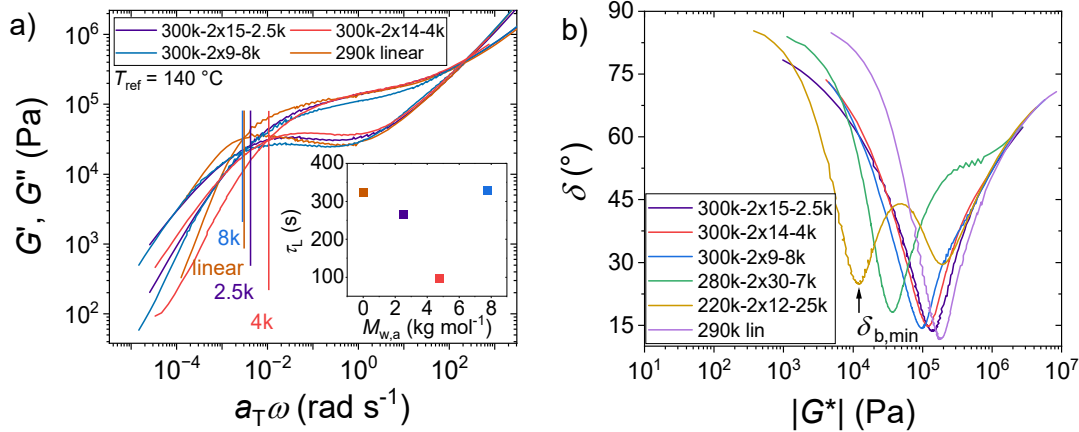

Figure 48: a) Mastercurves of the three pom-poms with short branches and a corresponding linear chain at a reference temperature of $T_{ref} = 140\ °C$, inset shows the longest relaxation time τ_L determined from the inverse crossover frequency as a function of arm molecular weight $M_{w,a}$, b) phase angle δ as a function of the absolute magnitude of the complex modulus $|G^*|$.

After relaxation, the arms act as a solvent around the backbone and dilute its entanglements. In Figure 49, the phase angle minimum of the backbone $\delta_{b.min}$ is shown as a function of the effective backbone entanglements

$$Z_{b,eff} = \phi_b * Z_b \qquad (55)$$

Pom-poms from Table 3 and from literature[12,36] are shown together with literature data on combs.[62,105,106,127,128] If $\delta_{b.min} < 45\ °$, the moduli display a rubber plateau which is caused by entangled backbone chains. For $\delta_{b,min} > 45\ °$, $G'' > G'$ and showing Rouse-like behavior relating to not self-entangled chains. Two regions can be identified for comb and pom-pom polymers. For $Z_{b,eff} > 3$, the backbone minimum phase angle is found to be below 45 °, indicating that the backbone is self-entangled. For $Z_{b,eff} < 3$, the $\delta_{b,min}$ phase angle is found to be above 45 °, indicating that the backbone is not self-entangled. These findings agree with the general dynamic dilution theory for linear polymer melts and solutions, where the critical entanglement number $Z_c \sim 3$ is found.[38] At a given phase angle, the effective backbone entanglements are lower for the pom-poms than for the combs as shown by the horizontal line at $\delta = 45\ °$ with $Z_{b,eff,comb} \sim 3$ and $Z_{b,eff,pom-pom} \sim 2$. The data suggests that the arms of the combs dilute the backbone more than the arms of the pom-poms and therefore the pom-pom melt shows a more elastic behavior than combs at the same $Z_{b,eff}$ in SAOS. The increased number of entanglements for pom-poms might be a result from the different branching positions, whereas entanglements are less efficiently formed when the branches are distributed along the backbone instead of at the ends. A comb and pom-pom with the same molecular parameters (same $M_{w,b}, q, M_{w,a}$) are needed to confirm this.
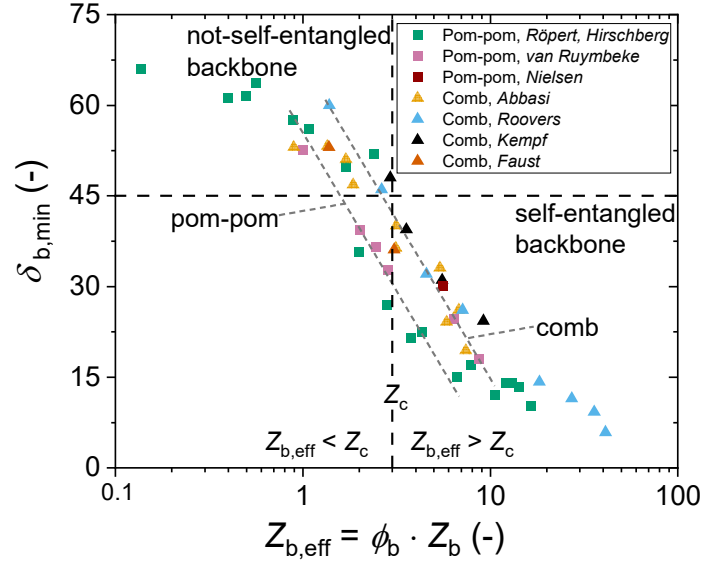
Figure 49: Phase angle $\delta_{b,min}$ of the backbone minimum shown as a function of effective backbone entanglements $Z_{b,eff}$. Dashed lines are a guide to the eye. Adapted from Schußmann et al.[175] under the Creative Commons Attribution 4.0 International License.

Dynamic tube dilution theory gives the relation

$$G_{N,s}^0 = G_N^0 * \phi_b^{1+\alpha} \tag{56}$$

to calculate the dynamically diluted modulus $G_{N,s}^0$ from the sample dependent plateau modulus G_N^0. The dilution exponent α is discussed to be either 1 or 4/3 depending on the system and the specific tube model resulting in a slope of 2 or 7/3 for $G_{N,s}^0$ vs ϕ_b.[61] The dynamically diluted modulus $G_{N,s}^0$ is obtained from the storage modulus at $\delta_{b,min}$. The samples show G_N^0 in the order of $G_N^0 \approx 2 \ 10^5$ Pa as expected for PS. In Figure 50, $G_{N,s}^0$ is given as a function of ϕ_b for pom-poms and combs.[62,106,175,177,178,181] Comb and pom-pom collapse onto one straight line in the log-log display with a slope of two. As a result, we experimentally find $\alpha = 1$ for our pom-pom and literature comb data. For linear chains and bimodal mixtures, it was found in simulations that $\alpha = 4/3$ matches the experimental data better.[66,200] This difference between linear and branched systems is not yet fully understood.
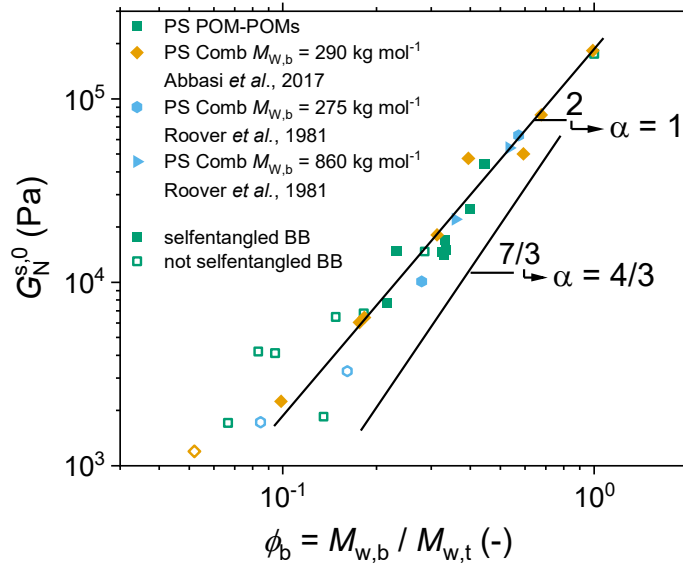
Figure 50: Dynamically diluted modulus $G_{N,s}^{0}$ shown as a function of the backbone volume fraction ϕ_b for pom-poms from this thesis and comb polymers from literature.

Fully unentangled pom-poms

The epoxy route (see chapter 6, page 47ff) was utilized to synthesize two fully unentangled pom-pom samples. This means that the arm and the backbone molecular weight are below the entanglement molecular weight of PS ($M_{e,PS}$ = 16,8 kg mol⁻¹). Two samples with the same backbone molecular weight of $M_{w,b}$ of 14.5 kg mol⁻¹ and two arm molecular weights of $M_{w,a}$ = 2.8 and 4.8 kg mol⁻¹ were synthesized. In Figure 51, the mastercurve of the pom-poms is shown at a reference temperature of T_{ref} = 140 °C. At high angular frequencies, the glassy region and the transition region can be seen. Followed by an extended Rouse regime with a slope of 0.6 between 10 and 1000 rad s⁻¹. At low angular frequencies, the terminal regime is found with a slightly longer relaxation time for the sample 14k-2x12-5k due to the higher span molecular weight. This order of relaxation characteristics is expected based on the molecular weights of the pom-poms and typical for unentangled polymers.

The samples were sent to Prof. Ianniruberto and Prof. Costanzo at the university of Naples to conduct startup shear experiments and compare the experimental data to a constitutive model they developed. The analysis is ongoing.
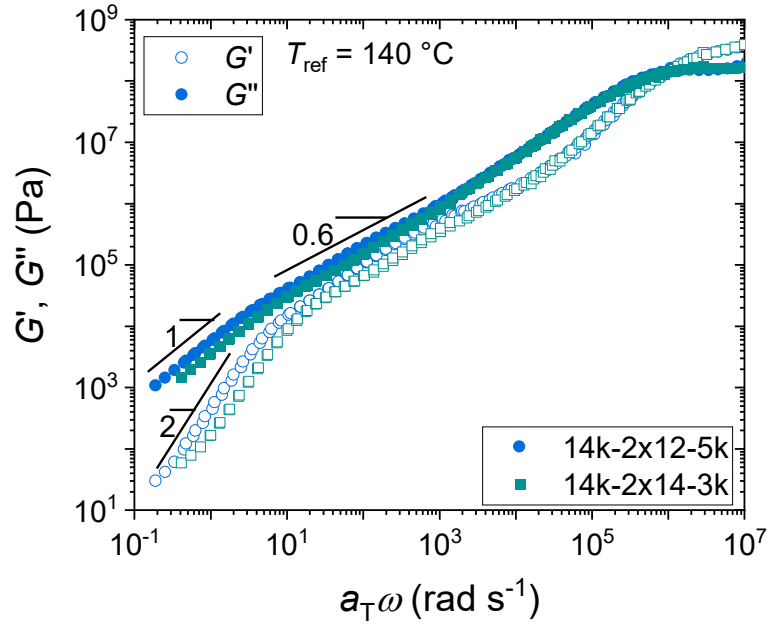
Figure 51: Mastercurve of the two fully unentangled pom-pom samples 14k-2x12-3k and 14k-2x14-5k at a reference temperature of T_{ref} = 140 °C.

7.1.2 Startup Shear

The experimental work in this chapter was conducted under the co-supervision of Professor Kyu Hyun (현 규) during my stay at the Pusan National University in Busan, Republic of Korea from January until May 2024.

Startup shear experiments can yield valuable insights for fundamental research as well as industrial processing. Information on chain stretch and orientation during the startup of steady flow at a constant shear rate of a polymer melt can be gained. Steady state shear viscosity information is highly relevant to industrial processing as steady shear is the main flow type during extrusion and the steady state shear viscosity is crucial in e.g. extruder design. Because steady shear is prone to flow instabilities, experimental data is rare especially for well-defined branched melts. The shear stress growth coefficient η^+ and LVE are shown as a function of time t at selected shear rates in Figure 52. Shear thinning can be observed for all samples and all shear rates. For pom-poms with short arms or low arm numbers and therefore higher backbone volume fractions, 100k-2x11-9k is shown exemplary in Figure 52 a). The shear stress growth coefficient η^+ has a strong overshoot followed by a steady state viscosity. This behavior is similar to previously reported studies on linear, star, and comb shaped polymers. At very low strain rates, the stress growth coefficient coincides with the zero-shear viscosity obtained from SAOS. At medium shear rates, a small undershoot can be observed.

For pom-poms with long arms or high arm numbers and therefore lower backbone volume fractions, 100k-2x12-24k is shown exemplary in Figure 52 b). Similarly, a viscosity overshoot ($\gamma_{2,pp}$, see Figure 53) followed by an undershoot and a steady state viscosity can be observed.

At high shear rates, no steady state viscosity is obtained at long times, but the viscosity increases steadily with time, e.g. at 1.5 s⁻¹. At around 0.5 s and 10^4 Pa s an increase of the transient data above the LVE is measured. This is atypical for polymer melts, as they show shear thinning in general, but can be observed for all category 3 samples (backbone not self-entangled, entangled arms, see Table 3, page 63). We suspect that the increase above the LVE is a result of the compliance of the rheometer transducer and no true material response. Other pom-poms with e.g. low arm numbers or self-entangled backbones are shown in Supplementary Figure 2, page 131.
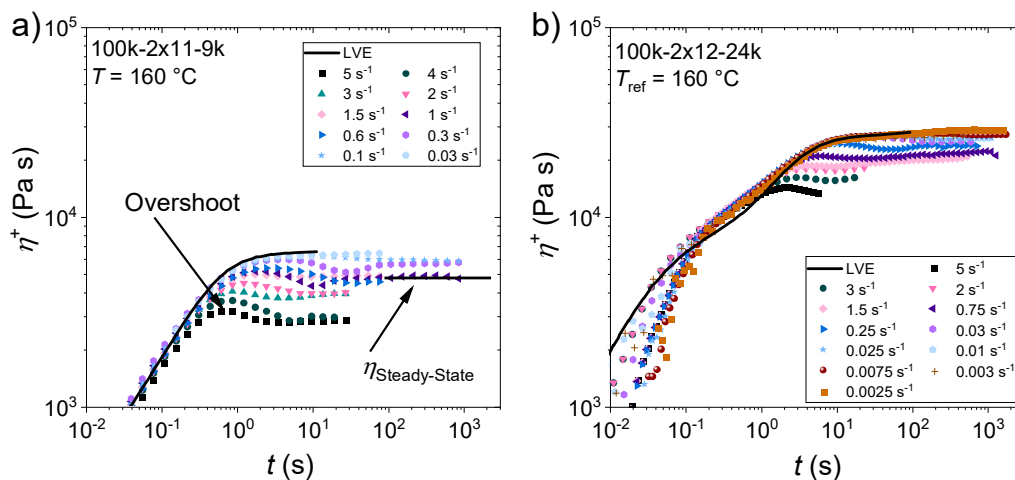

Figure 52: Shear stress growth coefficient η^+ of selected pom-poms is shown as a function of time t at selected shear rates for a) 100k-2x11-9k und b) for 100k-2x12-24k. For the shear rates $\dot{\gamma}$ = 3 s⁻¹ and $\dot{\gamma}$ = 5 s⁻¹ in b) the viscosity measurement is terminated by the normal force exceeding the transducer capacity. Adapted from Schußmann et al.[175] under the Creative Commons Attribution 4.0 International License.

The shear stress function σ^+ of 100k-2x12-40k is shown in Figure 53 as a function of the applied strain γ. Contrary to the general shape of σ^+ for pom-poms described beforehand, two distinct stress overshoots can be observed. The stress overshoots are numbered with increasing strain and the subscript "pp" is short for pom-pom. The first stress overshoot can be observed for strain rates above $\dot{\gamma}$ = 1 s⁻¹ with increasing strain, saturating at $\gamma_{1,pp}$ = 2.3 for $\dot{\gamma} > 4.5$ s⁻¹. As a result of tube orientation, σ^+_{max} occurs at γ = 2.3 for linear chains.[43,201] The second stress overshoot can be observed at $\gamma_{2,pp}$ = 1.3 for $\dot{\gamma} \geq 0.0135$ s⁻¹. With increasing shear rates, $\gamma_{2,pp}$ increases and then saturates at $\gamma_{2,pp} \approx 7$ for shear rates above $\dot{\gamma}$ = 1 s⁻¹. For the discussion of the origin of the second overshoot see Figure 56. Measurements at $\dot{\gamma} > 3$ s⁻¹ were typically terminated by normal force transducer overload before reaching a steady state. Surprisingly, a third stress maxima can be observed around $\gamma_{3,pp}$ = 650. Although measurements were conducted with great care to ensure reliable data, one cannot exclude a measurement artefact at so large strains.
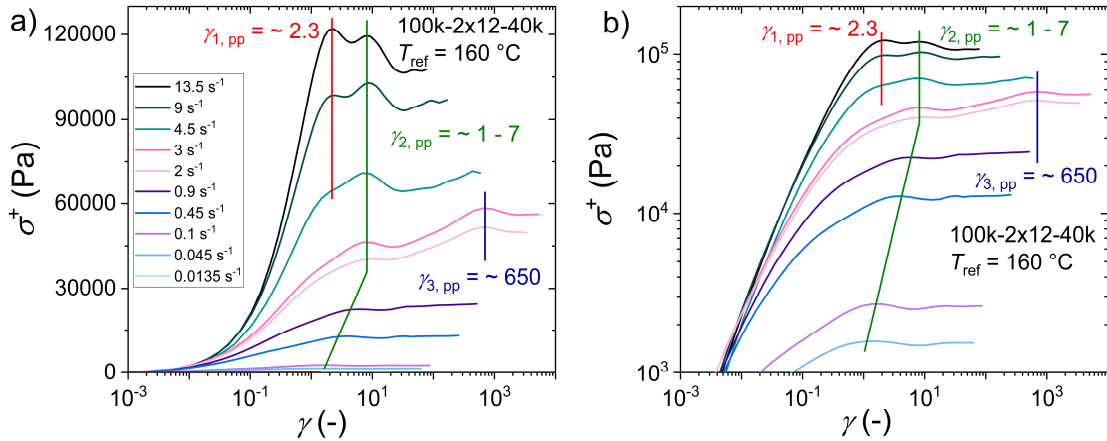
Figure 53: Shear stress growth function σ^+ in a) linear and b) logarithmic scaling shown as a function of applied strain γ for selected strain rates between 0.00135 s^{-1} and 13.5 s^{-1}. Adapted from Schußmann et al.[175] under the Creative Commons Attribution 4.0 International License.

Coarse grain simulations using multi-chain slip-links are a variation of molecular dynamics simulations and a powerful tool to predict the rheological behavior and analyze chain conformation during flow. They do not rely on any fitting parameter and can predict the stress response for flows like SAOS, startup shear and extension using only the molecular parameters.[171,202,203] Prof. Masubuchi kindly used his "New Algorithm for Polymeric Liquids Entangled and Strained code" (NAPLES) to simulate the startup shear response for the pom-
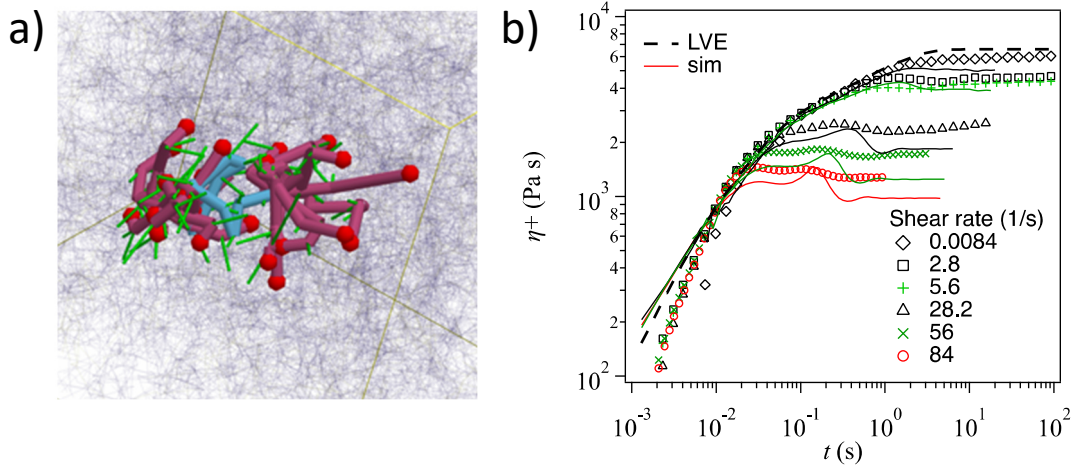
Figure 54: a) A typical snapshot of the simulation for pom-pom 100k-2x12-40k in the simulation box. One of the 390 molecules in the box is highlighted. Red segments and red spheres are the branching arms and their ends. Blue segments are the backbone between branch points. Green bold lines are entangled segments to the highlighted molecule. The other segments in the system are exhibited by thin gray lines. b) Shear stress growth coefficient η^+ is shown as a function of time t for the pom-pom 100k-2x12-40k. Open symbols exhibit experimental data for various shear rates, as shown in the figure legends. The linear viscoelastic envelopes are indicated by broken black curves. The simulation results are displayed by solid curves.

pom 100k-2x12-40k. A typical simulation box is shown in Figure 54 a). One of the molecules is highlighted in red for the arms and blue for the backbone.

The box can be subjected to various deformations. In Figure 54 b), the startup shear data from the experiment (open symbols) and the simulation (solid lines) are shown. The simulation reproduces the experimental data quantitively, clearly showing two viscosity peaks at high shear rates. The peak positions of the simulation are consistent with the experiment supporting the experimental findings. Through analysis of the chain conformation during the shear in the slip-link simulation, the overshoots can be attributed to the orientation of the arms for $\gamma_{1,pp}$ and stretch of the backbone for $\gamma_{2,pp}$. This attribution of the molecular origin is consistent with conclusions based on the experimental data.

The stress overshoot during startup shear for linear chains is caused by the chain orientation into the shear direction.[42,202] The flow behavior of the pom-poms investigated herein is highly dependent on the molecular parameters. To further investigate the second stress overshoot and its molecular origin, $\gamma_{2,pp}$ is shown as a function of Wi in Figure 55 a) for different $M_{w,b}, M_{w,a}$ and q. The grey dotted line displays the prediction of the Doi-Edwards tube model. For $Wi < 1$, a constant strain of $\gamma = 2.3$ is predicted, while for $Wi > 1$, a weak strain rate dependency on $\gamma_{2,pp}$ is obtained ($\gamma_{2,pp} \sim Wi^{1/3}$). For the pom-pom samples at $1 < Wi < 20$, a strain rate dependency of $\gamma_{2,pp} \sim Wi^{1/2}$ can be observed. The lower plateau of $\gamma_{2,pp}$ is found at $\gamma_{2,pp} \approx 1$, contrary to the prediction of the DE model at $\gamma_{2,pp} = 2.3$ and observed experimentally for linear chains[204]. For the sample 100k-2x12-40k, $\gamma_{2,pp}$ reaches a plateau strain of $\gamma_{2,pp} \sim 7$ for $Wi > 20$. The other samples could not be investigated at $Wi > 20$ due to normal force transducer limitations. For linear chains, no strain plateau at high Wi was observed in literature and only *Snijkers et al.* reported a $\gamma_{2,pp}$ plateau for a comb backbone.[132,205–207] The vertical, orange dashed line, shows $\gamma_{2,pp}$ at $Wi = 1$ at different arm molecular weight. In Figure 55 b), $\gamma_{2,pp}$ at $Wi = 1$ is shown as a function of the arm molecular weight in kg mol-1. For the arm molecular weight range investigated here ($M_{w,a} = 9 – 40$ kg mol-1), we find a linear decrease of the $\gamma_{2,pp}$ as a function of arm molecular weight with a slope of -0.073. The observed phenomena might be explained by the following hypothesis: Under shear, the macroscopic strain induces a microscopic orientation of the chains. The backbone end-to-end vector $\overrightarrow{v_b}$ is rotated into the flow direction, as shown by Brownian molecular dynamics simulation for pom-pom, H-shaped and linear chains.[171,205,208,209] If the arm length is increased, the relaxation of the star shaped branched point is slowed down, independent of the arm number.[63,198] Therefore movement of the two branch points at each end of the backbone is also reduced. As a result, the macroscopic strain to reach the same microscopic orientation of $\overrightarrow{v_b}$ is reduced with increased arm molecular weight as observed herein experimentally.
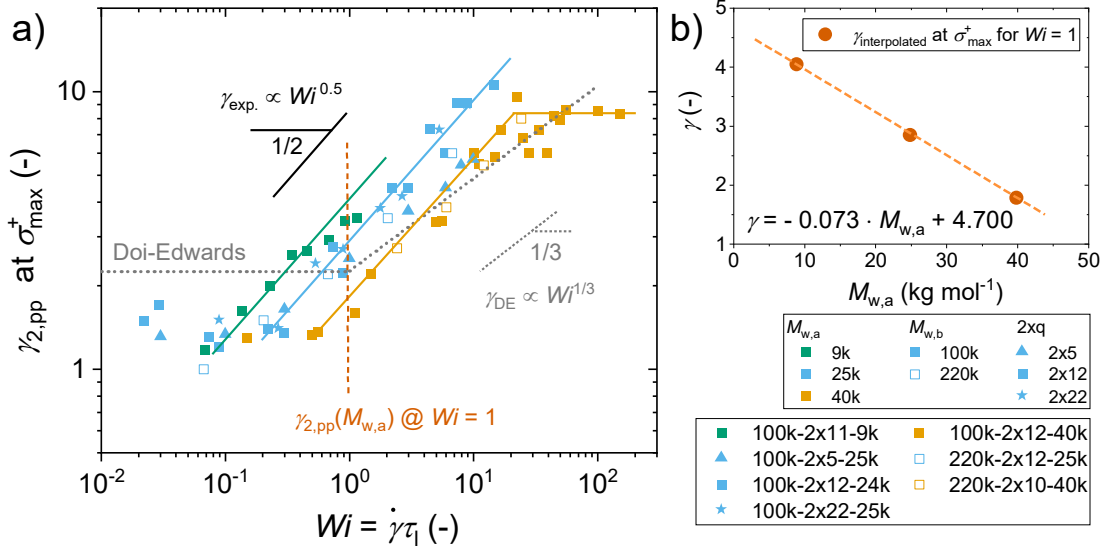
Figure 55: a) Strain of the second stress overshoot $\gamma_{2,pp}$ shown as a function of the Weissenberg number Wi for pom-pom shaped samples with different $M_{w,b}$, $M_{w,a}$ and q. For the determination of $\gamma_{2,pp}$ see Figure 53, page 71. b) Interpolated strain $\gamma_{2,pp}$ shown as a function of $M_{w,a}$ of all samples of a). Adapted from Schußmann et al.[175] under the Creative Commons Attribution 4.0 International License.

Previous reports on startup shear of defined branched polymers were mainly conducted by Prof. Vlassopoulos and coworkers at the University of Crete. They focused on well-defined, low disperse, and extensively characterized combs synthesized by Prof. Roovers at the National Research Council of Canada.[137] For the herein reported pom-pom sample 100k-2x12-40k as well as the previously reported data on the comb sample C642 (275k-29-47k),[132] γ_1 and γ_2 are further analyzed in Figure 56 as a function of Wi. The arm relaxation times of the pom-pom and comb are $\tau_{a,pp}$ and $\tau_{a,c}$, respectively. Both are determined from the local maximum of the phase angle as a function of frequency on SAOS. For both pom-pom and comb, γ_1 can be observed for strain rates faster than the arm relaxation time. Arm orientation as a molecular origin for the first stress overshoot is assumed since γ_1 is found around ~ 2 for $\dot{\gamma} > 1/\tau_a$. For comb and pom-pom, γ_2 increases with increasing shear rate before saturating at a constant value. A power law exponent of 0.5 for γ_1 and γ_2 as a function of Wi can be observed for their respective low shear rates. While the two overshoots of the comb can be observed at $\gamma_{1,c} \approx 2$ and $\gamma_{2,c} \approx 12$, the pom-pom exhibits its overshoots at $\gamma_{1,pp} \approx 2$ and $\gamma_{2,pp} \approx 7$. The different strains of γ_2 could be a result of the different backbone lengths of the two samples but indicating only a very weak $M_{w,b}$ dependency of γ_2. Investigations of the pom-poms in extensional flow revealed that τ_l, the inverse of the crossover into the terminal regime, is equal to the stretch relaxation time τ_s of the backbone.[86] In startup shear experiments, the overshoot strain is constant for chain orientation and increases if chain stretch contributes. $\gamma_{2,pp}$ is constant at $Wi < 1$ and increases for $Wi > 1$, therefore suggesting a backbone stretch contribution to $\gamma_{2,pp}$ for $Wi > 1$. This supports the findings from uniaxial extensional flow that for pom-poms $\tau_l \sim \tau_s$. One can estimate that $\tau_l \sim \tau_s$ is for comb C642 from the extensional data by Lentzakis et al.[138] Therefore we can assume that the backbone stretch contributes to $\gamma_{2,c}$ for $Wi > 1$ as assumed by *Snijkers et al.*[132] in their analysis. Startup shear data for $0.1 < Wi < 10$ of C642 is needed for confirmation.
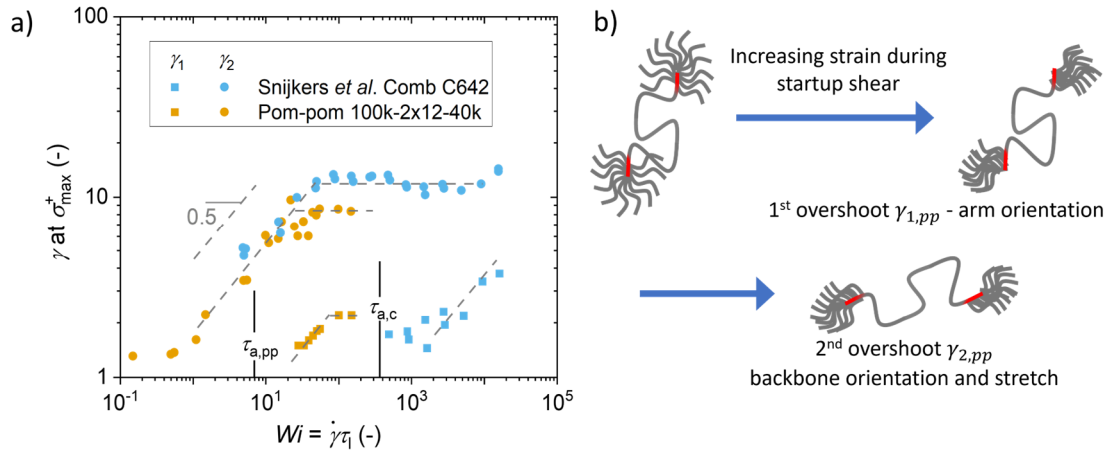
Figure 56: a) Strain of the stress overshoots, γ_1 and γ_2, shown as a function of the Weissenberg number Wi for sample 100k-2x12-40k and the comb C642 (275k-29-47k) investigated by Snijkers et al.[132] The arm relaxation times are given by $\tau_{a,pp}$ for the pom-pom and $\tau_{a,c}$ for the comb. Adapted from Schußmann et al.[175] under the Creative Commons Attribution 4.0 International License. b) Schematic illustration of the orientation and stretch of the backbone and the orientation of the arms during startup shear.

Based on the results from above, we attribute the two stress overshoots found for the pom-pom topology and their origin as follows: The first stress overshoot γ_1 is a result of the arm orientation. The second stress overshoot γ_2 is attributed to backbone orientation and stretch at higher shear rates. The conformation of the chains is illustrated in Figure 56 b). This interpretation of the data is in line with previous works on comb and linear samples.[132,210,211] A double stress overshoot in startup shear was previously reported by *Snijkers et al.*[132] and only observed for one comb sample. Solutions of bimodal linear polymers investigated by *Osaki et al.*[210] also showed a double stress overshoot for only one sample among many. All three systems showing the double stress overshoots have similar short chain molecular weights (40k, 40k and 47k), similar long chain volume fractions ($\phi_L = 0.1$, $\phi_{b,pp} = 0.09$, $\phi_{b,c} = 0.17$) and well separated relaxation times of the long and short chain. The mastercurves are similar in their overall shape, consisting of a high frequency rubber plateau followed by a Rouse and terminal regime at lower frequencies (Supplementary Figure 3, page 132). This data suggests that branched systems, pom-pom or comb, show no difference to the corresponding bimodal blends and solutions in linear and nonlinear shear experiments. Differences between bimodal linear blends and pom-poms arise in uniaxial extension and are discussed in chapter 7.4, page 96.

After the stress exhibits one or more maxima, a steady state viscosity is reached at large strains during startup shear, as shown in Figure 52 a). In Figure 57, the normalized steady state viscosity is shown as a function of Wi for a) pom-poms with $M_{w,b}$ = 100 kg mol^{-1}, $M_{w,a}$ = 25 kg mol^{-1} and increasing q (5, 12 and 22) and b) $M_{w,b}$ = 100 kg mol^{-1}, $q \sim 12$ and increasing $M_{w,a}$ (9, 24 and 40 kg mol^{-1}). At $Wi > 1$, a deviation of $|\eta^*(\omega)| < \eta_{Steady-State}(\dot{\gamma})$ can be observed. The deviation between $|\eta^*(\omega)|$ and $\eta_{Steady-State}(\dot{\gamma})$ is the largest around the backbone phase angle minimum $Wi(\delta_{b,min})$ of up to 40 %. Overall, the deviation between the steady state viscosity (startup) and the absolute value of the complex viscosity (SAOS) increases with increasing arm number and length, e.g., reduced backbone volume fraction.
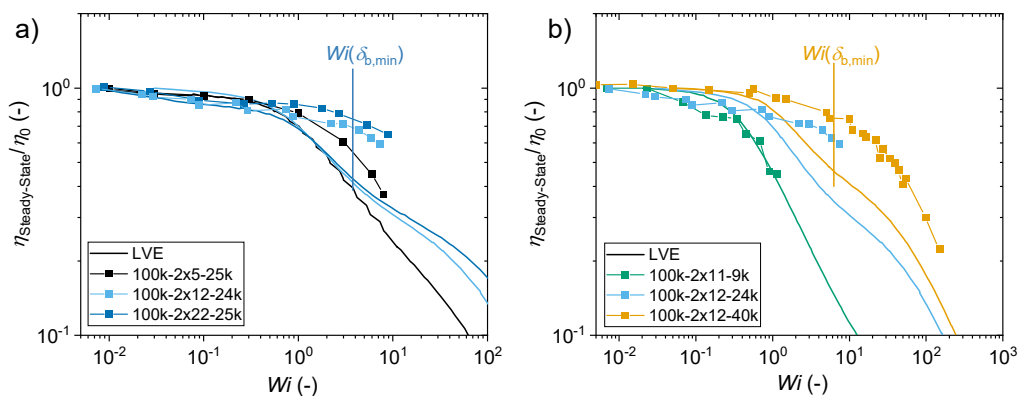
Figure 57: Steady state viscosity obtained from stress growth experiments normalized to the zero-shear viscosity $\eta_{Steady-State}/\eta_0$ is shown as a function of the Weissenberg number Wi for a) increasing arm number q and b) increasing arm molecular weight $M_{w,a}$. Adapted from Schußmann et al.[175] under the Creative Commons Attribution 4.0 International License.

The validity or failure of the Cox-Merz rule should depend on the molecular parameters. The failure typically occurs at frequencies where only the backbone is not yet relaxed and is showing Rouse relaxation. Therefore, we investigate the validity or failure of the Cox-Merz rule as a function of the $Z_{b,eff}$. The steady state viscosity $\eta_{Steady-State}(\dot{\gamma})$ is increased compared to the complex viscosity from SAOS with the maximum deviation around $Wi(\delta_{b,min})$ as illustrated in Figure 58 a). The deviation at $Wi(\delta_{b,min})$ is shown as a function of $Z_{b,eff}$ in Figure 58 b) for the herein investigated pom-poms and literature data on combs. Two distinct areas can be identified depending on $Z_{b,eff}$. For $Z_{b,eff}$ < 3, the deviation from the Cox-Merz rule increases with decreasing $Z_{b,eff}$. For $Z_{b,eff}$ > 3, the Cox-Merz rule is fulfilled at all Wi numbers investigated, showing that $Z_{b,eff}$ is the critical molecular criteria for the validity and failure of the Cox-Merz rule. Similar results were previously reported for some combs, with a deviation from the Cox-Merz rule at higher shear rates, which was attributed to their low $Z_{b,eff}$.[51] While deviations from the Cox-Merz rule have been observed before, they are fairly uncommon in monodisperse homopolymer melts. Literature data and our data suggest that the deviations can only be observed for systems with low effective backbone entanglements as a result of high branching density.[51] For unentangled polymer solutions, deviations from the Cox-Merz rule have been observed as well.[204]
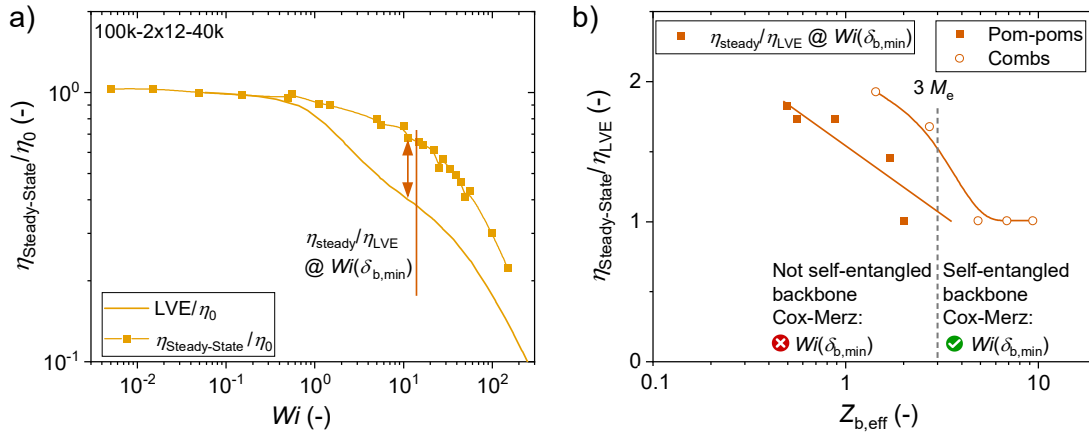
Figure 58: a) Determination of the deviation between the steady state shear viscosity $\eta_{Steady-State}/\eta_0$ at $Wi(\delta_{b,min})$ and the LVE. b) Deviation shown as a function of the effective backbone entanglements $Z_{b,eff}$ for pom-poms (this thesis) and combs[51]. Lines are a guide to the eye. Adapted from Schußmann et al.[175] under the Creative Commons Attribution 4.0 International License.

Surprisingly, the herein found difference between the startup shear measurements and the LVE obtained from SAOS was not observed in earlier works on extensional flow.[86,177] When the LVE is compared to the extensional viscosity at strains smaller than the occurrence of extensional hardening or thinning, the same viscosity is measured in extension and in SAOS.

The small undershoot during the startup shear behavior of pom-poms is only seen for medium shear rates as shown above in Figure 52. In general, undershoots can be observed for various samples in polymer melts and solution[101,212,213], but for all those samples, the undershoot increases with increasing shear rate. For the pom-pom samples herein, the undershoot is only observable at medium shear rates and is not detectable at higher and lower shear rates.

7.1.3 Uniaxial Extension

Long chain branched pom-poms

The tensile stress growth coefficients η_E^+ of the 24k-series as a function of time t are shown in Figure 59 a) at a reference temperature T_{ref} = 140 °C. To illustrate the different uniaxial extensional behavior, selected strain rates are shown. At high strain rates, the specimen of all samples fails with elastic rupture. This can be observed for example for sample 400k-2x12-23k at $\dot{\varepsilon}$ > 1 s^{-1}, visible by the sharp end to the tensile stress growth coefficient at strain smaller than ε < 4. The onset of the steady state viscosity is visible at medium strain rates ($\dot{\varepsilon}$ > 0.56 – 0.056 s^{-1}). At lowest strain rates, the extensional viscosity approaches the linear viscoelastic envelope (LVE) and the strain hardening substantially decreases, e.g. at $\dot{\varepsilon}$ > 0.0056 s^{-1} for the pom-pom 100k-2x12-24k. Similar observations can be made for the 40k-series as shown in Supplementary Figure 4. In Figure 59 b), all measured strain rates for the pom-pom 400k-2x12-23k are shown. Strain hardening can be observed over a large strain rate regime covering more than four dec-

ades of strain rates. At the lowest strain rate, the strain hardening decreases, and the tensile stress growth coefficient coincides with the LVE. This behavior can be observed for all pompoms and the span molecular weight $M_{w,span}$ determines the strain rate range. All other uniaxial extensional measurements of the pom-poms are shown in Supplementary Figure 5, page 133.
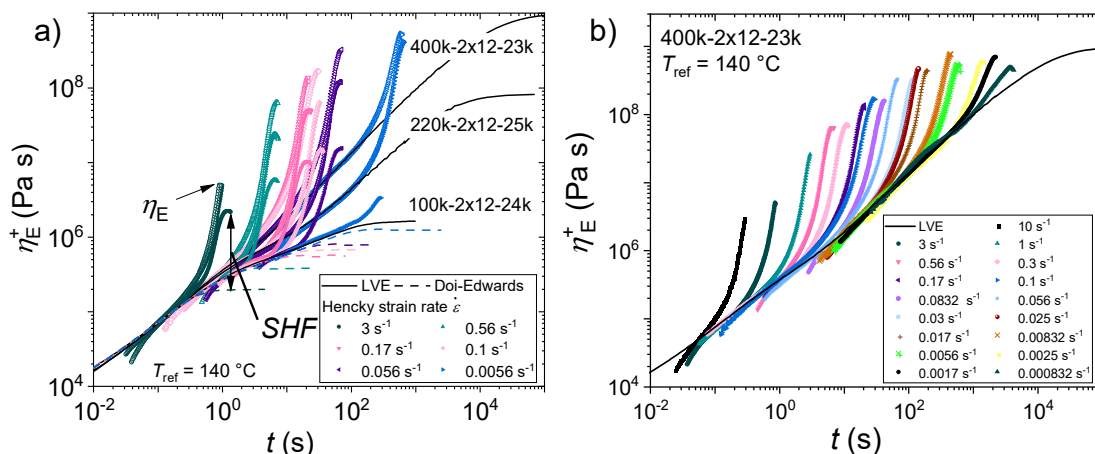

Figure 59: a) Tensile stress growth coefficient η_E^+ shown as a function of time t of the 24k-series for selected strain rates. Dashed lines show the prediction of the Doi-Edwards model to illustrate the strain hardening factor (SHF). b) Tensile stress growth coefficient η_E^+ shown as a function of time t for the pompom 400k-2x12-23k for all measured strain rates from 0.000832 to 10 s^{-1}. Both figures are shown at a reference temperature of T_{ref} = 140 °C. Adapted from Schußmann et al.[86] under the Creative Commons Attribution 4.0 International License.

The Considère criterion, originating from solid mechanics, states that a sample undergoes homogenous extensional until the deformation where the force maximum occurs. Hassager and McKinley[85] applied the Considère criterion onto the pompom constitutive equations giving a relation for the extensional viscosity using only the arm number $\eta_E = \eta_{LVE}^+ \left[q^2 / \ln(\sqrt{3}q) \right]$.[86] For a detailed introduction to the Considère criterion and the pom-pom constitutive equations see chapter 4.2, page 24. Together with the maximum theoretical fracture stress proposed by Wagner *et al*.,[214] the prediction of the extensional viscosity of a given pom-pom shaped polymer sample is enabled. In Figure 60, the extensional viscosity normalized to the zero-shear viscosity $\eta_E / 3\eta_0$, the LVE and the phase angle $\delta = \arctan(G''/G')$ of the SAOS mastercurve is shown as a function of the Weissenberg number $Wi = \tau_l \dot{\varepsilon}$ and Deborah number $De = \tau_l \omega$, respectively. Determined by the crossover into the terminal regime, τ_l is used as the longest relaxation time of a sample. A single mode Maxwell model is fitted to the terminal regime of G' for samples with not self-entangled backbones, e.g. 100k-2x12-24k, and the crossover frequency of the Maxwell model is set as τ_l. It appears that τ_l determined in this way is close to the stretch relaxation time of the backbone τ_s, see discussion below.
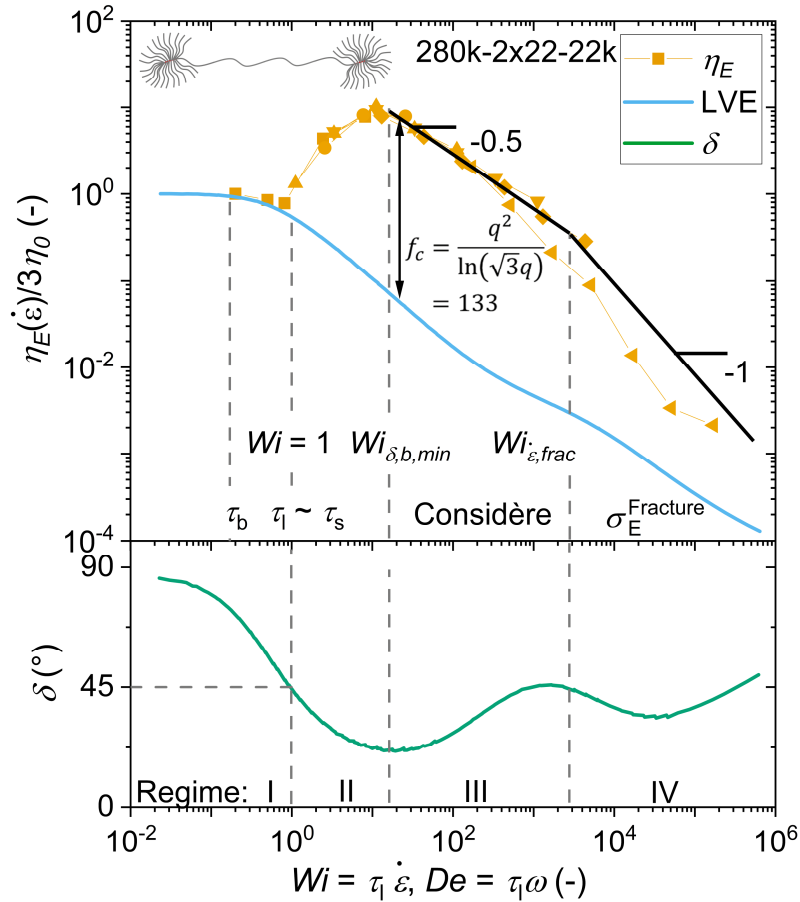
Figure 60: Extensional viscosity η_E normalized by three times the zero-shear viscosity η_0 shown as a function of the Weissenberg number Wi and the phase angle δ as a function of the Deborah number De of the pom-pom 280k-2x22-22k. Different yellow symbols represent measurement temperatures: square 220 °C, circle 200 °C, upwards triangle 180 °C, downwards triangle 160 °C, rhombus 150 °C, and leftwards triangle 130 °C. Black lines are drawn as a guide for the eyes. Adapted from Schußmann et al.[86] under the Creative Commons Attribution 4.0 International License.

For the pom-poms with self-entangled backbone ($\delta_{b,min} < 45\,°$), we can identify four regimes of the Wi-dependent extensional viscosity $\eta_E(Wi)$ and correlate it with the De-dependant shear relaxation behavior. Starting at the lowest deformation rates with $Wi, De < 1$, Regime I or the terminal regime can be found. In this regime, the backbone as well as the side chains are not stretched (equilibrium conformation), and the extensional viscosity matches the LVE. Shear and extensional thinning can be observed between $\sim 0.3 < Wi < 1$, indicated by the decrease in the normalized viscosity below 1. The shear thinning is caused by orientation of backbone chains into the flow direction. The orientation relaxation time τ_b can therefore be estimated at $Wi \sim 0.3$. Since the strain rate $\dot{\varepsilon}$ is smaller than the inverse stretch relaxation time τ_s, no strain hardening can be observed here. Orientation and stretch relaxation times are indicated in Figure 60 at their respective Wi number.

Regime II can be found between $Wi, De = 1$ and the first minimum of the phase angle $Wi_{\delta,b,min}$. The backbone chains are stretched out of their equilibrium due to $\dot{\varepsilon} > \tau_s^{-1}$ as $Wi, De > 1$. Therefore, strain hardening is observed by an increase of the extensional viscosity above the LVE. The extensional viscosity increases with increasing Wi until the minimum of the phase angle, where the highest extensional viscosities are measured. The highest η_E is obtained at $Wi(\delta_{b,min})$. Due to the transition from shear thinning to strain hardening, this regime is also referred to as the transition regime. Similar to a ring-shaped sample, the crossover relaxation time of pom-poms seems roughly similar to the experimentally observed onset of strain hardening and therefore the stretch relaxation time.[215] The thinning observed in regime I indicates a longer orientation relaxation time. Following the picture of the pom-pom model, the main stress in extensional flow in a pom-pom is generated on the backbone between the two branch points. At high strains, retraction of a single arm yields no stress relaxation on the backbone due to the other arms retaining the position of the branchpoint and therefore the stress on the backbone remains. Stress release of a (partially) stretched backbone can in this picture only be achieved by movement of the whole branch point. This molecular hypothesis could explain the experimentally observed onset of strain hardening of the pom-poms at the inverse of the crossover frequency.

Regime III is found between $Wi_{\delta,b,min}$ and $Wi_{\dot{\varepsilon},frac}$. We experimentally find that the extensional viscosity declines with a scaling exponent of -0.5 and matches the prediction of the Considère criterium. The extensional viscosity is a factor of $[q^2/\ln(\sqrt{3}q)] = 133$ above the LVE. The assumption that $t_q/\tau_b \ll 1$ is fulfilled at the Wi numbers found in regime III. The Considère factor f_c is for the pom-pom 280k-2x22-22k with $q = 22$ to be $f_c = 133$. In this regime, the arms of the pom-poms are still relaxed as in regime I and II, but the backbone chains are both oriented and stretched during the extension. Nielsen *et al.*[12] studied the extensional behavior of similar pom-pom shaped polystyrene melts with on average $q = 2.5$ arms. They find that branch-point withdrawal into the backbone tube is the reason for the transition to steady state stress at high Hencky strains in the regimes I – III. Similarly, we find an onset of steady-state viscosity for our samples. Therefore, we propose branch-point withdrawal as a stress release mechanism in regime II to III in addition to stretch and orientation. Together with the Considère limit, these findings suggest that the strain hardening (factor) ($SHF = \eta_E(\dot{\varepsilon})/\eta_{DE}(\dot{\varepsilon})$) of pom-pom systems depends only on the number of arms attached to the branchpoints and not on the length of the arms or the backbone. This SHF is given by the Considère limit as a function of the arm number. A scaling law of -0.5 can be found for η_E as a function of Wi and is in agreement with previous findings on linear, branched and ring systems.[12,67,138,215,216] In an ideal model like the pom-pom model, a slope of -1 for $\eta_E(Wi)$ is calculated. The Doi-Edwards model, which can predict the rheology of linear chains, a reduction to -0.853 is found. The experimentally observed slope of the LVE and the extensional viscosity is -0.5. It is suspected that the superposition of the relaxation of the arms and the backbone, which individually have the slope of -1, yield due to their partial superposition a resulting slope of -0.5.

Regime IV can be found at $Wi > Wi_{\dot{\varepsilon},frac}$. Due to the high strain rates, no stress relaxation mechanisms can dissipate stress, and the specimen fails due to elastic rupture. We find experimentally a limiting fracture stress of about $\sigma_E^{Fracture} = 2 \cdot 10^7$ Pa. In Figure 61, the extensional

stress σ_E is shown as a function of Wi number. At $Wi > Wi_{\dot{\varepsilon},frac}$ the extensional stress is constant around $\sigma_E^{Fracture}$. The scattering of the data points increases substantially due to the change from flow to the elastic rupture, a more solid like failure mechanism similar to for example tensile testing. The onset of the fracture stress at $Wi_{\dot{\varepsilon},frac}$ can be obtained from the onset of the stress plateau indicated by the change in power law from 0.5 to the plateau stress. Extensional stress data for the other pom-poms is shown in Supplementary Figure 6 and Supplementary Figure 7.
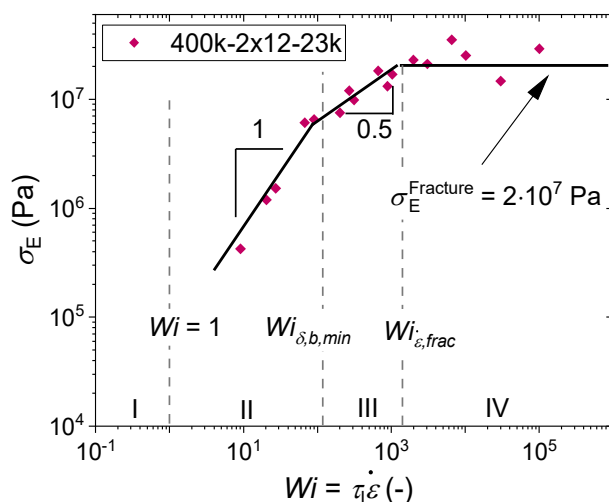

Figure 61: Fracture stress $\sigma_E^{Fracture}$ as a function of the Weissenberg number Wi for the pom-pom 400k-2x12-23k. Dashed lines indicate characteristic regimes. Solid lines are to guide the eye. Adapted from Schußmann et al.[86] under the Creative Commons Attribution 4.0 International License.

Wagner *et al.*[214] predicted a similar maximum fracture stress through consideration of a C-C bond energy and comparing to the stress energy acting on a Kuhn segment. Due to the strain rate independence of the stress, we assume that the fracture of the covalent C-C bonds is the main stress release mechanism for pom-poms in regime IV, similar to linear chains.[89] The experimental data on pom-poms confirms the predicted fracture stress. The onset of the fracture stress at $\dot{\varepsilon}_{frac}$ was extracted from the slope change (see Supplementary Figure 8, page 136) and is shown in Figure 62. It is found that $\dot{\varepsilon}_{frac}$ is a function of the span molecular weight $M_{w,span} = M_{w,b} + 2 \cdot M_{w,a}$ and scales with a power law of -2.4.
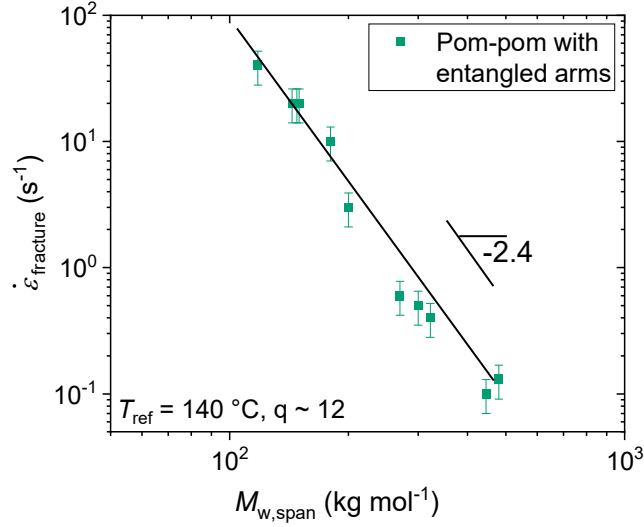
Figure 62: Onset strain rate $\dot{\varepsilon}_{frac}$ of the plateau stress $\sigma_E^{Fracture}$ as a function of the span molecular weight $M_{w,span}$ for pom-poms with entangled arms. Adapted from Schußmann et al., supplementary information[86] under the Creative Commons Attribution 4.0 International License.

Using these findings described above, the extensional viscosity can be predicted solely from the LVE for a pom-pom sample with known molecular parameters. Starting at high Wi in regime IV, the extensional viscosity is restricted by the fractures stress until $Wi = Wi_{\dot{\varepsilon},frac}$ (scaling -1 for $\eta_E\, vs.\, Wi$). Between $Wi_{\delta,b,min} < Wi < Wi_{\dot{\varepsilon},frac}$ in regime III, the Considère limit defines the extensional viscosity $[q^2/\ln(\sqrt{3}q)]$ above the LVE with a scaling exponent of -0.5. At slower rates in regime II, the extensional viscosity decreases from the maximum at $Wi_{\delta,b,min}$ to the LVE and matches is for $Wi < 1$ in regime I. With this procedure, the extensional viscosity can be predicted over the whole Weissenberg number range, with only the LVE and the topological parameters of the given pom-pom molecule. Additionally, it might be possible to invert this procedure. With the combination of the Considère factor $[q^2/\ln(\sqrt{3}q)]$ and the LVE data, the average arm number of an analogous pom-pom molecule for a low disperse branched system could be estimated. One would simply adjust the arm number to match the experimental extensional viscosity to the Considère limit.

The findings above are valid for all pom-poms with self-entangled backbones, arm numbers $q > 5$ and arm lengths of $M_{w,a} \geq M_e/2$ as shown with the pom-pom 280k-2x22-22k. The Considère limit applied to pom-poms with $q < 5$ is discussed at Figure 65, page 84. Pom-poms with lower arm molecular weights $M_{w,a} < M_e/2$ are discussed starting at Figure 68, page 87. The backbones of the pom-poms are considered self-entangled if the effective backbone entanglements $Z_{b,eff} = \phi_b \cdot Z_b$ are above three or alternative the backbone phase angle minimum is below 45 °. In Figure 63 two pom-poms with different $Z_{b,eff}$ are shown to illustrate the difference between self-entangled and not self-entangled backbones. The pom-pom 400k-2x13-40k shown in a) has $Z_{b,eff} = 6.61$, the Considère limit describes the extensional data well. For the pom-pom 100k-2x12-40k shown in b) a $Z_{b,eff} = 0.56$ is found and the extensional data falls below the prediction of the Considère limit. Comparison between the

Considère limit and the extensional viscosity for all other pom-poms are shown in Supplementary Figure 9, page 137 to Supplementary Figure 13, page 139.
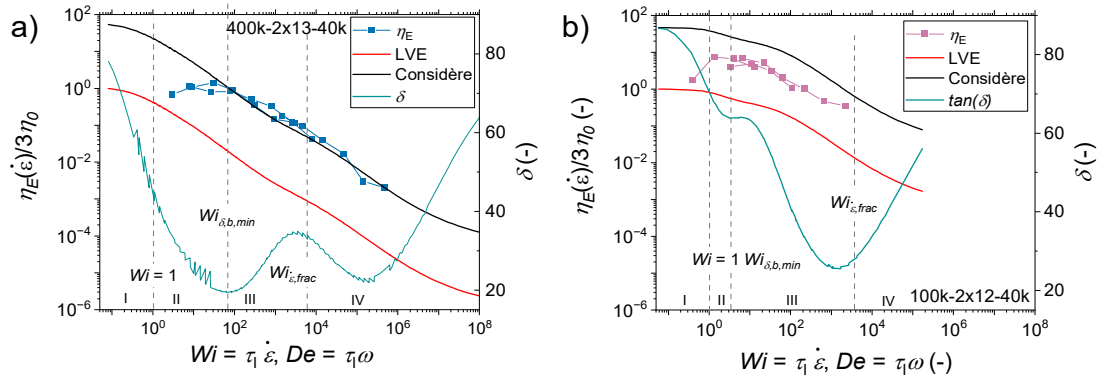

Figure 63: Extensional viscosity η_E normalized by three times the zero-shear viscosity η_0 shown as a function of the Weissenberg number Wi and the phase angle δ as a function of the Deborah number De of the pom-poms a) 100k-2x11-9k and b) 100k-2x12-40k. Grey dotted lines are drawn as a guide for the eye.

A generalized relationship between the molecular parameters of a pom-pom and the resulting strain hardening are shown in Figure 64. Same limits as discussed above apply ($Z_{b,eff} > 3$, $q \gtrsim 5$, $M_{w,a} \geq M_e/2$). The four Wi dependent regimes are defined by three distinct relaxation times. The stretch relaxation time τ_s defines the onset of the strain hardening between regime I and II and depends on the backbone molecular weight $M_{w,b}$. Regime III is defined by the separation between the phase angle backbone minimum $\delta_{b,min}$ and onset of the fracture stress. The phase angle minimum is dependent on $M_{w,b}$. The strain hardening in regime III is only a function of the number of arms predicted by the Considère limit. More arms result in higher strain hardening. In regime IV, the strain hardening is limited by chain scission at the fracture stress. This topology-strain hardening map allows the design of pom-pom molecules with a specific *SHF* at a specific $\dot{\varepsilon}$ and η_0.
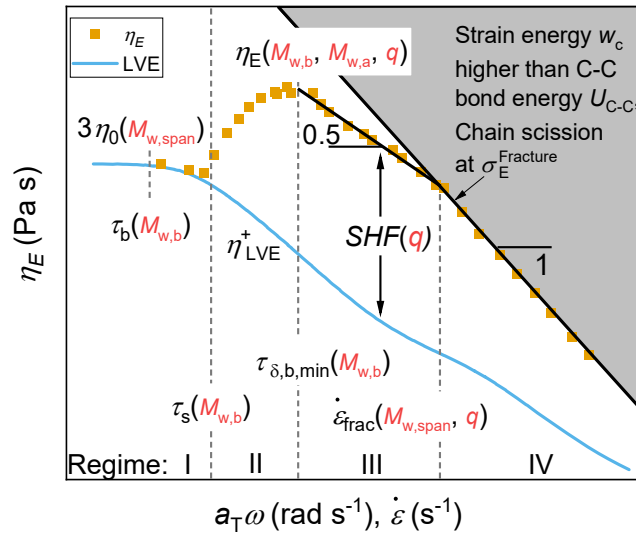
Figure 64: Overview of the impact of the molecular parameters of the pom-poms on the strain hardening behavior for pom-poms with entangled arms ($M_{w,a} \gtrsim M_{w,e}$) and self-entangled backbones ($Z_{b,eff} \gtrsim 3$), allowing to design pom-pom molecules with desired properties. Idealized extensional viscosities and LVE shown in orange squares and the light blue lines, respectively. Adapted from Schußmann et al.[86] under the Creative Commons Attribution 4.0 International License.

As discussed above, the Considère findings are only valid for pom-poms with $q \gtrsim 5$ as our data shows. For lower arm numbers, pom-poms converge into super H-shaped ($q = 3, 4$) and H-shaped ($q = 2$). As shown in Figure 65, the Considère limit is surpassed for these two samples. Since the arm numbers are low, topological impurities such as stars and linear chains are likely. Therefore, the observed differences are likely due to contributions of multiple species. An investigation into the topological purity to evaluate the source of the increased strain hardening would be highly desirable. Additionally, the uncertainties in the determination of the arm number lead to higher relative deviations in the Considére factor at low arm numbers. Alternatively, H-shaped polymers of Roover could be used, as thermal gradient interaction chromatography (TGIC), which can detect small molecular weight differences precisely, showed a pure product.[168] In case of a topologically pure sample, a change in the relaxation behavior as a function of arm number might be also observable here as with regular stars[217] and an arm alignment under high stretches.[218] The total strain hardening is still relatively low compared to other pom-poms and branched architectures.
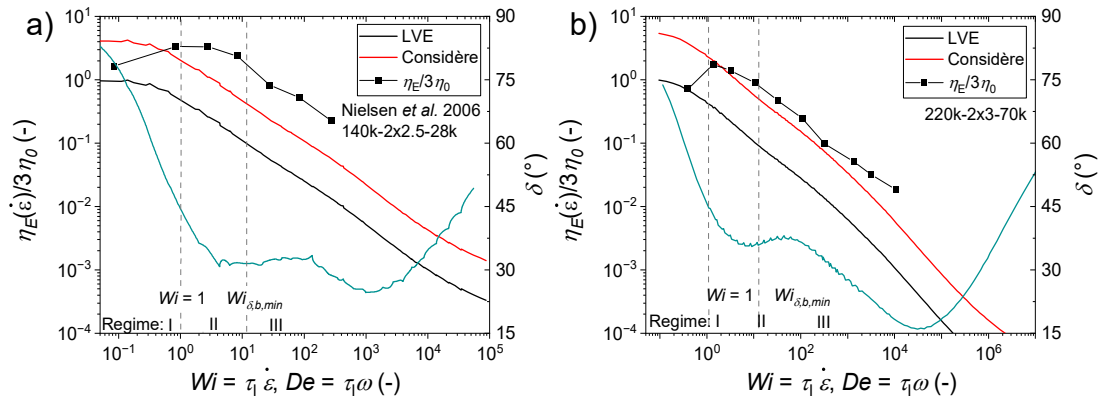
Figure 65: Extensional viscosity η_E normalized by three times the zero-shear viscosity η_0 shown as a function of the Weissenberg number Wi and the phase angle δ as a function of the Deborah number De of the pom-poms a) 140k-2x2.5k-28k synthesized by Nielsen et al.[12] and b) 220k-2x3-70k. Grey dotted lines are drawn as a guide for the eye.

The strain hardening factor (SHF) is widely used in industry to easily quantify the strain hardening of a material. Its advantages are the easy comparison between the strain hardening of different chemistries, architectures, viscosities of different materials, and measurement conditions. The SHF is strain rate dependent and can be summarized into the rate-independent, maximum strain hardening factor SHF_{max}. The SHF of the pom-pom 280k-2x22-22k is shown as a function of Wi in Figure 66. We experimentally find that the maximum strain hardening factor and the Considère factor are identical, $SHF_{max} = f_c$, within the experimental uncertainty for pom-poms with $Z_{b,eff} > 3$, $q \gtrsim 5$, $M_{w,a} \geq M_e/2$. The SHF_{max} can be found roughly between $Wi_{\delta,b,min}$ and $Wi_{\dot{\varepsilon},frac}$. Note the definition of the Considère factor based on the LVE

$$f_c = \left[\frac{q^2}{\ln(\sqrt{3}q)}\right] \simeq \frac{\eta_E(\dot{\varepsilon})}{\eta_{LVE}^+(rad\ s^{-1})} = SHF_{max} \tag{57}$$

The strain hardening factor is defined as the extensional viscosity normalized to the steady state viscosity of the Doi-Edwards model $SHF = \eta_E(\dot{\varepsilon})/\eta_{DE}(\dot{\varepsilon})$. When comparing η_{DE} to the absolute value of the complex viscosity as shown in Supplementary Figure 15 one can observe $\eta_{LVE}^+(rad\ s^{-1}) = \eta_{DE}(\dot{\varepsilon})$. With $\eta_{LVE}^+ = \eta_{DE}$, $SHF_{max} = f_c$ can directly be derived from the relation above. The SHFs of the other pom-poms are shown in Supplementary Figure 14, page 140.

To optimize the pom-pom topology for a high strain hardening factor, the maximum arm number and following that the maximum strain hardening factor can be calculated based on the backbone molecular weight and the limitations found above. The maximum strain hardening factor is shown in Table 4 for $Z_{b,eff} = 3$ and $M_{w,a} = M_e/2$. The SHF_{max} found for a pom-pom with $M_{w,b} = 300$ kg mol^{-1} could go up to 1540. This is higher than any commercial sample and most specially designed branched polymers.

Table 4: Maximum strain hardening factor SHF_{max} predicted by the Considère limit based on the limits found above. Calculations are based on the limitations found above and the optimized pom-poms are calculated with $Z_{b,eff} = 3$ and $M_{w,a} = M_e/2$.

$M_{w,b}$ [kg mol^{-1}]	q	SHF_{max}
100	5	12
200	35	298
300	88	1540
400	165	4814

The range in which the maximum strain hardening factor can be observed is between $Wi_{\delta,b,min}$ and $Wi_{\dot{\varepsilon},frac}$ as shown in Figure 66. The higher the backbone molecular weight, the larger this range.
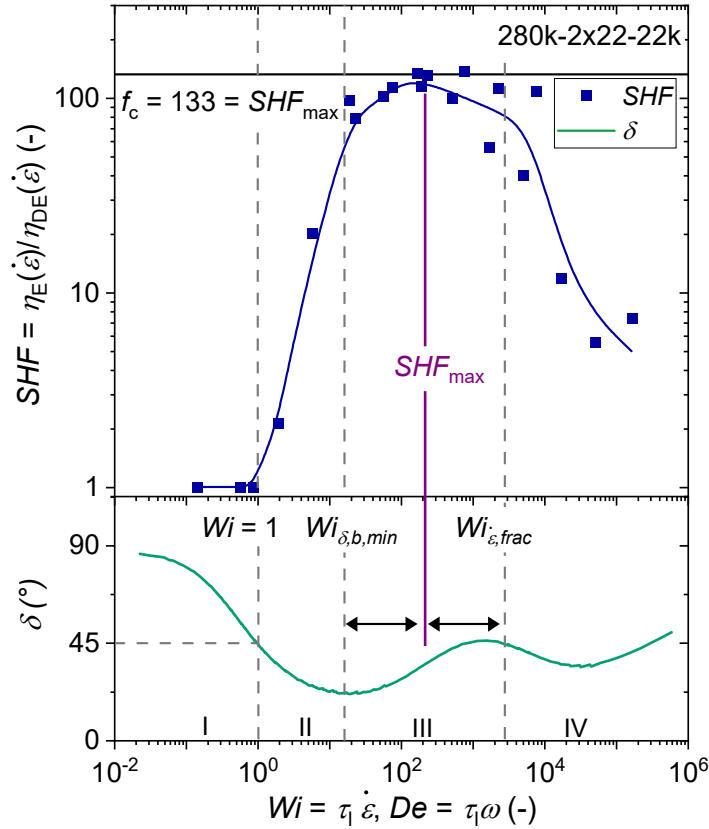
Figure 66: Experimental strain hardening factor SHF as a function of Wi and δ as a function of De of the pom-pom 280k-2×22-22k. The maximum reachable strain hardening factor can be predicted by assuming $SHF_{max} = f_c = 133$ for pom-pom topology. Blue line is as a guide to the eye. Adapted from Schußmann et al.[86] under the Creative Commons Attribution 4.0 International License.

The extensional viscosity in the pom-pom model is given as

$$\eta_E = \frac{15}{4} \frac{G_0 \phi_b^2 q^2}{\dot{\varepsilon}} = \frac{15}{4} \frac{G_{N,s}^0 q^2}{\dot{\varepsilon}} \tag{58}$$

and therefore, the extensional viscosity is predicted to scale quadratically with the backbone volume fraction. For the 24k-series, we show the extensional viscosity of different strain rates as a function of the backbone entanglement number in Figure 67 a) and find a scaling exponent of 2. Dilution theory predicts the dilution modulus $G_{N,S}^0$ to be related to the plateau modulus G_0 of linear PS by $G_{N,S}^0 = G_{N,S}^0 \cdot \phi_b^2$. This was also observed experimentally for PS combs[106] and pom-poms.[96] In Figure 67 b), the extensional viscosity normalized to the dilution modulus is shown as a function of the backbone volume fraction. We find that the extensional viscosity normalized to the dilution modulus $\eta_E/G_{N,S}^0$ is independent of the backbone molecular weight for pom-poms with $M_{w,b} > 100$ kg mol^{-1} and self-entangled backbone. Similar findings in extension are obtained for the 40k-series, as shown in Supplementary Figure 16.

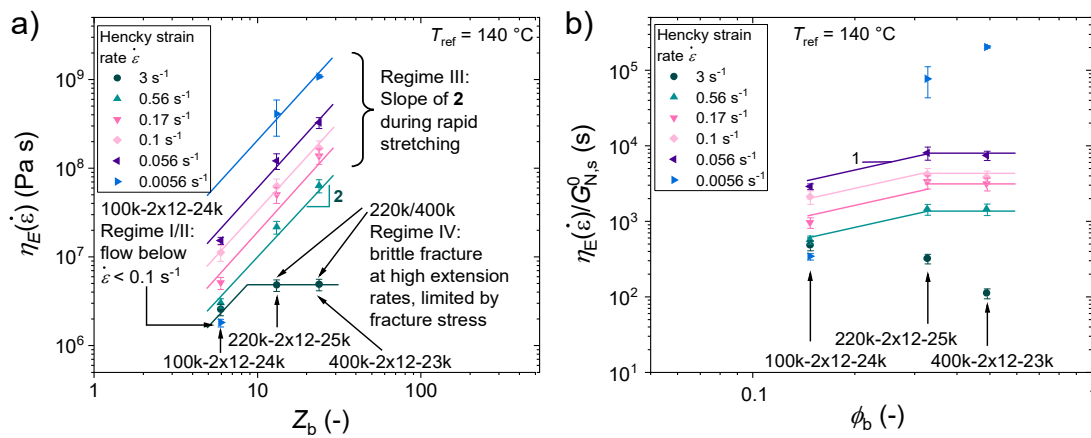*Figure 67: Extensional viscosity η_E as a function of the number of entanglements Z_b of the backbone for three pom-poms with varying backbone molecular weight. Selected strain rates between 3 s^{-1} and 0.0056 s^{-1} are shown to illustrate differences in the extensional behavior of the three pom-poms at a reference temperature of $T_{ref} = 140$ °C. At $\dot{\varepsilon} = 3$ s^{-1} the extensional viscosity is limited by the maximum fracture stress. b) Extensional viscosity normalized to the dilution modulus $\eta_E/G_{N,S}^0$ shown as a function of the volume fraction of the backbone ϕ_b. Error bars represent typical uncertainties in the experimental measurement of the extensional viscosity. Adapted from Schußmann et al.[86] under the Creative Commons Attribution 4.0 International License.*

Pom-poms with unentangled arms

The tensile stress growth coefficients η_E^+ of the 300k series (300k-2x15-2.5k, 300k-2x14-4k, 300k-2x9-8k) and a linear equivalent as a function of time t are shown in Figure 68. In general, strain hardening can be observed at the higher strain rates. The strain hardening decreases with lower rates and fully vanishes at the lowest investigated rates. The strain hardening of the linear chain in a) is similar to that of the pom-poms, especially at high rates. At lower rates differences in the extensional viscosity emerge.
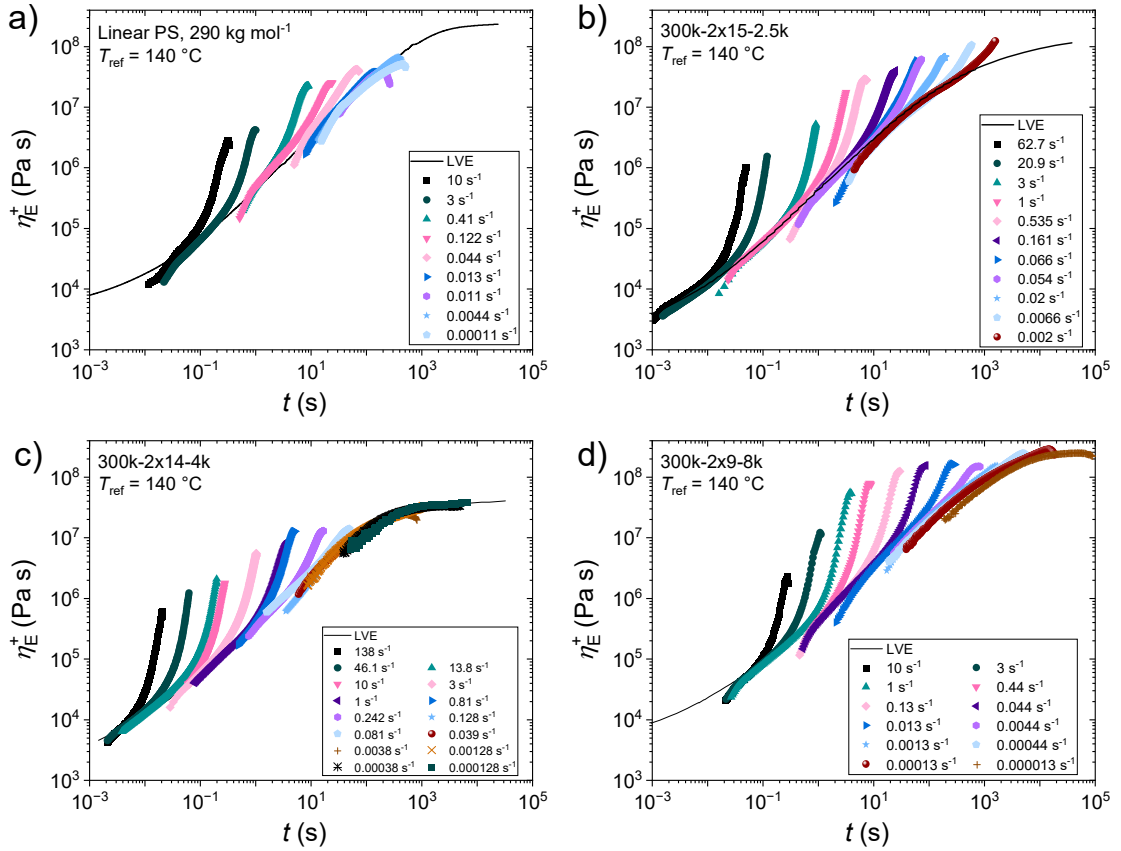
Figure 68: Tensile stress growth coefficient η_E^+ shown as a function of time t for linear PS with $M_w = 290\ kg\ mol^{-1}$ and three pom-poms (a) 300k-2x25-2.5k, b) 300k-2x14-4k, c) 300k-2x9-8k) at a reference temperature of $T_{ref} = 140\ °C$.

To analyse the extensional viscosity, especially at lower rates and the differences between the 300k series pom-poms, the linear equivalent and a pom-pom with an increased arm number is analysed in more detail in Figure 69. The extensional viscosity normalized to three times the zero shear viscosity $\eta_E/3\eta_0$ and the LVE are shown as a function of the Weissenberg number Wi. For the pom-pom 300k-2x15-2.5k, the extensional viscosity is the same as for the linear equivalent within the margin of uncertainty of the experiment. For the pom-poms 300k-2x14-4k and 300k-2x9-8k shown in b) and c), the extensional viscosity is the same as for the linear equivalent for $Wi = 10 - 1000$ within the margin of uncertainty of the experiment. In this Wi range, the pom-poms do not differ from the strain hardening of the linear chains. For $Wi = 0.1 - 5$, the pom-poms show extensional thinning as indicated by the decrease of the normalized extensional viscosity on to the LVE. This could be a result of the increased arm length compared to the pom-pom 300k-2x15-2.5k and clearly differentiates the two pom-pom samples from the linear equivalent shown as the dotted line. Nevertheless, no increased strain hardening is observed. If the arm number is increased from $q = 9$ to $q = 30$, as with the pom-pom 280k-2x30-7k shown in Figure 69 d), the extensional thinning remains at $Wi \sim 1$ and the extensional viscosity is significantly increased above the extensional viscosity of the linear chains for $Wi = 5 - 1000$.
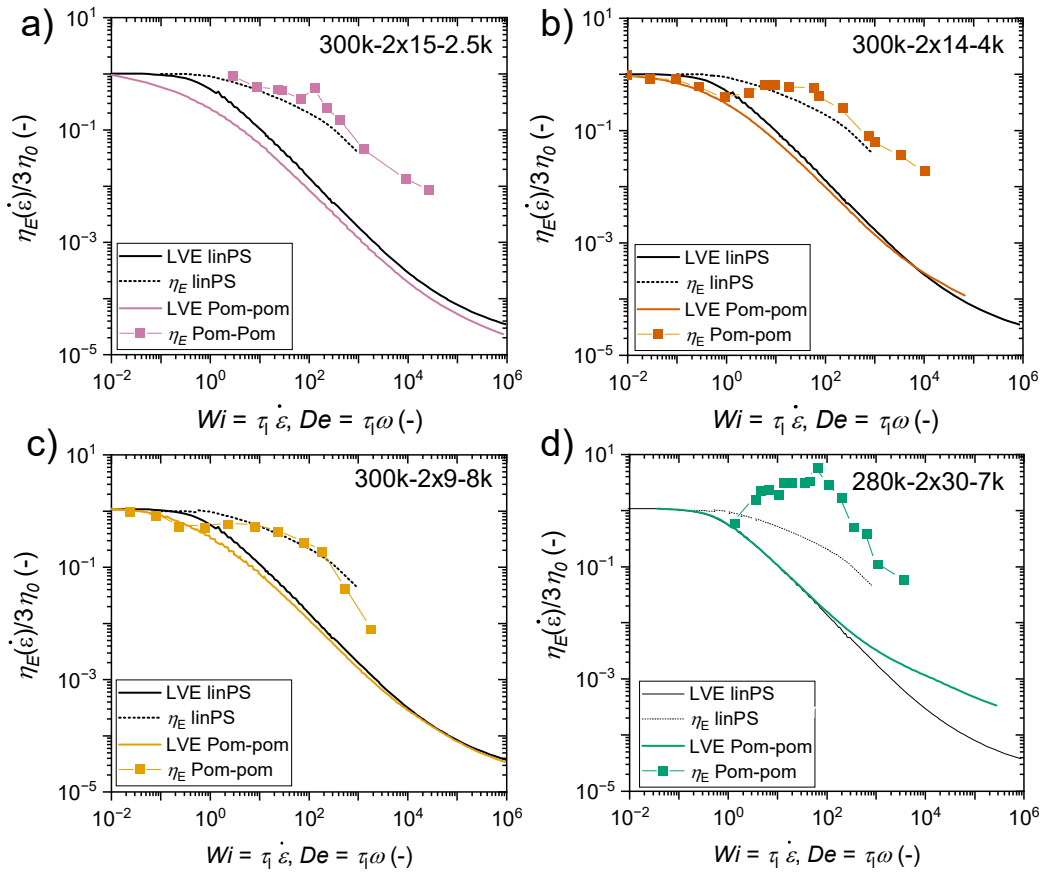
Figure 69: Extensional viscosity η_E normalized by three times the zero-shear viscosity η_0 shown as a function of the Weissenberg number Wi and the LVE for the samples a) 300k-2x15-2.5k, b) 300k-2x14-4k, c) 300k-2x9-8k and d) 280-2x30-7k. The extensional viscosity (dashed black line) and LVE (solid black line) of linear PS with 300kg mol⁻¹ is shown for comparison.

The uniaxial extensional experiments show the existence of very short branches ($M_{w,a}$ = 2.5 and 4 kg mol⁻¹) through extensional thinning and for longer branches through extensional thinning and strain hardening for high branching numbers. The analysed data suggests that short chain branching is found for $M_{w,a} < M_{w,e}/2$. For $M_{w,a} \geq M_{w,e}/2$, long chain branches are found although high branching numbers are required for strain hardening effects in the transition zone $M_{w,a} \sim M_{w,e}/2$. This agrees with findings in SAOS (see discussion at Figure 48, page 66).

7.1.4 Rheological Conclusions from Multiple Experiments

In this chapter, insights into the rheology of pom-poms are discussed which could be made based on a combination of different rheological experiments.

In Figure 70, the relationship between the rheological behavior in oscillatory shear and uniaxial extension and the ratio of the arm and backbone molecular weight for pom-poms is shown exemplary. If the ratio of arm to backbone of the pom-pom is large meaning the arms are way longer than the backbone ($M_{w,a} \gg M_{w,b}$), the pom-poms flow behavior is similar to a star. This apparent star topology can be identified by strain hardening which is indifferent to linear chains and stars in uniaxial extension. The mastercurve shows one maximum of the loss modulus in the rubber plateau at higher frequencies than the crossover into the terminal regime as stars do.[78,216,219,220] For the opposite relation, where the arms are short ($M_{w,b} \gg M_{w,a}$, $M_{w,a} < M_{w,e}/2$), the pom-pom behaves like a linear chain in shear and extension with the characteristic behavior with one rubber plateau and no strain hardening slower than the Rouse time. Between those two extremes, where the backbone is longer than the arms, but not too long, the pom-pom topology is showing its characteristic behavior. In uniaxial extension, the pom-poms show strong strain hardening. In oscillatory shear, a wide range of mastercurve shapes can be seen. Since the two relaxation times of the arms and the backbone are well separated, two relaxation regimes can be observed. Depending on the arm and effective backbone entanglements, rubber plateaus or Rouse regimes can be observed.
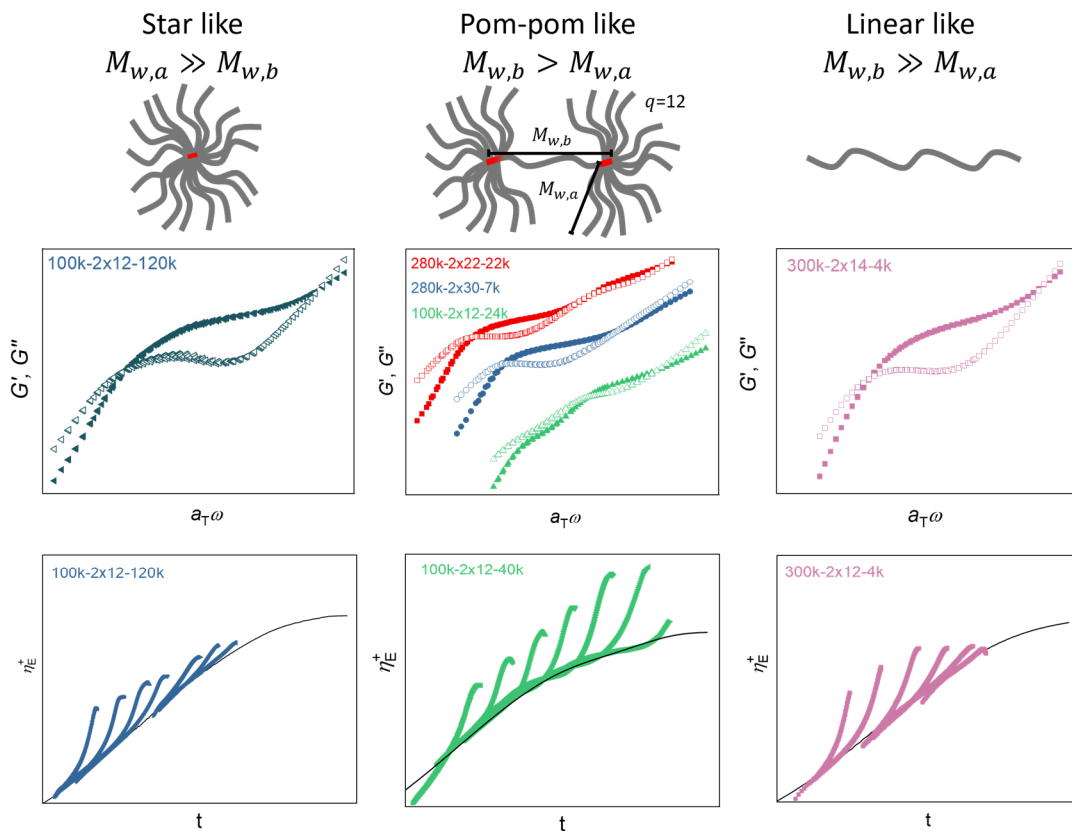

Figure 70: Influence of the arm to backbone molecular weight ratio onto the rheological behavior in oscillatory shear and uniaxial extension. The apparent rheological topology is shown schematically.

Chapter 7.1.2 investigates the startup shear behavior of the pom-pom samples and one of the main findings is that the Cox-Merz rule only holds for pom-poms with self-entangled backbones

and does not for pom-poms with not self-entangled backbones. In chapter 7.1.3, the uniaxial extensional behavior of the pom-poms is investigated and reveals among other findings that the Considère criterium can predict the extensional viscosity of the pom-pom based solely on the arm numbers via the Considère factor $f_c = [q^2 / \ln(\sqrt{3}q)]$ above the LVE. Deviations from the theoretical Considère factor are then fitted with the experimental Considère factor $f_{c,exp}$ where q is adjusted for the extensional viscosity to match the experimental extensional viscosity. The Cox-Merz rule as well as the Considère criterium holds true for the pom-poms if $Z_{b,eff} > 3$. Deviations to lower extensional viscosities in uniaxial extension and higher steady state viscosities in steady shear are found for pom-poms for $Z_{b,eff} < 3$ as shown in Figure 71. For extension and startup shear, some experimental data on combs is available. The literature data was subject to the same analysis and reveals a similar criterium for the combs. For $Z_{b,eff} > 3$, the Cox-Merz rule and the Considère limit predict the respective viscosities correctly. For $Z_{b,eff} < 3$, the same deviations for combs as with the pom-poms are observed. This shows that effective backbone entanglements are the deciding quantity for branched systems too.
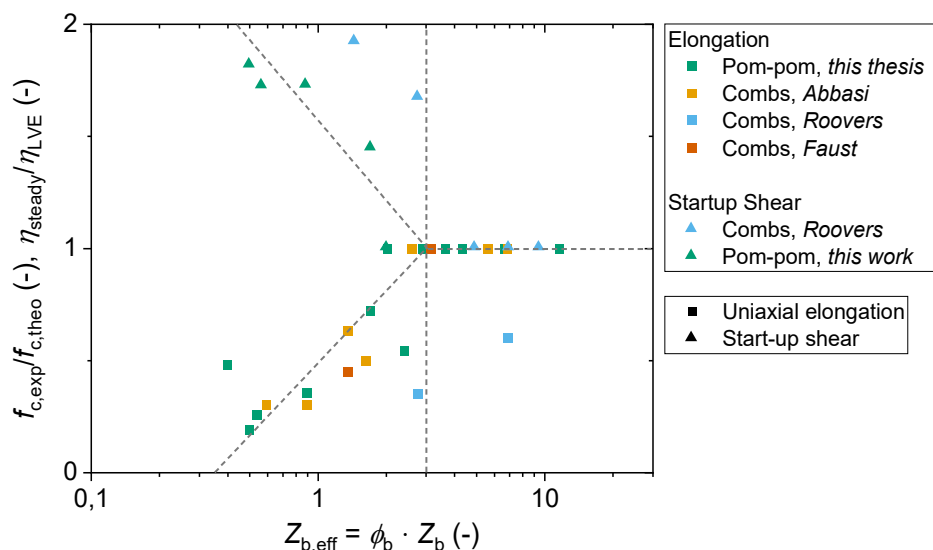
Figure 71: Relative Considère $f_{c,exp}/f_{c,theo}$ and relative Cox-Merz η_{Steady}/η_{LVE} shown as a function of effective backbone entanglements $Z_{b,eff}$ for pom-poms from this thesis and combs from literature.[62,86,96,105,106,177,178,181]

7.2   Multistars

In this chapter, two multistar samples are subject to additional rheological experiments. The two samples, one three threaded star and one four threaded star sample, were synthesized by Anika Goecke as a student and kindly provided for the following analysis. The synthesis, molecular characterization and analyzed rheological data is published in an article by M.-C. Röpert, A. Goecke, M. Wilhelm, and V. Hirschberg in Macromolecular Chemistry and

Physics.[181] *Analysis of the tensile stress growth coefficient using the EHMMSF-Modell was done by Prof. M. Wagner and is published in Rheologica Acta.*[100]

The synthesis is closely related to the pom-pom synthesis via the epoxy route. To yield multistar samples, a PS-PI multiblock copolymer is used as the backbone with three or four isoprene blocks with styrene blocks in between for the three star or four star sample, respectively. After the backbone synthesis, the epoxy group is introduced and grafted onto by living arms to yield the desired topology analogous to the synthesis route for the pom-pom (see chapter 6). The synthesis is shown schematically in Figure 72.
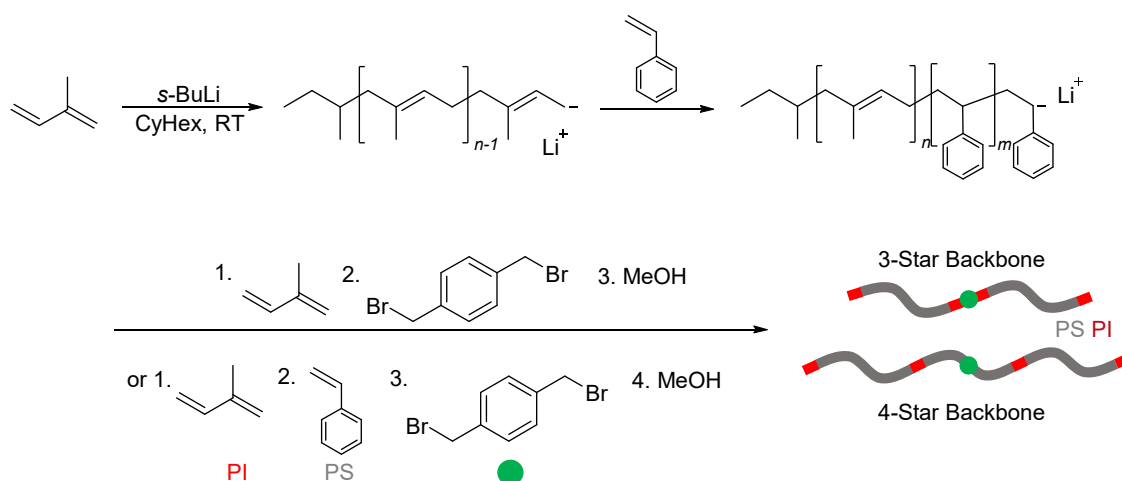
Figure 72: Schematic synthesis route to obtain the heptablock and pentablock copolymer used as the backbones for the 3-Star and 4-Star topology.

The molecular weight distribution of the backbones is reasonably narrow with $Đ = 1.15$ for the 3-Star backbone and $Đ = 1.34$ for the 4-Star backbone, however multiple species can be identified in the elugram. It is reasonable to assume linear chains due to the synthesis procedure. Therefore, a log-normal distribution is used to represent the contributions of the individual species deconvoluted from the overall molecular weight distribution obtained from SEC.[116] The apparent molecular weight of the backbones as recorded from the DRI trace is shown in Figure 73 in a) for the 3-Star backbone and in b) for the 4-Star backbone.

Figure 73: Size elution chromatogram of the backbones used for the a) 3-Star and b) 4-Star synthesis. The molecular weight is an apparent molecular weight obtained from a PS calibration due to the block copolymer nature of the sample. DRI trace of the backbones shown in black, individual contributions and their sum is shown in color.

Species are named after the resulting topology resulting from grafting onto them. For the 3-Star backbone, three species were identified and can be broken do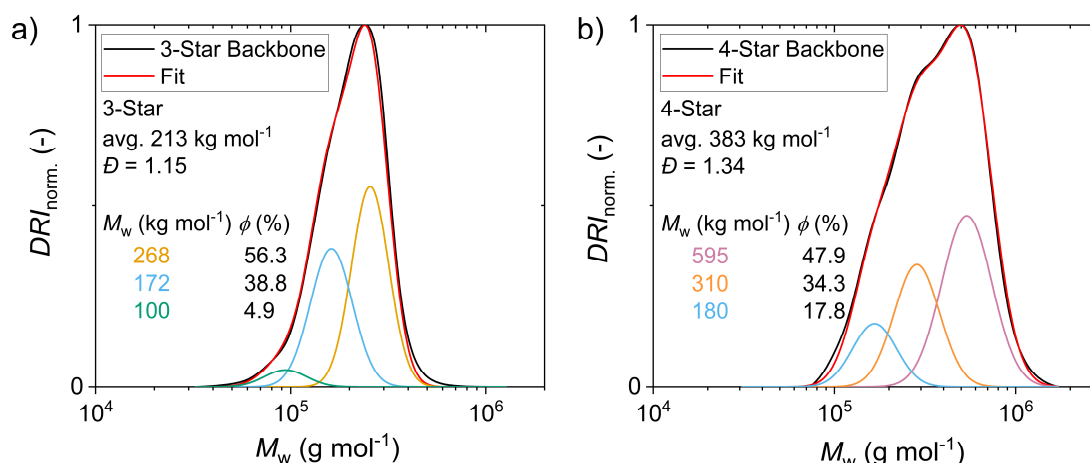wn in a small contribution from asymmetric star backbone (100 kg mol^{-1}, 4.9 %), larger contributions from 2-Star backbones (uncoupled product, 172 kg mol^{-1}, 38.8 %) and the majority of the desired product after coupling (3-Star backbone, 268 kg mol^{-1}, 56.3 %). The fitting onto the DRI trace of the 4-Star backbone yields similar results with contributions from three species identified as 2-Star backbone (180 kg mol^{-1}, 17.8 %), asymmetric 2-Star backbone (310 kg mol^{-1}, 34.3 %) and the desired product (4-Star backbone, 595 kg mol^{-1}, 47.9 %). The mentioned topologies of the side products are shown in Figure 74 for clarity.

Figure 74: Side products identified in the DRI traces of the 3-Star and 4-Star backbones.

The tensile stress growth coefficient of the 3-Star and 4-Star samples are shown in Figure 75. Both samples show exceptionally strong strain hardening in uniaxial extensional flow. For both samples, brittle fracture can be observed at high shear rates e.g. 3 s^{-1}, which can be identified by the sharp end of the tensile stress growth coefficient. At these fast rates, a maximum stress of $\sigma = 2\,10^7$ Pa is achieved. Together with the results from the other topologies (pom-poms, combs, linear), these results support the hypothesis of a topology-independent fracture stress at high rates as predicted by theoretical calculations.[214] At slower rates e.g. 0.167 s^{-1}, the tensile stress growth coefficients slope reduces at high strain and approaches a plateau value.
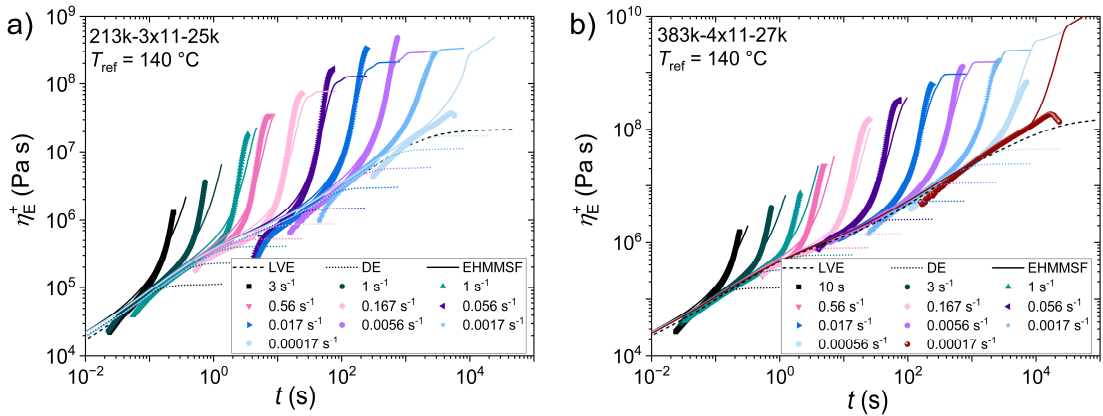
Figure 75: Tensile stress growth coefficient η_E^+ shown as a function of time t for the a) 3-Star and b) 4-Star samples at a reference temperature of T_{ref} = 140 °C for newly measured and already published data. Dots show experimental data, dashed lines show the LVE, dotted lines show the predictions of the Doi-Edwards model, and solid lines show the predictions of the EHMMSF model.

The Considère factor $f_c = \left[q^2 / \ln(\sqrt{3}q)\right]$ uses q as half of the total arm number (arm number of one pom). For other topologies such as combs, 3-Star and 4-Stars, q is set to half of the total arm number. For example, the 3-Star sample has three stars with on average eleven arms each. In total 33 arms are attached, giving for the Considère factor $q = 33/2 = 16.5$. The normalized extensional viscosity is shown as a function of Weissenberg number for the 3-Star and 4-Star sample in Figure 76. In contrast to the pom-poms investigated above, the experimental extensional viscosity does not match but rather exceeds the Considère prediction. The extensional viscosity is higher than the prediction of the Considère limit. Therefore, q is adjusted to fit the Considère limit resulting in $f_{c,expr}$. For both samples, the rheologically determined arm number is ~ 50% higher the arm number obtained from SEC: 3-Star q_{SEC} = 16.5, $q_{expr.,Rheo}$ = 24; 4-Star q_{SEC} = 22, $q_{expr.,Rheo}$ = 33.
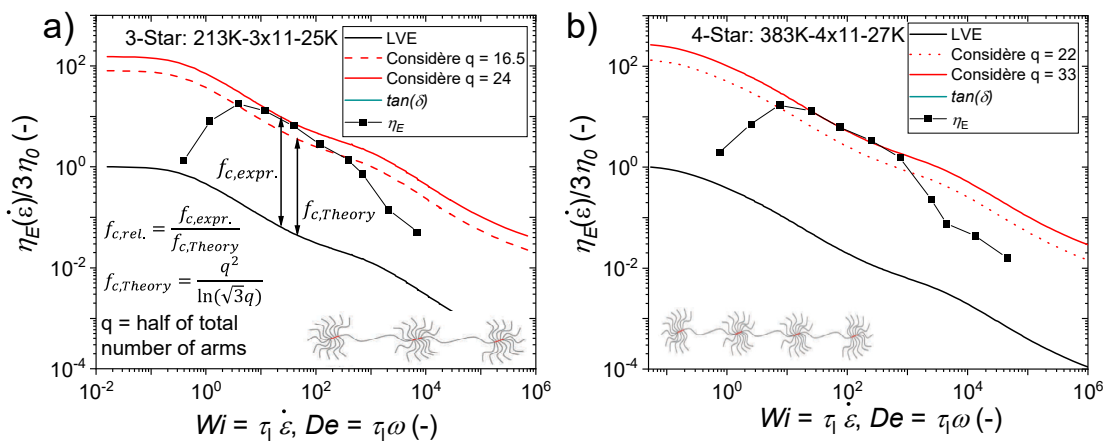

Figure 76: Extensional viscosity η_E normalized by three times the zero-shear viscosity η_0 shown as a function of the Weissenberg number Wi and the LVE as a function of the Deborah number De of the a) 3-Star and b) 4-Star sample. Considère limit is given for the arm number estimated from SEC and the arm number where the Considère limit matches the experimental data.

93

If multistar topologies can exceed the strain hardening predicted by the Considère limit, then they would be highly desirable for engineering high performance materials but also challenging the understanding of polymer physics used in the pom-pom model. The question presents itself what the origin of the increased strain hardening is.

In Figure 77, the experimental extensional viscosity in relation to the prediction of the Considère limit is investigated as a function of the effective backbone entanglements. The relative Considère limit $f_{c,rel} = f_{c,exp}/f_{c,Considère}$ describes the relation and can be obtained by adjusting the arm number for the Considère limit to fit the experimental extensional viscosity giving $f_{c,exp}$. The predicted extensional viscosity based on the determined arm number is called $f_{c,Considère}$. The pom-poms 220k-2x3-77k and 140k-2x2.5-28k[12] show an increased extensional viscosity above the Considère limit similar to the stars. For the two pom-poms, topological impurities are likely due to the low arm number where some fractions of the chains are of linear nature and the residual fraction contains increased arm numbers, e.g. 30% with 6 arms and the rest is linear yielding an average of 2.5.

To conclude on the strain hardening of the two pom-poms and the multistar samples: the increased strain hardening of the multistars above the LVE is remarkable. It is unclear whether it is an intrinsic property of the multistars topology or also due to the topological heterogeneity as suspected for the pom-poms with low arm number. Future works could investigate extensional rheology of mixtures of different topologies to find the differences and similarities from a fundamental point of view and the effect in uniaxial extensional flow.
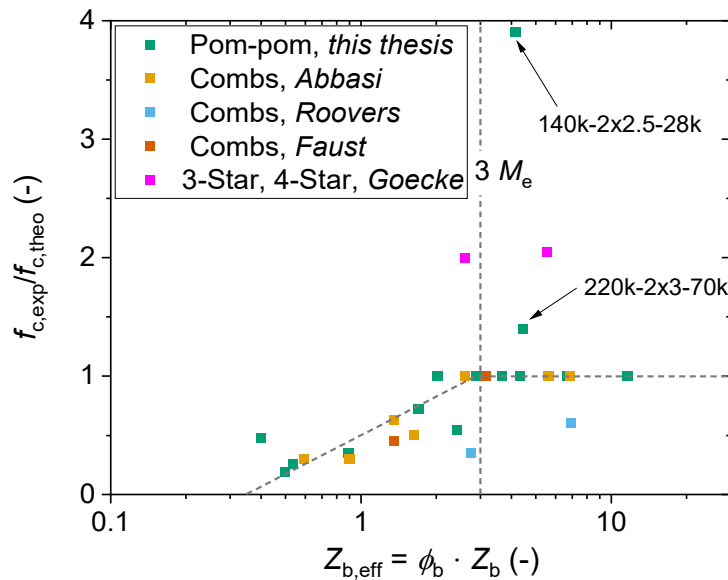
Figure 77: Relative Considère $f_{c,exp}/f_{c,theo}$ and relative Cox-Merz η_{Steady}/η_{LVE} shown as a function of effective backbone entanglements $Z_{b,eff}$ for samples with various topologies from this thesis and literature.[62,86,96,105,106,181]

7.3 Combs

In this chapter, extensional data of well-defined model comb polymers is shown in Figure 78, Figure 79, and Figure 80. The samples were synthesized by Lorenz Faust.[196] All samples show strong strain hardening due to the high number of branches. The Considère limit is also fulfilled for these combs as shown by the following figures. Detailed discussion and comparison to pom-poms can be found in chapter 7.1.3 and 7.1.4. Comparison to the pom-pom data in shear and uniaxial extension can be found in the respective chapters (7.1.1, 7.1.2, and 7.1.3).

Figure 78: a) Tensile stress growth coefficient η_E^+ shown as a function of time t for the sample 290k-50-6k at a reference time $T_{ref} = 140\ °C$. b) Normalized extensional viscosity η_E/η_0 shown as a function of the Weissenberg number Wi for the sample 290k-50-6k.

Figure 79: a) Tensile stress growth coefficient η_E^+ shown as a function of time t for the sample 290k-100-6k at a reference time $T_{ref} = 140\ °C$. b) Normalized extensional viscosity η_E/η_0 shown as a function of the Weissenberg number Wi for the sample 290k-100-6k.

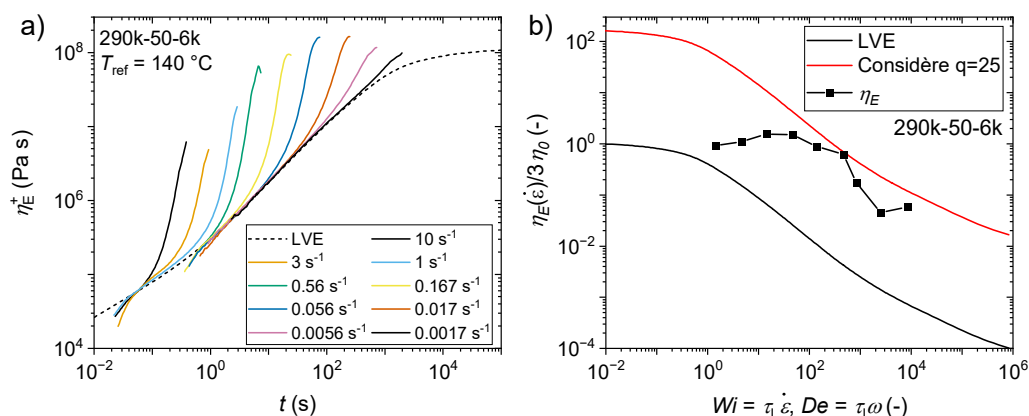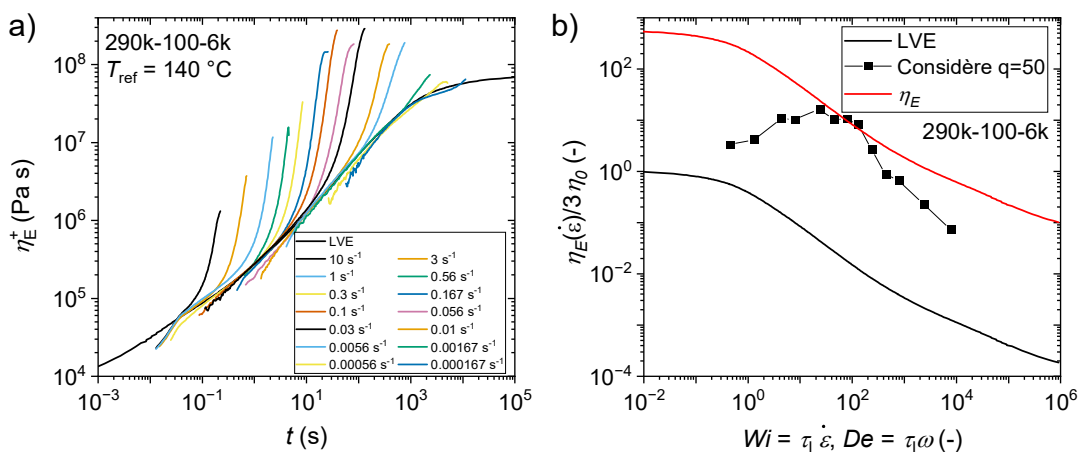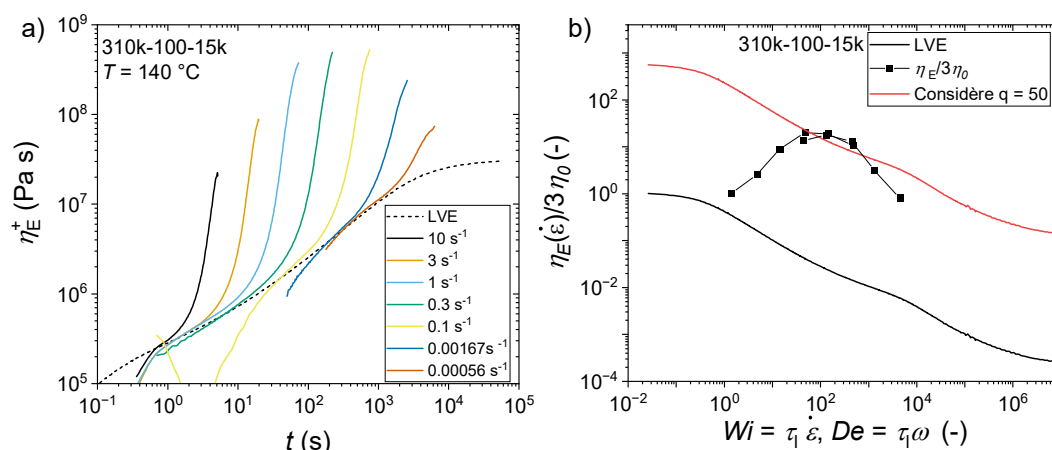*Figure 80: a) Tensile stress growth coefficient η_E^+ shown as a function of time t for the sample 310k-100-15k at a reference time T_{ref} = 140 °C. b) Normalized extensional viscosity η_E/η_0 shown as a function of the Weissenberg number Wi for the sample 310k-100-15k.*

7.4 Bidisperse Linear Blends

It is widely known that strain hardening in uniaxial extension is a unique characteristic of long chain branched polymers.[30] However, bidisperse blends of linear polymers with well separated relaxation times also show strain hardening behavior.[221] The pom-pom topology shows two relaxation times corresponding to the arms and the whole molecule. Similarly, a bidisperse melt can show two relaxation times, one for the short and one for the long chain. To differentiate between the strain hardening effect of two well separated relaxation times and the effect of the branching, the uniaxial extensional behavior of a pom-pom and a bidisperse melt with the same relaxation spectrum is compared. The bidisperse linear blend composition was determined by Dr. Céline Hannecart and Prof. Evelynne van Ruymbeke using the time marching algorithm (TMA).[122,222]

Using the TMA, the mastercurve of linear blend was calculated to be the same for the as for the pom-pom 280k-2x22-22k. The closest match was obtained for a long PS chain of 650 kg mol^{-1} diluted to 37 wt% in a matrix of 42 kg mol^{-1} as shown in Figure 81 a). To test the calculated bidisperse linear blend, two linear PS samples where synthesized using anionic polymerization. The synthesized long chain ($M_{w,L,exp}$ = 640 kg mol^{-1}, Đ = 1.10) was diluted to 37 wt% in the synthesized short chain ($M_{w,S,exp}$ = 46 kg mol^{-1}, Đ = 1.03). The mastercurves of the bidisperse linear blend and the pom-pom are shown in Figure 81 b). Both samples show nearly identical mastercurves, small deviations can be observed at ~ 50 rad s^{-1} and the low frequency rubber plateau. The crossover frequencies into the terminal regime for the blend (0.012 rad s^{-1}) and pom-pom (0.0084 rad s^{-1}) indicate very similar longest relaxation times. The small deviations in the high frequency response are probably due to the deviation between the calculated and experimental short chain molecular weight ($M_{w,S,exp}$ = 46 kg mol^{-1}, $M_{w,S,calc}$ = 42 kg mol^{-1}). The

matching longest relaxation time and dispersity indicate a good agreement between calculations and experiment in respect to the effect of dynamic dilution onto the relaxation times. The rubber plateau of the short chains in the bidisperse linear blend and of the arms of the pom-pom are very similar in frequency range, despite their different molecular weight ($M_{w,S} \sim 2M_{w,a}$). These observations suggest that the effective branch length of the pom-pom branches in SAOS is the whole chain length through the star i.e. molecular weight of two arms.
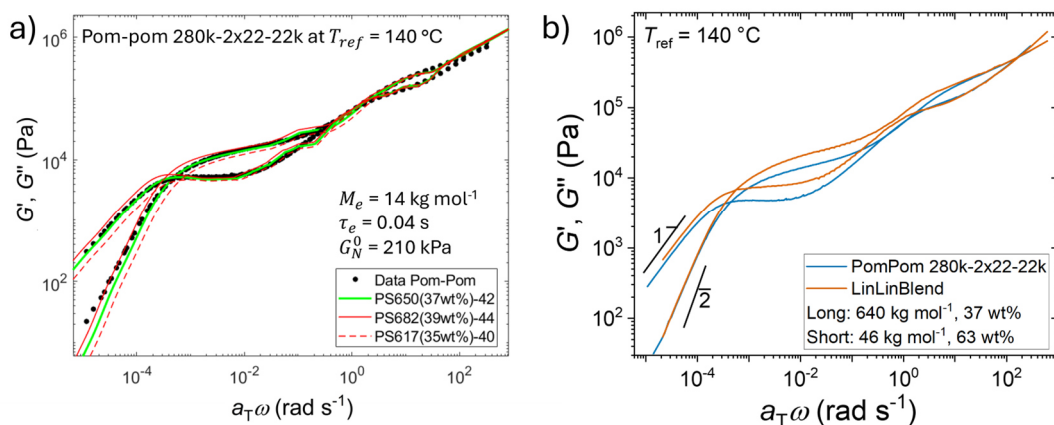
Figure 81: a) Calculated mastercurves of the different bidisperse blends in comparison with the experimental mastercurve of the pom-pom 280k-2x22-22k. b) Mastercurves of the synthesized bidisperse linear blend and the pom-pom shown at a reference temperature of T_{ref} = 160 °C.

The van Gurp-Palmen plot and the elugram of the pom-pom 280k-2x22-22k and the linear-linear blend are shown in Figure 82. The vGP plot of both samples is very similar showing two distinct minima. Based on the vGP plot, the bidisperse melt is indistinguishable from the branched pom-pom. In the elugram, the linear-linear blend shows two species as expected and the pom-pom shows only one species. Only the combination of vGP plot and the elugram can differentiate between a branched sample (vGP plot: 2 minima, elugram: 1 species) and a bidisperse linear blend (vGP plot: 2 minima, elugram: 2 species). Some residual, unattached arms can be found around V_e = 16.2 mL. Due to their low fraction under 5 wt%, they do not significantly contribute to the rheological response.
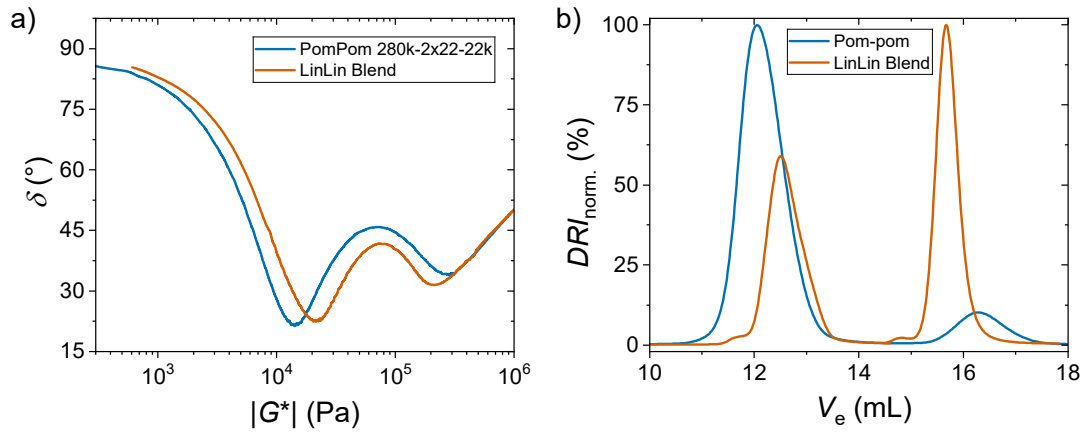
Figure 82: a) Van Gurp Palmen plot of the pom-pom 280k-2x22-22k and the linear-linear blend. b) Elugram of the pom-pom 280k-2x22-22k and the linear-linear blend.

The tensile stress growth coefficient of the bidisperse linear blend is shown in Figure 83 a). As expected for linear chains, strain hardening is observed at very high rates but vanishes below $\dot{\varepsilon} = 3$ s^{-1}. The normalized extensional viscosity of the bidisperse linear blend and the pom-pom is shown in Figure 83 b). A significant difference between the long chain branched pom-pom and the bidisperse linear blend can be identified. For $30 > Wi > 1$, the pom-pom shows strong strain hardening, while the bidisperse linear blend shows no hardening. This data clearly shows, that while two samples can be identical in experiments in the linear deformation regime, e.g. SAOS, there can be substantial differences in nonlinear experiments, e.g. uniaxial extension. Additionally, the data shows that the strain hardening in the range of $Wi = 1 - 200$ is a result of the branches and not two relaxation times.
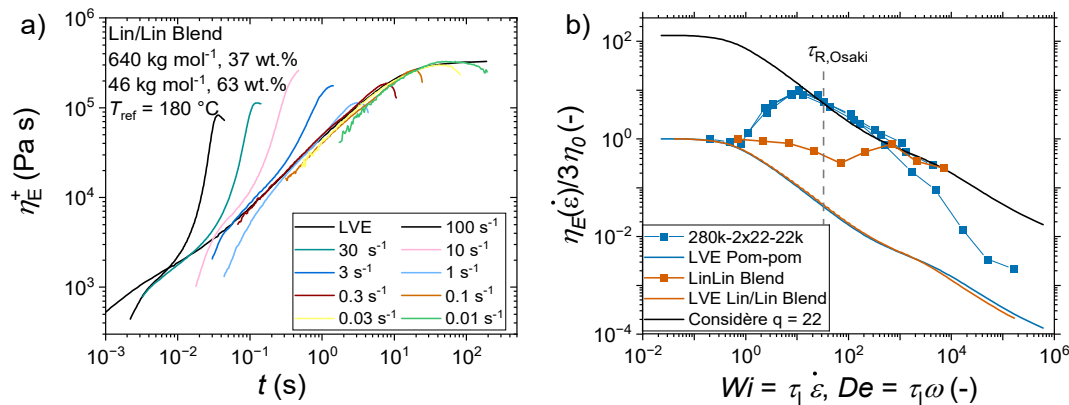
Figure 83: a) Tensile stress growth coefficient η_E^+ shown as a function of time t for the bidisperse linear blend at a reference time $T_{ref} = 160$ °C. b) Normalized extensional viscosity η_E/η_0 shown as a function of the Weissenberg number Wi for the bidisperse linear blends and the pom-pom.

Osaki *et al.*[223] derived the following relation to calculate the Rouse time $\tau_{R,L}$ for the long chain of a bidisperse blend of linear chains with the molecular weight M, critical molecular weight M_c, zero-shear viscosity η_0, density ρ, long chain volume fraction φ_L, and gas constant R.

$$\tau_{R,L} = \frac{12 M \eta_0}{\pi^2 \rho \varphi_L RT} \left(\frac{M_c}{M \varphi_L} \right)^{2.4} \tag{59}$$

For the investigated bidisperse linear blend, Osakis equation yields $\tau_{R,Osaki}$ = 2640 s, which corresponds to $Wi_{\tau,R,Osaki}$ = 32.2, for the long chain. As shown in Figure 83 b), around $\tau_{R,Osaki}$ the normalized extensional viscosity decreases, and the strain hardening vanishes as expected for linear chains with $\dot{\varepsilon} < 1/\tau_R$ confirming derived relation from Osaki.

7.5 Comparison of Experimental Data with Constitutive Models: Pom-pom and MSF-Model Predictions

The experimental tensile stress growth coefficient and the tensile stress growth coefficient calculated by the pom-pom constitutive equations are shown in Figure 84 a) for the pom-pom 100k-2x9-11k and b) for the pom-pom 400k-2x12-23k as a general representation for all pom-pom samples. All other samples are shown in Supplementary Figure 3. The tensile stress growth coefficient of 100k-2x11-9k and all other samples found in Supplementary Figure 3 are calculated based on the molecular parameters determined from synthesis (see Table 3, page 63) and PS specific material parameters (τ_e = 0.036 s, G_0 = 2 10^5 Pa).

Figure 84: Tensile stress growth coefficient η_E^+ as a function of time t for the pom-pom a)100k-2×11-9k and b) 400k-2×12-23k at a reference temperature of T_{ref} = 140 °C. Dots show experimental data. Simulated tensile stress growth coefficient calculated by the pom-pom model with the respective molecular parameters and PS specific material parameters for a), and with adjusted G_0 = 4 10^5 Pa for b) is shown by the solid, colored line. The dashed black line in b) was obtained after fitting of the model to the experimental data obtaining G_0 =1.8 10^5 Pa, τ_e = 0.05 s and Z_b = 38. Adapted from Schußmann et al.[86] under the Creative Commons Attribution 4.0 International License.

As illustrated in Figure 84 a) exemplary with pom-pom 100k-2x11-9k, when the experimentally determined molecular parameters are used in the pom-pom model, the experimental data is

poorly described by the pom-pom model. Especially the LVE and the zero shear viscosity η_0 is not well represented. As a result, also the calculated extensional data is offset from the experimental data. Contrary, the increase of the tensile stress growth coefficient above the LVE, the strain hardening, is predicted roughly correct. Investigated pom-poms have a backbone volume fraction between 0.09 and 0.42. The observed difference between experimental and calculated tensile stress growth coefficient could be explained by the dominance of the arm relaxation behavior. Due to the high arm volume fraction, the backbones are highly diluted with a low number of effective entanglements. In the pom-pom model, the strain hardening is implemented based on resistance against branchpoint withdrawal as function of the arm number. Since the strain hardening is predicted correctly for $q = 10 - 22$, the approach seems reasonably correct. As the arm contributions are neglected in the pom-pom model, the tensile stress growth coefficient of the pom-pom with the lowest arm volume fraction 400k-2x12-23k is shown in Figure 84 b). When an increased plateau modulus with $G_0 = 4\ 10^5$ Pa is used for the calculations, the experimental and simulated extensional data are in reasonable agreement. Yet, the η_0 is still underestimated by factor ~ 10, a result of incorrect backbone relaxation times. If the backbone and entanglement relaxation times are artificially increased using $G_0 = 1.8\ 10^5$ Pa, $\tau_e = 0.05$ s and $Z_b = 38$ as shown by the dashed line in Figure 84 b), the LVE including η_0 can be represented by the pom-pom, but as a result, the tensile stress growth coefficients differ significantly (not shown).

In conclusion, the pom-pom model can represent the experimental LVE and extensional data qualitatively but not quantitatively using the actual topological parameters. The experimental data can only be predicted correctly if the molecular parameters are adjusted and fitted to the experimental data. Contrary, the strain hardening prediction is roughly correct from the actual molecular parameters.

The extended hierarchical multimode stress function model (EHMMSF) is a tube-based model which can predict the stress in various flow responses of a polymer melt based on its relaxation spectrum. Together with Prof. Manfred Wagner, the EHMMSF-Model has been applied to the herein investigated pom-pom samples. As shown exemplary in Figure 85, the EHMMSF-Model can predict the tensile stress growth coefficient quantitively solely based on the relaxation spectrum obtained from SAOS. Detailed discussions can be found in the corresponding publication in Rheologica Acta by Hirschberg et al.[96]
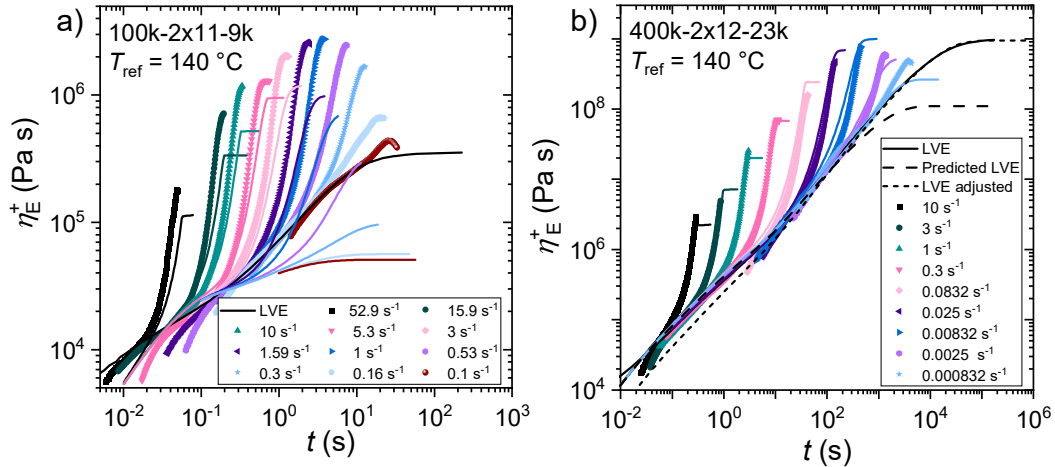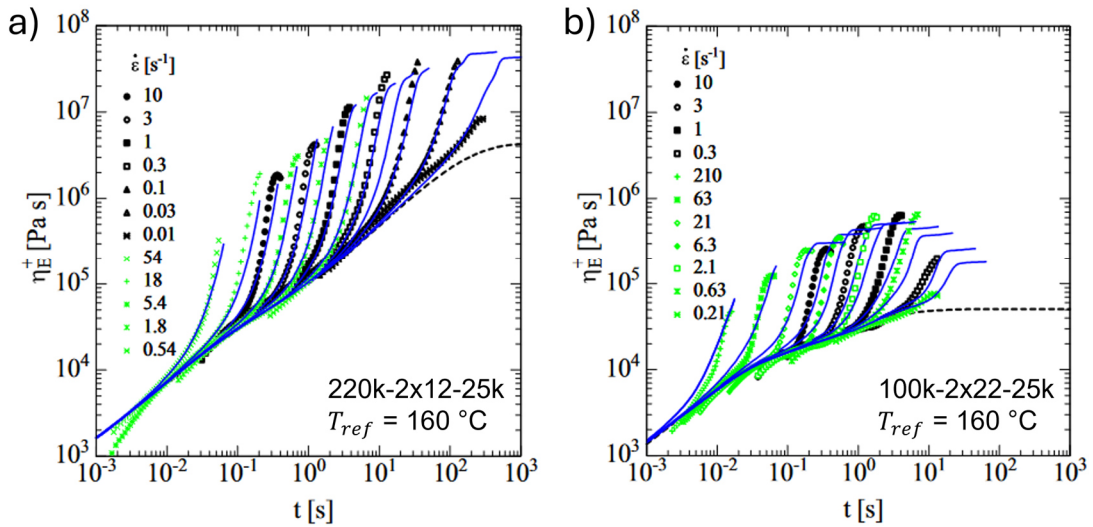
Figure 85: Tensile stress growth coefficient η_E^+ as a function of time t for the pom-poms a) 220k-2x12-25k and b) 100k-2x22-25k at a reference temperature of T_{ref} = 160 °C. Calculated data using the EHMMSF-Model shown as solid blue lines. Experimental data shown as dots measured at T = 160 °C in black and T = 140 °C in green. Adapted from Hirschberg et al.[96] under the Creative Commons Attribution 4.0 International License.

Within the EHMMSF model, the stress response of a variety of deformations can be calculated. Previously, the EHMMSF model was only used to predict disperse LDPE startup shear data.[93] Similar to the extensional data, the pom-pom startup shear data from chapter 7.1.2 can be predicted quantitatively solely based on the relaxation spectrum obtained from SAOS. A detailed discussion will follow in a separate manuscript.

To conclude, the nonlinear behavior of branched polymers in any deformation (shear and uniaxial extension) is contained in the linear relaxation spectrum and can be calculated by the EHMMSF model.

7.6 Pushing the Limits of the SER Geometry: 2D UXF

In this chapter, measurements with a modified procedure for Sentmanat Extensional Rheometer (SER) type extensional fixtures are described with the goal to increase the measurable Hencky strain. An universal extensional fixture geometry (UXF) mounted on an Anton Paar MCR702e MultiDrive rheometer is used. The initial idea for the modified measurement procedure is of Dr. Masood Khabazian Esfahani (previously KIT, now tesa SE). Special thanks to Dr. José Alberto Rodríguez Agudo and Dr. Jan Haeberle (both Anton Paar Germany GmbH) for the opportunity to measure on their rheometer and their help with the implementation. Prof. Dr. Qian Huang (previously Denmark Technical University (DTU), now Sichuan University) kindly provided comparison data measured on the filament stretch rheometer. The used comb sample was synthesized by Dr. Lorenz Faust[106] and was chosen due to the strong strain hardening behavior and its high stretchability.

The first apparatus to measure extensional properties of a polymer melt goes back to the work of Meissner and coworkers at the BASF Ludwigshafen in the 1960s.[224] An apparatus was developed using a silicon oil bath with a floating specimen being stretched by two sets of toothed gear pairs. Later developments lead by Münstedt yielded a extensional rheometer with reduced complexity in the sample preparation and considerably smaller required amounts of sample.[225] The currently most used extensional rheometers were developed in the early 2000s. Sentmanat developed the Sentmanat Extensional Rheometer (SER) as a interchangeable geometry for existing stress-controlled rotational rheometers as schematically shown in Figure 86.[226] The ease of use and compatibility with the already widely available rotational rheometers are reason for its popularity and wide spread. The adaption for strain-controlled rheometers by TA Instruments is called Extensional Viscosity Fixture (EVF). A major downside of the SER geometry is the incompatibility with polymer solutions. A relatively high zero shear viscosity of > 10,000 Pa s is required to prevent specimen deformation due to sagging during the temperature equilibration. Additionally, after one rotation of the drum the sample overlaps with itself limiting the maximum strain to $\varepsilon = 4$.[226] In parallel, the filament stretch rheometer (FSR) was developed by a number of researchers around McKinley, Sridhar and Hassager.[227,228] A true constant strain rate is applied due to an active diameter control of the filament with an laser micrometer. Assumptions of ideal deformation as used with the SER type geometries are not required. The FSR is suitable for polymer melts and solutions of a vast range of viscosities and a Hencky strain up to $\varepsilon = 9$.[229] To increase the Hencky strain limit for the SER/EVF geometry, Parisi *et al.* recently proposed an approach to place the sample at an angle as shown in Figure 86 in the upper central sketch. With this alternate placement, the overlap after one rotation of the geometry is avoided and the maximum Hencky strain is increased to $\varepsilon = 6$.[230] Due to the small sample angle typically below 10° the uniaxial extension is retained and the stress function is not altered.
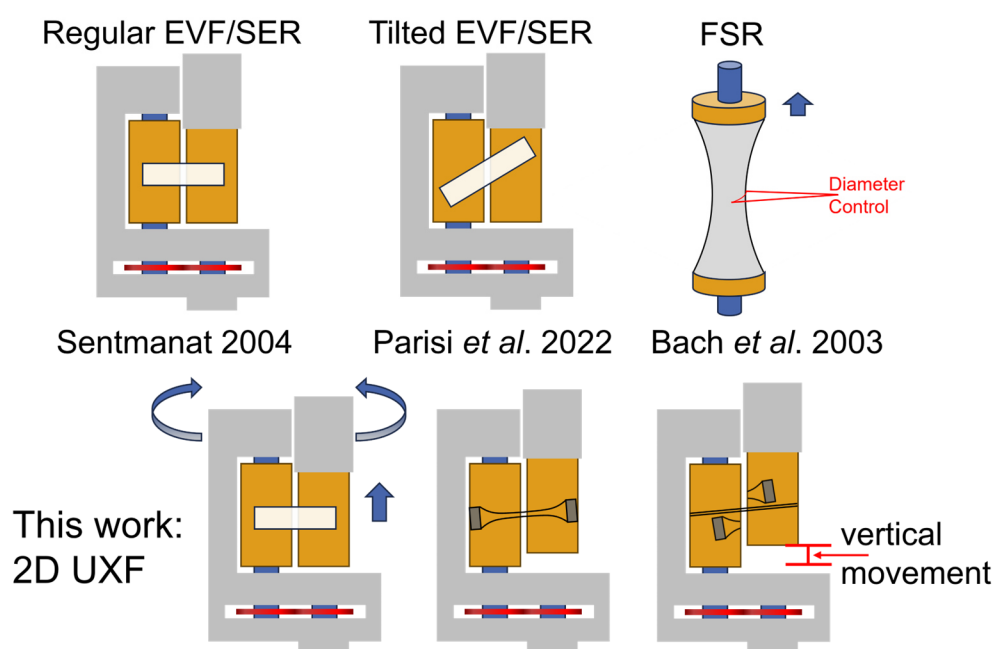

Figure 86: Overview over the currently most used rheometer configurations to measure uniaxial extensional properties as well as recently developed extensions.

To increase the Hencky strain limit even further, we propose a new measurement procedure utilizing helical wrapping of the specimen around the drums. This is achieved by superposition of a vertical movement of the upper geometry onto the rotation as shown in Figure 86 in the lower sketch. The sample is angled away from an orthogonal orientation to the drum axis as used in EVF/SER protocol due to the helical wrapping. During the measurements, the angle of the sample was obtained from evaluation of a video of the extension and the angle was found to be ~ 5 ° as shown in Figure 87. The stress can remain unchained between regular and 2D UXF application without introducing a significant error due to the small angle approximation of $\sin \theta \sim \theta$ (Difference $< 1\%$).
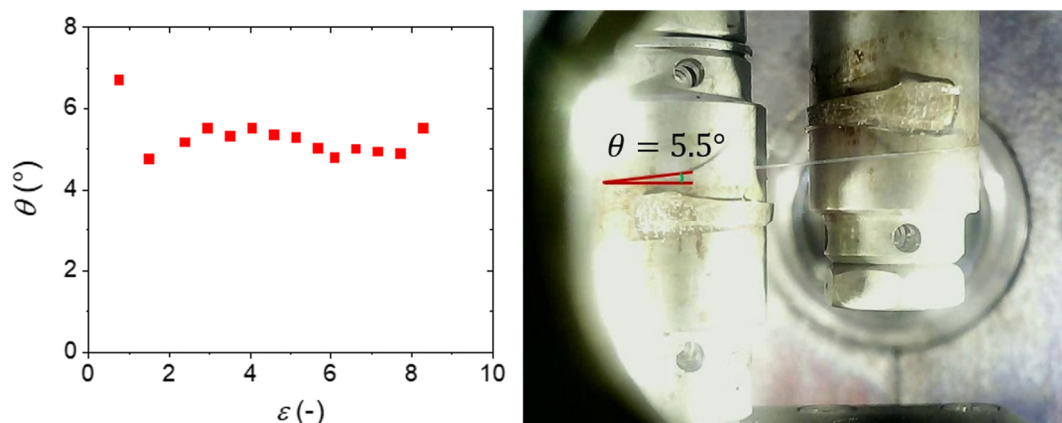
Figure 87: Optically determined angle of the specimen during extension θ as a function of the applied Hencky strain ε and a snapshot of the specimen on the UXF geometry during extension with the angle indicated.

To evaluate the tensile stress growth function of the newly proposed method a highly branched comb shaped sample named 290k-60-44k is used with a backbone of 290 kg mol^{-1} and 60 branches with 44 kg mol^{-1}. The sample shows high Hencky strains at break and strong strain hardening, which stabilizes the sample specimen especially at high strains. The tensile stress growth coefficient of the comb was measured using the regular EVF procedure, the tilted EVF procedure by Parisi and coworkers,[230] a filament stretch rheometer as well as the new 2D UXF technique. The results of all four methods at a temperature of $T = 180$ °C and strain rates of $\dot{\varepsilon} = 0.0003 - 1$ s^{-1} are shown in Figure 88. Overall, all methods are in agreement giving the same tensile stress growth coefficient and extensional viscosity within the typical uncertainty of the experiment. At small strains, the tensile stress growth coefficients overlap for all methods and strain rates, therefore giving a reproduction of the linear regime. Almost identical tensile stress growth coefficients between the methods are found for $\dot{\varepsilon} = 1 - 0.1$ s^{-1}. Minor differences at 0.03 s^{-1} and 0.01 s^{-1} can be found after the tensile stress growth coefficient starts to increase above the LVE. Nevertheless, similar extensional viscosities are obtained. For both ARES G2 and MCR702e MultiDrive, the torque falls below the detection limit at 0.003s^{-1}, giving no reasonable viscosity data. The FSR still produces reasonable viscosity data at this strain rate.

Figure 88: Tensile stress growth coefficient η_E^+ as a function of time t at T = 180 °C for the comb sample 290k-60-44k using four different techniques to measure the tensile stress growth coefficient.
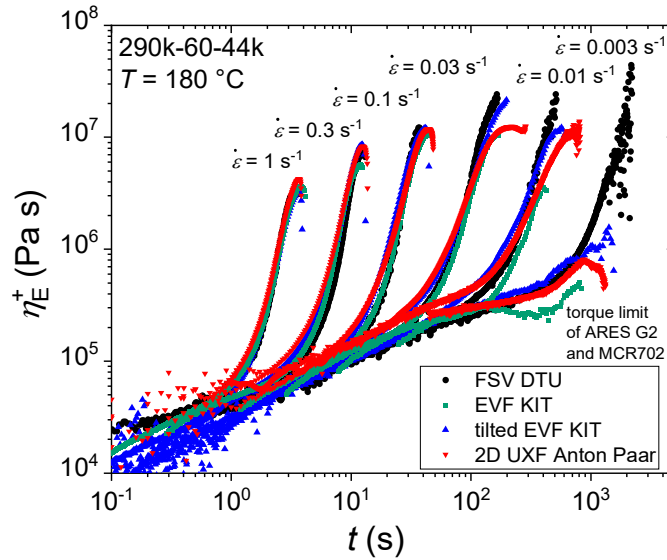
An overview of sample dimensions, instruments, locations, and operators is given in Table 5.

*Table 5: Detailed overview of the instrumentation and sample dimensions used for the different methods. *Mass calculated for the specimen for one measurement and a density of ρ = 1 g cm^{-3}.*

Method	Sample dimensions	Mass* [mg]	Instrument	Location	Operator	ε_{max}
EVF	18x5x0.5mm	45	ARES G2	KIT	Dr. Faust	4
Tilted EVF	20x3x1mm	60	ARES G2	KIT	Schußmann	6
FSR	4x2mm, cylindrical	100	Vader 1000, first generation	DTU	Prof. Huang	6.7
2D UXF	20x3x1mm	60	MCR 702e MultiDrive	AP Germany	Schußmann	8.3

In Figure 89, the tensile stress growth function σ_E^+ is shown as a function of the applied Hencky strain ε for the investigated comb sample. In this form, the strain at break ε_{break} can easily be identified. For faster strain rates $\dot{\varepsilon} \geq 0.1$ s^{-1}, the extensional stress σ_E, the steady state value of the tensile stress growth function, and the strain at break is reached at Hencky strains below $\varepsilon = 4$ for all methods. At slower strain rates, the strain at break increases substantially above $\varepsilon = 4$ for tilted EVF, 2D UXF and FSR. The highest strain at break of the tilted EVF is $\varepsilon_{break,max,tEVF} = 6$. For the FSR, $\varepsilon_{break,max,FSR} = 6.7$ and for the 2D UXF strains of up to $\varepsilon_{break,max,2DUXF} = 8.3$ can be achieved. The newly proposed method can therefore significantly increase the measurable strain range by 2.3 Hencky strain units or a factor of 10 as shown exemplary for the strain rate of 0.03 s^{-1}.
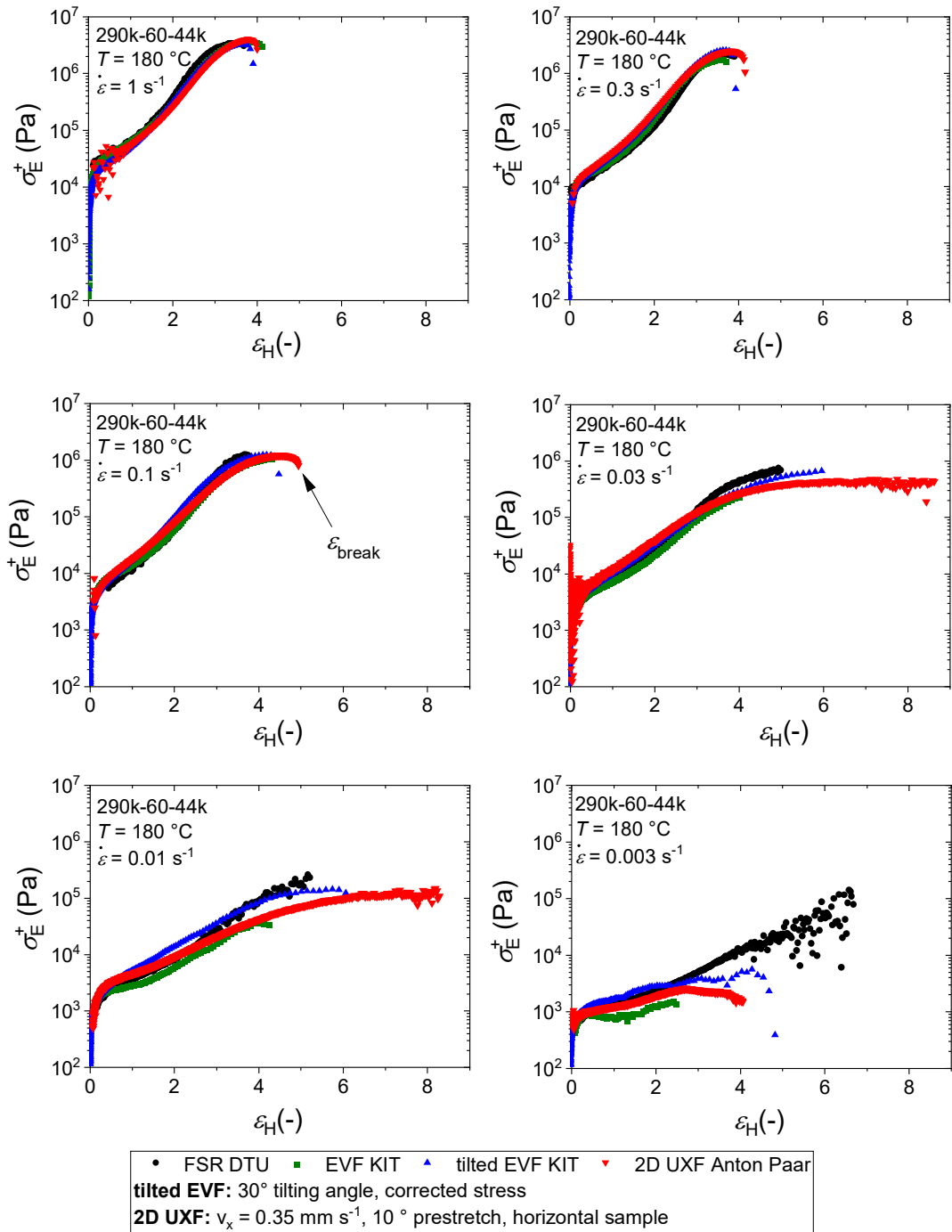
Figure 89: Tensile stress growth function σ_E^+ as a function of applied Hencky strain ε at different Hencky strain rates for the comb 290k-60-44k using four different techniques to measure the tensile stress growth function.

To better compare the strain at break of the four different methods, it is shown as a function of strain rate in Figure 90. Between the strain rates of 0.1 s⁻¹ and 0.01 s⁻¹, which correspond to the Weissenberg numbers of $Wi = 1 - 50$, the sample can be stretched further than $\varepsilon = 4$. At higher

and lower strain rates, the strain at break decreases to $\varepsilon = 4$ for all methods. Advanced techniques are therefore only useful in a small strain rate range faster than the inverse of the stretch relaxation time ($1/\tau_s \sim 0.01$ s^{-1}).
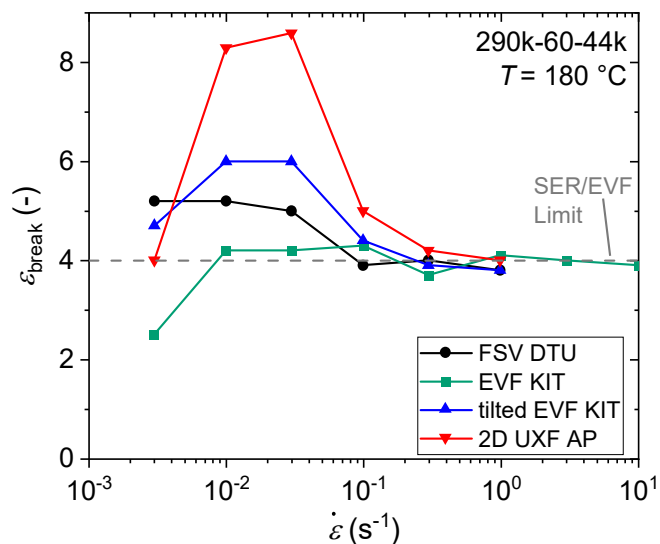
Figure 90: Hencky strain at break ε_{break} shown as a function of the Hencky strain rate for the comb 290k-60-44k at a temperature of T = 180 °C for all four methods.

Repeated measurements for strain rates of fast (1 s^{-1}) and slow (0.03 s^{-1}) strain rates are shown in Figure 91 using the 2D UXF protocol. The reproducibility using the 2D UXF protocol is similar to the regular UXF protocol. Typical deviations between measurements are on average ± 20 %.
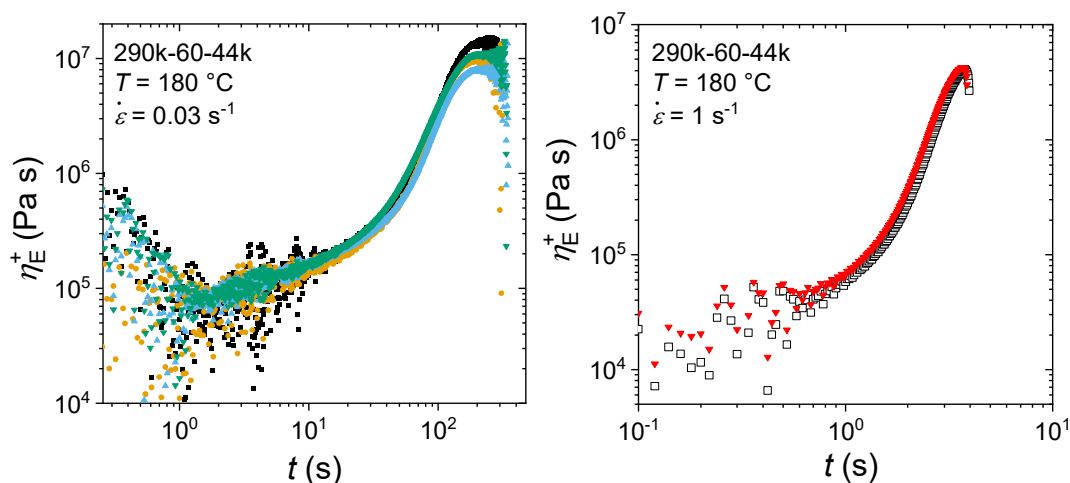
Figure 91: Repeated measurements with the 2D UXF protocol of the tensile stress growth coefficient η_E^+ as a function of time t for the comb 290k-60-44k for two strain rates of 0.03 s^{-1} and 1 s^{-1}.

8 Synthesis and Mechanical Properties of Branched PS-PI Block Copolymers

In this chapter, the synthesis of different topologies of branched block copolymers is described and the influence of the topology on their mechanical properties is investigated. Therefore, PS-PI block copolymers are grafted on varying backbones yielding different topologies. The mechanical properties are measured using tensile tests. The tensile testing and investigation of the phase separation behavior via SAXS and AFM are currently ongoing and preliminary results are shown. The multiblock copolymer backbones for the 3-Star and 4-Stars are synthesized by Anika Goecke and kindly provided.[181] Parts of this chapter have been published in preceding publications.[182]

Block copolymers are part of a huge interdisciplinary research field spanning from biomedicine to mechanical engineering and from fundamental research to commodity plastics for six decades.[231,232] The synthesis of defined block copolymers, their characterization in various environments and their application is the focus of polymer chemists since the development of polymerization techniques that allow the synthesis of defined block copolymers.[28,233–235] The first and one of the most suited methods is the anionic polymerization, due to the living character. After full conversion of the first monomer, the anionic reactive center remains active, and a second monomer can be added.[7]

The phase behavior of a block copolymer depends on the chemistry of the individual blocks, the architecture and the chains lengths. The interaction between two different monomers can be described by the Flory-Huggins theory.[231,232] In the event of phase separation, surface tension leads to a large variety of resulting morphologies. Properties in the melt and solid state are highly influenced by the morphologies. Trough many previous works (see literature data in Figure 99, page 112), the influence of the molecular architecture on chain confirmation has been investigated. The deciding quantity for the solid-state mechanical properties has been identified as the bridging ratio which is the ratio of block copolymers forming loops and bridges. For example, for a triblock copolymer of the type ABA, chains are bridging, when the outer blocks of the triblock copolymer terminate in different phases. Chains are looped, when the outer block terminate in the same domain.[236] High mechanical strength is associated with a high bridging ratio. [237,238]

8.1 Synthesis of Stars and Threaded Star-shaped Block Copolymers

The branched block copolymers described in this chapter, are synthesized using the same synthesis route as the PS homopolymers in the preceding chapter 6. This is possible due to similar reactivities of styrene and diene monomers such as isoprene. An overview of the different topologies investigated is shown in Figure 92. The grey parts are representing polystyrene (PS) blocks and red shows polyisoprene (PI) blocks. A short P2VP chain is used as a branching point for the stars as indicated in blue.
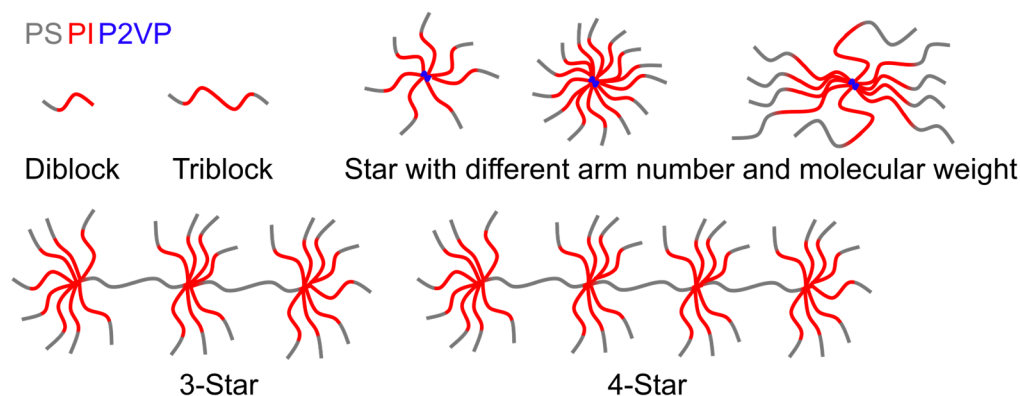
Figure 92: Overview of the molecular structure of the synthesized block copolymers.

The block copolymer star synthesis route is shown in Figure 93 in detail. In the first step, the P2VP backbone is polymerized by *s*-BuLi in THF at – 80 °C. In a second step, the arms are polymerized through sequentiell addition of the styrene and isoprene after initiation by *s*-BuLi in cyclohexane at room temperature. A monomer composition of 70 wt% isoprene and 30 wt% styrene is used. After completion of the polymersation, the living arms are grafted onto the pyridine rings of the backbone. Different arm numbers and molecular weights are achieved by varying the monomer, initiator, and backbone ratios.
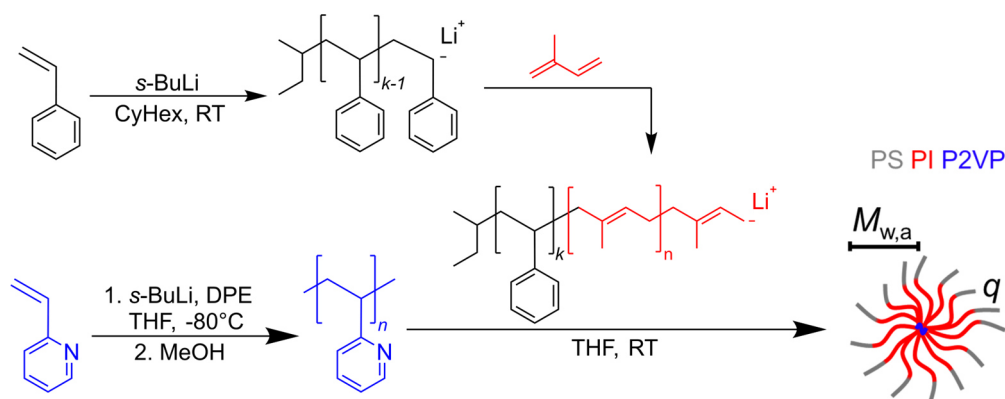
Figure 93: Synthesis of the block copolymer star through the grafting onto the pyridine ring. Different star arm numbers are achieved through adjusting the equivalents between backbone and arms..

The 3-Star and 4-Star samples are synthesized using the epoxy route as illustrated in Figure 94. The multiblock copolymers used as the backbones were synthesized by Anika Goecke and kindly provided.[181] The backbones are the same as used for the PS homopolymer 3-Star and 4-Star samples analyzed in chapter 7.2. Through epoxidation of the double bonds of the short isoprene blocks in the backbone, they are partially converted to epoxy groups. After separate polymerization of the arms using the same procedure as described for the stars above, the living arms are grafted onto the backbone.
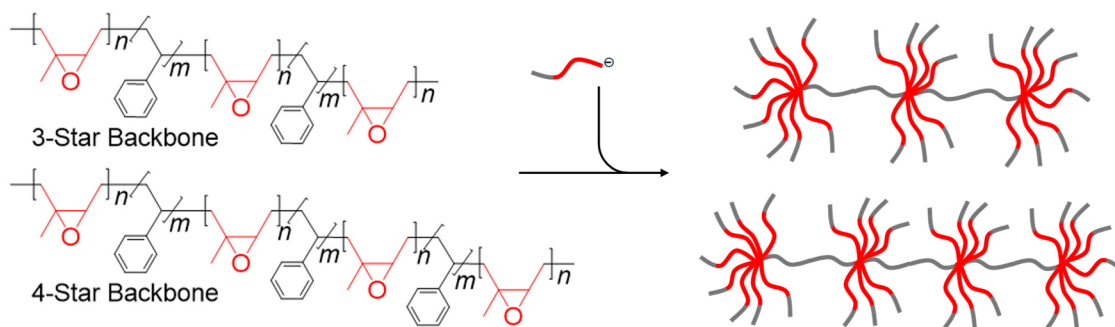
Figure 94: Overview of the synthesis of the threaded 3-Star and 4-Star based on the epoxidized back-bones. Typically, 30 % of the PI repeating units are epoxidized. Simplified microstructure shown.

An overview of the molecular parameters of the synthesized branched block copolymer samples is shown in Table 6.

Table 6: Overview of the synthesized branched block copolymer samples. Backbone branching point chemistry in a) P2VP b) epoxidized PI. c) PS content estimated via ^1H NMR.

Sample	$M_{w,a}$ (kg mol^{-1})	$Đ_a$	$M_{w,b}$ (kg mol^{-1})	$Đ_b$	q	PS (vol%)$^{c)}$	$Đ_t$	Purity (%)
1-Star	55	1.05	7.7$^{a)}$	1.3	8	28.5	1.08	90
1-Star	52	1.04	7.7$^{a)}$	1.3	15	26.0	1.08	92
1-Star	110	1.06	7.7$^{a)}$	1.3	10	27.0	1.17	92
3-Star	56	1.03	168$^{b)}$	1.16	8	32	1.26	98
4-Star	94	1.04	290$^{b)}$	1.35	7	33.9	1.2	96

Size elution chromatograms of all samples are shown in Figure 95 and Figure 96. The unreacted arms are separated by fractionation from cyclohexane and *iso*-propanol to obtain the purified product.
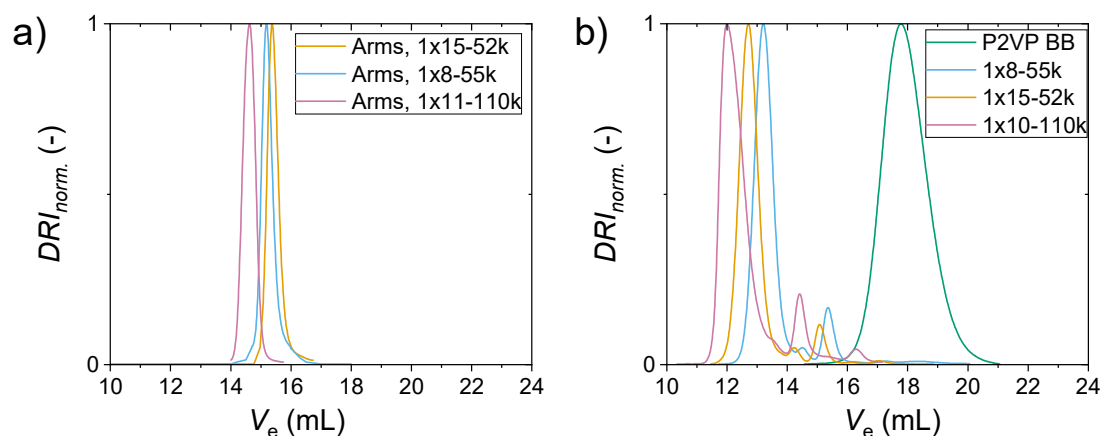
Figure 95: Elution chromatograms of the arm precursors before grafting in a) and the purified stars in b).
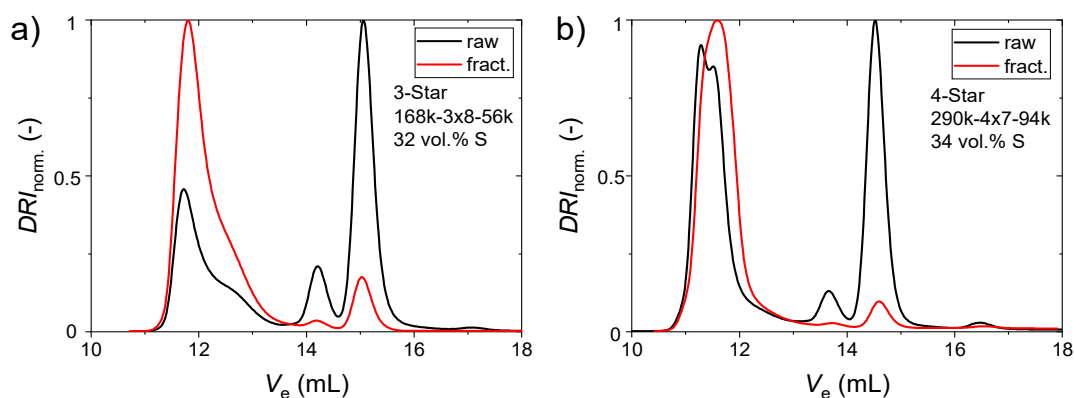
Figure 96: Elution chromatograms of the crude and fractionated product of the a) 3-Star and b) 4-Star samples.

8.2   Mechanical Testing

The influence of topology of branched block copolymer is investigated in this chapter. Two series with varying molecular parameters are investigated. The first series investigates the change from diblock to triblock to star block copolymer. In the second series, between one and four block copolymer stars are threaded along a backbone resulting in star, pom-pom, 3-Star and 4-Star architecture. The mechanical properties of the di- and triblock copolymer[239] and of the pom-pom[180] are taken from literature. All samples have similar ratios of styrene to isoprene.

For the first series, the strain at break ε_b and the ultimate tensile stress σ_{UTS} of these four samples are shown in Figure 97Figure 96 a). The diblock copolymer has the lowest σ_{UTS} and ε_b, slightly increasing for the triblock copolymer. For the star polymers, σ_{UTS} and ε_b is roughly double compared to the triblock copolymer, but no difference between eight and fifteen arms is found within the uncertainty of the experiment. Spencer and Matsen[240] used self-consistent

field theory simulations (SCFT) to predict the conformation probability distributions of block copolymer stars with a cylindrical morphology. They revealed that for stars with eight or more arms, only conformations occur where the arms are part of a minimum of two cylindrical phases. In Figure 97 b) a likely confirmation is shown on the left, where the arms are part of four grey phases. Connections between multiple phases are called bridges and are associated with high mechanical strength. The right star shows a very unlikely conformation (probability < 2 %) where all arms are part of the same cylindrical phase. Connections between only one phase are called loops and are associated with long mechanical strength. Within the uncertainty of the experiment, the predictions by the SCFT simulation can be confirmed by the experiment. Both methods show in agreement that for these stars with eight or more arms the mechanical properties of the block copolymer star stay constant and do not increase further. This suggests that for the design of block copolymers with high mechanical strength, a high arm number is beneficial, but the stress saturates above $q = 8$.
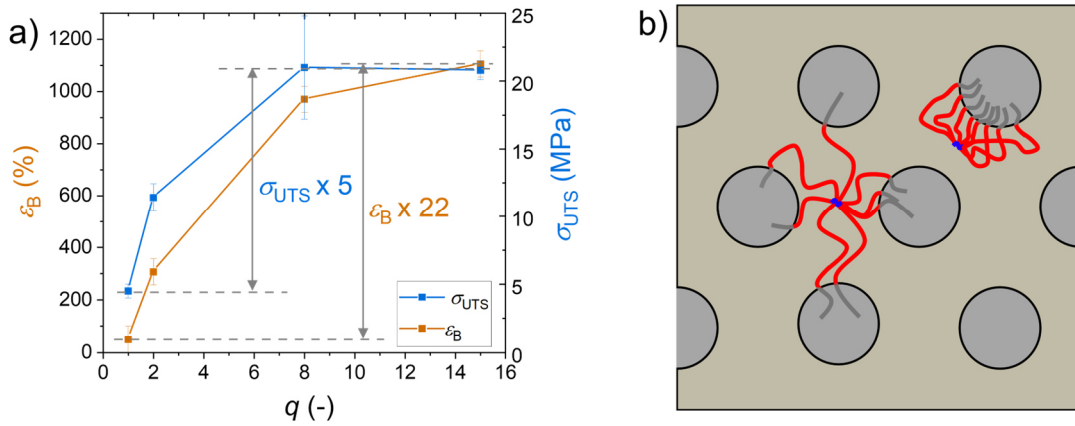
Figure 97: a) Strain at break ε_b and ultimate tensile stress σ_{UTS} shown as a function of the arm number for diblock (q = 1), triblock (q = 2), and two stars (q = 8, 15). b) Illustration of two possible conformations of a star block copolymer in a cylindrical morphology.

For the second series, the ultimate tensile stress σ_{UTS} is shown as a function of the number of threaded stars in Figure 98 a). While the two star and the 3-Star samples show similarly high σ_{UTS}, the pom-pom and 4-Star sample have increased σ_{UTS}. No clear trend can be identified. Since all samples have eight or more arms, all chains of the samples should form bridges as predicted by SCFT simulations. Therefore, the σ_{UTS} is analyzed as a function of the arm molecular weight. A clear trend can be observed where the σ_{UTS} increases with increasing arm molecular weight irrespective of the topology for eight or more arms. This suggests that the PS connector between the block copolymer stars does not contribute to the σ_{UTS} of the sample.
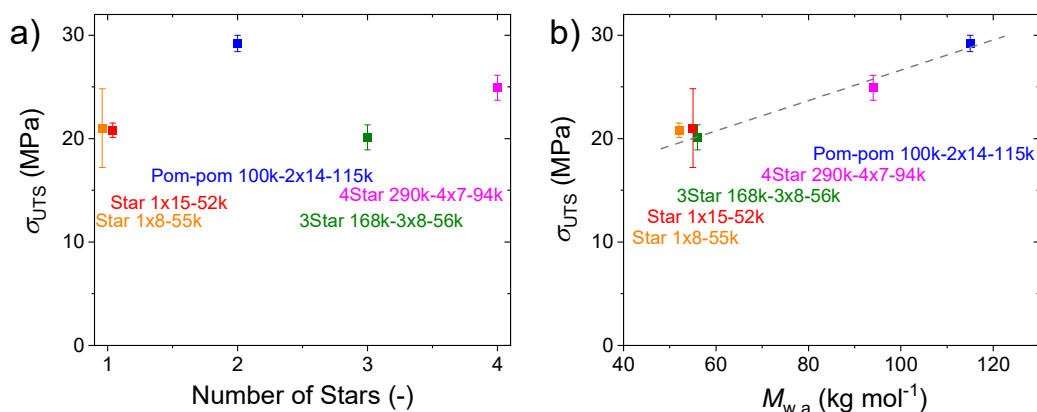
Figure 98: Ultimate tensile stress σ_{UTS} as a function of a) the threaded stars along the backbone and b) the arm molecular weight. Grey dashed line shown as a guide to the eye.

In Figure 99, literature data on other PS/PI block copolymer model systems is compared to the herein synthesized samples. In a) the σ_{UTS} and in b) the ε_b is shown as a function of the PI volume fraction ϕ_{PI}. A trend emerges, where most samples stay below a threshold of ~ 22 MPa. Only one sample from Weidisch *et al.*[241] and one pom-pom sample from Hirschberg *et al.*[180] as well as the 3-Star sample surpass this. This might be due to higher molecular weights of the outer PS block compared to other samples. As shown by the grey dotted line in b), the topology does not seem to influence the strain at break as all samples follow the same trend.
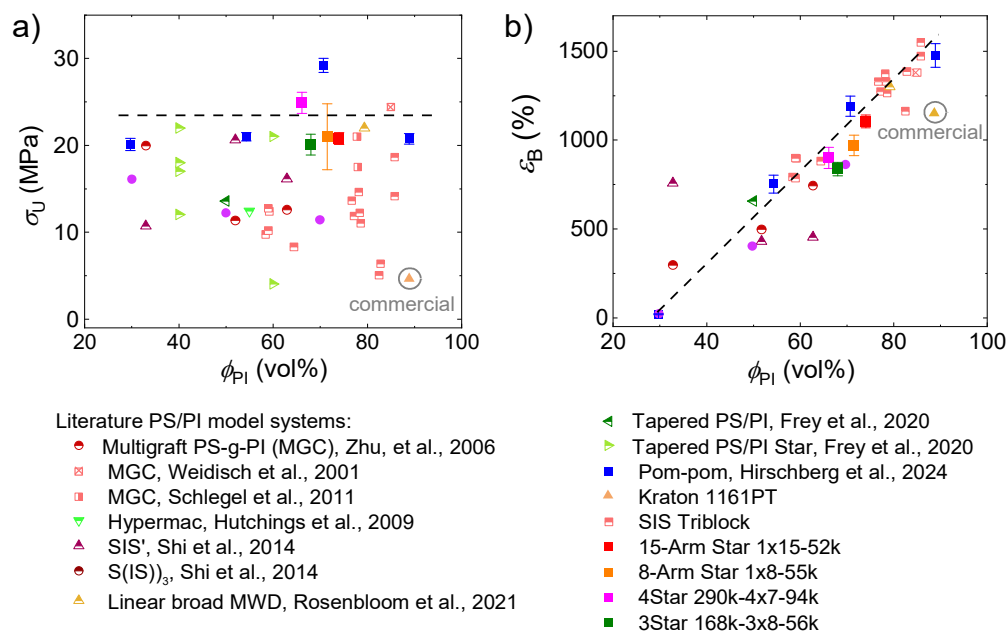
Figure 99: Strain at break ε_b and ultimate tensile stress σ_{UTS} shown as a function of PI volume fraction for the herein synthesized systems and data on other model systems from literature.[180,241–248]

In future works, the same threaded star topology may be synthesized using a PI connected between the star similar to the muli-graft copolymers by Weidisch *et al.*,[241] but with more arms

to increase the number of bridged hard phases even further and evaluate the influence on the tensile properties. Additionally, a larger range of arm molecular weights can be explored.

9   Conclusion and Outlook

In this thesis, the influence of complex branched topologies on the mechanical and rheological properties of homo and block copolymers was investigated. The investigations target the understanding of the dynamics of branched polymer melts fundamentally. A new synthesis strategy is developed to access well-defined branched structures easily and in large batches (> 300 g possible) due to a lack of existing well-defined branched materials. A large sample set of over 20 pom-poms was synthesized with systematic variations of molecular parameters (see schematic 1). A full rheological characterization of their flow properties in shear and uniaxial extension was conducted. Thereby, the largest rheological model data set on pom-poms was created. Using this data set, predictions made by the pom-pom model of McLeish and Larson[10] and derivation by McKinley and Hassager[85] in the late 1990s could be experimentally confirmed for the first time. A more detailed summary of the findings of this work and the conclusions is given in the following.
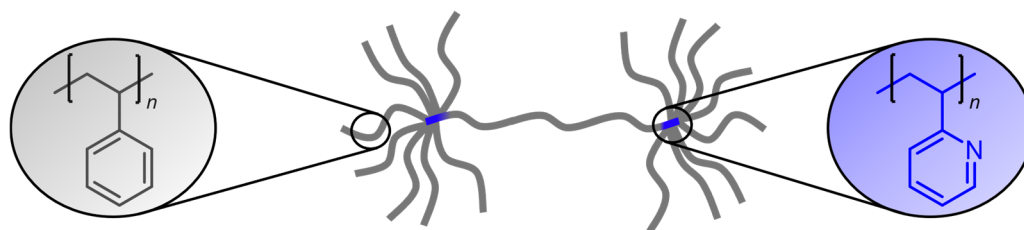
Schematic 1: Illustration of a pom-pom with eight arms at each end of the backbone. Pom-poms in this thesis are made of polystyrene (PS) shown in grey and the arms are attached using two short poly(2-vinylpyridine) blocks shown in blue at the end of the backbone.

Before the experimental work in this thesis, a review on previous works on defined branched systems with a focus on both their chromatographical and rheological characterization is given in chapter 5, page 30.

Anionic Synthesis

To enable the systematic rheological investigation of the pom-pom topology experimentally, twenty-one samples have been synthesized using two synthesis routes (chapter 6) over the past four years. Eleven samples were synthesized using an established synthesis route via an epoxide as the functional group in the branch point (epoxy route).[177] In this synthetic approach, anionic polymerization, post-polymerization modification (PPM), and grafting-onto techniques are utilized in a total of three reaction steps. Although a well-defined product is obtained, the PPM increases the synthesis time significantly and is prone to introduce impurities preventing the grafting onto in the third reaction step. To reduce complexity and synthetic effort, the P2VP route was developed. Herein, a poly(2-vinylpyridine-*b*-styrene-*b*-2-vinylpyridine) triblock copolymer (P2VP-*b*-PS-*b*-P2VP) is used as the backbone, followed by grafting onto the

pyridine rings of the short outer P2VP blocks. The route enables facile access in a two-step synthesis, eliminating the intermediate PPM step. The synthetic effort compared to the epoxy route is reduced by one third in respect to total time. For all 21 samples, the molecular parameters of homopolymer PS pom-poms were systematically varied for the backbone molecular weight $M_{w,b}$ = 100 – 400 kg mol^{-1}, the arm molecular weight $M_{w,a}$ = 2.5 – 300 kg mol^{-1}, and arm number q = 5 – 30. The P2VP route can also be used to synthesize block copolymers of PS and dienes. This was shown by the synthesis of three poly(styrene-*b*-isoprene) stars with varying arm molecular weight and arm number.

Beyond the synthetic work in this thesis, further possibilities of the P2VP route could be explored. The P2VP route could be used to synthesize additional topologies such as asymmetric stars, barbwire multigraft structures or Janus particles. As the P2VP Route is suitable for scale-up, analytical methods or applications which require larger amounts of sample could be conducted. Examples are capillary rheometers to access higher shear rates, foam extrusion or film blowing to investigate the use of defined branched topologies in more industry related applications. Similarly for block copolymers, previously unexplored, defined branched topologies could be synthesized and their mechanical properties investigated for their potentially higher strain and ultimate tensile stress. As the mechanical properties are highly influenced by the morphology, the phase separation in the bulk should be investigated by, e.g. small angle neutron scattering or transmission electron microscopy. Bridging between hard domains is mainly responsible for the mechanical strength of block copolymers. Topologies with a higher number of bridged hard domains per chain would be of interest here to make materials with a higher ultimate tensile stress. They might be synthesized through barbwire or multigraft topologies with high branching numbers. Additionally, the findings could be used to synthesize strong, biobased thermoplastic elastomers by replacing the crude oil based isoprene with myrcene or farnesene, for example.[249] Myrcene and farnesene are biobased dienes which can be extracted from pine trees.

Shear and Uniaxial Extensional Rheology

The rheological investigation of the homopolymer PS pom-poms was conducted in small amplitude oscillatory shear (SAOS), startup shear, and uniaxial extension to obtain a full characterization of the flow behavior of the pom-poms. The SAOS experiments of the pom-poms, which are discussed in chapter 7.1.1, page 61, revealed detailed insights into the relaxation behavior of the backbone and the arms. In a series of increasing backbone molecular weight from a star to pom-poms, the effect of dynamic dilution of the backbone by the arms could be demonstrated in the moduli. The longer the backbone, the slower the terminal relaxation and therefore crossover into the terminal regime is found at lower angular frequencies. The dilution modulus $G_{N,s}^0$ was found to scale quadratically with the backbone volume fraction for the pom-poms. The experimental findings for pom-poms confirm previously observed results from combs and oppose the theoretically predicted scaling exponent of 7/3. Analysis of the van Gurp Palmen plot (vGP) revealed two minima for all pom-poms with $M_{w,a} \geq M_e/2$. One minimum can be attributed to the arms and one to the backbone. The observation of two minima is characteristic for branched systems with many long branches. For $M_{w,a} < M_e/2$, no second minimum can be observed. When examining the second minima in

the vGP plot, a phase angle $\delta < 45\,°$ is found for effective backbone entanglements $Z_{b,eff} > 3$, indicating similar dynamic dilution of the backbone in the arms, resulting effective entanglement, and critical entanglement molecular weight as found for linear PS. Literature data reveals that a higher phase angle at the same $Z_{b,eff}$ is found for combs compared to pom-poms. This suggests that the arms of the combs dilute the backbone more than for pom-poms and therefore, the pom-pom melt is more elastic than combs in SAOS.

In startup shear, the polymer melt is subjected to a continuous shear deformation in one direction (simple shear). Startup shear results of pom-poms are discussed in chapter 7.1.2, page 69. Pom-poms generally show strong shear thinning. A stress overshoot can be observed before the steady state viscosity is reached as with other topologies such as linear, star, or comb. For the pom-poms, a scaling relation of the stress overshoot strain γ as a function of the Weissenberg number Wi of $\gamma^{0.5} \sim Wi$ was found in agreement with other highly branched samples and differing from linear chains ($\gamma^{1/3} \sim Wi$). For pom-poms, γ is only dependent on the arm molecular weight and independent of arm number and backbone molecular weight. This suggests that backbone orientation into the shear direction is mainly caused by the drag of the stars at the end of the backbone. For one pom-pom (100k-2x12-40k), two stress overshoots were observed at high shear rates for the first time. Analysis of the stress overshoot strain as a function of the shear rate suggests, that the first overshoot is a result of arm orientation and the second of backbone orientation and stretch. The observation of two stress overshoots has only been reported previously for one comb and one bidisperse linear sample suggesting that the phenomenon of two stress overshoots is universal for samples with two sufficiently separated relaxation times. The Cox-Merz rule is an empirical rule which states that the steady state shear viscosity is the same as the absolute magnitude of the complex viscosity $\eta(\dot{\gamma}) = |\eta^*(\omega)||_{\dot{\gamma}=\omega}$. The Cox-Merz rule is found to fail for pom-poms with $Z_{b,eff} < 3$, with the highest deviation around the backbone phase angle minimum $\delta_{b,min}$.

In the future, the investigations on the pom-poms in startup shear could be expanded. As discussed, the normal force capabilities of the current set-up using a 10 mm cone partitioned plate geometry (CPP) limit the measurable shear rates, especially for longer backbones due to the high elasticity of the melt. The measurement range could be expanded with the use of a small CPP, e.g. with 5 mm diameter.[45] Alternatively, the standard 10 mm CPP could be used on a rheometer with a higher normal force capacity. When the measurable shear rates are increased, shear instabilities might be an issue to reproducible measurements. Further techniques to delay instabilities like edge fracture could be implemented as described by Li *et al*.[250]

Uniaxial extensional experiments for the pom-poms are discussed in chapter 7.1.3, page 76. In general, pom-poms show high strain hardening due to their high branching number. For the extensional viscosity, four Weissenberg dependent regimes could be identified that allow the prediction of the extensional viscosity η_E solely based on the linear viscoelastic envelope (LVE) and the molecular parameters of the pom-pom, see schematic 2. Regime I is found for $Wi < 1$ and herein η_E coincides with the LVE. Regime II is found for $1 < Wi < Wi_{\delta,b,min}$. The extensional viscosity increases above the LVE and reaches its maximum at $Wi_{\delta,b,min}$ for all

samples. Regime III is found for $Wi_{\delta,b,min} < Wi < Wi_{\dot{\varepsilon},frac}$. In this regime, η_E is found above the LVE by the Considère factor $f_c = q^2/\ln(\sqrt{3}q)$. The extensional viscosity can be predicted solely based on the arm number of the pom-poms. Experimentally, we observe that the Considère factor f_c is equal to the maximum strain hardening factor $f_c = SHF_{max}$, which is commonly used in industry to compare strain hardening between samples and conditions and can therefore be calculated solely based on the branching number as well. Regime IV can be found for $Wi > Wi_{\dot{\varepsilon},frac}$. The strain rate is so high that the polymer chains cannot relax at all, and the melt fractures like a solid. We can experimentally confirm that a maximum fracture stress exists, $\sigma_E^{Fracture} = 2 \; 10^7$ Pa, previously only theoretically predicted. These four Wi-dependent regimes can be found for all pom-poms with $Z_{b,eff} > 3, q \gtrsim 5, M_{w,a} \geq M_e/2$. The herein observed strain hardening behavior is characteristic for long chain branching (LCB). Short chain branching (SCB) is known to cause no strain hardening. A series of pom-poms with increasing arm molecular weight was synthesized and strain hardening was found for $M_{w,a} \geq M_e/2$ and high arm numbers ($q = 30$). Extensional thinning at $Wi = 0.1 - 5$ was found for arms as short as $M_{w,a} = M_e/4$. Therefore, the data of the investigated PS pom-poms suggests that LCB can be assumed for $M_{w,a} \geq M_e/2$ and SCB for shorter branches.
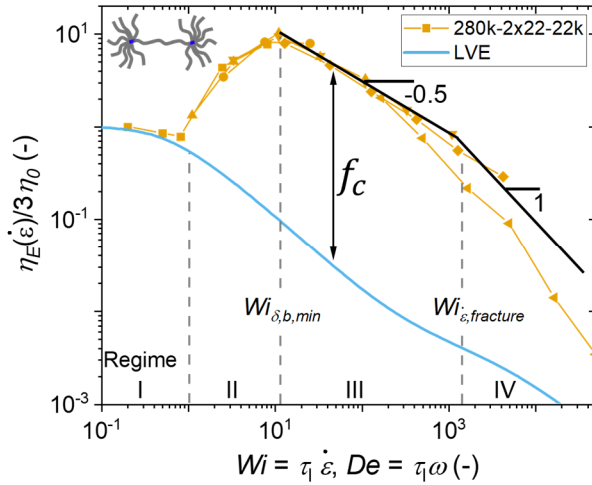
Schematic 2: Extensional viscosity η_E normalized by three times the zero-shear viscosity η_0 shown as the function of the Weissenberg number Wi and LVE shown as a function of the Deborah number De for the pom-pom 280k-2x22-22k. Right side shows the found relations between LVE and the extensional viscosity using the Considère factor f_c solely based on the arm number as well as the experimentally found relation for the maximum strain hardening factor $SHF_{max} = f_c$.

A strain hardening optimized pom-pom would use $Z_{b,eff} = 3$ and $M_{w,a} = M_e/2$. Using a PS backbone of 200 kg mol⁻¹, about 35 arms per pom / 70 arms total would be possible resulting in a maximum strain hardening factor of 298. When a longer PS backbone of 300 kg mol⁻¹ is used, a maximum arm number of 88 / 176 arms total and a resulting maximum strain hardening factor of 1540 would be possible.

Combining the findings from SAOS and extension (chapter 7.1.4, page 88), it becomes clear that backbone and arm molecular weight and their ratio is pivotal for the relaxation behavior of the pom-poms. If the arms are longer than the backbone ($M_{w,a} > M_{w,b}$), the flow behavior of a

pom-pom is similar to that of a star. For the opposite where the arms are much shorter than the backbone ($M_{w,b} \gg M_{w,a}$, $M_{w,a} < M_{w,e}/2$), the relaxation behavior of a pom-pom is similar to a linear chain. In between, where the backbone is longer than the arms, the characteristic pom-pom relaxation behavior can be observed with two distinct relaxation times and strong strain hardening. For pom-poms and for combs, as shown by literature data analysis, the flow behavior can be predicted based on the molecular properties and the LVE. For $Z_{b,eff} > 3$, the extensional viscosity can be predicted by the Considère limit and the shear viscosity by the Cox-Merz rule. For $Z_{b,eff} < 3$, the extensional viscosity is found below the prediction of the Considère limit, and the shear viscosity is higher than predicted by Cox-Merz.

Although some significant advances have been made to the understanding of the effect of branches, many topics remain unexplored. The flow behavior of defined branched polymers with low dispersity is well understood and can be quantitatively predicted by models. To move closer to the understanding of the flow behavior of randomly branched polymers like LDPE, which are common in industry, mixtures of well-defined systems could be a first step to move from well-defined polymers to more ill-defined samples. To project the distribution of arm lengths in LDPE, pom-poms with different arm molecular weights and constant remaining molecular parameters could be mixed and rheologically characterized.

The extensional viscosity of super H-shaped polymers or pom-poms with low arm number (chapter 7.1.3, page 76) and multistars (chapter 7.2, page 90), where multiple stars are threaded along a backbone, was found to be higher than predicted by the Considère limit. It should be investigated in the future whether this is a result of the topology, or the mixture of different species found in the samples.

An analysis of a pom-pom and a bidisperse linear blend (chapter 7.4, page 96) with the same SAOS mastercurve and vGP plots reveals that branching cannot be detected solely based on measurements in the linear regime. To detect branching, a monomodal molecular weight distribution and a vGP plot with two minima is needed. Uniaxial extension reveals differences in the extensional viscosity, showing higher strain hardening especially at lower strain rates for branched chains.

Constitutive Modelling

The experimental extensional data of the pom-poms was compared to calculated data based on two constitutive models, the pom-pom model and the extended hierarchical multimode molecular stress function model (EHMMSF). The results are shown in chapter 7.5, page 99. Calculations of the EHMMSF model are kindly provided by Prof. Manfred Wagner. For the pom-pom constitutive model, significant differences between the experimental and calculated data are revealed. Significant differences in the relaxation spectrum and therefore in the extensional stress arise due to the assumption in the pom-pom model on the arms. In the pom-pom model, it is assumed that the arms are always relaxed and therefore do not contribute to the stress response resulting in the differences between theoretical and experimental extensional stress. The higher the arm volume fraction, the higher the difference. The EHMMSF model can predict the extensional stress based on the relaxation spectrum e.g. obtained from SAOS. The

calculated extensional stress is in quantitative agreement with the experimental data over the whole investigated range. This agreement shows that the information about the nonlinear response of branched polymers is included in the linear relaxation spectrum and the EHMMSF model can use it to correctly predict the nonlinear response.

Sentmanat extensional rheometer fixtures (SER) are widely used as they can be mounted onto commercial rotation rheometers and are easy to operate. Extensional measurements are limited to a Hencky strain of $\varepsilon = 4$ due to sample overlap after one revolution of the geometry. A new measurement protocol has been investigated within this thesis to increase the maximum strain by superposition of vertical travel of the upper geometry and rotation of the lower geometry (chapter 7.6, page 101). With this adapted procedure, sample overlap after one revolution is avoided and the maximum Hencky strain could be extended up to $\varepsilon = 8.3$ before sample fracture as demonstrated for a highly branched comb sample.

Block Copolymers

The mechanical properties of block copolymers are highly dependent on their molecular structure. Using the epoxy and the P2VP route, PS-PI block copolymers were synthesized with a star, 3-Star and 4-Star topology. Tensile testing was conducted for all samples and compared with literature data. From diblocks to triblock to stars, the ultimate tensile stress increases sharply, leveling off at eight and more arms. No influence of the number of threaded stars (star, pom-pom, 3-Star, 4-Star) on the ultimate tensile stress could be observed but scaling linearly with the arm molecular weight independently of the topology. Detailed characterization of the phase separation will be conducted in the future.

Bibliography

[1]   F. Röthemeyer, F. Sommer, *Kautschuk Technologie: Werkstoffe – Verarbeitung – Produkte*, Carl Hanser Verlag GmbH & Co. KG, München, **2013**.

[2]   H. Ringsdorf, *Angewandte Chemie International Edition* **2004**, *43*, 1064–1076.

[3]   M. Wilhelm, in *Hierarchical Macromolecular Structures: 60 Years after the Staudinger Nobel Prize I* (Ed.: V. Percec), Springer International Publishing, Cham, **2013**, pp. 53–60.

[4]   H. Staudinger, **1953**.

[5]   D. Feldman, **2008**, *11*, 1–15.

[6]   E. Saldívar-Guerra, E. Vivaldo-Lima, Eds. , *Handbook of Polymer Synthesis, Characterization, and Processing*, Wiley, Hoboken New Jersey, **2013**.

[7]   N. Hadjichristidis, A. Hirao, *Anionic Polymerization: Principles, Practice, Strength, Consequences and Applications*, Springer Tokyo, Tokyo, **2015**.

[8]   Plastics Europe, *Plastics - the Fast Facts 2024*, **2025**.

[9]   T. Ishizone, R. Goseki, in *Encyclopedia of Polymeric Nanomaterials* (Eds.: S. Kobayashi, K. Müllen), Springer, Berlin, Heidelberg, **2015**, pp. 23–33.

[10]   T. C. B. McLeish, R. G. Larson, *Journal of Rheology* **1998**, *42*, 81–110.

[11]   G. Bishko, T. C. B. McLeish, O. G. Harlen, R. G. Larson, *Phys. Rev. Lett.* **1997**, *79*, 2352–2355.

[12]   J. K. Nielsen, H. K. Rasmussen, M. Denberg, K. Almdal, O. Hassager, *Macromolecules* **2006**, *39*, 8844–8853.

[13]   D. M. Knauss, T. Huang, *Macromolecules* **2002**, *35*, 2055–2062.

[14]   T. I. U. of P. and A. Chemistry (IUPAC), "IUPAC - macromolecule (M03667)," DOI 10.1351/goldbook.M03667can be found under https://goldbook.iupac.org/terms/view/M03667, **n.d.**

[15]   H. Ringsdorf, *Angewandte Chemie International Edition* **2004**, *43*, 1064–1076.

[16]   M. Szwarc, *Nature* **1956**, *178*, 1168–1169.

[17]   R. P. Quirk, in *Polymer Science: A Comprehensive Reference* (Eds.: K. Matyjaszewski, M. Möller), Elsevier, Amsterdam, **2012**, pp. 559–590.

[18]   H. Frey, T. Ishizone, *Macromolecular Chemistry and Physics* **2017**, *218*, 1700217.

[19]   K. Matyjaszewski, A. H. E. Müller, *Controlled and Living Polymerizations: Methods and Materials*, Wiley-VCH, Weinheim, **2009**.

[20]   G. Fraenkel, M. Henrichs, M. Hewitt, B. M. Su, *J. Am. Chem. Soc.* **1984**, *106*, 255–256.

[21]   Walter. Bauer, W. R. Winchester, P. V. R. Schleyer, *Organometallics* **1987**, *6*, 2371–2379.

[22]   W. Lee, H. Lee, J. Cha, T. Chang, K. J. Hanley, T. P. Lodge, *Macromolecules* **2000**, *33*, 5111–5115.

[23]   N. Hadjichristidis, M. Pitsikalis, S. Pispas, H. Iatrou, *Chemical reviews* **2001**, *101*, 3747–3792.

[24]   D. J. Read, D. Auhl, C. Das, J. den Doelder, M. Kapnistos, I. Vittorias, T. C. B. McLeish, *Science (New York, N.Y.)* **2011**, *333*, 1871–1874.

[25]   C. Weber, C. Remzi Becer, W. Guenther, R. Hoogenboom, U. S. Schubert, *Macromolecules* **2010**, *43*, 160–167.

[26]   M. Meier-Merziger, M. Fickenscher, F. Hartmann, B. Kuttich, T. Kraus, M. Gallei, H. Frey, *Polym. Chem.* **2023**, 2820–2828.

[27]   J. M. Ren, T. G. McKenzie, Q. Fu, E. H. H. Wong, J. Xu, Z. An, S. Shanmugam, T. P. Davis, C. Boyer, G. G. Qiao, *Chemical reviews* **2016**, *116*, 6743–6836.

[28] N. Corrigan, K. Jung, G. Moad, C. J. Hawker, K. Matyjaszewski, C. Boyer, *Progress in Polymer Science* **2020**, *111*, 101311.

[29] H. A. Barnes, *A Handbook of Elementary Rheology*, University Of Wales Institute Of Non-Newtonian Fluid Mechanics, Aberystwyth, **2000**.

[30] J. M. Dealy, D. J. Read, R. G. Larson, in *Structure and Rheology of Molten Polymers* (Eds.: J.M. Dealy, D.J. Read, R.G. Larson), Carl Hanser Verlag GmbH & Co. KG, München, **2018**, p. I–XVII.

[31] H. Münstedt, F. R. Schwarzl, *Deformation and Flow of Polymeric Materials*, Springer, Berlin, Heidelberg, **2014**.

[32] U. Eisele, *Introduction to Polymer Physics*, Springer, **2012**.

[33] Ad Hoc Committee on Official Nomenclature and Symbols, *Journal of Rheology* **2013**, *57*, 1047–1055.

[34] C. Iacob, M. Heck, M. Wilhelm, *Macromolecules* **2023**, *56*, 188–197.

[35] J. D. Ferry, *Viscoelastic Properties of Polymers*, Wiley, New York, **1980**.

[36] E. van Ruymbeke, M. Kapnistos, D. Vlassopoulos, T. Huang, D. M. Knauss, *Macromolecules* **2007**, *40*, 1713–1719.

[37] M. van Gurp, J. Palmen, *Rheology Bulletin* **1998**.

[38] L. J. Fetters, D. J. Lohse, S. T. Milner, W. W. Graessley, *Macromolecules* **1999**, *32*, 6847–6851.

[39] S. Trinkle, C. Friedrich, *Rheol. Acta* **2001**, *40*, 322–328.

[40] S. Trinkle, P. Walter, C. Friedrich, *Rheol. Acta* **2002**, *41*, 103–113.

[41] D. J. Lohse, S. T. Milner, L. J. Fetters, M. Xenidou, N. Hadjichristidis, R. A. Mendelson, C. A. Garcia-Franco, M. K. Lyon, *Macromolecules* **2002**, *35*, 3066–3075.

[42] S. Jeong, J. M. Kim, C. Baig, *Macromolecules* **2017**, *50*, 3424–3429.

[43] Th. Schweizer, *Journal of Rheology* **2003**, *47*, 1071–1085.

[44] F. Snijkers, D. Vlassopoulos, *Journal of Rheology* **2011**, *55*, 1167–1186.

[45] S. Costanzo, G. Ianniruberto, G. Marrucci, D. Vlassopoulos, *Rheologica Acta* **2018**, *57*, 363–376.

[46] W. P. Cox, E. H. Merz, *Journal of Polymer Science* **1958**, *28*, 619–622.

[47] H. C. Booij, P. Leblans, J. Palmen, G. Tiemersma-Thoone, *Journal of Polymer Science: Polymer Physics Edition* **1983**, *21*, 1703–1711.

[48] H. H. Winter, *Rheol Acta* **2009**, *48*, 241–243.

[49] Y. H. Shim, J. J. Griebler, S. A. Rogers, *Journal of Rheology* **2024**, *68*, 381–396.

[50] J. D. J. Rathinaraj, B. Keshavarz, G. H. McKinley, *Physics of Fluids* **2022**, *34*, 033106.

[51] F. Snijkers, D. Vlassopoulos, *Rheol Acta* **2014**, *53*, 935–946.

[52] RogerI. Tanner, E. Tanner, *Rheologica Acta* **2003**, *42*, 93–101.

[53] P. G. de Gennes, *The Journal of Chemical Physics* **1971**, *55*, 572–579.

[54] M. Doi, S. F. Edwards, *Journal of the Chemical Society, Faraday Transactions 2: Molecular and Chemical Physics* **1978**, *74*, 1789–1801.

[55] M. Doi, S. F. Edwards, *The Theory of Polymer Dynamics*, Clarendon Press, Oxford, **2013**.

[56] H. Watanabe, *Progress in Polymer Science* **1999**, *24*, 1253–1403.

[57] T. C. B. McLeish, *Advances in Physics* **2002**, *51*, 1379–1527.

[58] G. Marrucci, *Journal of Polymer Science: Physics Edition* **1985**, *23*, 159–177.

[59] M. J. Struglinski, W. W. Graessley, *Macromolecules* **1985**, *18*, 2630–2643.

[60] S. T. Milner, T. C. B. McLeish, R. N. Young, A. Hakiki, J. M. Johnson, *Macromolecules* **1998**, *31*, 9345–9353.

[61] Z. Wang, X. Chen, R. G. Larson, *Journal of Rheology* **2010**, *54*, 223–260.

[62] M. Kapnistos, D. Vlassopoulos, J. Roovers, L. G. Leal, *Macromolecules* **2005**, *38*, 7852–7862.

[63] S. T. Milner, T. C. B. McLeish, *Macromolecules* **1997**, *30*, 2159–2166.

[64]   C. Das, N. J. Inkson, D. J. Read, M. A. Kelmanson, T. C. B. McLeish, *Journal of Rheology* **2006**, *50*, 207–234.

[65]   R. G. Larson, *Macromolecules* **2001**, *34*, 4556–4571.

[66]   E. van Ruymbeke, Y. Masubuchi, H. Watanabe, *Macromolecules* **2012**, *45*, 2085–2098.

[67]   E. van Ruymbeke, E. B. Muliawan, S. G. Hatzikiriakos, T. Watanabe, A. Hirao, D. Vlassopoulos, *Journal of Rheology* **2010**, *54*, 643–662.

[68]   H. Watanabe, Y. Matsumiya, E. van Ruymbeke, *Macromolecules* **2013**, *46*, 9296–9312.

[69]   H. Watanabe, S. Ishida, Y. Matsumiya, T. Inoue, *Macromolecules* **2004**, *37*, 6619–6631.

[70]   D. R. Daniels, T. C. B. McLeish, B. J. Crosby, R. N. Young, C. M. Fernyhough, *Macromolecules* **2001**, *34*, 7025–7033.

[71]   T. C. B. McLeish, J. Allgaier, D. K. Bick, G. Bishko, P. Biswas, R. Blackwell, B. Blottière, N. Clarke, B. Gibbs, D. J. Groves, A. Hakiki, R. K. Heenan, J. M. Johnson, R. Kant, D. J. Read, R. N. Young, *Macromolecules* **1999**, *32*, 6734–6758.

[72]   N. J. Inkson, T. C. B. McLeish, O. G. Harlen, D. J. Groves, *Journal of Rheology* **1999**, *43*, 873–896.

[73]   H. Lentzakis, C. Das, D. Vlassopoulos, D. J. Read, *Journal of Rheology* **2014**, *58*, 1855–1875.

[74]   S. Coppola, F. Bacchelli, G. Marrucci, G. Ianniruberto, *Journal of Rheology* **2014**, *58*, 1877–1901.

[75]   W. M. H. Verbeeten, G. W. M. Peters, F. P. T. Baaijens, *Journal of Rheology* **2001**, *45*, 823–843.

[76]   L. G. D. Hawke, Q. Huang, O. Hassager, D. J. Read, *Journal of Rheology* **2015**, *59*, 995–1017.

[77]   Q. Huang, M. Mangnus, N. J. Alvarez, R. Koopmans, O. Hassager, *Rheol Acta* **2016**, *55*, 343–350.

[78]   Y. Wang, A. Goecke, V. Hirschberg, Y. Zhong, S. Liu, M. Wilhelm, Q. Huang, *ACS Macro Lett.* **2024**, 812–817.

[79]   A. Ya. Malkin, C. J. S. Petrie, *Journal of Rheology* **1997**, *41*, 1–25.

[80]   F. N. Cogswell, D. R. Moore, *Polymer Engineering and Science* **1974**, *14*, 573–576.

[81]   C. J. S. Petrie, *Chemical Engineering Science* **2009**, *64*, 4693–4700.

[82]   M. Considére, *Mémoire sur l'emploi du fer et de l'acier dans les constructions* **n.d.**

[83]   D. M. Hoyle, S. M. Fielding, *Journal of Rheology* **2016**, *60*, 1347–1375.

[84]   S. M. Fielding, *Physical review letters* **2011**, *107*, 258301.

[85]   G. H. McKinley, O. Hassager, *Journal of Rheology* **1999**, *43*, 1195–1212.

[86]   M. G. Schußmann, M. Wilhelm, V. Hirschberg, *Nature Communications* **2024**, *15*, 3545.

[87]   M. H. Wagner, V. H. Rolón-Garrido, *Journal of Rheology* **2008**, *52*, 1049–1068.

[88]   E. Ducrot, Y. Chen, M. Bulters, R. P. Sijbesma, C. Creton, *Science* **2014**, *344*, 186–189.

[89]   Q. Huang, O. Hassager, J. Madsen, *Macromolecules* **2022**, *55*, 9431–9441.

[90]   M. H. Wagner, E. Narimissa, Q. Huang, *Journal of Rheology* **2021**, *65*, 311–324.

[91]   V. H. Rolón-Garrido, *Rheol Acta* **2014**, *53*, 663–700.

[92]   M. H. Wagner, *Rheol Acta* **1976**, *15*, 136–142.

[93]   E. Narimissa, M. H. Wagner, *Rheol Acta* **2016**, *55*, 633–639.

[94]   M. H. Wagner, E. Narimissa, Q. Huang, *Rheologica Acta* **2022**, *61*, 415–425.

[95]   M. H. Wagner, S. Liu, Q. Huang, *Rheol Acta* **2024**, 573–584.

[96]   V. Hirschberg, M. G. Schußmann, M.-C. Röpert, M. Wilhelm, M. H. Wagner, *Rheologica Acta* **2023**, *62*, 269–283.

[97]   E. Narimissa, M. H. Wagner, *Journal of Rheology* **2016**, *60*, 625–636.

[98]   E. Narimissa, M. H. Wagner, *Polymer Engineering & Science* **2019**, *59*, 573–583.

[99]   V. Hirschberg, L. Faust, M. Abbasi, Q. Huang, M. Wilhelm, M. H. Wagner, *Journal of Rheology* **2024**, *68*, 229–246.

[100] V. Hirschberg, M. G. Schußmann, M.-C. Röpert, A. Goecke, M. Wilhelm, M. H. Wagner, *Rheol Acta* **2024**, *63*, 407–422.

[101] S. (刘双) Liu, M. H. Wagner, T. (崔腾) Cui, Q. (黄茜) Huang, *Physics of Fluids* **2024**, *36*, 093124.

[102] M. H. Wagner, *Rheol Acta* **2024**, *63*, 787–799.

[103] M. H. Wagner, H. Bastian, P. Hachmann, J. Meissner, S. Kurzbeck, H. Münstedt, F. Langouche, *Rheologica Acta* **2000**, *39*, 97–109.

[104] M. H. Wagner, V. Hirschberg, *Macromolecules* **2024**, 2110–2118.

[105] L. Faust, M. Röpert, M. K. Esfahani, M. Abbasi, V. Hirschberg, M. Wilhelm, *Macromolecular Chemistry and Physics* **2023**, *224*, 2200214.

[106] M. Abbasi, L. Faust, K. Riazi, M. Wilhelm, *Macromolecules* **2017**, *50*, 5964–5977.

[107] M. Abbasi, L. Faust, M. Wilhelm, *Polymer* **2020**, *193*, 122351.

[108] M. Abbasi, L. Faust, M. Wilhelm, *Polymer* **2020**, *193*, 122354.

[109] K. Riazi, J. Kübel, M. Abbasi, K. Bachtin, S. Indris, H. Ehrenberg, R. Kádár, M. Wilhelm, *Polymer* **2016**, *104*, 240–250.

[110] H. Y. Song, L. Faust, J. Son, M. Kim, S. J. Park, S. Ahn, M. Wilhelm, K. Hyun, *Polymers* **2020**, *12*, 365.

[111] P. Chambon, C. M. Fernyhough, K. Im, T. Chang, C. Das, J. Embery, T. C. B. McLeish, D. J. Read, *Macromolecules* **2008**, *41*, 5869–5875.

[112] C. M. Fernyhough, R. N. Young, D. Poche, A. W. Degroot, F. Bosscher, *Macromolecules* **2001**, *34*, 7034–7041.

[113] N. J. Inkson, R. S. Graham, T. C. B. McLeish, D. J. Groves, C. M. Fernyhough, *Macromolecules* **2006**, *39*, 4217–4227.

[114] F. Shahsavan, J. Keller, M. Wilhelm, K. Saalwächter, *Macromolecules* **2024**, *57*, 11030–11041.

[115] Z. Yuan, M. Gauthier, *Macromolecules* **2005**, *38*, 4124–4132.

[116] E. van Ruymbeke, H. Lee, T. Chang, A. Nikopoulou, N. Hadjichristidis, F. Snijkers, D. Vlassopoulos, *Soft matter* **2014**, *10*, 4762–4777.

[117] A. Nikopoulou, H. Iatrou, D. J. Lohse, N. Hadjichristidis, *Journal of Polymer Science Part A: Polymer Chemistry* **2009**, *47*, 2597–2607.

[118] F. Snijkers, K. M. Kirkwood, D. Vlassopoulos, L. G. Leal, A. Nikopoulou, N. Hadjichristidis, S. Coppola, *Journal of Rheology* **2016**, *60*, 451–463.

[119] D. Pantazis, I. Chalari, N. Hadjichristidis, *Macromolecules* **2003**, *36*, 3783–3785.

[120] A. Vazaios, N. Hadjichristidis, *Journal of Polymer Science Part A: Polymer Chemistry* **2005**, *43*, 1038–1048.

[121] J. H. Lee, P. Driva, N. Hadjichristidis, P. J. Wright, S. P. Rucker, D. J. Lohse, *Macromolecules* **2009**, *42*, 1392–1399.

[122] M. Ahmadi, C. Bailly, R. Keunings, M. Nekoomanesh, H. Arabi, E. van Ruymbeke, *Macromolecules* **2011**, *44*, 647–659.

[123] G. Koutalas, H. Iatrou, D. J. Lohse, N. Hadjichristidis, *Macromolecules* **2005**, *38*, 4996–5001.

[124] A. Vazaios, D. J. Lohse, N. Hadjichristidis, *Macromolecules* **2005**, *38*, 5468–5474.

[125] K. M. Kirkwood, L. G. Leal, D. Vlassopoulos, P. Driva, N. Hadjichristidis, *Macromolecules* **2009**, *42*, 9592–9608.

[126] A. Zografos, H. A. All, A. B. Chang, M. A. Hillmyer, F. S. Bates, *Macromolecules* **2023**, 2406–2417.

[127] M. Kempf, V. C. Barroso, M. Wilhelm, *Macromolecular Rapid Communications* **2010**, *31*, 2140–2145.

[128] M. Kempf, D. Ahirwal, M. Cziep, M. Wilhelm, *Macromolecules* **2013**, *46*, 4978–4994.

[129] M. H. Wagner, J. Hepperle, H. Münstedt, *Journal of Rheology* **2004**, *48*, 489–503.

[130] J. Hepperle, H. Münstedt, P. K. Haug, C. D. Eisenbach, *Rheol Acta* **2005**, *45*, 151–163.

[131] J. Hepperle, H. Münstedt, *Rheologica Acta* **2006**, *45*, 717–727.
[132] F. Snijkers, D. Vlassopoulos, G. Ianniruberto, G. Marrucci, H. Lee, J. Yang, T. Chang, *ACS Macro Letters* **2013**, *2*, 601–604.
[133] K. Hyun, M. Wilhelm, *Macromolecules* **2009**, *42*, 411–422.
[134] M. Kapnistos, G. Koutalas, N. Hadjichristidis, J. Roovers, D. J. Lohse, D. Vlassopoulos, *Rheol Acta* **2006**, *46*, 273–286.
[135] J. Roovers, P. M. Toporowski, *Macromolecules* **1987**, *20*, 2300–2306.
[136] F. Snijkers, D. Vlassopoulos, H. Lee, J. Yang, T. Chang, P. Driva, N. Hadjichristidis, *Journal of Rheology* **2013**, *57*, 1079–1100.
[137] J. Roovers, *Polymer* **1979**, *20*, 843–849.
[138] H. Lentzakis, D. Vlassopoulos, D. J. Read, H. Lee, T. Chang, P. Driva, N. Hadjichristidis, *Journal of Rheology* **2013**, *57*, 605–625.
[139] G. Liu, H. Ma, H. Lee, H. Xu, S. Cheng, H. Sun, T. Chang, R. P. Quirk, S.-Q. Wang, *Polymer* **2013**, *54*, 6608–6616.
[140] G. Liu, S. Cheng, H. Lee, H. Ma, H. Xu, T. Chang, R. P. Quirk, S.-Q. Wang, *Phys. Rev. Lett.* **2013**, *111*, 068302.
[141] M. Ahmadi, S. Pioge, C.-A. Fustin, J.-F. Gohy, E. van Ruymbeke, *Soft Matter* **2017**, *13*, 1063–1073.
[142] N. Hadjichristidis, M. Xenidou, H. Iatrou, M. Pitsikalis, Y. Poulos, A. Avgeropoulos, S. Sioula, S. Paraskeva, G. Velis, D. J. Lohse, D. N. Schulz, L. J. Fetters, P. J. Wright, R. A. Mendelson, C. A. García-Franco, T. Sun, C. J. Ruff, *Macromolecules* **2000**, *33*, 2424–2436.
[143] E. van Ruymbeke, K. Orfanou, M. Kapnistos, H. Iatrou, M. Pitsikalis, N. Hadjichristidis, D. J. Lohse, D. Vlassopoulos, *Macromolecules* **2007**, *40*, 5941–5952.
[144] J. H. Lee, K. Orfanou, P. Driva, H. Iatrou, N. Hadjichristidis, D. J. Lohse, *Macromolecules* **2008**, *41*, 9165–9178.
[145] K. Orfanou, H. Iatrou, D. J. Lohse, N. Hadjichristidis, *Macromolecules* **2006**, *39*, 4361–4365.
[146] I. Chalari, N. Hadjichristidis, *Journal of Polymer Science Part A: Polymer Chemistry* **2002**, *40*, 1519–1526.
[147] H. Watanabe, Y. Matsumiya, E. van Ruymbeke, D. Vlassopoulos, N. Hadjichristidis, *Macromolecules* **2008**, *41*, 6110–6124.
[148] N. Haraguchi, A. Hirao, *Macromolecules* **2003**, *36*, 9364–9372.
[149] A. Hirao, T. Watanabe, K. Ishizu, M. Ree, S. Jin, K. S. Jin, A. Deffieux, M. Schappacher, S. Carlotti, *Macromolecules* **2009**, *42*, 682–693.
[150] Q. Huang, S. Costanzo, C. Das, D. Vlassopoulos, *Journal of Rheology* **2017**, *61*, 35–47.
[151] S. M. Kimani, L. R. Hutchings, *Macromolecular Rapid Communications* **2008**, *29*, 633–637.
[152] L. R. Hutchings, S. J. Roberts-Bleming, *Macromolecules* **2006**, *39*, 2144–2152.
[153] L. R. Hutchings, S. M. Kimani, D. M. Hoyle, D. J. Read, C. Das, T. C. B. McLeish, T. Chang, H. Lee, D. Auhl, *ACS Macro Letters* **2012**, *1*, 404–408.
[154] D. M. Knauss, T. Huang, *Macromolecules* **2003**, *36*, 6036–6042.
[155] S. Perny, J. Allgaier, D. Cho, W. Lee, T. Chang, *Macromolecules* **2001**, *34*, 5408–5415.
[156] A. Hakiki, R. N. Young, T. C. B. McLeish, *Macromolecules* **1996**, *29*, 3639–3641.
[157] L. A. Archer, Juliani, *Macromolecules* **2004**, *37*, 1076–1088.
[158] M. T. Islam, Juliani, L. A. Archer, S. K. Varshney, *Macromolecules* **2001**, *34*, 6438–6449.
[159] Juliani, L. A. Archer, *Macromolecules* **2002**, *35*, 10048–10053.
[160] L. A. Archer, S. K. Varshney, *Macromolecules* **1998**, *31*, 6348–6355.
[161] M. S. Rahman, R. Aggarwal, R. G. Larson, J. M. Dealy, J. Mays, *Macromolecules* **2008**, *41*, 8225–8230.

[162] S. W. Li, H. E. Park, J. M. Dealy, M. Maric, H. Lee, K. Im, H. Choi, T. Chang, M. S. Rahman, J. Mays, *Macromolecules* **2011**, *44*, 208–214.

[163] X. Chen, M. S. Rahman, H. Lee, J. Mays, T. Chang, R. Larson, *Macromolecules* **2011**, *44*, 7799–7809.

[164] A. Zografos, E. M. Maines, J. F. Hassler, F. S. Bates, M. A. Hillmyer, *ACS Macro Letters* **2024**, 695–702.

[165] E. van Ruymbeke, C. Bailly, R. Keunings, D. Vlassopoulos, *Macromolecules* **2006**, *39*, 6248–6259.

[166] H. Lentzakis, S. Costanzo, D. Vlassopoulos, R. H. Colby, D. J. Read, H. Lee, T. Chang, E. van Ruymbeke, *Macromolecules* **2019**, *52*, 3010–3028.

[167] V. Ianniello, S. Costanzo, *Rheologica Acta* **2022**, *61*, 667–679.

[168] J. Roovers, *Macromolecules* **1984**, *17*, 1196–1200.

[169] Y. Masubuchi, *Macromolecules* **2018**, *51*, 10184–10193.

[170] J. Roovers, P. M. Toporowski, *Macromolecules* **1981**, *14*, 1174–1178.

[171] Y. Masubuchi, G. Ianniruberto, G. Marrucci, *Soft Matter* **2020**, *16*, 1056–1065.

[172] F. Snijkers, H. Lee, T. Chang, C. Das, D. Vlassopoulos, *European Polymer Journal* **2024**, *206*, 112806.

[173] S. Houli, H. Iatrou, N. Hadjichristidis, D. Vlassopoulos, *Macromolecules* **2002**, *35*, 6592–6597.

[174] V. Hirschberg, S. Lyu, M. G. Schußmann, *Journal of Rheology* **2023**, *67*, 403–415.

[175] M. G. Schußmann, H. Y. (송형용) Song, K. (현 규) Hyun, M. Wilhelm, V. Hirschberg, *Physics of Fluids* **2025**, *37*, 013109.

[176] H. Zhang, J. Zhu, J. He, F. Qiu, H. Zhang, Y. Yang, H. Lee, T. Chang, *Polym. Chem.* **2013**, *4*, 830–839.

[177] M.-C. Röpert, M. G. Schußmann, M. K. Esfahani, M. Wilhelm, V. Hirschberg, *Macromolecules* **2022**, *55*, 5485–5495.

[178] M.-C. Röpert, V. Hirschberg, M. G. Schußmann, M. Wilhelm, *Macromolecules* **2023**, *56*, 1921–1933.

[179] V. Hirschberg, S. Lyu, M. G. Schußmann, M. Wilhelm, M. H. Wagner, *Rheologica Acta* **2023**, *62*, 433–445.

[180] V. Hirschberg, M. G. Schußmann, M.-C. Röpert, N. Dingenouts, S. Buchheiser, H. Nirschl, J. Berson, M. Wilhelm, *Macromolecules* **2024**, 3387–3396.

[181] M. Röpert, A. Goecke, M. Wilhelm, V. Hirschberg, *Macromolecular Chemistry and Physics* **2022**, *223*, 2200288.

[182] M. G. Schußmann, L. Kreutzer, V. Hirschberg, *Macromolecular Rapid Communications* **2024**, *45*, 2300674.

[183] Y. Masubuchi, Y. Matsumiya, H. Watanabe, G. Marrucci, G. Ianniruberto, *Macromolecules* **2014**, *47*, 3511–3519.

[184] Y. Doi, Y. Ohta, M. Nakamura, A. Takano, Y. Takahashi, Y. Matsushita, *Macromolecules* **2013**, *46*, 1075–1081.

[185] Y. Doi, Y. Iwasa, K. Watanabe, M. Nakamura, A. Takano, Y. Takahashi, Y. Matsushita, *Macromolecules* **2016**, *49*, 3109–3115.

[186] Y. Doi, J. Kitamura, T. Uneyama, Y. Masubuchi, A. Takano, Y. Takahashi, Y. Matsushita, *Polym J* **2022**, *54*, 1267–1277.

[187] H. Iatrou, A. Avgeropoulos, N. Hadjichristidis, *Macromolecules* **1994**, *27*, 6232–6233.

[188] S. P. Gido, C. Lee, D. J. Pochan, S. Pispas, J. W. Mays, N. Hadjichristidis, *Macromolecules* **1996**, *29*, 7022–7028.

[189] M. Xenidou, N. Hadjichristidis, *Macromolecules* **1998**, *31*, 5690–5694.

[190] M. G. Schußmann, **2021**.

[191] H. Watanabe, T. Amemiya, T. Shimura, T. Kotaka, *Macromolecules* **1994**, *27*, 2336–2338.

[192] D. R. Armstrong, R. E. Mulvey, D. Barr, R. Snaith, D. Reed, *Journal of Organometallic Chemistry* **1988**, *350*, 191–205.

[193] R. Mulvey, L. Dunbar, W. Clegg, L. Horsburgh, *Angewandte Chemie International Edition* **1996**, *35*, 753–755.

[194] D. Barr, R. Snaith, R. E. Mulvey, D. Reed, *Polyhedron* **1988**, *7*, 665–668.

[195] S. D. Robertson, A. R. Kennedy, J. J. Liggat, R. E. Mulvey, *Chemical Communications* **2015**, *51*, 5452–5455.

[196] L. Faust, Synthesis of Highly Branched Polystyrene Model Systems with Superior Strain Hardening and Their Influence on Foaming Properties, Dissertation, Karlsruher Institut für Technologie, **2021**.

[197] M. Heck, Orientierungsvorgänge in Diblockcopolymeren mit ähnlichen Dynamiken der Polymerblöcke bei oszillatorischer Deformation mit großen Amplituden, Dissertation, Karlsruher Institut für Technologie, **2018**.

[198] H. Y. Song, S. J. Park, K. Hyun, *ACS Macro Letters* **2023**, *12*, 968–973.

[199] K. Klimke, M. Parkinson, C. Piel, W. Kaminsky, H. W. Spiess, M. Wilhelm, *Macromolecular Chemistry and Physics* **2006**, *207*, 382–395.

[200] S. J. Park, R. G. Larson, *Journal of Rheology* **2003**, *47*, 199–211.

[201] T. Schweizer, J. van Meerveld, H. C. Öttinger, *Journal of Rheology* **2004**, *48*, 1345–1363.

[202] Y. Masubuchi, H. Watanabe, *ACS Macro Lett.* **2014**, *3*, 1183–1186.

[203] Y. Masubuchi, *Annual Review of Chemical and Biomolecular Engineering* **2014**, *5*, 11–33.

[204] S. Costanzo, V. Ianniello, R. Pasquino, N. Grizzuti, G. Ianniruberto, G. Marrucci, *Macromolecules* **2022**, *55*, 9206–9219.

[205] J. Cao, A. E. Likhtman, *ACS Macro Lett.* **2015**, *4*, 1376–1381.

[206] S. Ravindranath, S.-Q. Wang, *Journal of Rheology* **2008**, *52*, 681–695.

[207] K. S. Schweizer, S.-J. Xie, *ACS Macro Lett.* **2018**, *7*, 218–222.

[208] S. H. Jeong, J. M. Kim, C. Baig, *Macromolecules* **2017**, *50*, 4491–4500.

[209] S. H. Jeong, S. Cho, C. Baig, *Polymer* **2023**, *281*, 126101.

[210] K. Osaki, T. Inoue, T. Isomura, *Journal of Polymer Science Part B: Polymer Physics* **2000**, *38*, 2043–2050.

[211] Y. Masubuchi, **2024**, arxiv.org/pdf/2404.14629.

[212] S. Costanzo, Q. Huang, G. Ianniruberto, G. Marrucci, O. Hassager, D. Vlassopoulos, *Macromolecules* **2016**, *49*, 3925–3935.

[213] D. Parisi, E. Vereroudakis, Y. Masubuchi, G. Ianniruberto, G. Marrucci, D. Vlassopoulos, *Journal of Non-Newtonian Fluid Mechanics* **2023**, *315*, 105028.

[214] M. H. Wagner, E. Narimissa, Q. Huang, *Journal of Rheology* **2018**, *62*, 221–233.

[215] Q. Huang, J. Ahn, D. Parisi, T. Chang, O. Hassager, S. Panyukov, M. Rubinstein, D. Vlassopoulos, *Physical Review Letters* **2019**, *122*, 208001.

[216] Q. Huang, S. Agostini, L. Hengeller, M. Shivokhin, N. J. Alvarez, L. R. Hutchings, O. Hassager, *Macromolecules* **2016**, *49*, 6694–6699.

[217] S. Holler, A. J. Moreno, M. Zamponi, P. Bačová, L. Willner, H. Iatrou, P. Falus, D. Richter, *Macromolecules* **2018**, *51*, 242–253.

[218] K. Mortensen, A. L. Borger, J. J. K. Kirkensgaard, C. J. Garvey, K. Almdal, A. Dorokhin, Q. Huang, O. Hassager, *Physical review letters* **2018**, *120*, 207801.

[219] L. M. Polgar, H. Lentzakis, D. Collias, F. Snijkers, S. Lee, T. Chang, G. Sakellariou, D. A. Z. Wever, C. Toncelli, A. A. Broekhuis, F. Picchioni, A. D. Gotsis, D. Vlassopoulos, *Macromolecules* **2015**, *48*, 6662–6671.

[220] F. Snijkers, K. Ratkanthwar, D. Vlassopoulos, N. Hadjichristidis, *Macromolecules* **2013**, *46*, 5702–5713.

[221] T. Shahid, C. Clasen, F. Oosterlinck, E. van Ruymbeke, *Macromolecules* **2019**, *52*, 2521–2530.

[222] E. van Ruymbeke, R. Keunings, C. Bailly, *Journal of Non-Newtonian Fluid Mechanics* **2005**, *128*, 7–22.

[223] K. Osaki, K. Nishizawa, M. Kurata, *Macromolecules* **1982**, *15*, 1068–1071.

[224] J. Meissner, *Journal of Applied Polymer Science* **1972**, *16*, 2877–2899.

[225] H. Münstedt, *Journal of Rheology* **1979**, *23*, 421–436.

[226] M. L. Sentmanat, *Rheologica Acta* **2004**, *43*, 657–669.

[227] G. H. McKinley, T. Sridhar, *Annual Review of Fluid Mechanics* **2002**, *34*, 375–415.

[228] A. Bach, H. K. Rasmussen, O. Hassager, *Journal of Rheology* **2003**, *47*, 429–441.

[229] "RHEO FILAMENT," can be found under https://www.rheofilament.com/index.html, **n.d.**

[230] D. Parisi, S. Coppola, S. Righi, G. Gagliardi, F. S. Grasso, F. Bacchelli, *Rubber Chemistry and Technology* **2022**, *95*, 241–276.

[231] R. H. Diaz, A. P. Ferguson, *Block Copolymers: Phase Morphology, Material Applications & Future Challenges*, Nova Science Publishers Inc, New York, **2014**.

[232] I. Hamley, *The Physics of Block Copolymers*, Oxford University Press, Oxford, **1999**.

[233] F. S. Bates, M. A. Hillmyer, T. P. Lodge, C. M. Bates, K. T. Delaney, G. H. Fredrickson, *Science* **2012**, *336*, 434–440.

[234] G. Polymeropoulos, G. Zapsas, K. Ntetsikas, P. Bilalis, Y. Gnanou, N. Hadjichristidis, *Macromolecules* **2017**, *50*, 1253–1290.

[235] C. M. Bates, F. S. Bates, *Macromolecules* **2017**, *50*, 3–22.

[236] F. S. Bates, G. H. Fredrickson, *Annu. Rev. Phys. Chem.* **1990**, *41*, 525–557.

[237] F. Drolet, G. H. Fredrickson, *Macromolecules* **2001**, *34*, 5317–5324.

[238] A. J. Meuler, M. A. Hillmyer, F. S. Bates, *Macromolecules* **2009**, *42*, 7221–7250.

[239] M. Steube, M. Plank, M. Gallei, H. Frey, G. Floudas, *Macromolecular Chemistry and Physics* **2021**, *222*, 2000373.

[240] R. K. W. Spencer, M. W. Matsen, *Macromolecules* **2017**, *50*, 1681–1687.

[241] R. Weidisch, S. P. Gido, D. Uhrig, H. Iatrou, J. Mays, N. Hadjichristidis, *Macromolecules* **2001**, *34*, 6333–6337.

[242] Y. Zhu, E. Burgaz, S. P. Gido, U. Staudinger, R. Weidisch, D. Uhrig, J. W. Mays, *Macromolecules* **2006**, *39*, 4428–4436.

[243] R. Schlegel, Y. X. Duan, R. Weidisch, S. Hölzer, K. Schneider, M. Stamm, D. Uhrig, J. W. Mays, G. Heinrich, N. Hadjichristidis, *Macromolecules* **2011**, *44*, 9374–9383.

[244] L. R. Hutchings, J. M. Dodds, D. Rees, S. M. Kimani, J. J. Wu, E. Smith, *Macromolecules* **2009**, *42*, 8675–8687.

[245] W. Shi, N. A. Lynd, D. Montarnal, Y. Luo, G. H. Fredrickson, E. J. Kramer, C. Ntaras, A. Avgeropoulos, A. Hexemer, *Macromolecules* **2014**, *47*, 2037–2043.

[246] S. I. Rosenbloom, R. J. Sifri, B. P. Fors, *Polym. Chem.* **2021**, *12*, 4910–4915.

[247] C. Wahlen, J. Blankenburg, P. von Tiedemann, J. Ewald, P. Sajkiewicz, A. H. E. Müller, G. Floudas, H. Frey, *Macromolecules* **2020**, *53*, 10397–10408.

[248] P. von Tiedemann, J. Yan, R. D. Barent, R. J. Spontak, G. Floudas, H. Frey, R. A. Register, *Macromolecules* **2020**, *53*, 4422–4434.

[249] M. Rauschenbach, M. Meier-Merziger, H. Frey, *Polym. Chem.* **2024**, *15*, 4297–4311.

[250] B. Li, C. Pyromali, S. Costanzo, A. Mavromanolakis, D. Vlassopoulos, *Physics of Fluids* **2024**, *36*, 037148.

Appendix

Materials and Methods

Materials and Purification Methods

Styrene (99% extra pure, stabilized, Sigma-Aldrich), 2-vinylpyridine (97%, stabilized, Fisher Scientific), and 1,1-diphenylethene (Sigma-Aldrich) was stirred over calcium hydride (CaH$_2$, 92% Fisher Scientific) over night, degassed by three freeze-pump-thaw cycles, and freshly distilled prior to use. Isoprene (98%, stabilized, VWR) was stirred in an ice bath over *n*-butyllithium (2.5 M in cyclohexane, Sigma-Aldrich). As soon as the solution turned slightly yellow, isoprene was distilled into ampules. Cyclohexane (99%, Fisher Scientific) was purified by stirring over polystyrenyllithium, degassed by three freeze-pump-thaw cycles, and freshly distilled prior to use. Tetrahydrofuran (THF, 99.5%, Roth) was distilled from CaH$_2$, stored over sodium/benzophenone, degassed by three freeze-pump-thaw cycles, and freshly distilled before use. Methanol (>99%, Fisher Scientific) was degassed by three freeze-pump thaw cycles to use for termination of the anionic polymerizations. 1,4-Dioxane (>98%, Fisher) is purified by distillation under reduced pressure before use. Toluene (>99%, Roth), hydrogen peroxide (H$_2$O$_2$, 30 wt%, Acros Organics), formic acid (98%, Roth), *sec*-butyllithium (*s*-BuLi, 1.4 M in hexane, Aldrich), sodium (>99%, Merck), THF (HPLC grade, Fisher), methanol (>99%, Fisher) and benzophenone (Sigma-Aldrich) were used as received.

List of instruments used

The SEC instrument was an Agilent 1200 series equipped in a fourdetector configuration with UV, multiangle laser-light scattering (MALLS, SLD7000/BI-MwA, PSS, Brookhaven Instruments), viscometer, and a DRI detector (Polymer Standard Service, PSS, Germany), using an autosampler for sample injection. The columns (SDV-Lux 5 μm (guard column), SDV-Lux-1000 Å, SDV-Lux 100000 Å, PSS) were calibrated with monodisperse linear PS standards with weight-average molecular weights, between 476 and $2.5 \cdot 10^6$ gmol^{-1}. HPLC grade THF was used as the eluent with a flow rate of 1 ml min^{-1}. Injected volume of 100 μl was used for each measurement. dn/dc values were calculated based on the ratio of the blocks (mol.%) as determined by ^{1}H NMR. Samples were dissolved in 2 mL THF and with a concentration between 0.3 mg ml^{-1} and 5 mg ml^{-1}. The lower the molecular weight, the lower the concentration.

^{1}H NMR spectra were obtained in deuterated chloroform at 25 °C using a 400 MHz Bruker Avance III Microbay spectrometer.

Differential scanning calorimetry was measured on a TA Instruments Q-200 under nitrogen atmosphere. Scans were conducted between 25 °C and 200 °C at a rate of 10 K min^{-1}. The inflection point of the second heating run was used for estimation of the glass transition temperature.

The tensile machine was a Hegewald und Peschke InspectTable 10kN. Specimen preparation: 1g block copolymer was dissolved in 20 mL THF and slowly dried under ambient conditions in an aluminum dish. After 4 days, residual solvent was removed under vacuum at 120 °C for 2 h. Dog bone specimen were cut from the resulting film with a thickness of about 0.25 mm. Dimensions of the specimen follow the elastomer testing standard DIN 53504 S3A. A linear strain rate of 5 mm min^{-1} was used.

Rheological characterization was conducted on a TA Instruments ARES G2 using a 13 mm parallel plate, 13 mm 0.1 rad cone plate or a 10 mm partitioned plate with a 25mm 0.1 rad cone. For extensional measurements, the extensional viscosity fixture (EVF) geometry was used. For measurements to develop the new 2D UXF procedure described in chapter 7.6 an Anton Paar MCR 703 multidrive rheometer equipped with a universal extensional fixture (UXF) was used. All measurements were conducted under nitrogen atmosphere. All samples were hot pressed at 180 °C for 15 min under vacuum into disc shape for shear experiments and rectangular shape (20 mm x 10 mm x 0.5 mm or 1 mm) for extensional measurements.

The Rheo Hub software by IRIS Development LLC was used to calculate the tensile stress growth coefficients for the Doi-Edwards, pom-pom and HMMSF model.

Supplementary Data and Figures

Additional figures to support the discussion in the respective chapter are given below.
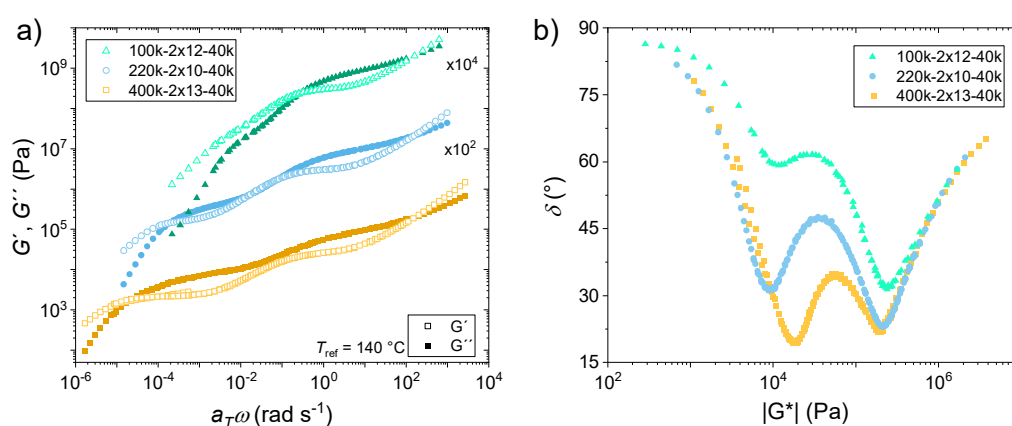

Supplementary Figure 1: a) Mastercurves of three pom-poms of the 40k-series at a reference temperature of T_{ref} = 140 °C. b) Phase angle δ shown as a function of the complex modulus $|G^*|$.
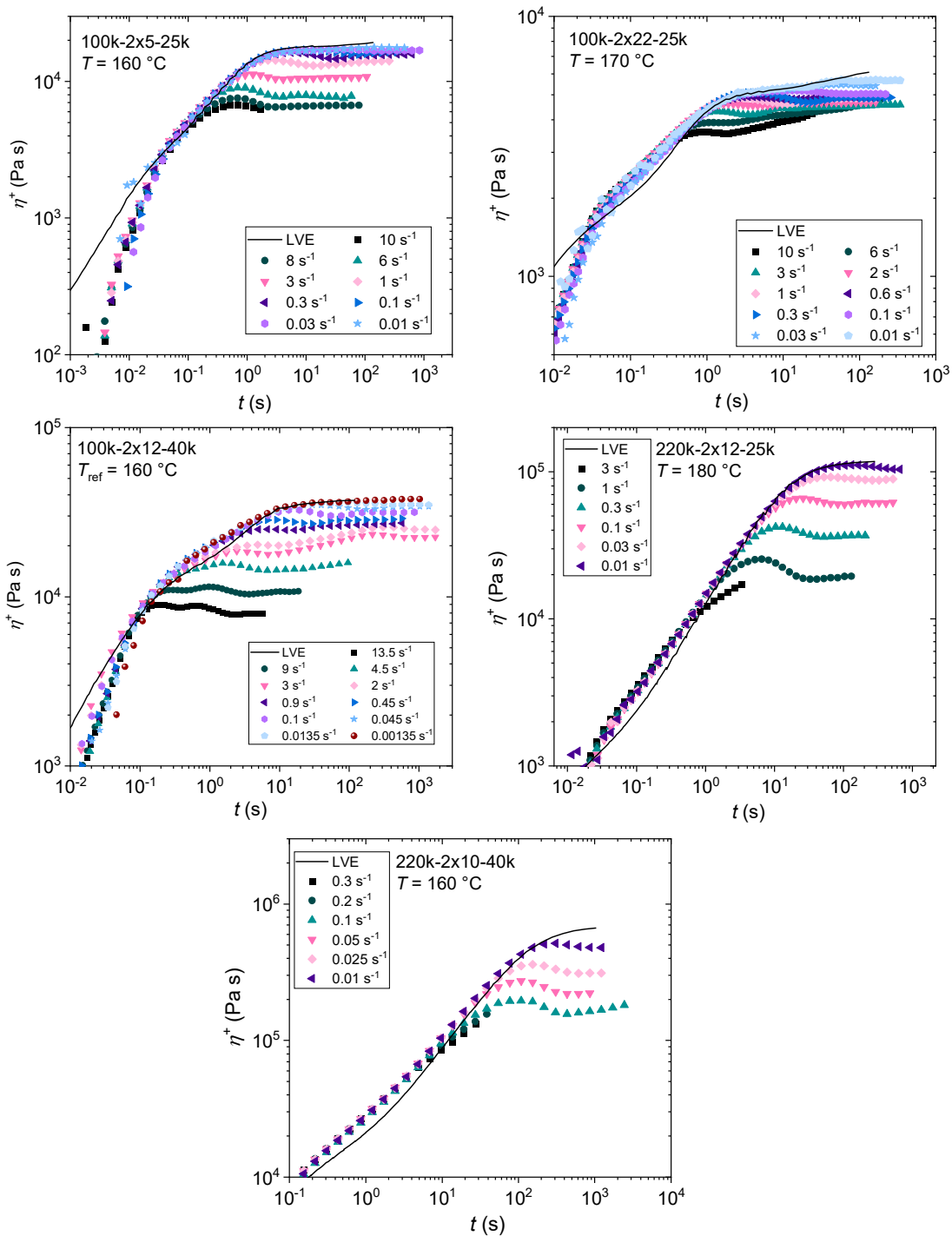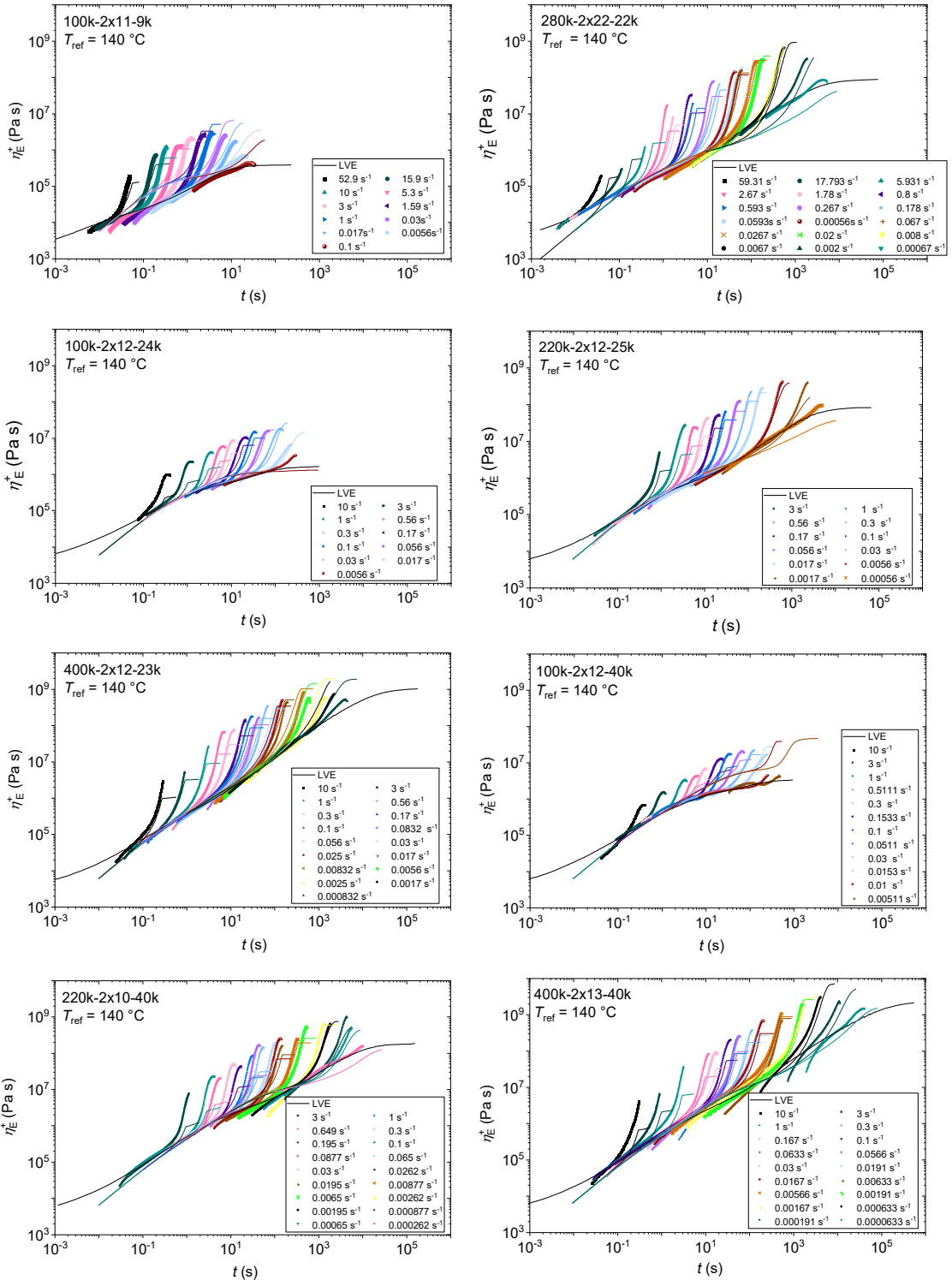
Supplementary Figure 2: Shear stress growth coefficient is shown as a function of time at selected shear rates for multiple pom-poms. For higher shear rates, the viscosity measurement is terminated by the normal force exceeding the transducer capacity.
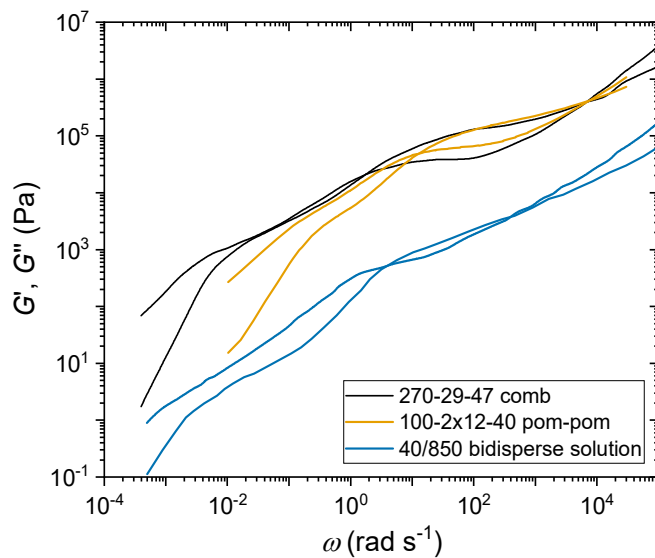
Supplementary Figure 3: Mastercurves of all three samples showing a double stress overshoot.
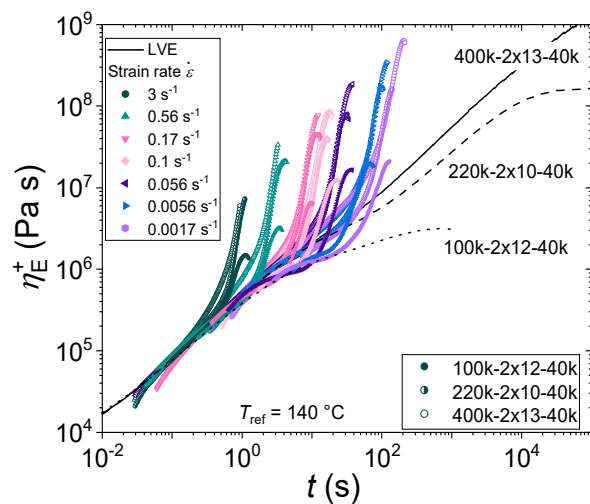
Supplementary Figure 4: Tensile stress growth coefficient η_E^+ for the 40k-series shown at selected strain rates $\dot{\varepsilon}$ at a reference temperature $T_{ref} = 140$ °C.

Supplementary Figure 5: Tensile stress growth coefficient η_E^+ for all pom-poms and all measured strain rates $\dot{\varepsilon}$ at a reference temperature T_{ref} = 140 °C. Solid lines show predictions by the pom-pom model.
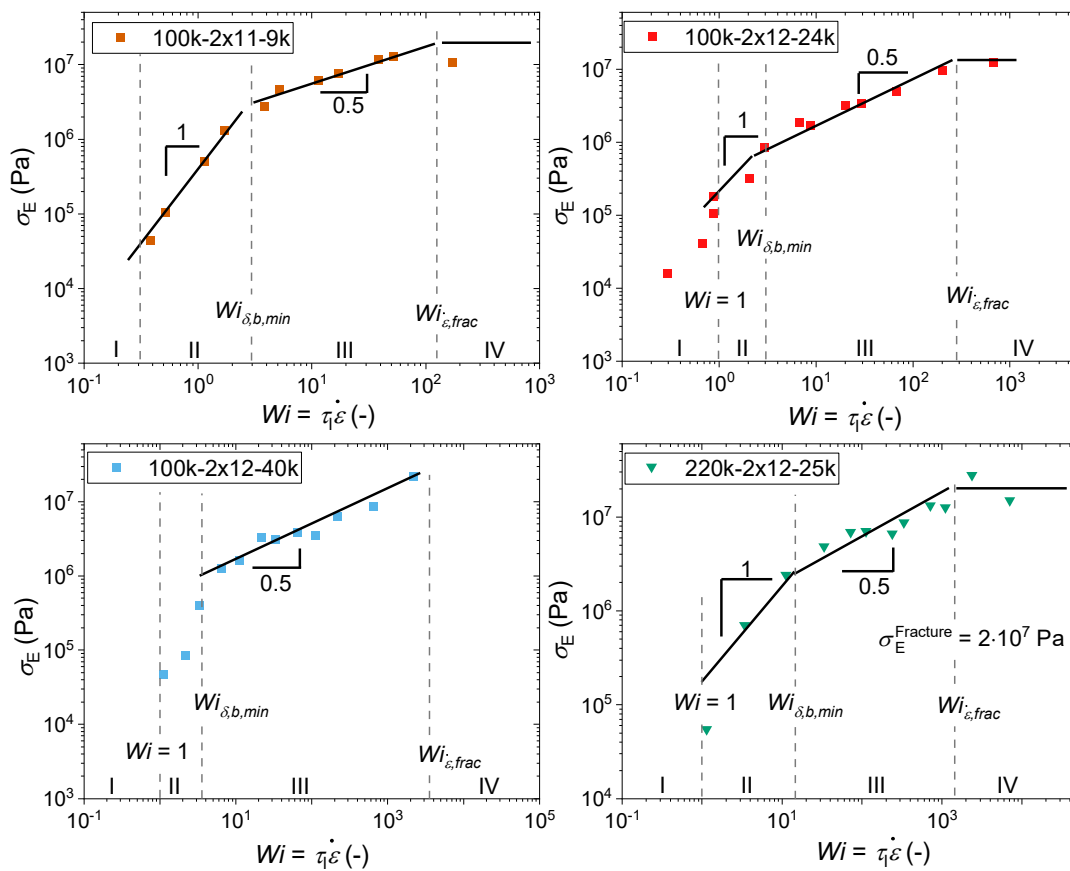
Supplementary Figure 6: Fracture stress $\sigma_E^{Fracture}$ as a function of the Weissenberg number Wi for four different pom-poms. Dashed lines indicate characteristic regimes. Solid lines are to guide the eye.
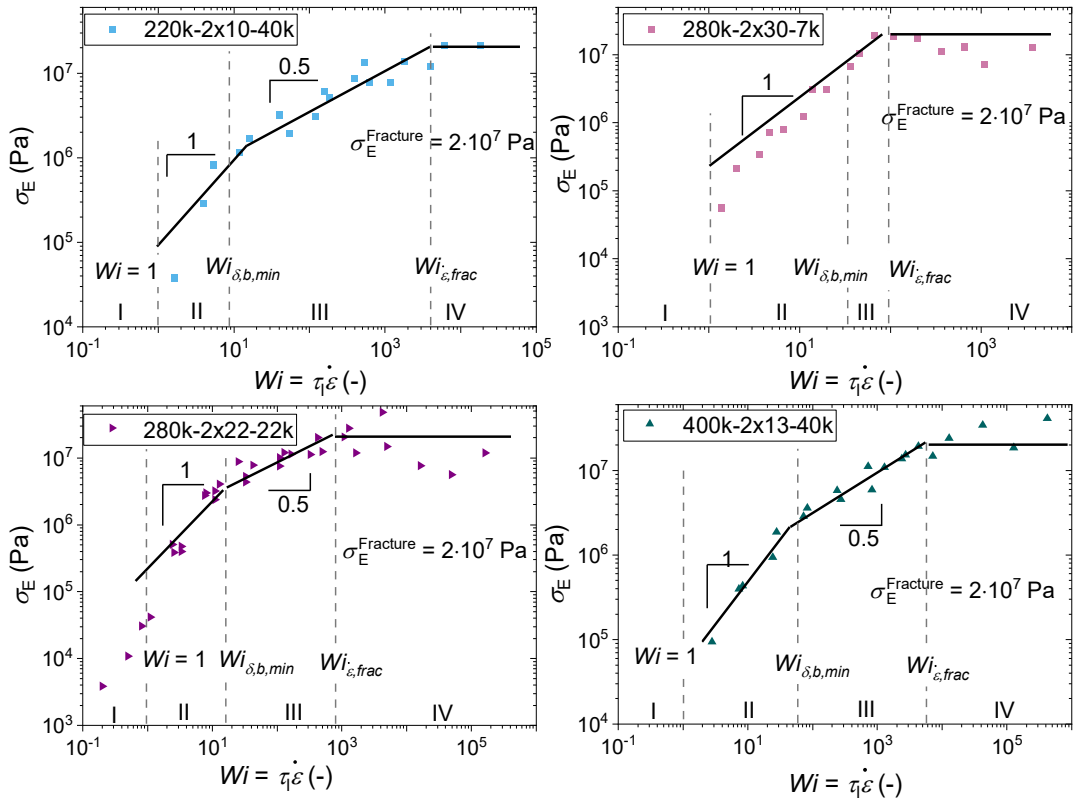
Supplementary Figure 7: Fracture stress $\sigma_E^{Fracture}$ as a function of the Weissenberg number Wi for four different pom-poms. Dashed lines indicate characteristic regimes. Solid lines are to guide the eye.
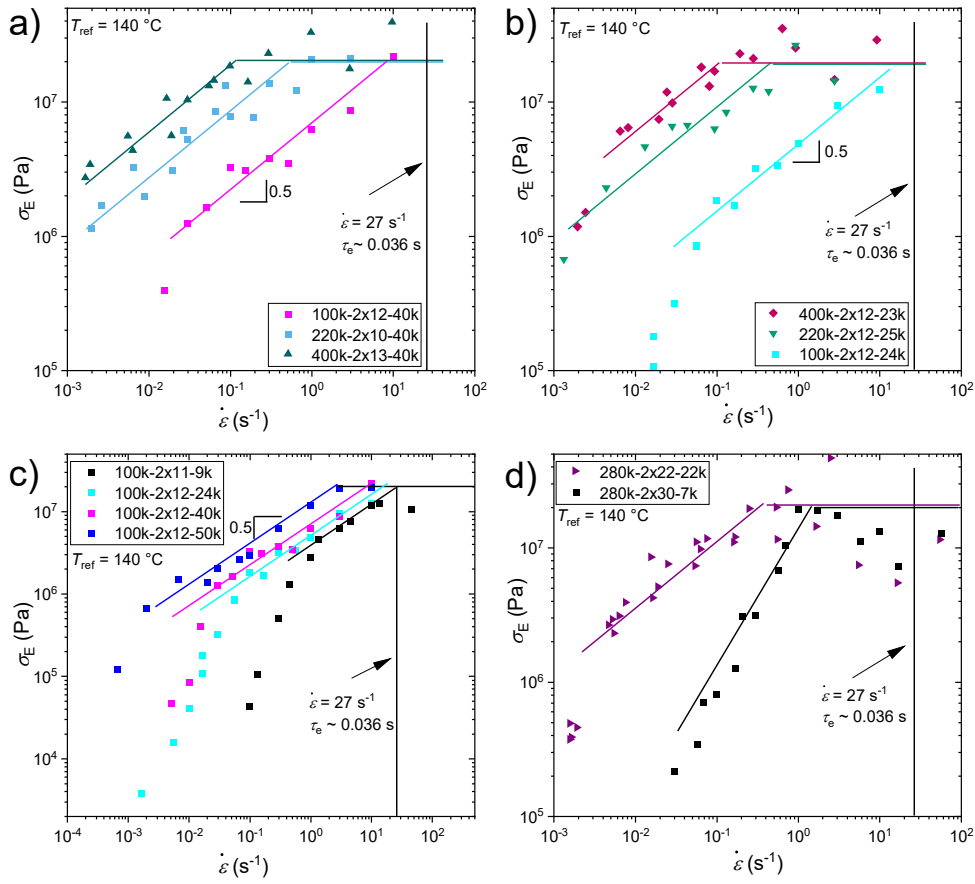
Supplementary Figure 8: Fracture stress $\sigma_E^{Fracture}$ as a function of the extensional rate $\dot{\varepsilon}$ for different pom-poms at a reference temperature $T_{ref} = 140$ °C. Solid lines are to guide the eye.
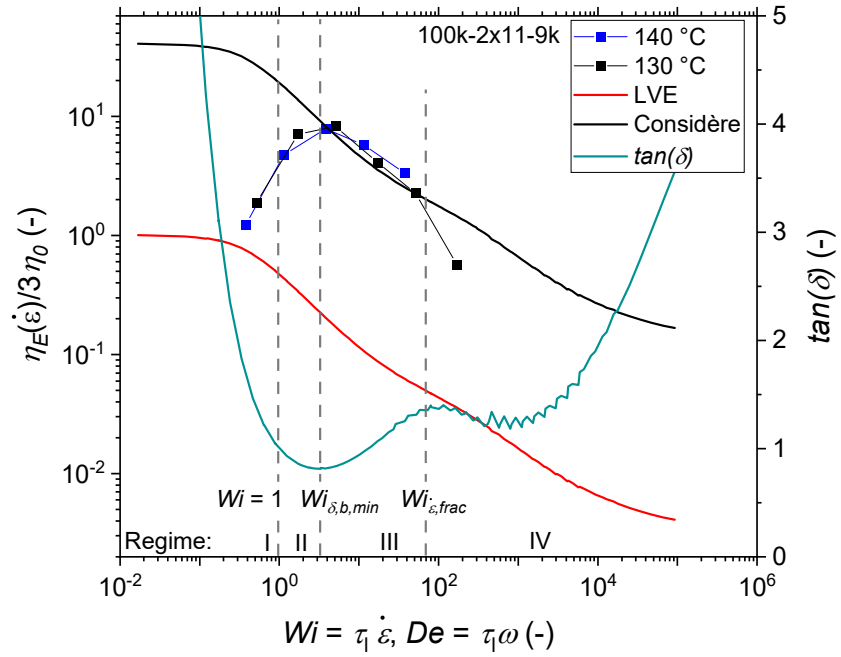
Supplementary Figure 9: Extensional viscosity η_E normalized to the zero-shear viscosity η_0 shown as a function of the Weissenberg number Wi and the phase angle $\tan\delta$ as a function of the Deborah number De of the pom-pom 100k-2x11-9k.
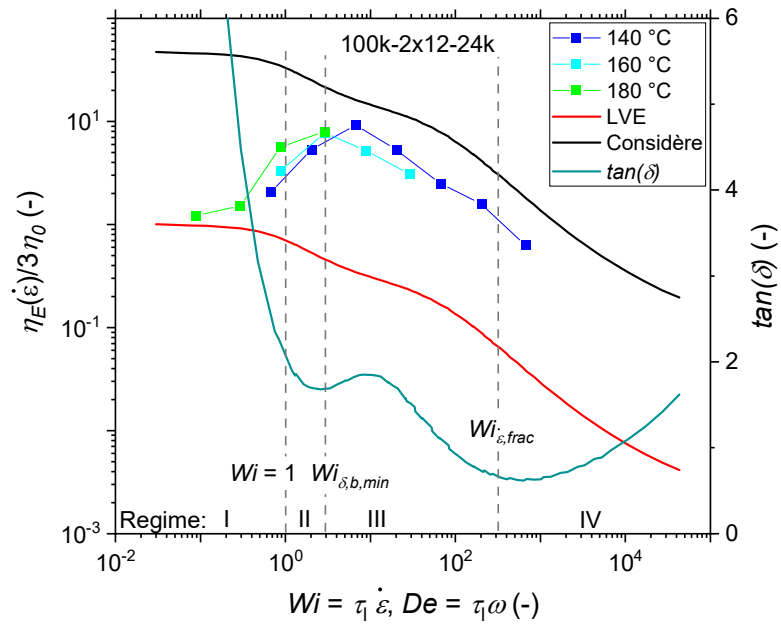
Supplementary Figure 10: Extensional viscosity η_E normalized to the zero-shear viscosity η_0 shown as a function of the Weissenberg number Wi and the phase angle $\tan\delta$ as a function of the Deborah number De of the pom-pom 100k-2x12-24k.
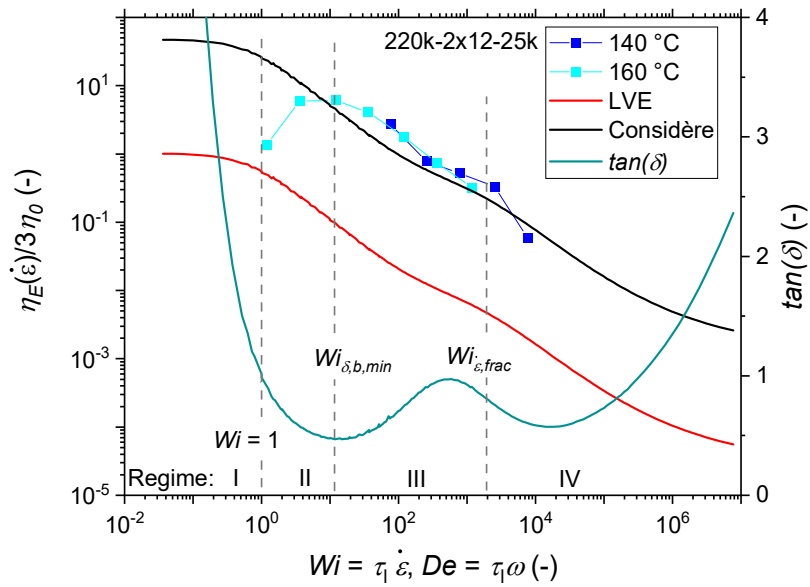
Supplementary Figure 11: Extensional viscosity η_E normalized to the zero-shear viscosity η_0 shown as a function of the Weissenberg number Wi and the phase angle $\tan\delta$ as a function of the Deborah number De of the pom-pom 220k-2x12-25k.
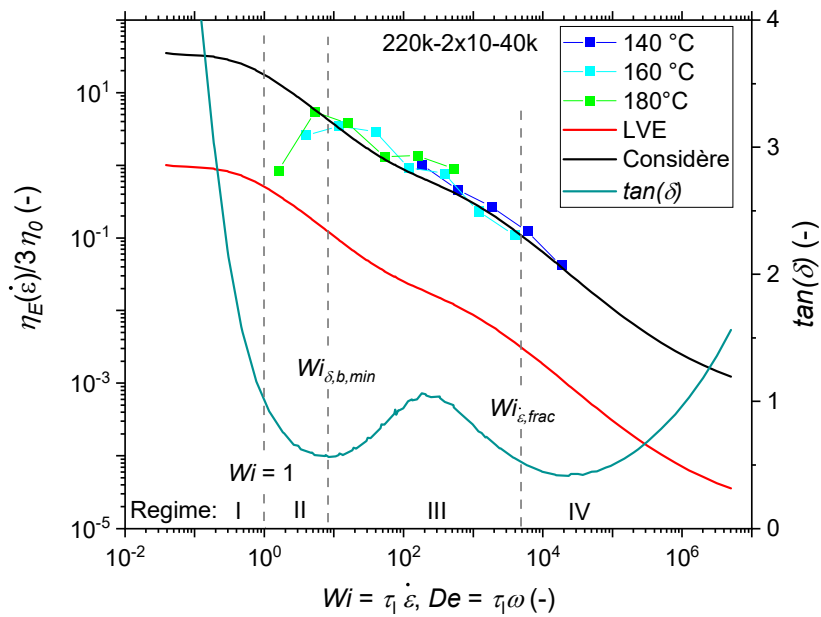
Supplementary Figure 12: Extensional viscosity η_E normalized to the zero-shear viscosity η_0 shown as a function of the Weissenberg number Wi and the phase angle $\tan\delta$ as a function of the Deborah number De of the pom-pom 220k-2x10-40k.

Supplementary Figure 13: Extensional viscosity η_E normalized to the zero-shear viscosity η_0 shown as a function of the Weissenberg number Wi and the phase angle $\tan\delta$ as a function of the Deborah number De of the pom-pom 400k-2x12-23k.
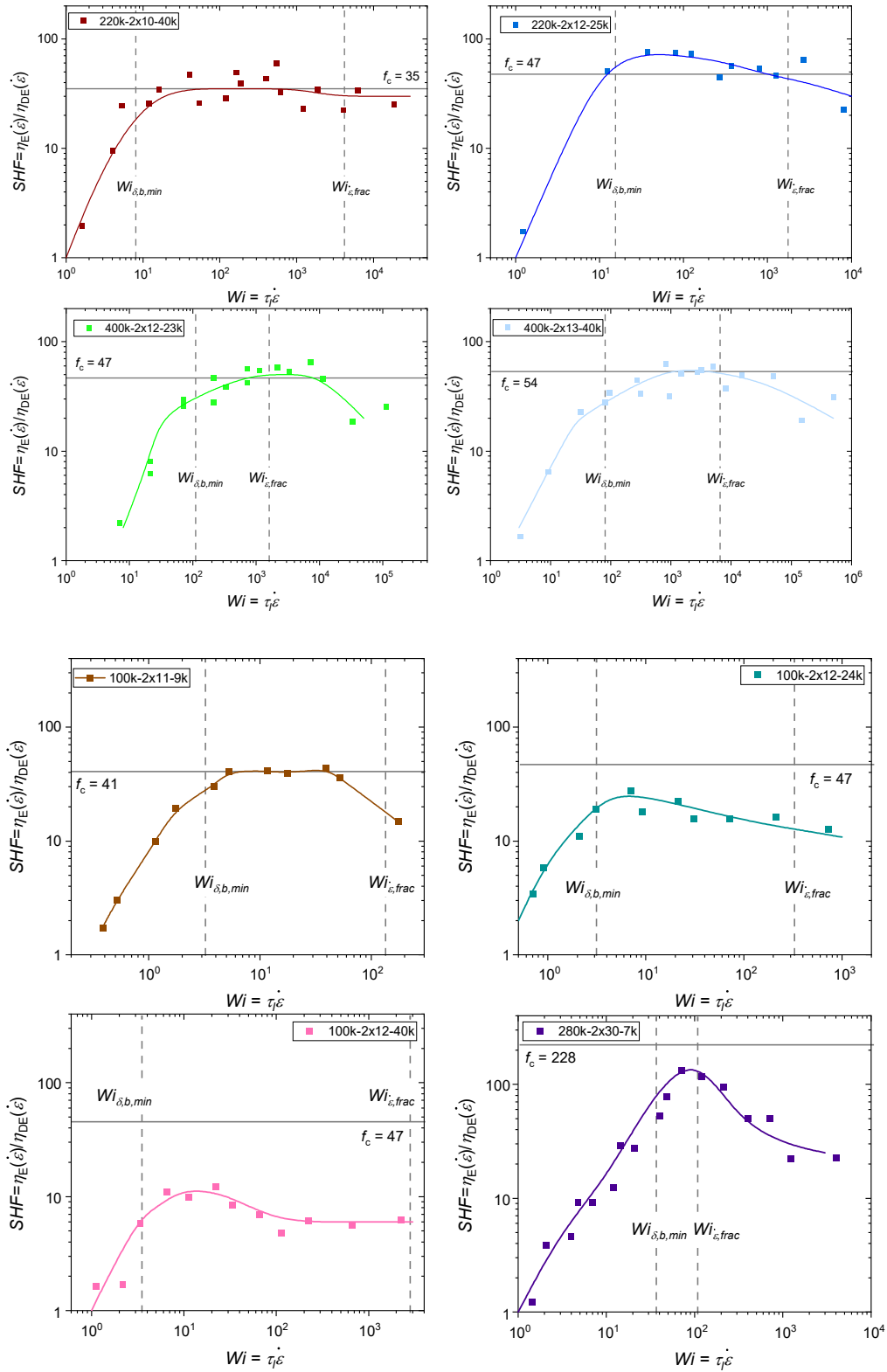
Supplementary Figure 14: Strain hardening factor SHF shown as a function of Weissenberg number Wi for eight pom-poms. Solid lines are a guide to the eye.
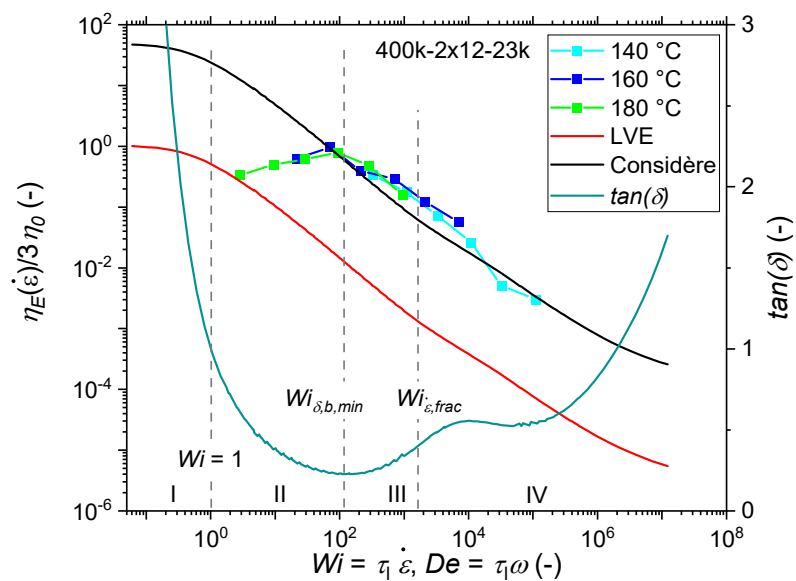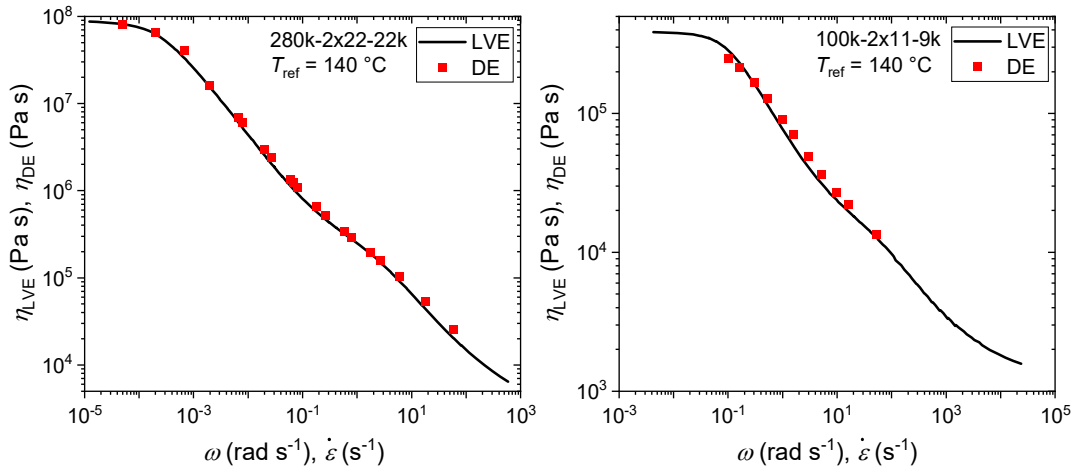
Supplementary Figure 15: LVE and the plateau viscosity of the DE model η_{DE} is shown as a function of angular frequency ω and strain rate $\dot{\varepsilon}$, respectively.
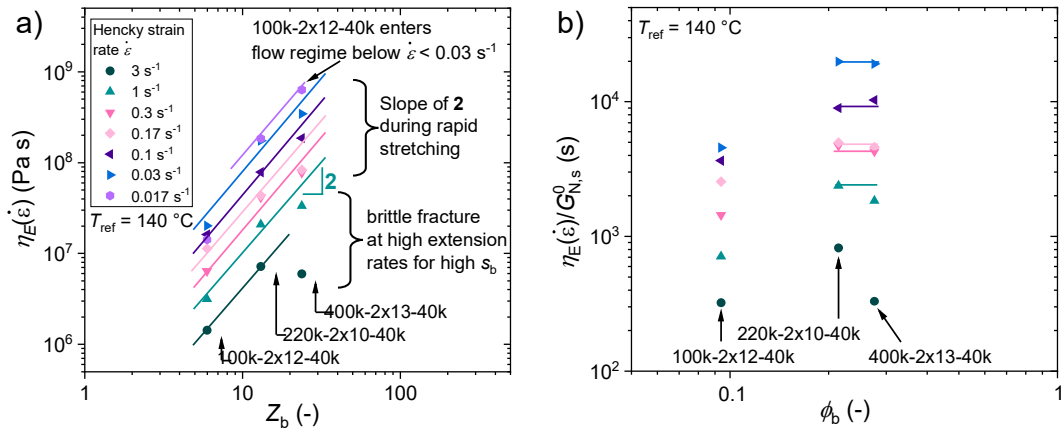
Supplementary Figure 16: Extensional viscosity η_E as a function of the number of entanglements of the backbone Z_b for three pom-poms with varying molecular weight of the backbone. b) Extensional viscosity η_E normalized to the dilution modulus $G_{N,s}^0$ as a function of the volume fraction of the backbone ϕ_b. Selected strain rates between 3 s^{-1} and 0.0017 s^{-1} are shown to illustrate differences in the extensional behavior of the three pom-poms.

Nomenclature

Abbreviations

AFM   Atomic force microscopy

BHT   2,6-Di-tertbutyl-4-methylphenole

BoB   Branch-on-branch

CCR   Convective constraint release

CLF   Contour length fluctuation

CP   Cone plate

CPP   Cone partitioned plate

DE   Dendrimer

DE   Doi Edwards

DOSY   Diffusion-ordered spectroscopy

DPE   1,1-Diphenylethylene

DRI   Differential refractive index

DSC   Differential scanning calorimetry

DTD   Dynamic tube dilution

EVF   Extensional viscosity fixture

FSR   Filament stretch rheometer

HMMSF   Hierarchical multimode molecular stress function

LCB   Long chain branched

LDPE   Low density polyethylene

LLS   Large laboratory scales

MALLS   Multi-angle laser light scattering

MSF   Molecular stress function

NaNp   Sodium naphthalene

NMR   Nuclear Magnetic Resonance

P2VP   Poly(2-vinylpyridine)

PB   Polybutadiene

PE   Polyethylene

PEG   Polyethyleneglycol

PET   Polyethyleneterephthalate

PI   Polyisoprene

PLA   Polylactic acid

PMMA   Polymethylmethacrylate

PnBA   Poly(n-butylacrylate)

PPG   Polypropyleneglycol

PPM   Post-polymerization modification

PpMS   Poly(p-methylstyrene)

PS   Polystyrene

RI   Refractive index

SAOS   Small amplitude oscillatory shear

SAXS   Small-angle x-ray scattering

s-BuLi   *Sec*-Butyllithium

SCFT   Self consistent field theory

SEC   Size exclusion chromatography

SER   Sentmanat extensional rheometer

SCB   Short chain branched

TEM   Transmission electron spectroscopy

TGIC   Thermal gradient interaction chromatography

THF   Tetrahydrofurane

TMA   Time marching algorithm

TTS   Time-temperature superposition

UV   Ultraviolet

UXF   Universal extensional fixture

vGP   Van Gurp-Palmen plot

WLF   Williams-Landell-Ferry

Physical Quantities

Roman

A Area (m²)

a_T Horizontal shift factor (-)

b_T Vertical shift factor (-)

C_1, C_2 WLF parameters (-, K)

$Đ$ Polydispersity index (-)

$Đ_t$ Total dispersity of the pom-pom (-)

$Đ_b$ Backbone length dispersity (-)

$Đ_a$ Arm length dispersity (-)

De Deborah number, $De = \tau_l \omega$ (-)

F Force (N)

f_c Considère factor (-)

G Shear modulus (Pa)

G' Storage modulus (Pa)

G'' Loss modulus (Pa)

$G_{N,s}^0$ Dilution modulus (Pa)

G_0 Plateau modulus (Pa)

$|G^*|$ Absolute magnitude of the complex shear modulus (Pa)

h Height (m)

L_0 Initial sample length (m)

$L(t)$ Time dependent sample length (m)

M_n Number average molecular weight (-)

M_w Weight average molecular weight (-)

$M_{w,span}$ Span molecular weight of a pom-pom, $M_{w,span} = M_{w,b} + 2 \cdot M_{w,a}$ (kg mol⁻¹)

$M_{w,b}$ Backbone molecular weight (kg mol⁻¹)

$M_{w,a}$ Arm molecular weight (kg mol⁻¹)

M_e Entanglement molecular weight (kg mol⁻¹), $M_{e,PS}$ = 16.8 kg mol⁻¹

P_n number average degree of polymerization

q Arm number (-)

$\boldsymbol{S}$ Orientation tensor (-)

s_c Branch point withdrawal parameter (-)

s Distance (m)

SHF Strain hardening factor (-)

SHF_{max} Maximum strain hardening factor (-)

t Time (s), step time (s)

T Temperature (°C)

T_{ref} Reference temperature of time-temperature superposition (°C)

t_q Time at maximum backbone stretch (s)

V_e Elution volume (mL)

$Wi = \tau_l \dot{\varepsilon}$ Weissenberg number (-)

$Wi_{\delta,b,min}$ Weissenberg number of the phase angle minimum of the backbone (-)

$Wi_{\dot{\varepsilon},frac}$ Weissenberg number where $\sigma_E^{Fracture}$ reaches plateau value (-)

Z Number of entanglements of a linear polymer (-)

Z_a Number of entanglements of the arms (-)

Z_b Number of entanglements of the backbone (-)

Greek

γ Strain (-)

$\dot{\gamma}$ Shear rate (s^{-1})

γ_1 Strain of the first stress overshoot (-)

γ_2 Strain of the second stress overshoot (-)

δ Phase angle (°)

$\delta_{b,min}$ Phase angle minimum of the backbone (°)

ε, ε_H Hencky strain (-)

$\dot{\varepsilon}$ Hencky strain rate (s^{-1})

$\dot{\varepsilon}_{frac}$ Strain rate at which fracture stress plateau is reached (s^{-1})

ε_b Strain at break, tensile (%)

ε_{break} Hencky strain of sample failure, extensional, experimental (-)

ε_f Hencky strain to sample failure, pom-pom model (-)

ε_q Hencky strain at maximum backbone stretch (-)

η Dynamic viscosity (Pa s)

η Shear viscosity (Pa s)

$\eta^+(t, \dot{\gamma})$ Shear stress growth coefficient (Pa s)

$\eta_{Steady-State}$ Steady state shear viscosity (Pa s), $\eta_{Steady-State} = \eta^+(t, \dot{\gamma})|_{t \to \infty}$

η_0 Zero-shear viscosity (Pa s)

η_{DE} Steady state viscosity of the Doi-Edwards model (Pa s)

η_E Extensional viscosity, $\eta_E = \eta_E^+(t)|_{t \to \infty}$ (Pa s)

$\eta_E^+(t)$ Tensile stress growth coefficient (Pa s)

η_{LVE}^+ Viscosity of linear viscoelastic envelope (Pa s)

$|\eta^*|$ Absolute magnitude of the complex viscosity (Pa s)

λ Backbone stretch parameter (-)

σ Stress (Pa)

$\boldsymbol{\sigma}$ Stresstensor

$\sigma^+(t, \dot{\gamma})$ Shear stress growth function (Pa)

$\sigma_E^+(t, \dot{\varepsilon})$ Tensile stress growth function (Pa s)

$\sigma_E^{Fracture}$ Maximum fracture stress of a C-C bond (Pa)

σ_{UTS} Ultimate tensile stress (Pa)

τ Relaxation time (s)

τ_e Rouse time of an entanglement (s)

τ_R Rouse relaxation time of a linear polymer (s)

τ_a Arm relaxation time (s)

τ_b Orientation relaxation time of the backbone (s)

τ_l Longest relaxation time (s)

τ_s Stretch relaxation time of the backbone (s)

ϕ_{PI} Polyisoprene volume fraction in block copolymer (vol%)

ϕ_b Volume fraction of the backbone (-)

ω Angular frequency (rad s^{-1})

Publications and Conference Contributions

Publications

14) "Nonlinear Influence of Blending Star and Triblock Copolymers on Morphological and Mechanical Properties of Thermoplastic Elastomers"
M. G. Schußmann, L. Rocha Dias, S. Buchheiser, H. Nirschl, J. Berson, M. Wilhelm, V. Hirschberg*
Macromolecular Rapid Communications, under revision

13) "Double stress overshoot in startup shear flow and failure of Cox–Merz rule of pom-pom polymers"
M. G. Schußmann, H. Y. Song (송형용), K. Hyun (현 규), M. Wilhelm, V. Hirschberg*
Physics of Fluids, **2025,** *37*, 013109; doi: 10.1063/5.0250133
Featured article

12) "Predicting maximum strain hardening factor in elongational flow of branched pom-pom polymers from polymer architecture"
M. G. Schußmann, M. Wilhelm, V. Hirschberg*
Nature Communications, **2024,** *15*, 3545; doi: 10.1038/s41467-024-47782-8

11) "Supertough Thermoplastic Elastomers of Polystyrene and Polyisoprene via the Pom-Pom Topology"
V. Hirschberg*, M. G. Schußmann, M.-C. Röpert, N. Dingenouts, S. Buchheiser, H. Nirschl, J. Berson, M. Wilhelm
Macromolecules, **2024,** *57*, 3387; doi: 10.1021/acs.macromol.3c02450

10) "Fast and Scalable Synthetic Route to Densely Grafted, Branched Polystyrenes and Poly-dienes via Anionic Polymerization Utilizing P2VP as Branching Point"
M. G. Schußmann, L. Kreutzer, V. Hirschberg*
Macromolecular Rapid Communications, **2024**, *45*, 2300675; doi: 10.1002/marc.202300674

9) "Elongational rheology of 2, 3 and 4 polymer stars connected by linear backbone chains"
V. Hirschberg*, M. G. Schußmann, M. Röpert, A. Goecke, M. Wilhelm, M. H. Wagner*
Rheologica Acta, **2024**, *63*, 407; doi: 10.1007/s00397-024-01455-x

8) "Modeling elongational viscosity of polystyrene Pom-Pom/linear and Pom-Pom/star blends"
V. Hirschberg*, S. Lyu, and <u>M. G. Schußmann</u>, Manfred Wilhelm, Manfred H. Wagner*
Rheologica Acta, **2023**, *62*, 433; doi: 10.1007/s00397-023-01411-1

7) "Shear and elongational rheology of model polystyrene pom-poms"
V. Hirschberg*, <u>M. G. Schußmann</u>, M. Röpert
AIP Conference Proceedings, **2023**, *2997*, 020003; doi: 10.1063/5.0159506

6) "Modelling elongational viscosity and brittle fracture of 10 polystyrene Pom-Poms by the Hierarchical Molecular Stress Function model"
V. Hirschberg*, <u>M. G. Schußmann</u>, M. Röpert, M. Wilhelm, M. H. Wagner*
Rheologica Acta, **2023**, *62*, 269; doi: 10.1007/s00397-023-01393-0

5) "Impact of Topological Parameters on Melt Rheological Properties and Foamability of PS POM-POMs"
M. Röpert, V. Hirschberg*, <u>M. G. Schußmann</u>, M. Wilhelm*
Macromolecules, **2023**, *56*, 1921; doi: 10.1021/acs.macromol.2c02051

4) "Complex polymer topologies in blends: Shear and elongational rheology of linear/pom-pom polystyrene blends"
V. Hirschberg*, S. Lyu, and <u>M. G. Schußmann</u>
Journal of Rheology, **2023**, *67*, 403; doi: 10.1122/8.0000544

3) "Molecularly Defined Polyolefin Vitrimers from Catalytic Insertion Polymerization"
L. Odenwald, F. P. Wimmer, N. K. Mast, <u>M. G. Schußmann</u>, M. Wilhelm, S. Mecking*
Journal of the American Chemical Society, **2023**, *144*, 13226; doi: 10.1021/jacs.2c03778

2) "Effect of Side Chain Length in Polystyrene POM−POMs on Melt Rheology and Solid Mechanical Fatigue"
M. Röpert, <u>M. G. Schußmann</u>, M. K. Esfahani, M. Wilhelm, V. Hirschberg*
Macromolecules, **2023**, *55*, 5485; doi: 10.1021/acs.macromol.2c00199

1) "Phosphine-functionalized tris(pyrazolyl)methane ligands and their mono- and heterobimetallic complexes"
H. E. Wagner, S. Hohnstein, <u>M. G. Schußmann</u>, L. A. Steppe, and F. Breher*
Dalton Transactions, **2019**, *48*, 15397; doi: 10.1039/c9dt02057h

Conference Contributions

DRG Symposium 2024
Ludwigshafen, Deutschland, 12./13.09.2024
M. G. Schußmann, H. Y. Song, K. Hyun, M. Wilhelm, V. Hirschberg
Double stress overshoot in startup shear flow and failure of Cox–Merz rule of pom-pom polymers
Oral

17th International Workshop for Young Rheologists
Busan, Republic of Korea, 23.-26.01.2024
M. G. Schußmann, M. Wilhelm, V. Hirschberg
New Insights into Elongational Rheology of Polystyrene Pom-poms
Oral

International Congress on Rheology 2023
Athens, Greece, 29.07.-04.08.2023
M. G. Schußmann, M. Wilhelm, V. Hirschberg
New Insights into Elongational Rheology of Polystyrene Pom-poms
Oral

European Young Rheologists Symposium 2023
online, rheology-esr.org/eyrs-2023/welcome, 08./09.05.2023
M. G. Schußmann, M. Wilhelm, V. Hirschberg
New Insights into Elongational Rheology of Polystyrene Pom-poms
Oral

14th International Symposium on Ionic Polymerization
Ghent, Belgium, 11.-16.09.2022
M. G. Schußmann, V. Hirschberg, M.-C. Röpert, M. Wilhelm
High performance polystyrene-polyisoprene thermoplastic elastomers using PS-PI block copolymers and the pom-pom topology
Poster

Annual European Rheology Conference 2022
Sevilla, Spain, 26.-28.04.2022
M. G. Schußmann, V. Hirschberg, M.-C. Röpert, M. Wilhelm
High performance polystyrene-polyisoprene thermoplastic elastomers using PS-PI block copolymers and the pom-pom topology
Poster

Invited Seminars

"Synthesis and rheology of branched (block co-) polymer model systems"
M. G. Schußmann, V. Hirschberg*, and M. Wilhelm*
Invited by Prof. Yuichi Masubuchi, Nagoya University, 08.03.2024

"Elongational Rheology of PS Pom-pom Model Systems"
M. G. Schußmann, M. Röpert, V. Hirschberg*, and M. Wilhelm*
Invited by Prof. Evelyne van Ryumbeke, UC Louvain, 16.09.2022